ANALYSIS AND PREDICTION OF DRYLAND LAND-SURFACE PROCESSES AND THEIR INFLUENCE ON THE METEOROLOGY OF THE INTERMOUNTAIN WEST

by

Jeffrey Duffus Massey

A dissertation submitted to the faculty of
The University of Utah
in partial fulfillment of the requirements for the degree of

Doctor of Philosophy

Department of Atmospheric Sciences

The University of Utah

August 2015

The University of Utah Graduate School

STATEMENT OF DISSERTATION APPROVAL

The dissertation of **Jeffrey Duffus Massey**

has been approved by the following supervisory committee members:

William James Steenburgh	, Chair	**28 May 2015** Date Approved
Jason C. Knievel	, Member	**28 May 2015** Date Approved
Sebastian W. Hoch	, Member	**28 May 2015** Date Approved
John D. Horel	, Member	**28 May 2015** Date Approved
Zhaoxia Pu	, Member	**28 May 2015** Date Approved

and by **Kevin D. Perry** , Chair/Dean of

the Department/College/School of **Atmospheric Sciences**

and by David B. Kieda, Dean of The Graduate School.

ABSTRACT

This dissertation examines the performance of Weather Research and Forecasting (WRF) model near-surface temperature and surface energy balance forecasts over Dugway Proving Ground (DPG) in northwest Utah during the Mountain Terrain Atmospheric Modeling and Observations Program (MATERHORN) field campaigns. This region of complex terrain has two distinct land surfaces, playa and sparsely vegetated desert shrub, which are common in other dryland regions. Operational WRF forecasts show persistent underprediction of the diurnal temperature range due to a nighttime warm bias and a daytime cold bias. The former is especially strong over the desert shrub. The nighttime warm bias can be improved through the utilization of in situ soil moisture observations and by replacing Johansen's 1975 parameterization of soil thermal conductivity in the Noah land surface model with that proposed by McCumber and Pielke in 1981 for silt loam and sandy loam soils.

The daytime cold bias extends from the surface to above the top of the planetary boundary layer and is primarily caused by a regional overestimation of near-surface soil-moisture in operational land-surface analyses, which do not currently assimilate in situ soil-moisture observations. Bias correction of the soil-moisture analyses across the Intermountain West using North American Soil Moisture Database observations reduces the daytime cold bias.

Utilization of observed soil moisture and the McCumber and Pielke soil thermal conductivity parameterization also improves the surface energy balance forecast over the desert shrub, but degrades it over the playa. Land surface processes unique to the playa are not currently accounted for in the Noah land surface model. Nevertheless, a larger and more accurate temperature gradient develops between the playa and desert shrub that forces a stronger daytime off-playa breeze. However, 10-m wind speed and direction forecasts show limited statistically significant improvement.

This dissertation also presents a climatology of episodic dust events across the Intermountain West and locates dust source regions through a dust retrieval algorithm adapted for data from geostationary operational environmental satellites.

TABLE OF CONTENTS

ABSTRACT iii

LIST OF TABLES viii

ACKNOWLEDGEMENTS ix

Chapters

1. INTRODUCTION 1

    1.1 Motivation 1
    1.2 Systematic NWP Temperature Errors 2
    1.3 Soil Moisture 4
    1.4 MATERHORN Field Campaigns 8
    1.5 Objectives and Outline 9
    1.6 References 13

2. SENSITIVITY OF NEAR-SURFACE TEMPERATURE FORECASTS TO SOIL PROPERTIES OVER A SPARSELY VEGETATED DRYLAND REGION 18

    2.1 Abstract 18
    2.2 Introduction 19
    2.3 Data and Methods 22
        2.3.1 Operational NST Forecasts 22
        2.3.2 Case Studies 24
        2.3.3 Validation and Methods 27
        2.3.4 MATERHORN Observations 28
    2.4 Results 29
        2.4.1 Systematic Biases in Operational NST Forecasts 29
        2.4.2 Potential Error Sources 30
        2.4.3 Case Studies 34
            2.4.3.1 2011-DRY 34
            2.4.3.2 2011-WET 37
            2.4.3.3 MATERHORN-IOP5 38
        2.4.4 Observed Soil Thermal Conductivity 40
    2.5 Conclusions 41
    2.6 References 64

3. REGIONAL SOIL-MOISTURE BIASES AND THEIR INFLUENCE ON WRF MODEL TEMPERATURE FORECASTS OVER THE INTERMOUNTAIN WEST 70

3.1 Abstract 70
3.2 Introduction 71
3.3 Data and Methods 74
3.3.1 WRF Modeling 74
3.3.1.1 Operational WRF (4DWX-DPG) Forecasts 74
3.3.1.2 Single-Column Model (SCM) 77
3.3.1.3 Retrospective Simulations 78
3.3.2 Validation Data and Methods 78
3.3.3 Soil Moisture Observations 79
3.4 Results 80
3.4.1 Bias Error Characteristics 80
3.4.2 Near-Surface Soil Moisture Biases 83
3.4.3 SCM Simulations 84
3.4.3.1 Soil Moisture 85
3.4.3.2 Zilitinkevich Coefficient 85
3.4.3.3 Radiation Schemes 86
3.4.3.4 PBL Schemes 87
3.4.4 Retrospective Simulations 88
3.5 Conclusions 92
3.6 References 112

4. SIMULATED AND OBSERVED SURFACE ENERGY BALANCE CONTRASTS AND RESULTING PLAYA BREEZES DURING THE MATERHORN FIELD CAMPAIGNS 117

4.1 Abstract 117
4.2 Introduction 118
4.3 Data and Methods 121
4.3.1 Surface Energy Balance Stations 121
4.3.1.1 SEB Measurements 122
3.3.1.2 Residual Correction 123
4.3.2 Surface Temperature and Wind Observations 124
4.3.3 WRF Modeling 125
4.4 Results 130
4.4.1 SEB Validation 130
4.4.1.1 MATERHORN-Fall 130
4.4.1.2 MATERHORN-Spring 133
4.4.2 *H* and 2-m Temperature Contrasts Between EFS-DS and EFS-Playa 135
4.4.3 Playa Breezes 138
4.5 Conclusions 141
4.6 References 165

5. EPISODIC DUST EVENTS OF UTAH'S WASATCH FRONT AND ADJOINING REGION 169

5.1 Abstract 169
5.2 Introduction 170
5.3 Data and Methods 173
5.3.1 Long-Term Climatology 173
5.3.2 Synoptic Classification of Recent Dust Events 175
5.3.5 Dust Emission Sources 176
5.4 Results 178
5.4.1 Long-Term Climatology 178
5.4.2 Recent (2001–10) Events 181
5.4.3 Dust Emission Sources 185
5.5 Conclusions 186
5.6 References 211

6. CONCLUSION 216

6.1 Summary of Findings 216
6.2 Future Work 219

LIST OF TABLES

2.1. Mean initialized 5-cm volumetric soil moisture (m^3 m^{-3})..... 44

3.1 Summary of 4DWX-MATERHORN simulations.....95

4.1 MATERHORN-Fall EFS site availability.....145

4.2 Mean albedos at EFS-DS and EFS-Playa during MATERHORN-Fall and MATERHORN-Spring.....146

5.1 The DS-3505 dust-related present-weather categories, along with full and abbreviated descriptions (the latter are used in the text), total number of reports, and number of reports used in the analysis (in parentheses).....189

5.2 Date and primary synoptic conditions of recent (2001–10) dust events at KSLC. Abbreviations are AC (airmass convection), CF/BT (cold front or baroclinic trough entering Utah from the west or northwest), SF/BT (stationary or slowly moving front or baroclinic trough to the west or northwest of Utah), and O (other synoptic conditions).....191

ACKNOWLEDGEMENTS

I would first like to acknowledge my wife, Courtney, without whom this work would not be possible. This work was conducted in pursuit of a Doctor of Philosophy degree with valuable guidance and input provided by committee members Drs. Jim Steenburgh, Jason Knievel, Sebastian Hoch, John Horel, and Zhaoxia Pu. I want to thank Jim in particular for his outstanding advising over the past five years. I also thank my fellow MATERHORN participants, especially Eric Pardyjak, Joshua Hacker, Fotini Chow, Stephan de Wekker, and Dave Whiteman for their input and contributions. I also thank Trenton Ford and Steven Quiring of Texas A&M for providing the North American Soil Moisture Database data and Will Cheng, Michael Barlage, Fei Chen of NCAR for their input and contributions during visits to NCAR made possible by the NCAR Advanced Study Program. I gratefully acknowledge the provision of datasets, software and/or computer time and services provided by NCDC, NCEP, NCAR, Unidata, the University of Wyoming, and the University of Utah Center for High Performance Computing. This research was funded by Office of Naval Research Award N00014-11-1-0709, the U.S. Army Test and Evaluation Command, the National Science Foundation Grant AGS-0627937, NASA Grant NNX10AO97G, and USDA Forest Service Agreement 10-PA-11041914-045. Any opinions, findings, and conclusions or recommendations expressed in this dissertation are those of the author and do not necessarily reflect the views of the funding agencies.

CHAPTER 1

INTRODUCTION

1.1 Motivation

Near-surface weather forecasts are critical for the protection of life and property, economic and operational activities, and routine day-to-day planning. Aviation, military, wind energy, and energy consumption operations rely on accurate near-surface forecasts and even small forecast errors can have major consequences. Temperature, wind, and precipitation are some of the more important variables to forecast, but visibility reducing phenomena, such as dust, fog, and smog, also need to be accurately forecast. Therefore, improving forecasts for any of these near-surface variables has far reaching significance.

Northern Utah, located in the Great Basin region of the continental United States, is a forecast sensitive region of complex terrain with two major interstates, the Salt Lake City international airport, and several military installations. Dugway Proving Ground, Hill Air Force Base, and the Utah Test and Training Range, in particular, conduct many temperature, wind, and visibility sensitive military operations. However, northern Utah also experiences a variety of high-impact weather phenomena such as strong cold fronts, dust events, and extreme heat and cold that affect near-surface conditions and need to be forecasted accurately. Identifying and reducing NWP near-surface and boundary layer

errors will improve weather forecasts and strengthen the decision-making ability of industries that rely on accurate near-surface weather forecasts.

1.2 Systematic NWP Temperature Errors

Systematic temperature errors in NWP models have been observed in many different modeling systems throughout the world. For example, systematic biases were found over complex terrain in the Global Forecast System (GFS) model (Werth and Garrett 2001), over the high latitudes in the European Centre for Medium-Range Weather Forecasts (ECMWF) model (Viterbo and Betts 1999), over the European Alps in the Weather Research and Forecasting (WRF; Skamarock et al. 2008) model (Garcia-Diez et al. 2012), and over Oklahoma in the operational Eta model (Marshall et al. 2003). These studies ran many sequential simulations over a long period to identify these errors and to ensure they are robust and systematic. Many model validation studies only validate a particular event at a particular location, precluding the identification of systematic model errors. However, systematic model errors can be identified by examining recurring model errors over similar geographical regions. For example, several studies identify an underprediction of the diurnal 2-m temperature cycle (DTR) over the western United States, with an overprediction of 2-m temperatures in the early morning and an underprediction during the afternoon for a wide range of modeling systems, resolutions, and configurations (e.g., Cheng and Steenburgh 2005; Hart et al. 2005; Zhang et al. 2013; Massey et al. 2014).

Recently, NCAR's Development Testbed Center (DTC) ran 239 sequential 36-h WRF simulations at 15 km resolution for a domain covering the entire continental United

States and not only confirmed the underestimation of the 2-m diurnal temperature cycle across the western United States, but also uncovered a myriad of other systematic errors. These errors include a persistent cold bias that is strongest in the winter, a daytime high dewpoint temperature bias over the upper Midwest, and a high wind bias that is greatest at night (Michelle Harrold; personal communication). The goal of this DTC study was to compare the Noah and Noah-MP land surface models (LSMs), but both LSMs produced similar bias errors. Optimizing model performance by changing parameterization schemes can be beneficial, but in order to uncover the fundamental problems that plague mesoscale models, like the ones found in the DTC study, a more in depth examination of the parameterizations and their initialization is needed.

This dissertation focuses on the systematic underestimation of the diurnal temperature cycle across the Great Basin because this error was the most pervasive during the study period. Hypothesized contributors to the DTR underprediction include inadequate vertical or horizontal resolution, near-surface turbulence flux errors, inaccurate land-surface characteristics and processes, differences between model and observation site elevations, radiation parameterization errors due to the absence of 3-dimensional scattering in complex terrain or tuning for lower elevations, inadequate planetary boundary layer parameterization, or excessive mountain cloud development (e.g., Hanna and Yang 2001; Mass et al. 2002; Marshall et al. 2003; Zhong and Fast 2003; Cheng and Steenburgh 2005; Liu et al. 2008; Hu et al. 2010; Wyszogrodzki et al. 2013; Massey et al. 2014). An investigation of all of these error sources is beyond the scope of this dissertation, so we focus on errors relating to the land surface initialization

and parameterization. Unpublished sensitivity tests showed these errors to be most important to the model errors observed over the Great Basin.

Mesoscale NWP models, such as the WRF, use a coupled LSM to diagnose the surface heat and moisture fluxes into the atmosphere. Recent increases to model resolution and sophistication have required more advanced LSMs, such as the Noah LSM, that attempt to simulate the land-surface forcing by topography, soil moisture, surface vegetation, and other land-surface characteristics (Chen and Dudhia 2001; Ek et al. 2003). These land-surface characteristics can affect convection initiation and precipitation distribution (e.g., Holt et al. 2006; Trier et al. 2008; Case et al. 2011), near-surface temperatures (e.g., Huang et al. 1996; Davis et al. 1999; Marshall et al. 2003) and thermally forced circulations resulting from land-surface heterogeneities (e.g., Ookouchi et al. 1984; Avissar and Pielke 1989; Banta and Gannon 1995; Rife et al. 2002) in NWP models. In most LSMs, land surface parameters (e.g., albedo, roughness length, and soil porosity) are defined in lookup tables and dependent upon the initialized landuse and soil texture class classifications, whereas soil moisture and temperature are derived from observational data and/or land surface modeling. In either case, the incorrect specification of these land surface characteristics contributes to NWP model errors (e.g., Huang et al. 1996; Dirmeyer et al. 2000; Rife et al. 2004).

1.3 Soil Moisture

Soil moisture is an important land-surface variable because it influences not only the temperature, wind, and relative humidity in the planetary boundary layer (PBL), but also the convective available potential energy (CAPE) and convective inhibition (CIN)

(e.g., Trier et al. 2008; Zhou and Geerts 2013). CAPE and CIN help control the occurrence and intensity of moist convection, which can in turn affect the large-scale circulation (Weaver et al. 2004). Soil moisture also affects the PBL through its control on the surface energy balance, which is the partitioning among the surface sensible, latent, and ground heat fluxes. Soil moisture influences the ratio between the sensible and latent heat fluxes (Bowen ratio; Bowen 1926) because soil moisture is evapotranspired from the surface, and influences the ground heat flux because of the soil thermal conductivity's dependence on soil water content. When soil moisture is high, the Bowen ratio is lower because more energy is used to evapotranspire soil moisture, which increases the latent heat flux and decreases the sensible heat flux. Soil moisture is evaporated from bare soils near the surface, and transpired from vegetated regions, where plants can tap into deeper soil moisture. Higher soil moisture also increases the magnitude of the ground heat flux because water has a higher thermal conductivity than the air it replaces in the soil (Cosenza et al. 2003). It also affects the net radiation at the surface by altering the surface albedo. An increase in soil moisture tends to decrease the surface albedo, especially for playa land surfaces with dissolvable salt crusts (Isdo et al. 1975; Tapper 1988).

Several studies identify soil moisture as the single most important land-surface variable for determining the magnitudes of the surface energy fluxes (e.g., Clark and Arritt 1995; Sun and Bosilovich 1995; Crawford et al. 2001). For example, Sun and Bosilovich (1995) found that an increase in soil moisture from a very dry state to a very wet state increased the latent heat flux by 525 W m^{-2} and reduced the sensible heat flux by 300 W m^{-2} in their single column model experiments. Huang et al. (1996) found soil-

moisture anomalies to provide extra skill in predicting near-surface temperatures at lead times greater than one month.

Soil-moisture gradients may also induce near-surface thermally forced flows. Heterogeneous soil moisture creates a surface sensible heat flux gradient, and thus a near-surface temperature gradient, which drives nonclassical mesoscale circulations similar to sea breezes (Ookouchi et al. 1984; Avissar and Pielke 1989). Banta and Gannon (1995) also found soil moisture to have a large effect on the strength of katabatic flows. A slope with drier soil moisture has stronger katabatic flows than that same slope with wetter soils.

Limited-area mesoscale models, like the WRF, typically obtain their soil moisture initial conditions from operational modeling systems such as the National Centers for Environmental Prediction (NCEP) Global Forecast System (GFS) or the European Centre for Medium-Range Weather Forecasts (ECMWF) Integrated Forecast System (IFS). The LSMs that predict the land-surface state in these operational modeling systems do not currently utilize in situ soil-moisture observations (Dirmeyer et al. 2002; Dee et al. 2014). Instead, the soil moisture in the GFS LSM is nudged towards a soil-moisture climatology (Dee et al. 2014), whereas the IFS uses an extended Kalman-filter data assimilation approach that utilizes surface temperature, relative humidity, and satellite data as proxy observations to analyze soil moisture (Albergel et al. 2012a). Although we know of no published study examining soil moisture biases in the GFS, the operational IFS and Era-Interim Reanalysis are known to overestimate soil moisture, especially in drier regions (Albergel et al. 2012b).

To improve global analyses of soil moisture, a number of studies have utilized near-surface soil moisture estimates from spaceborne microwave remote sensing platforms (e.g., Jackson et al. 2010; Kerr et al. 2010). Such platforms include the Soil Moisture and Ocean Salinity mission (SMOS; Kerr et al. 2010), Advanced Microwave Scanning Radiometer–Earth Observing System (AMSR–E), and the Advanced Scatterometer (ASCAT). Although satellite soil moisture retrieval algorithms have improved in recent years, their coarse spatial resolution (> 10–30 km) and large discrepancies with in situ soil moisture observations currently limit their utility (Crow et al. 2010; Jackson et al. 2010; Al Bitar et al 2012; Albergel et al. 2012a). However, the Soil Moisture Active/Passive (SMAP) mission launched in early 2015 will measure soil moisture at higher resolution (9 km) and will provide more detailed measurements.

The Great Basin is a semi-arid region with annual precipitation of ~200–300 mm (PRISM Climate Group, Oregon State University, http://prism.oregonstate.edu), leading to relatively low climatological soil moisture. It lies in the rain shadow of the Sierra Nevada to its west, and the Rocky Mountains to its east, which prevents humid air intrusions from the Gulf of Mexico. Cloud cover is also low, especially in the summer, resulting in large potential evapotranspiration. Fortunately, the Great Basin has a relatively dense network of soil-moisture observing sites from the U.S. Department of Agriculture's Soil Climate Analysis Network (SCAN; Schaefer et al. 2007) and from Global Positioning System (GPS) soil moisture stations (Larson et al. 2008), which this dissertation will use to validate analyzed soil moisture over this unique region.

1.4 MATERHORN Field Campaigns

This dissertation also utilizes data and observations collected during the Mountain Terrain Atmospheric Modeling and Observations (MATERHORN) field campaigns that occurred 25 September – 25 October 2012 and 1 May – 31 May 2013 at Dugway Proving Ground (DPG) in northwest Utah. MATERHORN was designed to investigate complex-terrain meteorology across a range of scales using mesoscale modeling, new physical parameterizations, field experiments, and new experimental technology that symbiotically diagnose model deficiencies and critical knowledge gaps (Fernando et al. 2015). This dissertation explores deficiencies in mesoscale models and their parameterizations using observational data taken during the field campaigns.

DPG is characterized by complex basin-and-range topography (Fig. 1.1a), distinct and varying landuse types (Fig. 1.1b) and soil texture classes (Fig. 1.1d), and spatially varying albedo (Fig. 1.1c). Complicated thermally forced flows arise from these heterogeneities (e.g., Davis et al. 1999; Rife et al. 2002), which is one reason why DPG was selected as the MATERHORN experiment site. DPG sits between a playa to its northwest and a desert shrub landscape to its southeast, with Granite Peak (see Fig 1.1a for location), the focus area for the MATERHORN instrumentation, lying between these land surfaces. The playa has a higher albedo, lower Bowen ratio, and higher soil thermal conductivity than the surrounding desert shrub. These properties contribute to a lower diurnal temperature range compared to the surrounding desert shrub, resulting in a diurnally oscillating thermally forced circulation with an off-playa breeze during the day and on-playa breeze at night (Rife et al. 2002). Accurately forecasting this thermally

forced circulation is critical for DPG's wind-sensitive military testing operations (Liu et al. 2008).

MATERHORN's high spatio-temporal observations network provides a wealth of data on micro- and mesoscale phenomena and their interaction. Some of MATERHORN's key observing platforms include research aircraft and unmanned aerial systems, radiosondes, tethersondes, LiDARs, SoDARs, wind profilers, ceilometers, flux towers, radiometers, soil sensors, and surface stations. Figure 1.2 provides the location of many of these instruments during the fall 2012 and spring 2013 field campaigns. The range of observations is designed to resolve mountain and land-surface phenomena ranging from the Kolmogorov to the mesoscale (10^{-3}–10^{5} m). This dissertation will validate the WRF model using data collected from the radiosondes, soil sensors, radiometers, flux towers, and surface stations.

Although precipitation plays an important role in atmospheric phenomena in complex terrain, MATERHORN focused resources on dry and quiescent events to isolate the local scale forcing phenomena. There were 10 intensive operating periods (IOPs) for each MATERHORN period when radiosondes were launched every 3 hours for 24 or more hours. All IOPs were precipitation free, but at least 5 had a dry airmass boundary propagate through DPG allowing for synoptic scale interactions to also be sampled.

1.5 Objectives and Outline

The primary goal of this dissertation is to improve near-surface NWP predictability over an area of complex terrain and heterogeneous land surfaces. Several months of operational WRF forecasts centered over DPG underpredict the strength of the

diurnal temperature cycle compared to surface stations and sounding observations taken during the MATERHORN field campaigns. This dissertation will show how a better soil thermal conductivity parameterization, along with observed soil moisture and albedo, can mitigate the 2-m diurnal temperature cycle biases, and improve predictions of the surface energy balance. Although not directly related to the primary goal of the dissertation, a climatology of episodic dust events in the Great Basin that was completed during the early part of the author's graduate research is also presented.

The remainder of this dissertation is organized as follows. Chapter 2 describes the 2-m temperature biases over DPG and illustrates how a different soil thermal conductivity parameterization applied to silt loam and sandy loam soils, along with the use of observed soil moisture, greatly reduces the nighttime warm bias. Chapter 3 shows how the afternoon cold bias is primarily the result of a regional-scale overestimation of near-surface soil moisture and errors can be greatly reduced by bias correcting the near-surface soil moisture analyses throughout the Great Basin. Chapter 4 validates the desert shrub and playa surface energy balance and near-surface winds using observations taken during MATERHORN. This chapter also highlights some of the Noah LSM deficiencies over playa land surfaces. Chapter 5 presents a climatology of episodic dust events across the Great Basin and locates source regions through a dust retrieval algorithm adapted for data from geostationary operational environmental satellites. Chapter 6 offers conclusions gained from this dissertation and recommendations for future work to advance the understanding of boundary layer processes over the Great Basin and beyond.

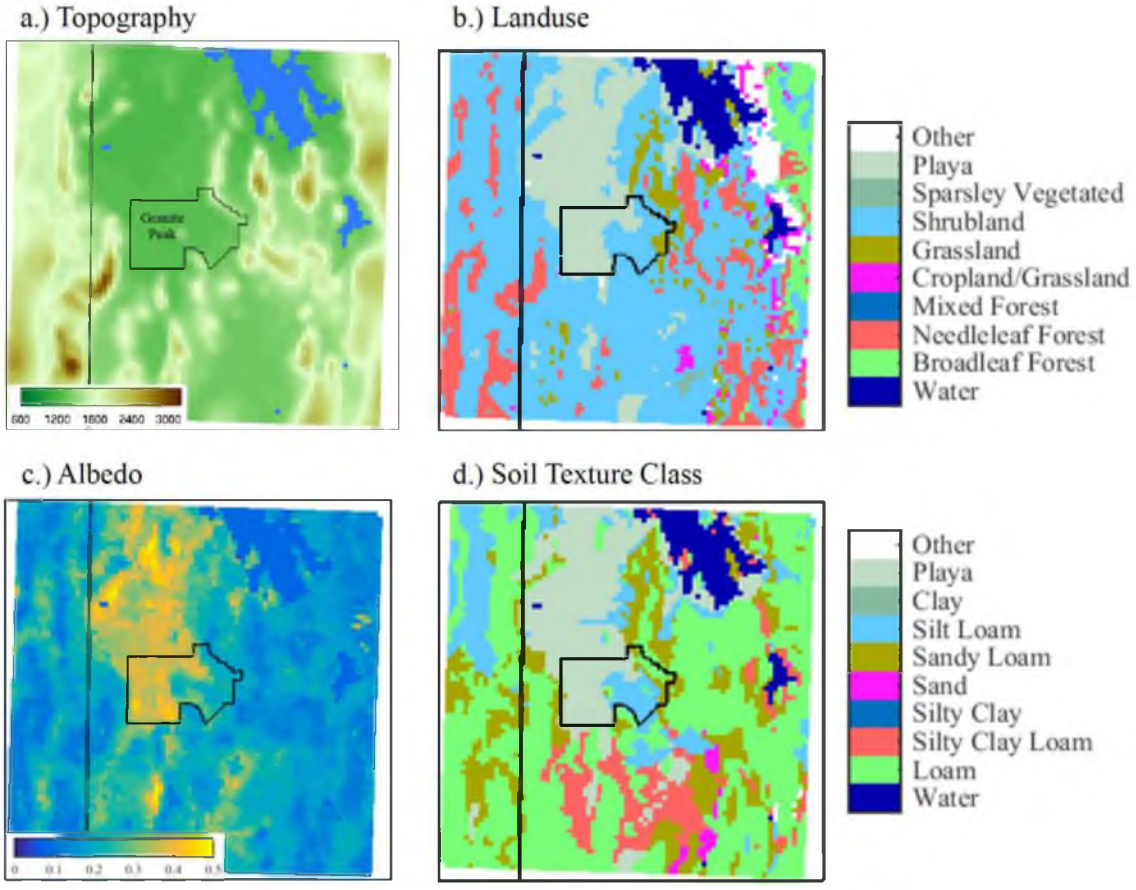

Fig. 1.1. 4DWX-DPG 3.3 km domain (a) terrain, (b) NLCD 33-category land-cover data, (c) MODIS derived albedo, and (d) USGS 19-category soil texture class. DPG and Utah/Nevada border are annotated for reference.

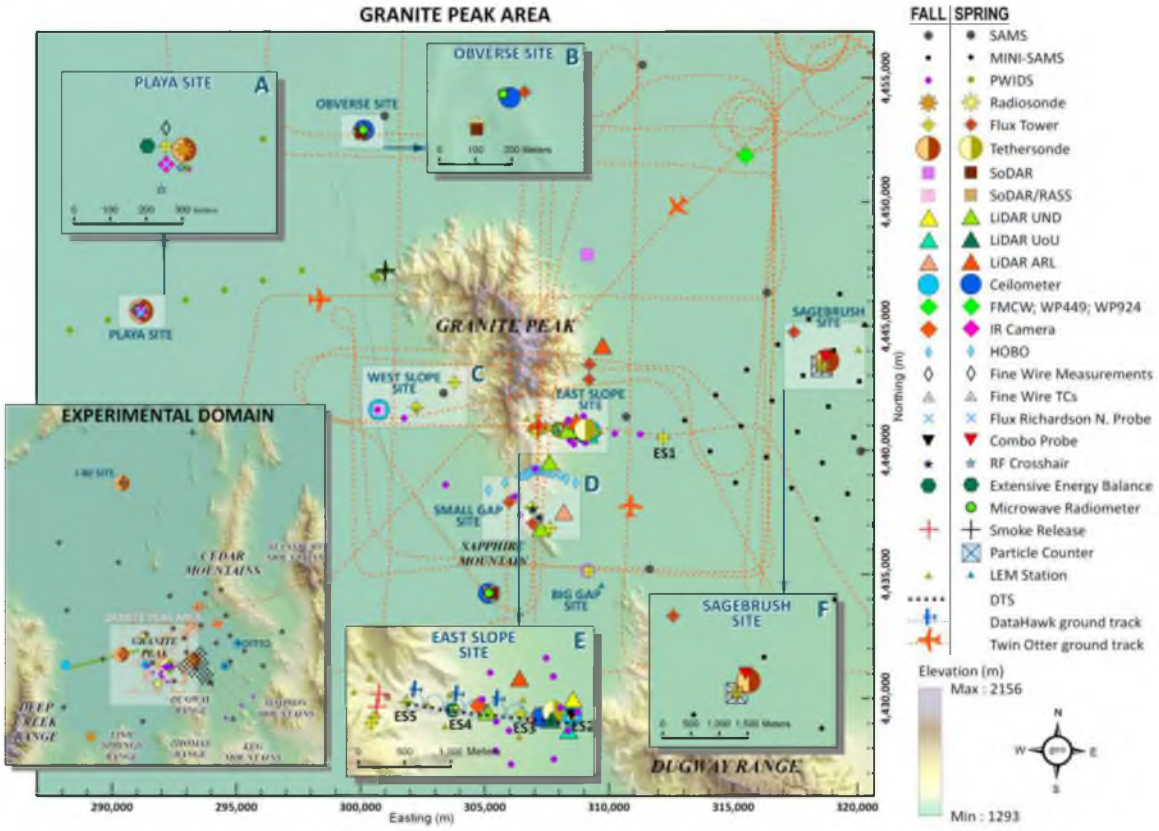

Fig. 1.2. Instrument placement during fall and spring MATERHORN campaigns. Insets provide details of specific locations as well as the full experimental domain (lower left). Only the additional instruments deployed (or relocated) for the spring experiment are shown under the SPRING column (reprinted from Fernando et al. 2015).

1.6 References

Al Bitar, A., D. Leroux, Y. H. Kerr, O. Merlin, P. Richaume, A. Sahoo, and E. F. Wood, 2012: Evaluation of SMOS soil moisture products over continental U.S. using the SCAN/SNOTEL network. *IEEE Trans. Geosci. Remote Sens.*, **50**, 1572–1586.

Albergel, C., P. de Rosnay, G. Balsamo, L. Isaksen, and J. Muñoz-Sabater, 2012a: Soil moisture analyses at ECMWF: Evaluation using global ground-based in situ observations. *J. Hydrometeor*, **13**, 1442–1460.

Albergel, C., P. de Rosnay, C. Gruhier, J. Muñoz-Sabater, S. Hasenauer, L. Isaksen, Y. Kerr, and W. Wagner, 2012b: Evaluation of remotely sensed and modelled soil moisture products using global ground-based in situ observations. *Remote Sens. Environ.,* **118**, 215–226.

Avissar, R., and R. A. Pielke, 1989: A parameterization of heterogeneous land surfaces for atmospheric numerical models and its impact on regional meteorology. *Mon. Wea. Rev.,* **117,** 2113–2136.

Banta, R. M., and P. T. Gannon, 1995: Influence of soil moisture on simulations of katabatic flow. *Theor. Appl. Climatol.*, **52,** 85–94.

Bowen, I. S., 1926: The ratio of heat losses by conduction and by evaporation from any water surface. *Phys. Rev.*, **27**, 779–787.

Case, J. L., S. V. Kumar, J. Srikishen, and G. J. Jedlovec, 2011: Improving numerical weather predictions of summertime precipitation over the southeastern United States through a high-resolution initialization of the surface state. *Wea. Forecasting*, **26**, 785–807.

Chen, F., and J. Dudhia, 2001: Coupling an advanced land surface–hydrology model with the Penn State–NCAR MM5 modeling system. Part I: Model implementation and sensitivity. *Mon. Wea. Rev.*, **129**, 569–585.

Cheng, W. Y. Y., and W. J. Steenburgh, 2005: Evaluation of surface sensible weather forecasts by the WRF and the Eta Models over the western United States. *Wea. Forecasting*, **20**, 812–821.

Clark, C. A., and R. W. Arritt, 1995: Numerical simulations of the effect of soil moisture and vegetation cover on the development of deep convection. *J. Appl. Meteor*, **34**, 2029–2045.

Cosenza, P., R. Guerin, and A. Tabbagh, 2003. Relationship between thermal conductivity and water content of soils using numerical modeling. *European Journal of Soil Science*, **54**, 581-587.

Crawford, T. M., D. Stensrud, F. Mora, J. Merchant, and P. Wetzel, 2001: Value of incorporating satellite-derived land cover data in MM5/PLACE for simulating surface temperatures. *J. Hydrometeor.*, **2**, 453–468.

Crow W. T., D. G. Miralles, and M. H. Cosh, 2010: A quasi-global evaluation system for satellite-based surface soil moisture retrievals. *IEEE Trans. Geosci. Remote Sens.*, **48**, 2516–2527.

Davis, C., T. Warner, E. Astling, and J. Bowers, 1999: Development and application of an operational, relocatable, meso-gammascale weather analysis and forecasting system. *Tellus*, **51A**, 710–727.

Dee, D. P, M. Balmaseda, G. Balsamo, R. Engelen, A. J. Simmons, and J.-N. Thépaut, 2014: Toward a consistent reanalysis of the climate system. *Bull. Amer. Meteor. Soc.*, **95**, 1235–1248.

Dirmeyer, P. A., F. J. Zeng, A. Ducharne, J. C. Morrill, and R. D. Koster, 2000: The sensitivity of surface fluxes to soil water content in three land surface schemes. *J. Hydrometeor.*, **1**, 121–134.

Dirmeyer, P. A., X. Gao, and T. Oki, 2002: The Second Global Soil Wetness Project (GSWP2). International GEWEX Project Office Publication, **37**, 75.

Ek M. B., K. E. Mitchell, Y. Lin, E. Rogers, P. Grunmann, V. Koren, G. Gayno, and J. D. Tarplay, 2003: Implementation of the Noah land-use model advances in the NCEP operational mesoscale Eta model. *J. Geophys. Res.*, **108**, 8851.

Fernando, H. J., and Coauthors, 2015: The MATERHORN – Unraveling the intricacies of mountain weather. *Bull. Amer. Meteor. Soc.*, in press.

García-Díez, M., J. Fernández, L. Fita, and C. Yagüe, 2013, Seasonal dependence of WRF model biases and sensitivity to PBL schemes over Europe, *Q. J. R. Meteorol. Soc.*, **139**, 501–514.

Hanna, S. R., and R. Yang, 2001: Evaluations of mesoscale models' simulations of near-surface winds, temperature gradients, and mixing depths. *J. Appl. Meteor.*, **40**, 1095–1104.

Hart, K. A., W. J. Steenburgh, and D. J. Onton, 2005: Model forecast improvements with decreased horizontal grid spacing over finescale intermountain orography during the 2002 Olympic Winter Games. *Wea. Forecasting*, **20**, 558–576.

Holt, T. R., D. Niyogi, F. Chen, K. Manning, M. A. LeMone, and A. Qureshi, 2006: Effect of land–atmosphere interactions on the IHOP 24–25 May 2002 convection case. *Mon. Wea. Rev.*, **134**, 113–133.

Hu, X-M., J. W. Nielsen-Gammon, and F. Zhang, 2010: Evaluation of three planetary boundary layer schemes in the WRF model. *J. Appl. Meteor. Climatol.*, **49**, 1831–1844.

Huang, J., H. M. van den Dool, and K. P. Georgarakos, 1996: Analysis of model-calculated soil moisture over the United States (1931–1993) and applications to long-range temperature forecasts. *J. Climate*, **9**, 1350–1362.

Idso, S., R. Jackson, B. Kimball, and F. Nakayama, 1975: The dependence of bare soil albedo on soil water content. *J. Appl. Meteor.*, **14**, 109–113.

Jackson, T. J., and Coauthors, 2010: Validation of advanced microwave scanning radiometer soil moisture products. *IEEE Trans. Geosci. Remote Sens.*, **48**, 4256–4272.

Kerr, Y. H., and Coauthors, 2010: The SMOS mission: New tool for monitoring key elements of the global water cycle. *Proc. IEEE*, **98**, 666–687.

Larson, K. M., E. E. Small, E. Gutmann, A. Bilich, J. Braun, and V. Zavorotny, 2008: Use of GPS receivers as a soil moisture network for water cycle studies, *Geophys. Res. Lett.*, **35**, L24405.

Liu, Y., and Coauthors, 2008: The operational mesogamma-scale analysis and forecast system of the U.S. army test and evaluation command. Part I: Overview of the modeling system, the forecast products, and how the products are used. *J. Appl. Meteor. Climatol.*, **47**, 1077–1092.

Marshall, C. H., K. C. Crawford, K. E. Mitchell, and D. J. Stensrud, 2003: The impact of the land surface physics in the operational NCEP eta model on simulating the diurnal cycle: evaluation and testing using Oklahoma mesonet data. *Wea. Forecasting*, **18**, 748–768.

Marshall, C. H., K. C. Crawford, K. E. Mitchell, and D. J. Stensrud, 2003: The impact of the land surface physics in the operational NCEP eta model on simulating the diurnal cycle: evaluation and testing using Oklahoma mesonet data. *Wea. Forecasting*, **18**, 748–768.

Mass, C. F., D. Ovens, K. Westrick, and B. A. Colle, 2002: Does increasing horizontal resolution produce more skillful forecasts? The results of two years of real-time numerical weather prediction over the Pacific Northwest. *Bull. Amer. Meteor. Soc.*, **83,** 407–430.

Massey, J. D., W. J. Steenburgh, S. W. Hoch, and J. C. Knievel, 2014: Sensitivity of near-surface temperature forecasts to soil properties over a sparsely vegetated dryland region. *J. Appl. Meteor. Climatol.*, **53**, 1976–1995.

Ookouchi, Y., M. Segal, R. C. Kessler, and R. A. Pielke, 1984: Evaluation of soil moisture effects on the generation and modification of mesoscale circulations. *Mon. Wea. Rev.*, **112,** 2281–2292.

Rife, D. L., T. T. Warner, F. Chen, and E. G. Astling, 2002: Mechanisms for diurnal boundary layer circulations in the Great Basin Desert. *Mon. Wea. Rev.*, **130**, 921–938.

Rife, D. L., C. A. Davis, Y. Liu, T. T. Warner, 2004: Predictability of low-level winds by mesoscale meteorological models. *Mon. Wea. Rev.*, **132**, 2553–2569.

Schaefer, G. L., M. H. Cosh, and T. J. Jackson, 2007: The USDA natural resources conservation service soil climate analysis network (SCAN). *J. Atmos. Oceanic Technol.*, **24**, 2073–2077.

Skamarock, W. C., and Coauthors, 2008: A description of the advanced research WRF version 3. NCAR Tech. Note TN-475_STR, 113 pp.

Sun, W. Y., and M. G. Bosilovich, 1996: Planetary boundary layer and surface layer sensitivity to land surface parameters. *Boundary-Layer Meteorology*, 77, 353−378.

Tapper, N. J., 1988: Some evidence for a mesoscale thermal circulation at The Salt Lake, New South Wales. *Aust. Meteor. Mag.*, **36**, 101–102.

Trier, S. B., F. Chen, K. W. Manning, M. A. LeMone, and C. A. Davis, 2008: Sensitivity of the PBL and precipitation in 12-day simulations of warm-season convection using different land surface models and soil wetness conditions. *Mon. Wea. Rev.*, **136**, 2321–2343.

Viterbo, P. and A. K. Betts, 1999: The impact on ECMWF forecasts to changes to the albedo of the boreal forests in the presence of snow. *J. Geophys. Res.*, **104**, 361– 366.

Weaver, C. P., 2004: Coupling between large-scale atmospheric processes and mesoscale land–atmosphere interactions in the U.S. Southern Great Plains during summer. Part I: Case studies. *J. Hydrometeor.*, **5**, 1223–1246.

Werth, D., and A. Garrett, 2011: Patterns of land surface errors and biases in the Global Forecast System. *Mon. Wea. Rev.*, **139**, 1569–1582.

Wyszogrodzki, A. A., Liu, Y., Jacobs, N., Childs, P., Zhang, Y., Roux, G., & Warner, T. T., 2013: Analysis of the surface temperature and wind forecast errors of the NCAR-AirDat operational CONUS 4-km WRF forecasting system. *Meteorology and Atmospheric Physics*, ***122***, 125-143.

Zhang, H., Z. Pu, X. Zhang, 2013: Examination of errors in near-surface temperature and wind from WRF numerical simulations in regions of complex terrain. *Wea. Forecasting*, **28**, 893–914.

Zhong, S., and J. Fast, 2003: An evaluation of the MM5, RAMS, and Meso-Eta models at subkilometer resolution using VTMX field campaign data in the Salt Lake Valley. *Mon. Wea. Rev.*, **131,** 1301–1322.

Zhou, X., and B. Geerts, 2013: The Influence of soil moisture on the planetary boundary layer and on cumulus convection over an isolated mountain. Part I: Observations. *Mon. Wea. Rev.*, **141**, 1061–1078.

CHAPTER 2[1]

SENSITIVITY OF NEAR-SURFACE TEMPERATURE FORECASTS TO SOIL PROPERTIES OVER A SPARSELY VEGETATED DRYLAND REGION

2.1 Abstract

Weather Research and Forecasting Model forecasts over the Great Salt Lake Desert erroneously underpredict nocturnal cooling over the sparsely vegetated silt loam soil area of Dugway Proving Ground in northern Utah, with a mean positive bias error in temperature at 2 m AGL of 3.4°C in the early morning [1200 UTC (0500 LST)]. Positive early-morning bias errors also exist in nearby sandy loam soil areas. These biases are related to the improper initialization of soil moisture and parameterization of soil thermal conductivity in silt loam and sandy loam soils. Forecasts of 2-m temperature can be improved by initializing with observed soil moisture and by replacing Johansen's 1975 parameterization of soil thermal conductivity in the Noah land surface model with that proposed by McCumber and Pielke in 1981 for silt loam and sandy loam soils. Case studies illustrate that this change can dramatically reduce nighttime warm biases in 2-m temperature over silt loam and sandy loam soils, with the greatest improvement during

[1] Chapter 2 is reprinted from the following journal article: Jeffrey D. Massey, W. James Steenburgh, Sebastian W. Hoch, and Jason C. Knievel, 2014: Sensitivity of near-surface temperature forecasts to soil properties over a sparsely vegetated dryland region. *J. Appl. Meteor. Climatol.*, **53**, 1976–1995.

periods of low soil moisture. Predicted ground heat flux, soil thermal conductivity, near-surface radiative fluxes, and low-level thermal profiles also more closely match observations. Similar results are anticipated in other dryland regions with analogous soil types, sparse vegetation, and low soil moisture.

2.2 Introduction

Near-surface (2 m) temperature (NST) forecasts are critical for the protection of life and property, for economic and operational activities, and for routine day-to-day planning but remain a major challenge for numerical weather prediction. Modeling systems in many regions of the world have trouble simulating NSTs and typically underpredict the diurnal NST cycle, which largely reflects a pronounced nighttime NST warm bias (e.g., Steeneveld et al. 2008; Edwards et al. 2011; Kilpelainen et al. 2012; Holtslag et al. 2013; Ngan et al. 2013). These errors are especially prevalent in high-resolution modeling systems (<5-km grid spacing) over many regions of the western United States (e.g., Mass et al. 2002; Cheng and Steenburgh 2005; Hart et al. 2005; Zhang et al. 2013). By influencing low-level stratification, boundary layer depth and mixing, thermally driven flows, and convective initiation, NST forecast errors ultimately affect the prediction of precipitation (amount and type), fog and clouds, air quality, and surface and boundary layer winds (e.g., Hanna and Yang 2001; Rife et al. 2002; Marshall et al. 2003; Holt et al. 2006).

There have been numerous hypotheses concerning the sources of these NST forecast errors ranging from inadequate horizontal or vertical resolution to the inaccurate initialization and parameterization of boundary layer and land surface characteristics and

processes (e.g., Hanna and Yang 2001; Mass et al. 2002; Marshall et al. 2003; Cheng and Steenburgh 2005). In this paper, we concentrate on the initialization and parameterization of land surface characteristics and processes, which control the surface energy budget and contribute to NST errors through the inaccurate partitioning of sensible, latent, and ground heat fluxes (e.g., Huang et al. 1996; Davis et al. 1999; Marshall et al. 2003; Reeves et al. 2011). In most land surface models (LSMs), land surface parameters (e.g., albedo, roughness length, and soil porosity) are specified using land-use and soil-type databases, whereas soil moisture and temperature are derived from observational data and/or land surface modeling. In either case, the incorrect specification of these land surface characteristics is at least partly responsible for NST forecast errors (e.g., Huang et al. 1996; Dirmeyer et al. 2000; Rife et al. 2004; Wen et al. 2012).

Soil moisture is an important initialized variable because it strongly influences NSTs, surface and boundary layer winds, and the development of moist convection (e.g., Ookouchi et al. 1984; Avissar and Pielke 1989; Segal et al. 1989; Doran and Zhong 1995; Banta and Gannon 1995; Huang et al. 1996; Holt et al. 2006; Zhou and Geerts 2013), but a lack of in situ observations, combined with instrument and representativeness errors, limits reliable soil-moisture assimilation (e.g., Dirmeyer et al. 2000; Godfrey and Stensrud 2008; Liu et al. 2011). As a result, most soil-moisture analyses are based on either land surface model simulations forced by meteorological data (Dirmeyer et al. 2002) or low-resolution satellite soil-moisture retrievals that can only retrieve shallow soil moisture (Jackson et al. 2010).

Soil moisture has a direct influence on the ratio of surface sensible and latent heat fluxes (i.e., the Bowen ratio; Bowen 1926) but can also affect the surface energy balance

by altering the surface albedo and the soil thermal conductivity. An increase in soil moisture tends to decrease the surface albedo, especially for playa land surfaces with dissolvable salt crusts (Idso et al. 1975; Tapper 1988), and to increase the soil thermal conductivity since water has a higher thermal conductivity than the air it replaces (Cosenza et al. 2003). Soil thermal conductivity is difficult to estimate because it is a function of the volume fractions of water, air, and soil; the mineral composition of the soil; and the numerous interactions among these variables (Farouki 1986). Although there are several soil thermal conductivity estimates (e.g., Kersten 1949; de Vries 1963; Johansen 1975; McCumber and Pielke 1981; McInnes 1981; Campbell 1985), the complexity of soil structure and the processes involved preclude a physically accurate and mechanistically based predictive model (Tarnawski et al. 2009). McCumber and Pielke (1981) offer a simple method (hereinafter referred to as MP81) to estimate soil thermal conductivity that was incorporated into several LSMs, including early versions of the National Centers for Environmental Prediction–Oregon State University–U.S. Air Force–Office of Hydrologic Development LSM known as Noah (e.g., Noilhan and Planton 1989; Ek and Mahrt 1991; Viterbo and Beljaars 1995; Chen and Dudhia 2001; Ek et al. 2003). MP81 produces higher-than-observed soil thermal conductivity in very wet conditions and lower-than-observed soil thermal conductivity in dry conditions for some soil textures (Peters-Lidard et al. 1998). For this reason, MP81 was replaced by the Johansen (1975) method (hereinafter referred to as J75) in the version of the Noah LSM that is coupled to the Weather Research and Forecasting (WRF) Model (Skamarock et al. 2008), which is considered to be one of the most accurate parameterizations for land surface modeling (e.g., Farouki 1986; Peters-Lidard et al. 1998). More recent

parameterizations have adopted J75 but have modified its variables (Tarnawski and Leong 2000; Balland and Arp 2005; Côté and Konrad 2005; Lu et al. 2007).

In this paper we examine the causes of NST forecast errors produced by WRF over Dugway Proving Ground (DPG) in the Great Salt Lake Desert of northwestern Utah (Fig. 2.1). This dryland region features an extensive playa that is surrounded by sparsely vegetated desert, which has a lower albedo, lower soil moisture, larger Bowen ratio, and lower soil thermal conductivity than the playa. These properties contribute to a larger diurnal temperature range (DTR) over the sparsely vegetated desert than the playa (Rife et al. 2002), and forecasting the resulting thermally forced flows (Tapper 1988) is paramount to DPG's wind-sensitive military testing operations (Liu et al. 2008). We will show that operational and retrospective WRF simulations typically underpredict the diurnal temperature cycle over silt loam and sandy loam soils in the sparsely vegetated desert, with a pronounced nighttime warm bias. This bias can be reduced by improving the initialization of soil moisture and by using MP81 for silt loam and sandy loam soils.

2.3 Data and Methods

2.3.1 Operational NST Forecasts

Four months of NST forecasts for DPG were examined to identify biases in WRF. We concentrate on September and October of 2011 and 2012 because these months are most relevant to the Mountain Terrain Atmospheric Modeling and Observations (MATERHORN) autumn 2012 field campaign, held at DPG from 25 September to 25 October 2012. We refer to September–October of 2011 and September–October of 2012 as the pre-MATERHORN and MATERHORN periods, respectively.

The source of the forecasts is the U.S. Army Test and Evaluation Command Four-Dimensional Weather System (4DWX), developed by the National Center for Atmospheric Research (NCAR). We used two versions of the 4DWX run for DPG (4DWX-DPG). In 2011 the system was based on version 3.2 of WRF, and in 2012 it was based on version 3.3.1 of WRF, which updated the urban land-use parameters and allows the Noah LSM to take seasonal roughness-length changes into account. The 4DWX-DPG has 30-, 10-, 3.3-, and 1.1-km one-way nested domains centered over DPG (Liu et al. 2008; Fig. 2.2). The use of one-way nesting reflects its superiority over two-way nesting in unpublished test cases. The vertical spacing of the 36 half-η levels varies from ~30 m near the surface, with the lowest half-η level at ~15 m AGL, to ~1250 m in the upper troposphere and lower stratosphere. The physics packages include the Rapid Radiative Transfer Model longwave radiation parameterization (Mlawer et al. 1997), Dudhia shortwave radiation parameterization (Dudhia 1989), Noah LSM (Chen and Dudhia 2001), Yonsei University planetary boundary layer parameterization (Hong et al. 2006), Lin et al. (1983) microphysics, new Kain–Fritsch cumulus parameterization (Kain 2004), and explicit sixth-order numerical diffusion (Knievel et al. 2007). The atmospheric data assimilation cycle uses Newtonian nudging over a 3-h period to assimilate observations from aviation routine weather report (METAR) stations, rawinsondes, profilers, buoys, aircraft, satellites, and other observing platforms (Liu et al. 2008). 4DWX-DPG is run every 3 h for eight times per day (0200, 0500, 0800, 1100, 1400, 1700, 2000, and 2300 UTC) and produces 48-h forecasts. Liu et al. (2008) provide additional information on the physic packages and data assimilation of 4DWX.

Land surface (e.g., albedo, roughness length, and emissivity) and soil (e.g., porosity, quartz content, and wilting point) parameters are fixed for each land-use category and soil-texture class, respectively. These parameters are found in lookup tables, which were compiled from a variety of studies (e.g., Cosby et al. 1984; Mahfouf et al. 1995; Peters-Lidard et al. 1998). In 2011 4DWX-DPG was initialized with the standard geographic data available with the community version of the WRF Model, modified to include three additional land-cover categories of playa, white sand, and lava. In 2012, the land-cover and terrain elevation were updated on the basis of the newer 33-category National Land Cover Database dataset (Fry et al. 2011), which increased the area defined as playa. The soil-texture class is defined by a 16-category U.S. Geological Survey dataset, which is also modified to include playa, white sand, and lava soil-texture classes. Initial soil-moisture and soil-temperature fields at 5-, 25-, 70-, and 150-cm depths are obtained from a relatively coarse 1.0° Global Forecasting System (GFS) analysis because anecdotal evidence suggests that under some circumstances it outperforms the 12-km North American Model (NAM) analysis at DPG. These fields are interpolated to 4DWX-DPG using the default WRF preprocessing interpolation schemes of 16-point parabolic interpolation away from water bodies and four-point or nearest-neighbor interpolation near water bodies.

2.3.2 Case Studies

We examine in detail three 36-h periods with quiescent large-scale conditions during the pre-MATERHORN and MATERHORN periods to isolate local land–atmosphere processes. The first, hereinafter called 2011-DRY (1200 UTC 22 September

2011–0000 UTC 24 September 2011), and the second, hereinafter called 2011-WET (1200 UTC 11 October 2011–0000 UTC 13 October 2011), occurred during the pre-MATERHORN period and offer contrasting soil moistures (0.12 vs. 0.19 $m^3 m^{-3}$, respectively, at DPG). Skies were clear for both events, but 19–24 mm of rain fell at DPG 3–7 days before 2011-WET, moistening the near-surface soil. The third event is MATERHORN intensive observing period 5 (MATERHORN-IOP5; 1200 UTC 9 October 2012–0000 UTC 11 October 2012). It also features dry soils (0.13 $m^3 m^{-3}$ at DPG), although high cirrus clouds were present, reducing the net radiation at the surface. Surface energy balance and tethersonde observations collected during MATERHORN-IOP5 enable a more thorough verification of the model solutions. We simulate these three cases using version 3.4 of the community Advanced Research version of WRF, with the same physics packages as in the 4DWX-DPG system but with three larger one-way nested domains (12-, 4-, and 1.3-km grid spacing) and cold-start initial conditions (Fig. 2.2). The initial 6 h of each simulation are excluded from the study to reduce the influence of model spinup of the atmosphere. The large 1.3-km domain allows us to cover the entire playa and to use a broader range of regional surface observations for model validation.

We generate a nine-member ensemble for each of the three cases on the basis of three different parameterizations of soil thermal conductivity and three different top-layer (5 cm) soil-moisture initial analyses in the 1.3-km domain. The three parameterizations of soil thermal conductivity are J75, MP81, and a hybrid that uses MP81 over silt loam and sandy loam soils and J75 elsewhere. The three top-layer soil-moisture analyses are the interpolated 1.0° GFS analysis, an interpolated 12-km NAM analysis, and a soil-moisture

analysis that is created using data from the U.S. Department of Agriculture's Soil Climate Analysis Network (SCAN; Schaefer et al. 2007).

The SCAN-based soil-moisture analysis uses data from five SCAN stations located in the 1.3-km domain. SCAN stations use Stevens Water Monitoring Systems, Inc., Hydra Probes to measure soil moisture, and the probes are calibrated differently for different soil-texture classes (Seyfried et al. 2005). Of the five SCAN stations in our innermost domain, three are in loam soil (Morgan, Nephi, and Grantsville), one is in sandy loam soil (Goshute), and one is in silt loam soil (Dugway; see Fig. 2.3 for locations). All five stations measure soil moisture hourly at depths of 5.1, 10.2, 20.3, 50.8, and 101.6 cm, but the Noah LSM is configured with depths centered at 5, 25, 70, and 150 cm below the surface, making only the 5.1-cm SCAN measurement directly relevant for initialization and validation without vertical interpolation. Sensitivity studies suggest, however, that NST forecasts are relatively insensitive to deep (25 cm or greater) soil moisture and the vertical gradient in soil during the study period (not shown).

Our SCAN-based soil-moisture analyses begin with GFS soil moisture but replace the 5-cm soil moisture over the areas defined as silt loam with the Dugway 5.1-cm soil moisture, the areas defined as sandy loam with the Goshute 5.1-cm soil moisture, and the areas defined as loam with the mean of the Morgan, Nephi, and Grantsville 5.1-cm soil moistures. SCAN data are used for validation and initialization in other numerical weather prediction studies (e.g., Case et al. 2011; Li et al. 2012), but point soil-moisture observations are usually spatially and temporally interpolated to produce an observed soil-moisture field (e.g., Marshall et al. 2003; Robock et al. 2003; Godfrey and Stensrud 2008). Our approach of delineating soil moisture by soil-texture class is crude, but

observed and simulated soil moistures depend critically on soil-texture class (Mostovoy and Anantharaj 2008). Figure 2.4 compares the 5-cm soil moisture from the three analyses. For all three cases, the GFS has the highest mean 5-cm soil moisture, followed by the NAM and then the SCAN.

2.3.3 Validation and Methods

NST (2-m) forecasts, which are diagnosed from the WRF-Model half-η and skin-level fields using similarity theory, are validated against 2-m temperature observations obtained from the Mesowest cooperative networks (Horel et al. 2002). Bias error (*BE*) values were calculated as follows:

$$BE = \frac{1}{N}\sum_{i=1}^{N}(f_i - o_i),$$

where N is the number of forecast/observation pairs in the sample, f_i is the forecast, and o_i is the observation. Positive (negative) NST *BE* values represent a warm (cold) bias.

4DWX-DPG NST forecasts are verified using *BE*s for seven stations over playa soil (DPG-PLAYA) and 10 stations over silt loam soil (DPG-SL) between 1257 and 1335 m MSL at or near DPG (Fig. 2.5). One playa and two silt loam stations were not considered because they sit on the playa margin and often had relatively erratic and unrepresentative NSTs in comparison with the other stations. Since the 4DWX-DPG 1.1-km domain includes only two DPG-PLAYA stations, we use forecasts from the 3.3-km domain for verification over both soil-texture classes since there is little difference between the NST forecasts from the 1.1- and 3.3-km domains. For both DPG-PLAYA and DPG-SL stations, the *BE*s consider all eight 4DWX-DPG forecasts initialized 14–34 h before the forecast hour to avoid contamination from observational nudging.

For the case studies, *BE*s are calculated for stations in each represented soil-texture class to examine model performance over different soil textures. This includes approximately 87 loam, 56 sandy loam, 35 silt loam, 15 silty clay, 9 playa, 8 silty clay loam, 4 water, and 2 sand Mesowest stations below 1750 m MSL in our 1.3-km domain (Fig. 2.3). The silty clay loam, water, and sand stations are not considered in the analysis. Some stations were not consistently active, and therefore the exact number of stations used for verification varied among the three case studies. Most stations are clustered along the Wasatch Front, and no stations are located over far northwestern Utah. The vast majority of these stations are either over shrubland or urban land cover, except for the nine playa stations, which are all over playa land cover. Although no formal quality control was performed on any of the observational datasets, missing and obviously erroneous observations were removed.

2.3.4 MATERHORN Observations

During MATERHORN, soil and radiation observations were taken from 5 to 26 October 2012 at an extended flux site located near the DPG-SL stations (EFS-sage; Fig. 2.3). Soil temperatures were measured with thermocouples (Omega Engineering, Inc.) at depths of 1, 2.5, 5, 7.5, 10, 15, 25, and 70 cm. Thermal-property sensors (model TP01; Hukseflux Thermal Sensors B.V.) were installed at depths of 5, 10, and 25 cm and measured soil thermal conductivity [with a mean uncertainty of 0.01 W m^{-1} K^{-1} within the range of 0.3–4.0 W m^{-1} K^{-1} (Overduin et al. 2006)], soil thermal diffusivity, and volumetric heat capacity. Two self-calibrating heat flux plates (Hukseflux HFP-SC) measured the subsurface heat flux at 5-cm depths at two locations separated by

approximately 1 m. The individual shortwave and longwave components of the surface radiation balance at EFS-sage were measured with Kipp & Zonen B.V. up- and down-facing CMP21 pyranometers and CGR4 pyrgeometers, respectively, mounted 2 m AGL. The surface ground heat flux at EFS-sage was calculated as the sum of the average measured ground heat flux at a 5-cm depth and the heat-storage change in the soil layer between 0 and 5 cm. The heat storage was calculated using the direct measurements of the thermal heat capacity at 5 cm below the surface and the soil temperatures at depths of 1, 2.5, and 5 cm.

A tethered balloon system (Vaisala, Inc., DigiCORA) was also flown up to 400 m AGL at regular intervals during MATERHORN near EFS-sage, collecting atmospheric temperature, humidity and wind profiles. For brevity, we compare observed and model profiles for a time near the peak strength of the nocturnal inversion (~1200 UTC).

2.4 Results

2.4.1 Systematic Biases in Operational NST Forecasts

At 1200 UTC (0500 MST), the 4DWX-DPG *BE* is 3.4°C at the DPG-SL stations during the pre-MATERHORN and MATERHORN periods. At 0000 UTC (1700 MST), the *BE* at these sites is -1.1°C. This diurnal variation of *BE* at DPG-SL stations, especially the 1200 UTC (0500 LST) warm bias, is fairly consistent throughout the validation period and is most pronounced during quiescent large-scale conditions (Fig. 2.6). For example, when 700-hPa (~1000 m AGL) winds from the KSLC sounding are < 8 m s^{-1}, the 1200 UTC warm bias at DPG-SL stations increases to 3.9°C and sometimes exceeds 6°C. Rife et al. (2002) documented similar nocturnal warm biases at their non-

playa DPG stations during an event they simulated from July 1998. Meanwhile, the *BE*s at the DPG-PLAYA stations show little diurnal variation and are -0.7 and -0.6°C at 1200 UTC and 0000 UTC, respectively, suggesting the largest errors are confined to the DPG-SL stations.

The observed diurnal temperature range (DTR)[2] is substantially larger at DPG-SL than DPG-PLAYA stations. As shown by forecasts initialized at 1100 UTC the day prior, the 4DWX-DPG DTR is similar for both station types (Fig. 2.7). At DPG-SL stations, the mean observed DTR is 19.2°C, with some days exceeding 25°C, but the mean 4DWX-DPG DTR is only 12.7°C. At DPG-PLAYA stations, the mean observed DTR is 13.8°C, while the mean 4DWX-DPG DTR is only slightly smaller at 12.5°C. Therefore, the DTR at DPG-SL stations is underpredicted, resembling that at the DPG-PLAYA stations where it is relatively well predicted. This suggests that soil properties at the DPG-SL stations are inaccurately represented in 4DWX-DPG.

2.4.2 Potential Error Sources

The analysis above illustrates the existence of a 1200 UTC warm bias and reduced DTR at DPG-SL stations but not at DPG-PLAYA stations. Rife et al. (2002) state that the major differences between the sparsely vegetated desert containing the DPG-SL stations and the playa are associated with the vegetation cover, albedo, soil thermal conductivity, and near-surface soil moisture. Therefore, the error at the DPG-SL stations is likely related to the initialization or parameterization of at least one of these

[2] Calculated by subtracting the maximum daily (0000–0000 UTC) hourly temperature from the minimum hourly temperature at each station, and then averaging for all DPG-PLAYA and DPG-SL stations.

surface properties. The WRF land cover at the DPG-SL stations is shrubland, which has a prescribed albedo of 0.25–0.30 that appears reasonable on the basis of comparisons with the Moderate Resolution Imaging Spectroradiometer (MODIS) white-sky albedo (known as MOD43B3) 16-day 1-km product (not shown). Therefore, the likely sources of the NST errors over DPG-SL are the parameterization and initialization of soil thermal conductivity and soil moisture.

Soil thermal conductivity affects NSTs through the ground heat flux G:

$$G = \left(\kappa \frac{\partial T}{\partial z}\right)_{z=0},$$

where T is the temperature of the soil, z is the soil depth, and κ is the soil thermal conductivity. Flux G is positive, or upward, at night when the temperatures increase with depth, and therefore higher soil thermal conductivity increases the upward heat flux and the nighttime NSTs. During the day, G is negative, or downward into the soil since temperatures decrease with depth, and therefore the higher downward heat flux reduces daytime NSTs. Because there is a large nighttime warm bias and an underprediction of the DTR at DPG-SL stations, the simulated soil thermal conductivity might be too large.

The Noah LSM presently coupled to the WRF uses a slightly modified version of J75 to calculate soil thermal conductivity as a function of the dry thermal conductivity, κ_{dry}, and saturated thermal conductivity, κ_{sat}, weighted by a normalized thermal conductivity, K_e, or Kersten number:

$$\kappa_{J75} = K_e(\kappa_{sat} - \kappa_{dry}) + \kappa_{dry},$$

wherein K_e is a function of the degree of saturation and phase of water, κ_{dry} is a function of the porosity of the soil, and κ_{sat} is a function of the porosity, quartz content, and unfrozen volume fraction (Peters-Lidard et al. 1998).

J75 replaced MP81 in the WRF version of the Noah LSM in 2001. MP81 fits a logarithmic relationship between the soil thermal conductivity and soil water potential data of Al Nakshabandi and Kohnke (1965, their Fig. 4). The soil water potential is a measure of how easily soil water moves within a soil. The relationship is

$$\kappa_{MP81} = \begin{cases} 420exp[-(pF + 2.7)], & pF \leq 5.1 \\ 0.1744, & pF > 5.1 \end{cases}$$

where pF, the base-10 logarithm of the magnitude of the soil water potential, is approximated [following Clapp and Hornberger (1978)] as

$$pF = \log_{10}[\psi_s(\theta_s/\theta)^b],$$

where ψ_s is the saturated soil potential (suction), θ_s and θ are the porosity and volumetric soil moisture, respectively, and b is the slope of the retention curve on a logarithmic graph. Chen and Dudhia (2001) limit κ_{MP81} to 1.9 W m^{-1} K^{-1} since MP81 overestimates κ_{MP81} during wet periods. The Al Nakshabandi and Kohnke (1965) dataset only compared three soil texture classes: clay, fine sand, and silt loam, the latter the soil texture at DPG-SL stations.

Figure 2.8 shows κ_{J75} and κ_{MP81} as a function of unfrozen volumetric soil-moisture content for 5 different soil-texture classes. Both methods have increasing thermal conductivity with increasing soil moisture since the water has a larger thermal conductivity than the air it replaces (Cosenza et al. 2003). κ_{MP81} is more variable amongst the different soil texture classes compared to κ_{J75}, and κ_{MP81} is more sensitive to soil moisture over certain soil moisture ranges (i.e., 0.15 – 0.33 m^3 m^{-3} for silt loam). κ_{MP81} and κ_{J75} are substantially different over silt loam at low and high soil moistures. For example, when the silt loam soil moisture is relatively moist at 0.33 m^3 m^{-3}, κ_{MP81} is

1.9 W m^{-1} K^{-1}, but κ_{J75} is only 1.14 W m^{-1} K^{-1}, and when the soil moisture is relatively dry at 0.12 m^3 m^{-3}, κ_{MP81} is 0.17 W m^{-1} K^{-1}, but κ_{J75} is 0.64 W m^{-1} K^{-1}. The κ_{J75} and κ_{MP81} are similar near their intersection point at 0.25 m^3 m^{-3}. For playa and silty clay soil textures, κ_{J75} and κ_{MP81} are even more dissimilar at low soil moistures than for silt loam, and they do not intersect until the soils are much more saturated. The κ_{J75} and κ_{MP81} are also very sensitive to the WRF-defined soil parameters, such as soil porosity (not shown), but the representativeness of those parameters is not examined in this study.

The κ_{J75} and κ_{MP81} are sensitive to soil moisture and there is considerable soil moisture disagreement amongst the GFS and NAM analyses and the Dugway SCAN soil moisture observations. For example, at the Dugway SCAN station during the pre-MATERHORN and MATERHORN periods, the GFS, NAM and observed 5-cm soil moistures average 0.22 m^3 m^{-3}, 0.19 m^3 m^{-3} and 0.16 m^3 m^{-3}, respectively (Fig. 2.9)[3]. All three values are between the WRF prescribed vegetation wilting point of 0.084 m^3 m^{-3} and porosity of 0.476 m^3 m^{-3} assigned to silt loam soil. The moist bias in the analyzed fields is more pronounced during the pre-MATERHORN period, especially in the GFS, which averages 70% more soil moisture than is observed at the Dugway SCAN station. The GFS soil moisture is nudged toward a soil-moisture "climatology" that may be too wet over this area. During MATERHORN, after a significant rain event on 2 September 2012 there is fair agreement among all three soil moistures, with the GFS slightly wetter, until the precipitation event on 12–13 October 2012. The NAM did not respond significantly, the GFS responded suddenly, and the Dugway SCAN station responded

[3] The small (~0.01 m^3 m^{-3}) diurnal cycle in the observed soil moisture at the Dugway SCAN station may either be an upward diffusion of soil moisture during the day or instrument error since the diurnal fluctuations are in phase with the 5.1-cm soil temperatures (not shown).

slowly. In general, the accumulated daily precipitation at the Dugway SCAN station helps to explain many of the observed soil-moisture increases but only partially explains the NAM and GFS soil-moisture increases. The GFS analyzed soil moisture is a function of its precipitation output, whereas the NAM analyzed soil moisture is a function of radar-derived and gauge-based precipitation. These differing inputs help to explain why the soil-moisture analyses react differently after a rain event (Liu et al. 2011).

2.4.3 Case Studies

Sensitivity to the initialization of soil moisture and the parameterization of soil thermal conductivity is illustrated through simulations of 2011-DRY, 2011-WET, and MATERHORN-IOP5. We simulate these events using a nine-member ensemble with varying 5-cm soil-moisture initialization among the GFS-, NAM-, and SCAN-derived soil-moisture analyses and varying soil thermal conductivity parameterizations among J75, MP81, and a hybrid approach that uses MP81 over silt loam and sandy loam soil-texture classes and J75 over the other texture classes. All three cases occurred during quiescent large-scale conditions, and we only focus on NST *BE*s for silt loam, playa, sandy loam, loam, and silty clay soil-texture stations.

2.4.3.1 2011-DRY

The 2011-DRY case featured an amplifying upper-level ridge centered over Utah (not shown). In fact, the observed 700-hPa winds from the 1200 UTC 22 September KSLC sounding were only 4.6 m s^{-1}. Soils were generally dry in the SCAN network (e.g., 0.12 m^3 m^{-3} at the Dugway SCAN station), but relatively moist in the GFS and

NAM analyses (e.g., 0.24 m^3 m^{-3} and 0.21 m^3 m^{-3}, respectively, over silt loam; Table 2.1). The quiescent conditions and dry soils contributed to a difference of 6.1°C between the mean observed temperature at the DPG-PLAYA and DPG-SL stations at 1200 UTC 23 September and a large mean observed DTR at the DPG-SL stations of 24.7°C (Fig. 2.10). The control ensemble member (J75-GFS) for this case produces a 1200 UTC warm bias of 6.8°C at the DPG-SL stations, which results in a mean difference of only 0.2°C between the DPG-PLAYA and DPG-SL stations at 1200 UTC 23 September and a mean DTR at the DPG-SL stations of only 13.0°C.

Figures 2.11a–c show the *BE*s over the five different soil textures for the ensemble members that use J75 with varying soil moisture. In J75-GFS, silt loam, playa, sandy loam, loam, and silty clay stations have consistent 0000 UTC cool biases of 3.1°–3.5°C but varying 1200 UTC warm biases of 0.8°–4.9°C on 23 September (Fig. 2.11a). Silt loam stations have the greatest 1200 UTC warm bias, with a mean late-night (0600–1200 UTC) warm bias of 4.9°C (Fig. 2.12). Reducing the soil moisture reduces the late-night warm biases modestly. For example, J75-NAM and J75-SCAN initialize silt loam soil moisture to 12% and 50% lower than that for J75-GFS, respectively, but these changes only reduce the late-night *BE*s at silt loam stations by 0.1° and 1.1°C, respectively (Fig. 2.12).

Figures 2.11d–f show the *BE*s for the ensemble members that use MP81 with varying soil moisture. The *BE*s for silt loam, sandy loam, and loam stations in MP81-GFS (Fig. 2.11d) are very similar to J75-GFS (Fig. 2.11a), but MP81-GFS introduces a large nighttime cool bias at playa and silty clay stations. Nighttime NST forecasts from MP81 members are also more sensitive to soil moisture than the J75 members. For

example, mean late-night *BE*s at the loam soil stations decrease by 3.1°C between MP81-GFS and MP81-SCAN, respectively, but they only decrease by 0.8°C between J75-GFS and J75-SCAN (Fig. 2.12). The greatest mean late-night *BE* improvement occurs at silt loam stations where mean late-night *BE*s are 4.6°C in MP81-GFS but are reduced to 0.3°C in MP81-SCAN. MP81 introduces an unfortunate evening-transition cool bias at 0100 UTC, especially in MP81-SCAN (Fig. 2.11f). Figure 2.13 shows mean observed, J75-SCAN, and MP81-SCAN NSTs for the DPG-SL stations and how MP81-SCAN begins to cool rapidly after 0000 UTC, an hour earlier than observed, which introduces the 0100 UTC cool bias. Perhaps MP81-SCAN predicts the onset of the evening transition too early. Figure 2.13 also illustrates how MP81-SCAN slightly reduces the afternoon cool bias but significantly reduces the nighttime warm bias in comparison with J75-SCAN. At night, after the initial rapid cooling after sunset, the temperature tendency of J75-SCAN and MP81-SCAN is nearly identical to the observed tendency, suggesting that κ and G have the greatest influence on NST immediately following sunset.

Figures 2.11g–i show the *BE*s for the hybrid ensemble members that use κ_{MP81} for silt loam and sandy loam soils, and κ_{J75} for all other soil textures. The *BE*s in hybrid-GFS (Fig. 2.11g) and hybrid-NAM (Fig. 2.11h) are similar to the *BE*s in J75-GFS and J75-NAM, respectively, but the large nighttime warm bias at silt loam stations nearly disappears in hybrid-SCAN (Fig. 2.11i). Hybrid-SCAN also has less variance in *BE*s among the different soil-texture stations. Of interest is that the hybrid ensemble members introduce additional errors over some soil textures that are unrelated to soil moisture and κ. For example, MP81-GFS and hybrid-GFS yield a mean late-night *BE* of 1.9° and 2.9°C, respectively, at sandy loam stations even though sandy loam uses MP81 for both

members (Fig. 2.12). This may be related to temperature advection from areas with other soil textures that have an adjusted κ, or a sensitive land–atmosphere feedback process. Also of interest, the significant NST changes in hybrid-SCAN did not greatly affect the 10-m winds in 2011-DRY or the other case studies. For example, silt loam mean late-night wind speed *BE*s are −0.4 m s^{-1} in J75-GFS and −0.2 m s^{-1} in hybrid-SCAN (not shown).

2.4.3.2 2011-WET

The 2011-WET case occurred during a quiescent period that followed 19–24 mm of rainfall over DPG from 4 to 8 October 2011, with a corresponding increase in area-averaged GFS, NAM, and SCAN 5-cm soil moisture of 11%, 16%, and 31% relative to 2011-DRY, respectively (Fig. 2.4). The increase in soil moisture likely helped to reduce the difference in mean observed temperature at the DPG-PLAYA and DPG-SL stations at 1200 UTC to 3.9°C, which is 2.2°C lower than in 2011-DRY, and to lower the mean observed DTR at DPG-SL stations to 18.4°C, which is 6.3°C lower than in 2011-DRY (Fig. 2.10). Our control J75-GFS forecast produced a 1200 UTC warm bias of 4.2°C at the DPG-SL stations as compared with 6.8°C in 2011-DRY. Forecast DTRs are similar between 2011-DRY and 2011-WET, but because the observed DTR is 6.3°C smaller during 2011-WET the DTR underprediction is also reduced.

Figures 2.14a–c show the *BE*s for the J75 members. Relative to 2011-DRY, J75-GFS has similar 0000 UTC cool biases of 2.4°–3.0°C over all soil textures but a smaller range in the 1200 UTC warm biases of 0.5°–2.9°C (Fig. 2.14a). Silt loam stations again have the highest mean late-night *BE* of 1.9°C (Fig. 2.12). Silt loam soil moisture reduces

by 0.09 m^3 m^{-3} between the GFS and SCAN analyses from 0.28 m^3 m^{-3} to a value of 0.19 m^3 m^{-3} (Table 2.1), but this change only translates to a mean late-night *BE* reduction of 0.3°C (Fig. 2.12). For comparison, silt loam soil moisture also reduces by 0.09 m^3 m^{-3} in 2011-DRY, but from 0.21 m^3 m^{-3} to a value of 0.12 m^3 m^{-3} between the NAM and SCAN analyses (Table 2.1), and mean late-night *BE*s reduce by 1.0°C under this drier regime. Therefore, NSTs at silt loam stations are less sensitive to the higher soil moisture in 2011-WET than in 2011-DRY, which is to be expected from Fig. 2.8.

Figures 2.14d–f and 14g–i show the *BE*s for the MP81 and hybrid members, respectively, during 2011-WET. Similar to 2011-DRY, MP81 members introduce a significant cool bias at silty clay and playa stations and also make nighttime *BE*s more sensitive to soil moisture than do J75 members. The 0100 UTC cool bias in the MP81 members of the 2011-DRY case is no longer apparent, however. The hybrid-SCAN member has improved late-night *BE*s over all soil textures relative to those in J75-GFS, and the *BE* at silt loam stations is reduced to 1.0°C (Fig. 2.12).

2.4.3.3 MATERHORN-IOP5

MATERHORN-IOP5 was also characterized by quiescent large-scale conditions, with 700-hPa winds of only 5.2 m s^{-1} in the 0000 UTC 10 October KSLC sounding. An upper-level cutoff low off the Californian coast drove high cirrus clouds over the region throughout the period, but precipitation was not observed (not shown). In fact, only 1–7 mm of rain was observed at DPG-SL stations since 2 September 2012. As a result, MATERHORN-IOP5 had the lowest 5-cm soil moisture of the three cases (Fig. 2.4). The SCAN soil moisture over loam soil was especially low at 0.05 m^3 m^{-3} (Table 2.1), which

is the mean of 0.12 $m^3 m^{-3}$ at Nephi, 0.03 $m^3 m^{-3}$ at Morgan, and 0.01 $m^3 m^{-3}$ at Grantsville. Cloud cover was likely responsible for a reduced 1200 UTC temperature difference of 4.2°C between DPG-PLAYA and DPG-SL stations and for a DTR of 22.7°C at DPG-SL stations on 10 October 2012, which is 2°C lower than in 2011-DRY and 4.3°C lower than 2 days prior on 8 October 2012 (i.e., Fig. 2.7). J75-GFS forecast a 1200 UTC *BE* of 6.0°C at DPG-SL stations and underpredicted the mean DTR at these stations by 9°C (Fig. 2.10).

Figure 2.15 shows a very similar *BE* pattern in comparison with 2011-DRY except that the daytime cool bias is not as large and the mean nighttime warm bias at silt loam stations is not as pronounced. The mean late-night warm bias at silt loam stations decreases from 4.3°C in J75-GFS to 1.6°C in hybrid-SCAN (Fig. 2.12). The mean late-night *BE*s for the rest of the soil textures, except for loam, are very similar (≥1.3°C) in hybrid-SCAN. This suggests the presence of a nighttime warm bias unrelated to the LSM. The *BE*s at loam stations in J75-SCAN, MP81-SCAN, and hybrid-SCAN are relatively lower than at the other stations because the SCAN soil moisture for loam is very low and may not be representative.

MATERHORN observations taken at EFS-sage during MATERHORN-IOP5 indicate that hybrid-SCAN also improves forecasts of other near-surface variables. A comparison of the potential temperature profile of a tethersonde ascending between 1201 and 1221 UTC 10 October with the 1200 UTC Hybrid-SCAN and J75-GFS profiles at EFS-sage illustrates how Hybrid-SCAN is colder than J75-GFS and closer to the observations below ~150 m AGL (Fig. 2.16). Figure 2.17 illustrates how hybrid-SCAN better predicts *G* at EFS-sage than does J75-GFS. J75-GFS overpredicts the diurnal

amplitude of G, leading to more subsurface heat storage during the day and thus warmer surface temperatures and larger longwave radiation emission at night. For example, J75-GFS predicts a G of −167 W m^{-2} at 1800 UTC 10 October, which is 50 W m^{-2} lower than observed, and 93 W m^{-2} at 0100 UTC, which is 42 W m^{-2} higher than observed. Hybrid-SCAN slightly underpredicts the magnitude of G during the day but nearly matches the nighttime observations. Hybrid-SCAN also forecasts upwelling longwave radiation better than J75-GFS does, especially at night (Fig. 2.18a). There are only minor differences between the hybrid-SCAN and J75-GFS downwelling longwave radiation (Fig. 2.18b), and there are no discernable upwelling and downwelling shortwave radiation differences (Figs. 2.18c,d). Latent and sensible heat flux data were not available during this IOP and could not be verified.

2.4.4 Observed Soil Thermal Conductivity

Figure 2.19 shows 3 weeks of observed TP01 κ in comparison with κ_{J75} and κ_{MP81} calculated using interpolated GFS, NAM, and SCAN 5-cm soil moisture at EFS-sage. Before the rain event on 12–13 October 2012, κ_{J75} is nearly double the observed TP01 κ, but κ_{MP81} produces soil thermal conductivities that are within 0.21 W m^{-1} K^{-1} of the observed TP01 κ. After the rain event, there is considerable variability among the soil-moisture analyses (e.g., Fig. 2.9), and this variability is also evident in κ_{MP81}, but little variability is seen in κ_{J75}. The soil-moisture sensor at EFS-sage was not working properly during MATERHORN, and therefore the soil moisture at this site is unknown.

2.5 Conclusions

Four months of operational WRF near-surface temperature forecasts in September and October of 2011 and 2012 show a pronounced warm bias of 3.4°C at 1200 UTC over the sparsely vegetated silt loam soil area of Dugway Proving Ground. The WRF forecasts also underpredict the magnitude of the diurnal temperature range at DPG-SL stations, producing a DTR similar to that over the adjacent playa region. Because NST forecasts over DPG-PLAYA are relatively accurate, the DPG-SL errors are likely related to the specification or parameterization of soil characteristics and properties in the Noah LSM.

Case studies reveal that *BE*s at DPG-SL stations, as well as at other stations in the surrounding region with silt or sandy loam soils, are highly sensitive to the soil thermal conductivity κ, which controls the ground heat flux G in the Noah LSM. The methods introduced by Johansen (1975) and by McCumber and Pielke (1981) have become the two most widely used κ parameterizations in LSMs, and both depend on soil moisture. We mitigate the nighttime warm bias in silt loam and sandy loam soil regions by switching from J75 to MP81 for these soils only and by using a soil-texture-class-dependent soil-moisture analysis created from SCAN observations at 5 cm. The κ_{MP81} is more sensitive to soil moisture than κ_{J75}, and, since SCAN observations are mostly drier than the analyzed soil-moisture fields of the NAM and GFS, the reduced soil moisture combined with MP81 greatly reduces κ and the nighttime NST warm bias. The greatest NST improvements occurred over areas with silt loam soil textures, like the area near the DPG-SL stations, which relies on accurate near-surface forecasts for military operations. Mean late-night *BE*s decreased by more than 4°C during 2011-DRY at all silt loam stations and decreased from 2.1°C to a value of −0.4°C at sandy loam stations. The

variance in bias error among the different soil textures also reduces when these changes are incorporated. The *BE* improvement was substantially less during 2011-WET, which had higher soil moistures. The soil moistures in 2011-WET were still considerably below saturation, preventing us from validating MP81 over silt loam and sandy loam during very wet conditions. A daytime cool bias was evident in each case study before and after the changes were made to soil moisture and κ, suggesting that the cool bias depends on more than just the Noah LSM and may be related to errors in the surface-layer parameterization.

MP81 used in conjunction with 5-cm SCAN soil moisture over silt loam and sandy loam soils not only improved NST forecasts but also improved the predicted κ, G, longwave and shortwave radiation, and low-level thermal profile. The κ_{MP81} more closely matched observations of κ taken from a TP01 sensor at EFS-sage during dry periods than did κ_{J75}. The κ_{MP81} variability also more closely matched the observed TP01 κ variability after a rain event than did the κ_{J75} variability. The G was observed during MATERHORN-IOP5 at EFS-sage, and the run that used MP81 and SCAN soil moisture more closely matched observed G than did the run that used J75 and GFS soil moisture. Upwelling longwave emission also improved at night, with no detrimental effects to the other surface energy balance components, and the low-level 1200 UTC potential temperature profile improved in the lowest 150-m AGL.

Peters-Lidard et al. (1998) provided the rationale for replacing MP81 with J75 in the Noah LSM on the basis of a comparison with data collected in Kansas during the first International Satellite Land Surface Climatology Project. They verified κ_{MP81} and κ_{J75} against observed κ from sand, clay, and peat soil textures and found that κ_{J75} better

predicted the κ values and associated surface fluxes. In their study, MP81 underestimated κ at low soil moisture and overestimated it at high soil moisture. The change to J75 in the WRF version of the Noah LSM occurred in 2001, which may explain why Rife et al. (2002) and Davis et al. (1999) noted a pronounced cold bias over the playa but Reeves et al. (2011) discovered only a slight morning warm bias. Peters-Lidard et al. (1998) never mentioned any simulations involving silt loam and sandy loam soils textures, which we have shown to perform better using MP81.

We expect other dryland regions with silt loam and sandy loam soil textures to have improved NST forecasts when MP81 is used in conjunction with improved soil-moisture initialization. Therefore, we recommend that the Noah LSM incorporate an optional MP81 soil thermal conductivity parameterization for use over dryland regions with silt loam and sandy loam soils.

Table 2.1. Mean initialized 5-cm volumetric soil moisture (m^3 m^{-3}).

		Sandy Loam	Silt Loam	Loam	Silty Clay	Playa
2011-DRY	GFS	0.24	0.24	0.24	0.23	0.21
	NAM	0.17	0.21	0.19	0.20	0.19
	SCAN	0.09	0.12	0.12	0.23	0.21
2011-WET	GFS	0.27	0.28	0.28	0.26	0.24
	NAM	0.22	0.24	0.23	0.26	0.25
	SCAN	0.16	0.19	0.20	0.26	0.24
MATERHORN-IOP5	GFS	0.20	0.20	0.20	0.18	0.17
	NAM	0.14	0.15	0.14	0.17	0.19
	SCAN	0.14	0.13	0.05	0.18	0.17

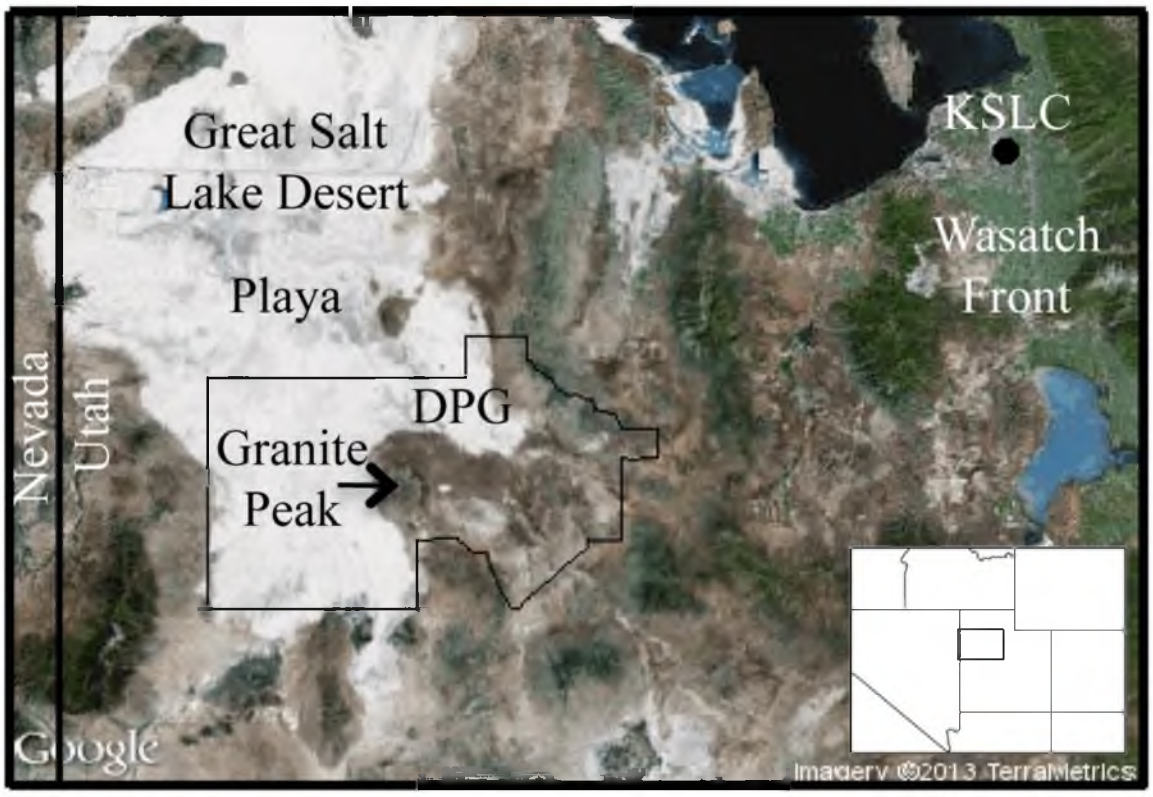

Fig 2.1. Google Earth image of northwestern Utah with relevant landmarks. The perimeter of DPG is outlined (copyright 2013 Google; imagery copyright 2013 TerraMetrics).

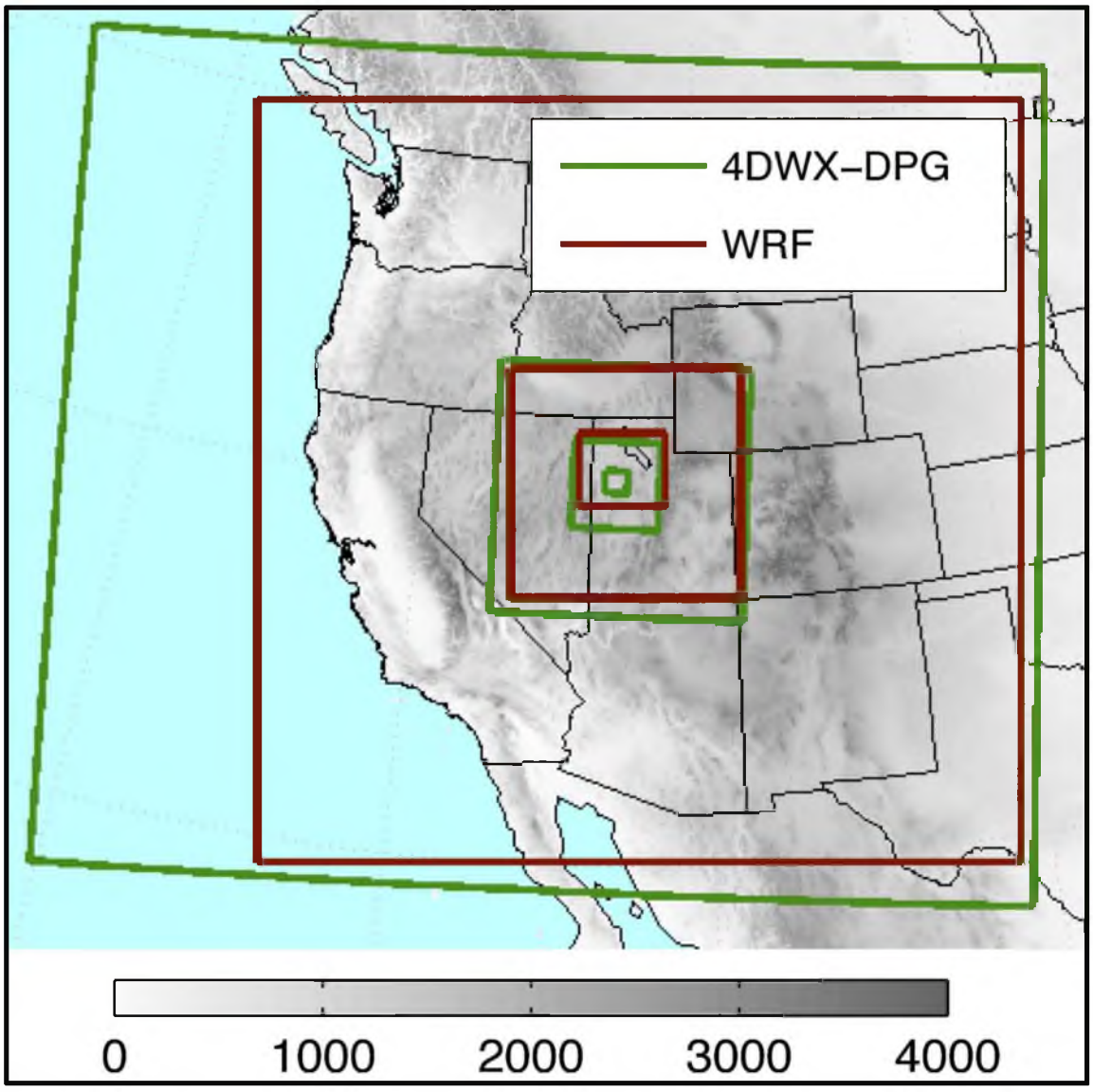

Fig. 2.2. Domains used for 4DWX-DPG (30, 10, 3.3, and 1.1 km) and the ARW case studies (12, 4, and 1.3 km); the 30-s-resolution elevation (m) is shaded.

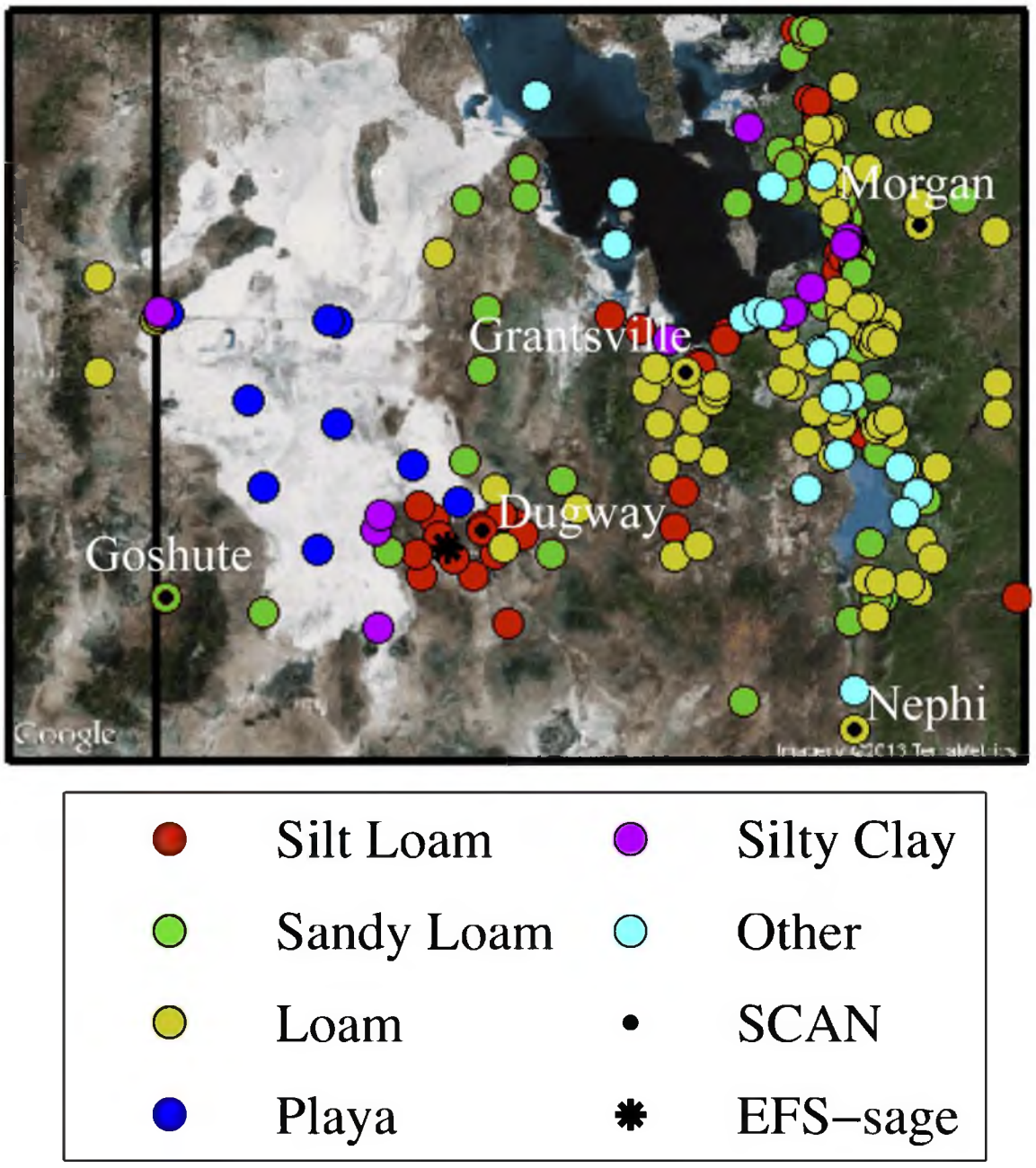

Fig. 2.3. Google Earth image of the innermost 1.3 km ARW domain with Mesowest (categorized by soil-texture class), SCAN, and EFS-sage stations annotated (copyright 2013 Google; imagery copyright 2013 TerraMetrics).

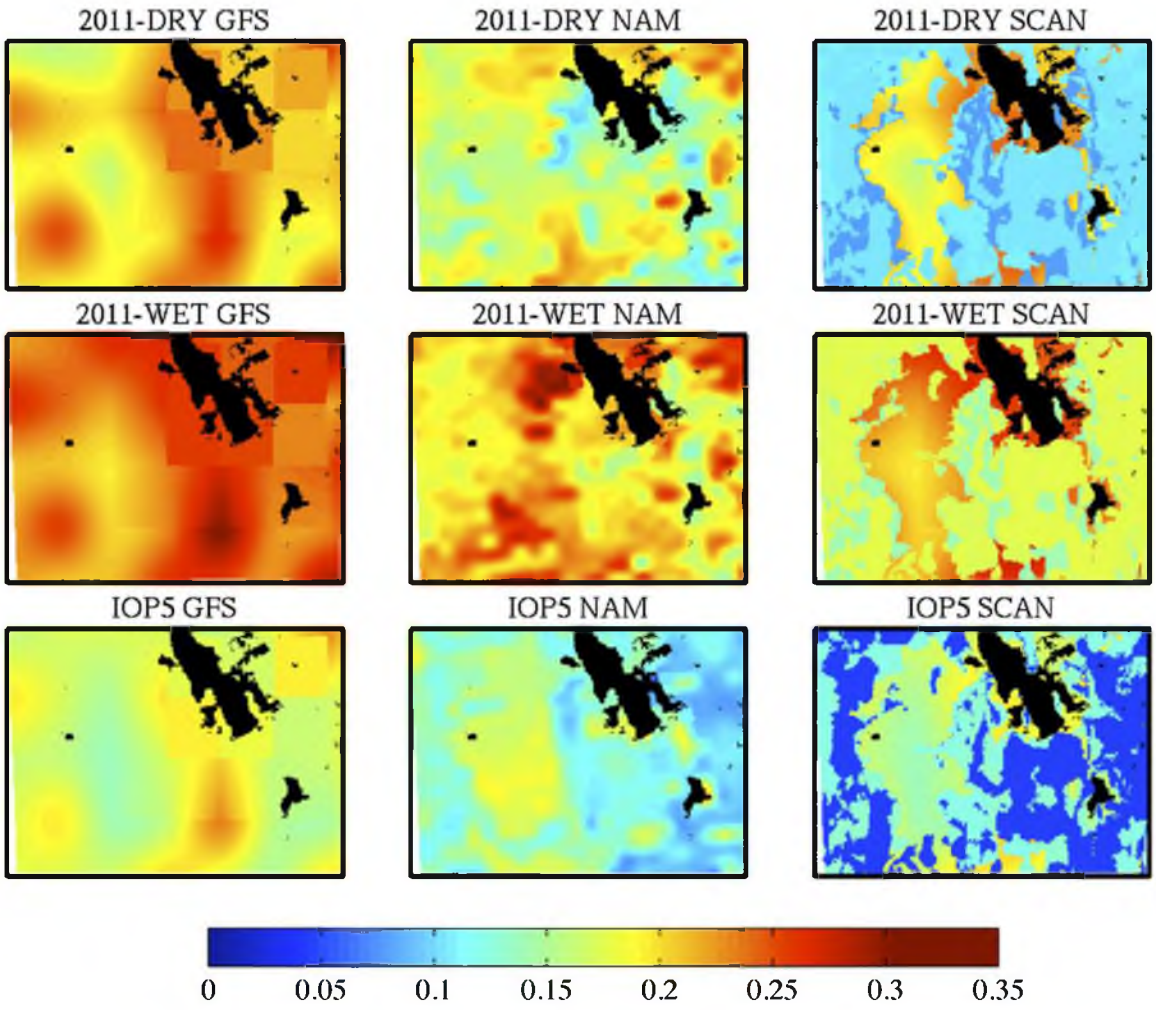

Fig. 2.4. GFS-, NAM-, and SCAN-derived 5-cm volumetric soil-moisture content for the three case studies. Grids are interpolated during WRF preprocessing.

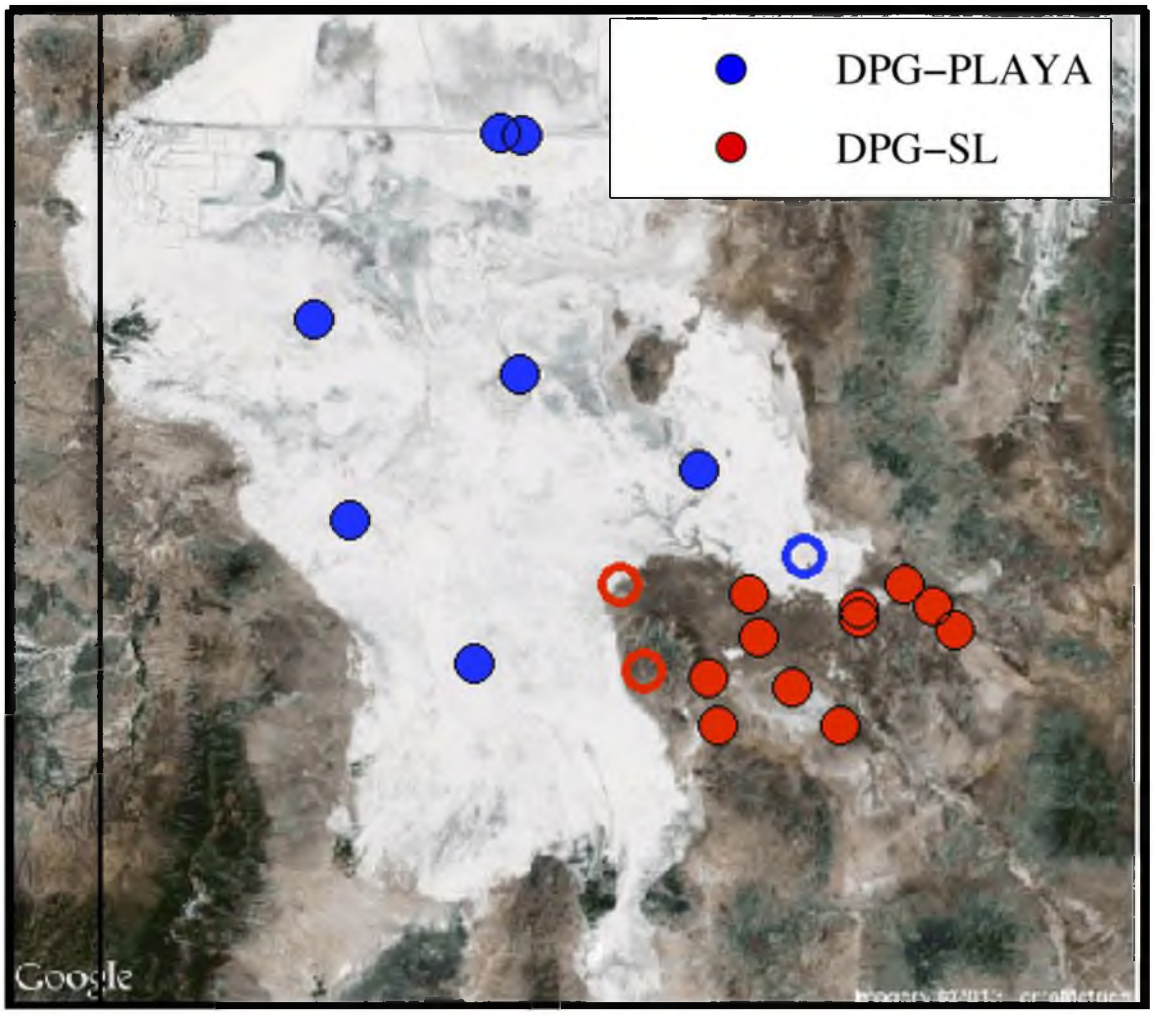

Fig. 2.5. Google Earth image of DPG and surrounding area with DPG-PLAYA (blue) and DPG-SL (red) stations used for verification. Open circles represent stations on the playa margin that were not considered for the validation (copyright 2013 Google; imagery copyright 2013 TerraMetrics).

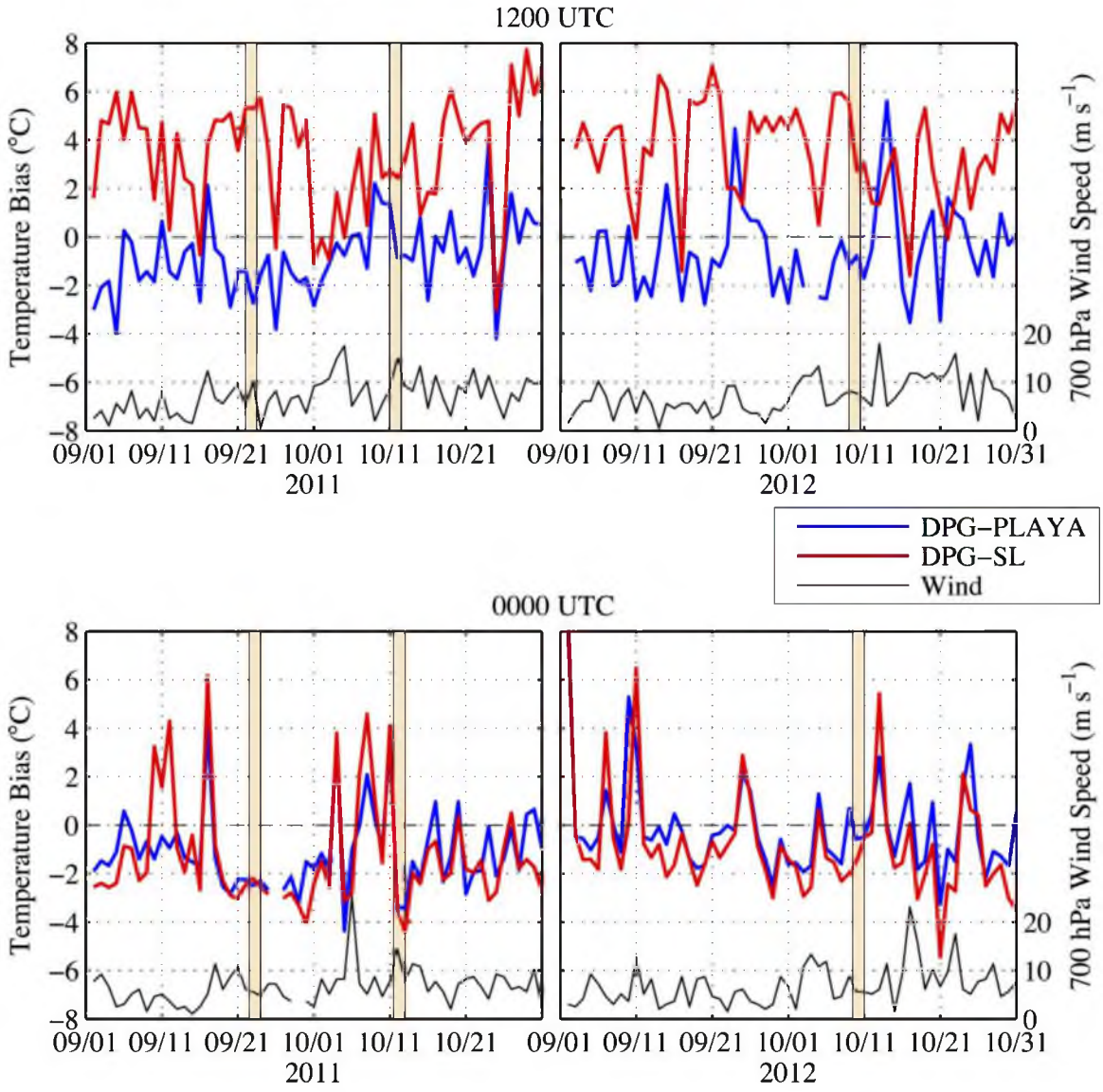

Fig. 2.6. 4DWX-DPG NST BEs for DPG-PLAYA (blue) and DPG-SL (red) stations and the observed KSLC 700-hPa wind speed (black) at (top) 1200 and (bottom) 0000 UTC. The three case studies are highlighted for reference.

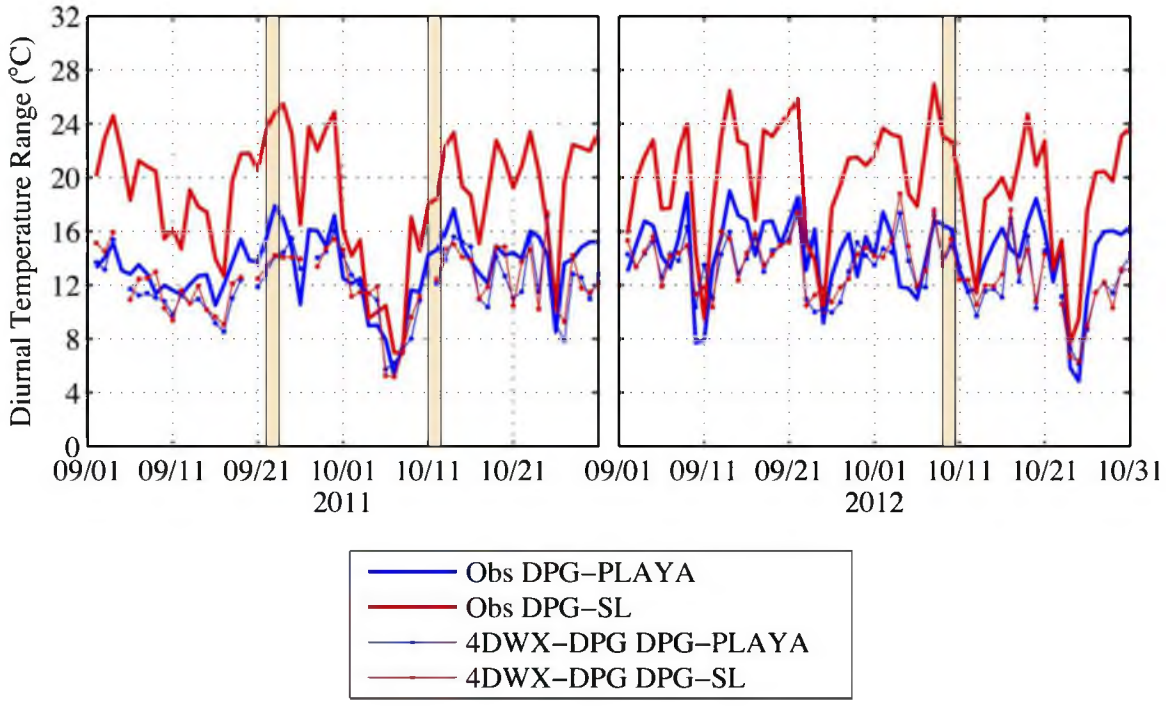

Fig. 2.7. Observed (thick lines) and 4DWX-DPG (thin lines) DTRs at DPG-SL and DPG-PLAYA stations. The three case studies are highlighted for reference.

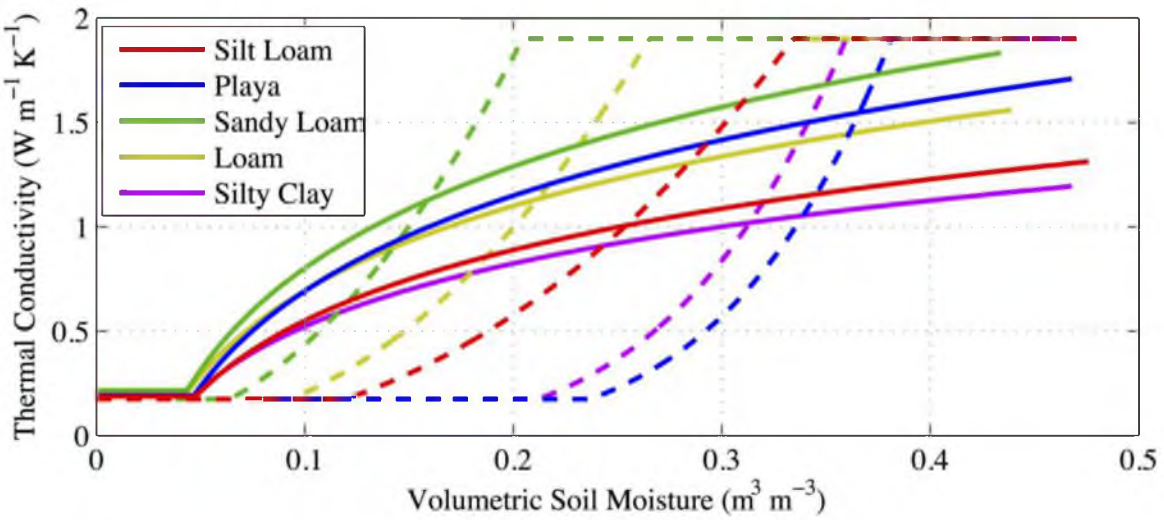

Fig. 2.8. Calculated J75 (κ_{J75}; solid lines) and MP81 (κ_{MP81}; dashed lines) thermal conductivity as a function of volumetric soil moisture for silt loam, playa, sandy loam, loam, and silty clay soil textures.

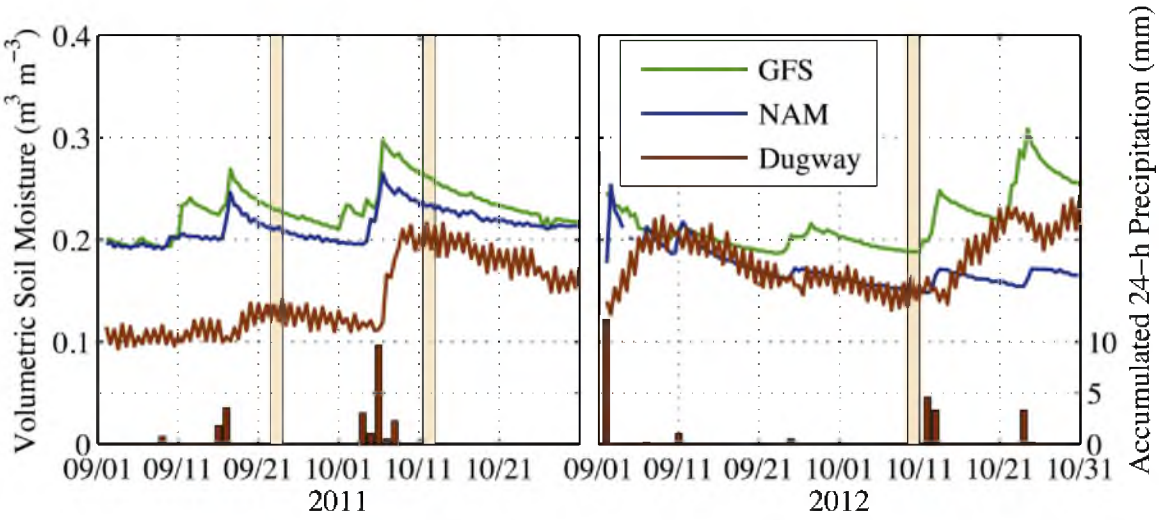

Fig. 2.9. Time series of 0000 and 1200 UTC 5-cm volumetric soil moisture with accumulated 24-h precipitation (0000–0000 UTC; bars) at the Dugway SCAN station. The three case studies are highlighted for reference.

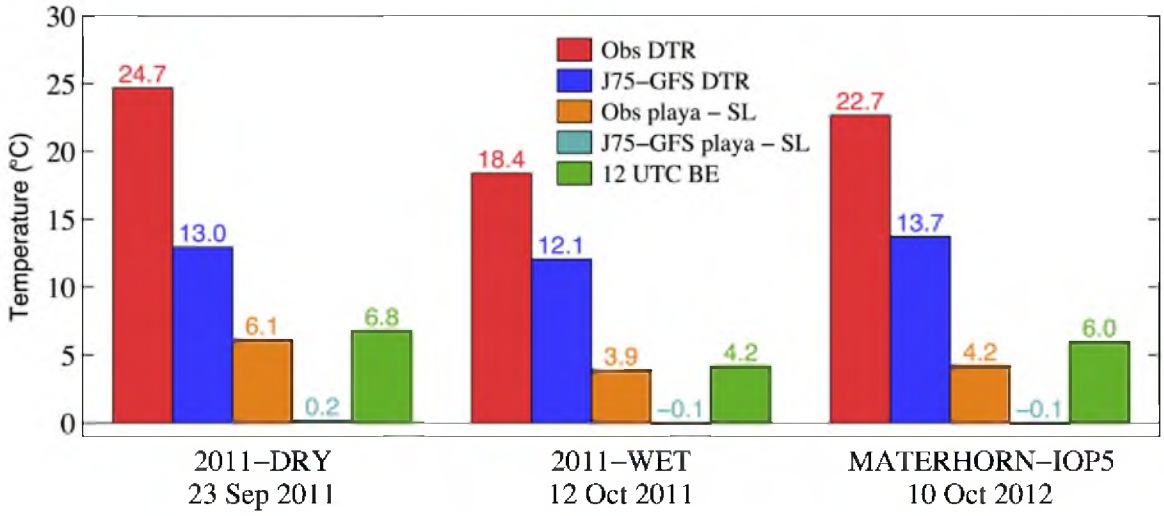

Fig. 2.10. Mean observed and simulated DTRs for DPG-SL stations, mean observed and simulated temperature difference between DPG-PLAYA and DPG-SL stations at 1200 UTC, and the BE at DPG-SL stations at 1200 UTC for each case study.

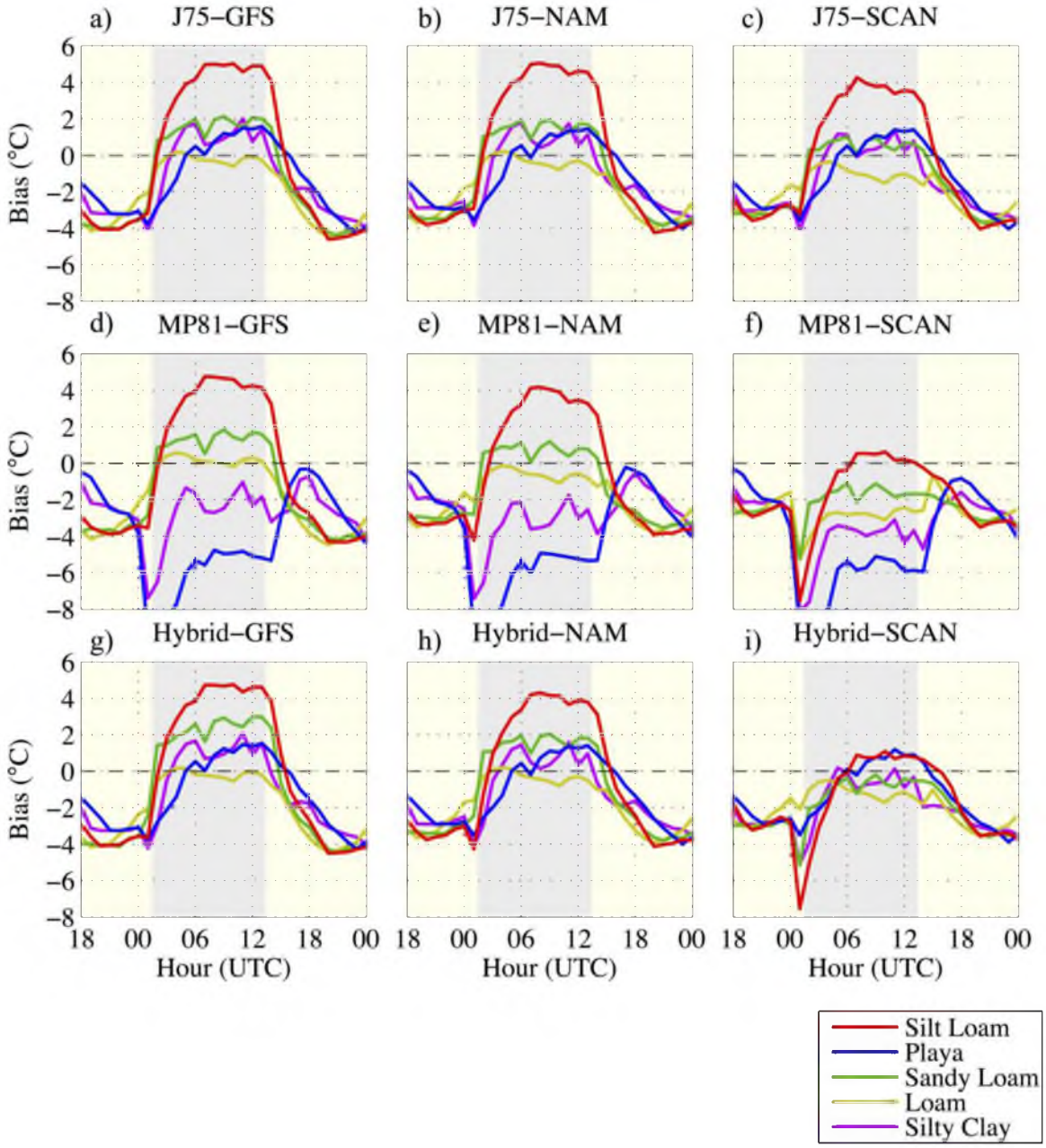

Fig. 2.11. The BE over each soil-texture class during 2011-DRY (1800 UTC 22 Sep–0000 UTC 24 Sep 2011) for (a) J75-GFS, (b) J75-NAM, (c) J75-SCAN, (d) MP81-GFS, (e) MP81-NAM, (f) MP81-SCAN, (g) hybrid-GFS, (h) hybrid-NAM, and (i) hybrid-SCAN. Yellow shading and gray shading represent daylight and nighttime hours, respectively.

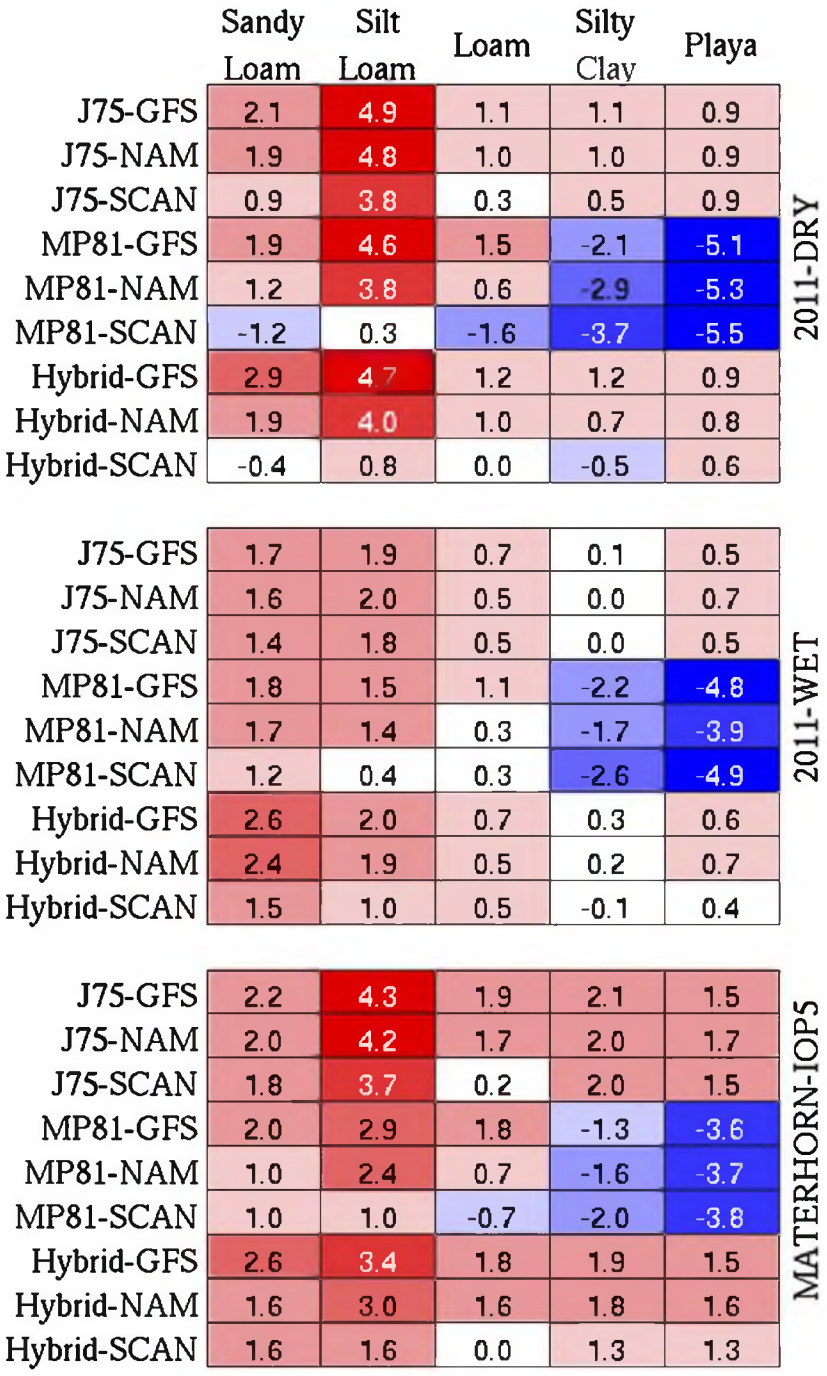

Fig. 2.12. 2011-DRY, 2011-WET, and MATERHORN-IOP5 mean 0600–1200 UTC BEs (°C) over each soil type for each ensemble member.

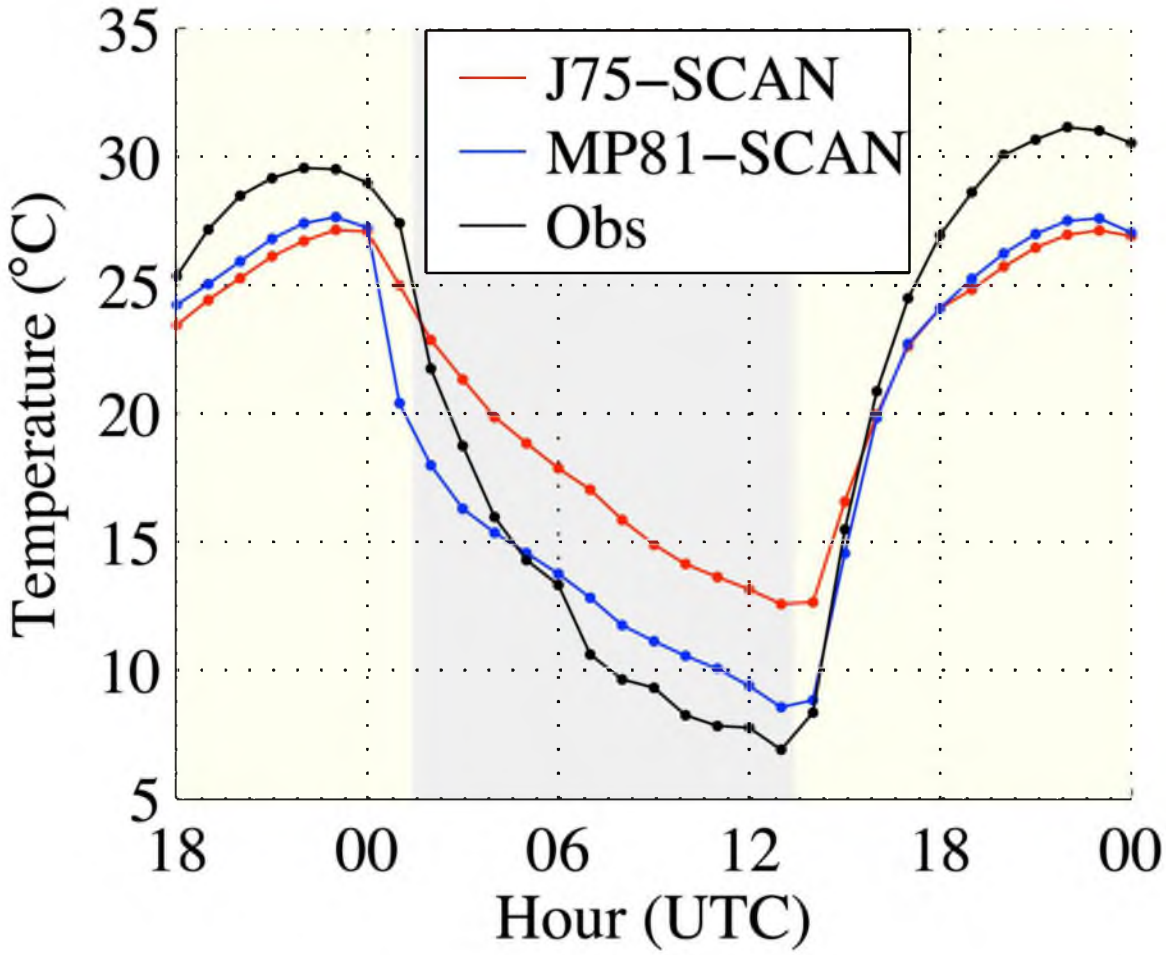

Fig 2.13. Time series of mean observed and simulated NST at DPG-SL stations from 1800 UTC 22 Sep to 0000 UTC 24 Sep 2011. Yellow shading and gray shading represent daylight and nighttime hours, respectively.

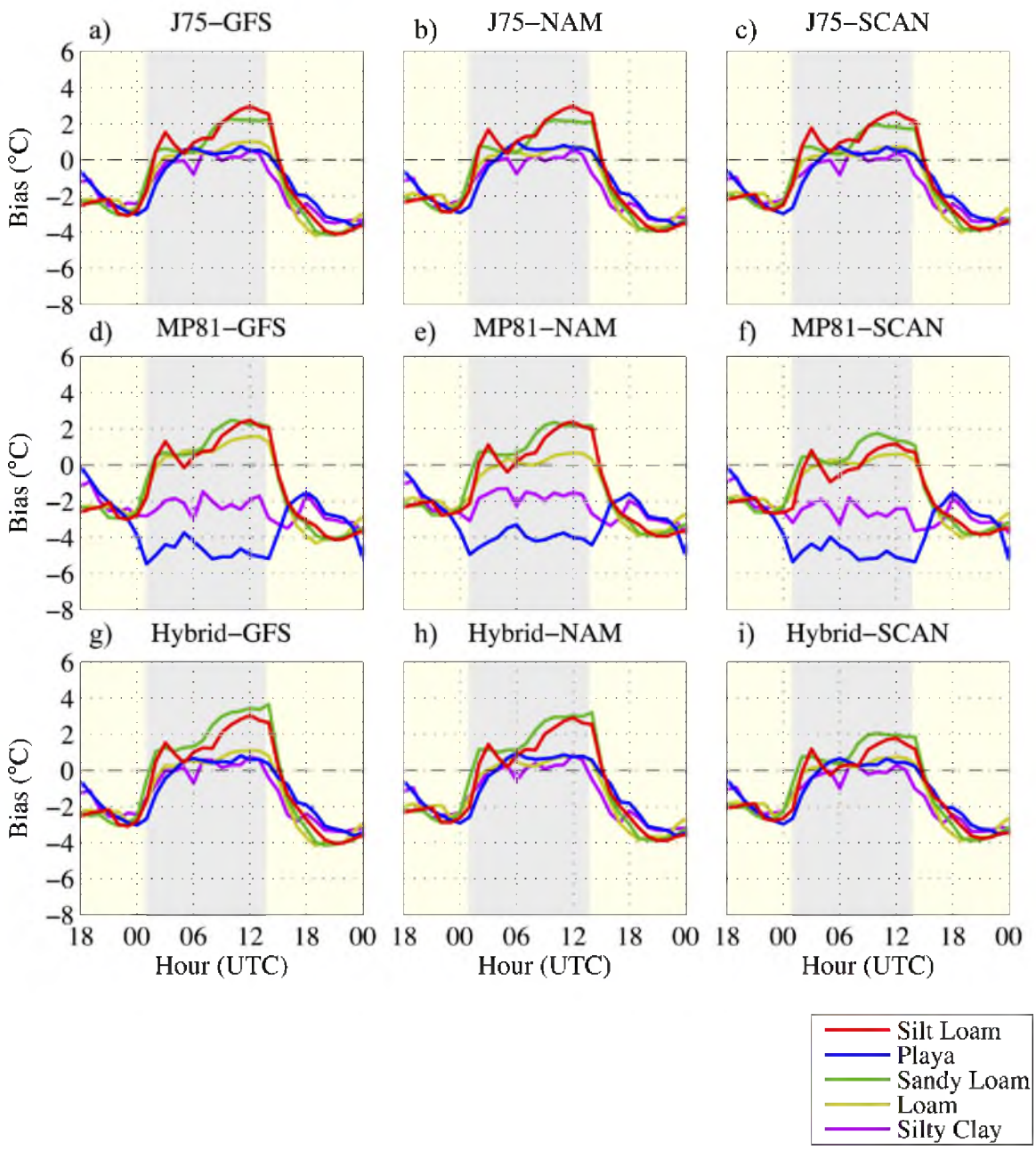

Fig. 2.14. As in Fig. 2.11, but for 2011-WET (1800 UTC 11 Oct–0000 UTC 13 Oct 2011).

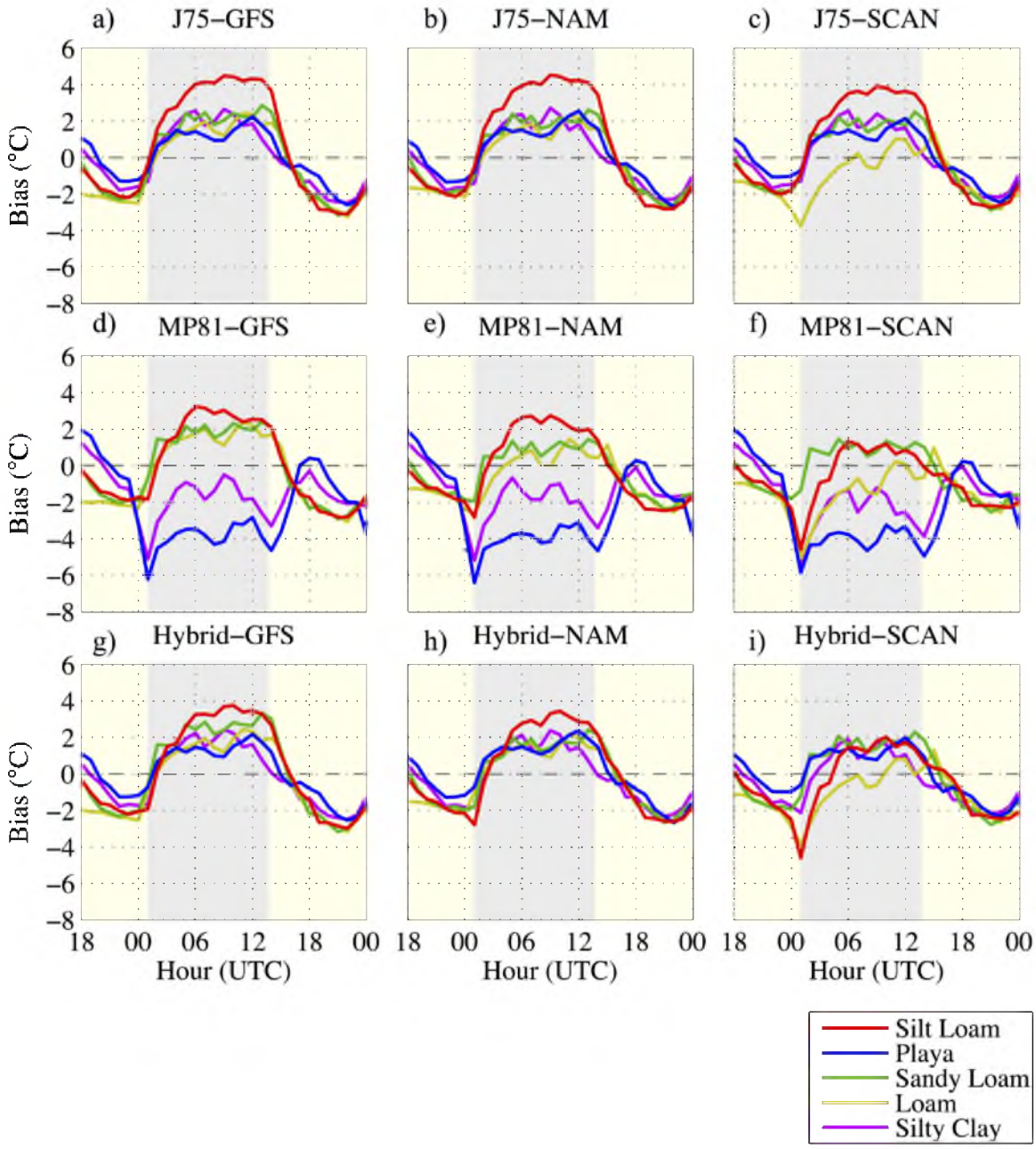

Fig. 2.15. As in Fig. 2.11, but for MATERHORN-IOP5 (1800 UTC 9 Oct–0000 UTC 11 Oct 2012).

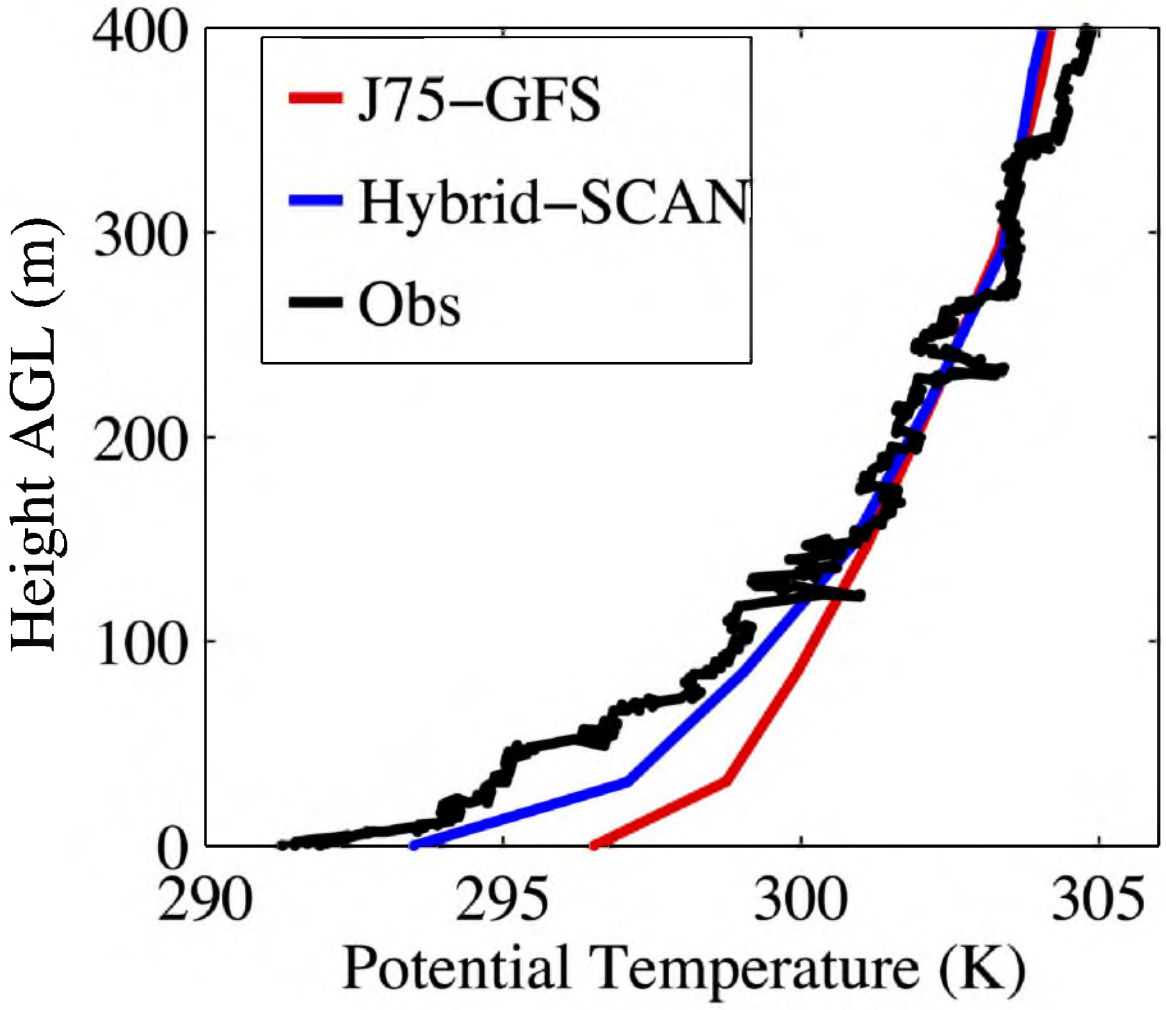

Fig. 2.16. Simulated 1200 UTC 10 Oct 2012 potential temperature (K) profiles at EFS-sage and an observed potential temperature profile taken between 1201 and 1221 UTC 10 Oct 2012 from an ascending tethersonde.

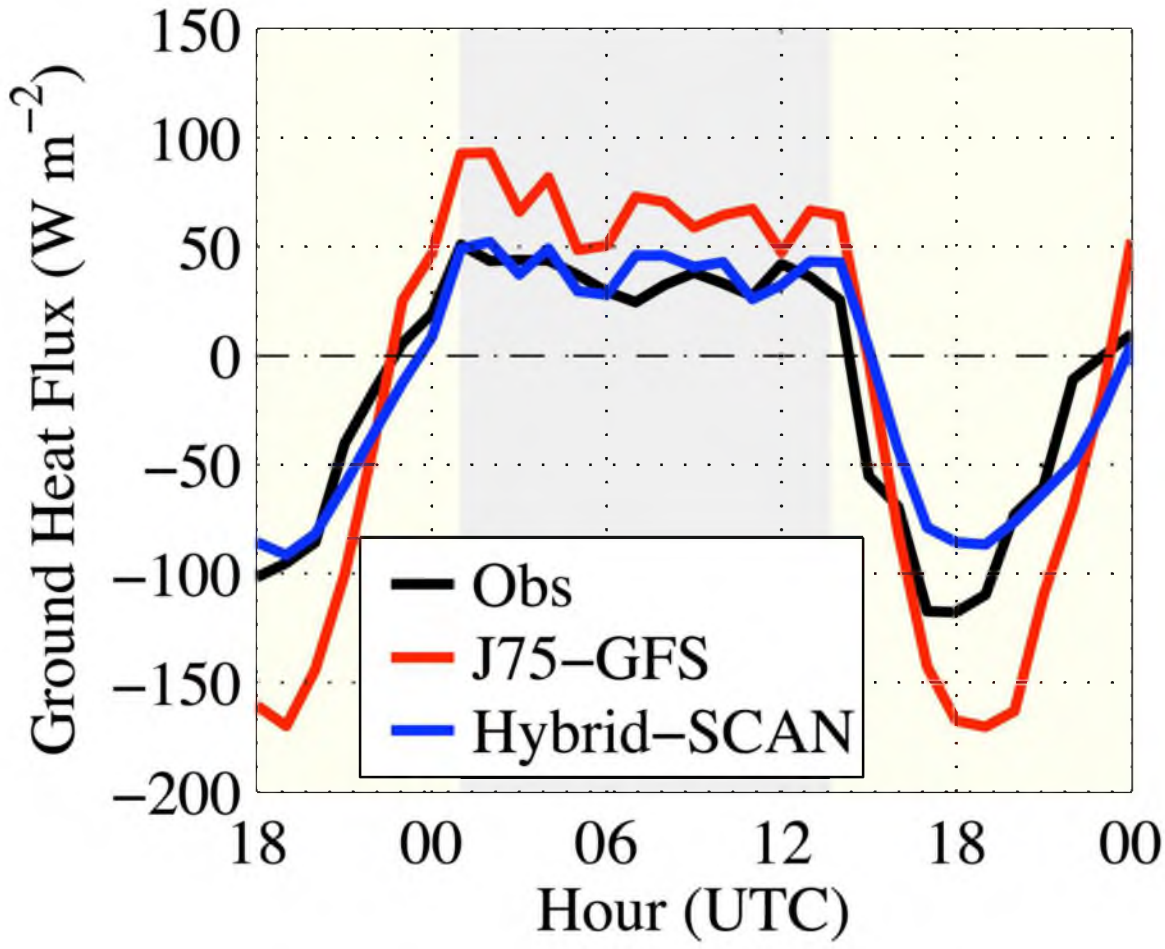

Fig. 2.17. Observed and simulated ground heat flux at EFS-sage from 1800 UTC 9 Oct to 0000 UTC 11 Oct 2012. Yellow shading and gray shading represent daylight and nighttime hours, respectively.

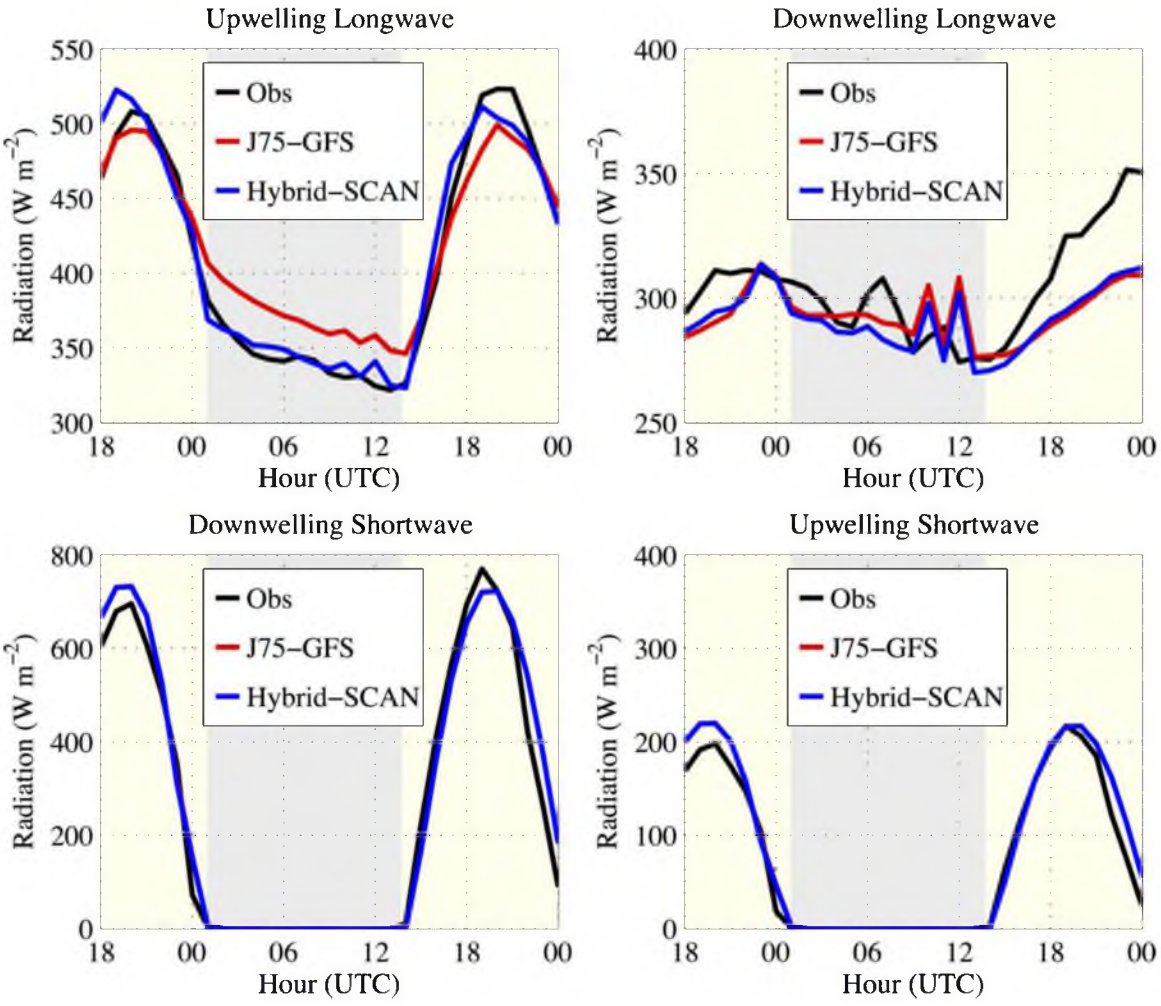

Fig. 2.18. As in Fig. 2.17, but for the longwave and shortwave components of the surface energy balance.

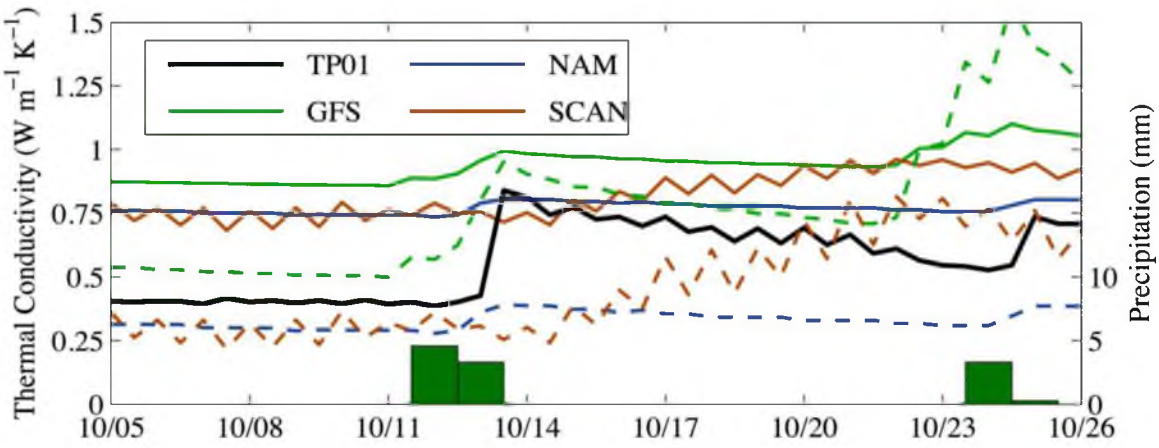

Fig. 2.19. Time series of 0000 and 1200 UTC observed 5-cm soil thermal conductivity at EFS-sage (solid black line) and calculated κ_{J75} (solid lines as in color key) and κ_{MP81} (dashed lines as in color key) using interpolated or SCAN observed 5-cm soil moisture. Accumulated 24-h precipitation at the Dugway SCAN station is also shown (green bars).

2.6 References

Al Nakshabandi, G., and H. Kohnke, 1965: Thermal conductivity and diffusivity of soils as related to moisture tension and other physical properties. *Agric. Meteor.,* **2,** 271–279.

Avissar, R., and R. A. Pielke, 1989: A parameterization of heterogeneous land surfaces for atmospheric numerical models and its impact on regional meteorology. *Mon. Wea. Rev.,* **117,** 2113–2136.

Balland, V., and P. A. Arp, 2005: Modeling soil thermal conductivities over a wide range of conditions. *J. Eng. Environ. Sci.,* **4**, 549–558.

Banta, R. M., and P. T. Gannon, 1995: Influence of soil moisture on simulations of katabatic flow. *Theor. Appl. Climatol.*, **52,** 85–94.

Bowen, I. S., 1926: The ratio of heat losses by conduction and by evaporation from any water surface. *Phys. Rev.*, **27,** 779–787.

Campbell, G. S., 1985. Soil Physics with Basic: Transport Models for Soil-Plant Systems. Elsevier Sci. Publ. Co., New York.

Case, J. L., S. V. Kumar, J. Srikishen, and G. J. Jedlovec, 2011: Improving numerical weather predictions of summertime precipitation over the southeastern United States through a high-resolution initialization of the surface state. *Wea. Forecasting*, **26**, 785–807.

Chen, F., and J. Dudhia, 2001: Coupling an advanced land surface–hydrology model with the Penn State–NCAR MM5 modeling system. Part I: Model implementation and sensitivity. *Mon. Wea. Rev.*, **129**, 569–585.

Cheng, W. Y. Y., and W. J. Steenburgh, 2005: Evaluation of surface sensible weather forecasts by the WRF and the Eta Models over the western United States. *Wea. Forecasting*, **20**, 812–821.

Clapp, R. B., and G. M. Hornberger, 1978: Empirical equations for some soil hydraulic properties. *Water Resour. Res.,* **14,** 601–604.

Cosby, B. J., G. M. Hornberger, R. B. Clapp, and T. R. Ginn, 1984: A statistical exploration of the relationship of moisture characteristics to the physical properties of soils. *Water Resour. Res.,* **20,** 682–690.

Cosenza, P., R. Guerin, and A. Tabbagh, 2003. Relationship between thermal conductivity and water content of soils using numerical modeling. *European Journal of Soil Science*, **54**, 581-587.

Côté, J., and J. M. Konrad. 2005: A generalized thermal conductivity model for soils and construction materials. *Can. Geotech. J.*, **42**, 443–458.

Davis, C., T. Warner, E. Astling, and J. Bowers, 1999: Development and application of an operational, relocatable, meso-gammascale weather analysis and forecasting system. *Tellus*, **51A**, 710–727.

de Vries, D. A., 1963: Thermal properties of soils. *Physics of Plant Environments,* W. R. van Wijk, Ed., North-Holland, 210–235.

Dirmeyer, P. A., F. J. Zeng, A. Ducharne, J. C. Morrill, and R. D. Koster, 2000: The sensitivity of surface fluxes to soil water content in three land surface schemes. *J. Hydrometeor.*, **1**, 121–134.

Dirmeyer, P. A., X. Gao, and T. Oki, 2002: The Second Global Soil Wetness Project (GSWP2). International GEWEX Project Office Publication, **37**, 75.

Doran, J. C., and S. Zhong, 1995: Variations in mixed-layer depths arising from inhomogeneous surface conditions. *J. Climate*, **8,** 1965–1973.

Dudhia, J., 1989: Numerical study of convection observed during the winter monsoon experiment using a mesoscale two-dimensional model. *J. Atmos. Sci.*, **46**, 3077–3107.

Edwards, J. M., J. R. McGregor, M. R. Bush, and F. J. Bornemann, 2011: Assessment of numerical weather forecasts against observations from Cardington: Seasonal diurnal cycles of screen-level and surface temperatures and surface fluxes. *Quart. J. Roy. Meteor. Soc.,* **137**, 656-672.

Ek, M., and L. Mahrt, 1991: OSU 1-D PBL model user's guide. Version 1.04, 120 pp. [Available from Department of Atmospheric Sciences, Oregon State University, Corvallis, OR 97331-2209.]

Ek M. B., K. E. Mitchell, Y. Lin, E. Rogers, P. Grunmann, V. Koren, G. Gayno, and J. D. Tarplay, 2003: Implementation of the Noah land-use model advances in the NCEP operational mesoscale Eta model. *J. Geophys. Res.*, **108**, 8851.

Farouki, O. T., 1986: *Thermal Properties of Soils.* Series on Rock and Soil Mechanics, Vol. 11, Trans Tech, 136 pp.

Fry, J., G. Xian, S. Jin, J. Dewitz, C. Homer, L. Yang, C. Barnes, N. Herold, and J. Wickham, 2011: Completion of the 2006 national land cover database for the conterminous United States, *PE&RS*, **77**, 858-864.

Godfrey, C. M., and D. J. Stensrud, 2008: Soil temperature and moisture errors in operational Eta Model analyses. *J. Hydrometeor.*, **9**, 367–387.

Hanna, S. R., and R. Yang, 2001: Evaluations of mesoscale models' simulations of near-surface winds, temperature gradients, and mixing depths. *J. Appl. Meteor.*, **40**, 1095–1104.

Hart, K. A., W. J. Steenburgh, and D. J. Onton, 2005: Model forecast improvements with decreased horizontal grid spacing over finescale intermountain orography during the 2002 Olympic Winter Games. *Wea. Forecasting*, **20**, 558–576.

Holt, T. R., D. Niyogi, F. Chen, K. Manning, M. A. LeMone, and A. Qureshi, 2006: Effect of land–atmosphere interactions on the IHOP 24–25 May 2002 convection case. *Mon. Wea. Rev.*, **134**, 113–133.

Holtslag, A. A. M., G. Svensson, P. Baas, S. Basu, B. Beare, A. C. M. Beljaars, F. C. Bosveld, J. Cuxart, J. Lindvall, G. J. Steeneveld, M. Tjernström, and B.J.H. Van De Wiel, 2013: Stable atmospheric boundary layers and diurnal cycles – challenges for weather and climate models. *Bull. Amer. Meteor. Soc.*, available as online early release.

Hong, S. Y., Y. Noh, and J. Dudhia, 2006: A new vertical diffusion package with an explicit treatment of entrainment processes. *Mon. Wea. Rev.*, **134**, 2318–2341.

Horel, J., and Coauthors, 2002: MesoWest: Cooperative mesonets in the western United States. *Bull. Amer. Meteor. Soc.*, **83,** 211–225.

Huang, J., H. M. van den Dool, and K. P. Georgarakos, 1996: Analysis of model-calculated soil moisture over the United States (1931–1993) and applications to long-range temperature forecasts. *J. Climate*, **9**, 1350–1362.

Idso, S., R. Jackson, B. Kimball, and F. Nakayama, 1975: The dependence of bare soil albedo on soil water content. *J. Appl. Meteor.*, **14**, 109–113.

Jackson, T. J., and Coauthors, 2010: Validation of advanced microwave scanning radiometer soil moisture products. *IEEE Trans. Geosci. Remote Sens.*, **48**, 4256–4272.

Johansen, O., 1975: Thermal conductivity of soils. Ph.D. thesis, University of Trondheim, 236 pp. [Available from Universitetsbiblioteket i Trondheim, Høgskoleringen 1, 7034 Trondheim, Norway.].

Kain, J. S., 2004: The Kain-Fritsch convective parameterization: An update. *Journal of Applied Meteorology*, **43**, 170-181.

Kersten, M. S., 1949: Thermal properties of soils. University of Minnesota Engineering Experiment Station Bulletin 28, 227 pp. [Available from University of Minnesota Agricultural Experiment Station, St. Paul, MN 55108.].

Kilpelainen T., T. Vihma, M. Manninen, A. Sjoblom, E. Jakobson, T. Palo, and M. Maturilli, 2012: Modelling the vertical structure of the atmospheric boundary layer over Arctic fjords in Svalbard. *Q. J. R. Meteorol. Soc.*, **138**, 1867-1883.

Knievel, J. C., G. H. Bryan, and J. P. Hacker, 2007: Explicit diffusion in the WRF model. *Mon. Wea. Rev.*, **135**, 3808–3824.

Li, B., D. Toll, X. Zhan, and B. Cosgrove, 2012: Improving estimated soil moisture fields through assimilation of AMSR-E soil moisture retrievals with an ensemble Kalman filter and a mass conservation constraint, *Hydrol. Earth Syst. Sci.*, **16**, 105–119.

Lin, Y.-L., R. D. Farley, and H. D. Orville, 1983: Bulk parameterization of the snow field in a cloud model. *J. Climate Appl. Meteor.*, **22**, 1065–1092.

Liu, Y., and Coauthors, 2008: The operational mesogamma-scale analysis and forecast system of the U.S. army test and evaluation command. Part I: Overview of the modeling system, the forecast products, and how the products are used. *J. Appl. Meteor. Climatol.*, **47**, 1077–1092.

Liu, Q., and Coauthors, 2011: The contributions of precipitation and soil moisture observations to the skill of soil moisture estimates in a land data assimilation system. *J. Hydrometeor*, **12**, 750–765.

Lu, S., T. S. Ren, Y. S. Gong, and R. Horton, 2007: An improved model for predicting soil thermal conductivity from water content at room temperature. *Soil Sci. Soc. Amer. J.*, **71**, 8–14.

Mahfouf, J. F., A. O. Manzi, J. Noilhan, H. Giordani, and M. Deque, 1995: The land surface scheme ISBA within the Meteo-France climate model ARPEGE. Part I: Implementation and preliminary results. *J. Climate*, **8**, 2039–2057.

Marshall, C. H., K. C. Crawford, K. E. Mitchell, and D. J. Stensrud, 2003: The impact of the land surface physics in the operational NCEP eta model on simulating the diurnal cycle: evaluation and testing using Oklahoma mesonet data. *Wea. Forecasting*, **18**, 748–768.

Mass, C. F., D. Ovens, K. Westrick, and B. A. Colle, 2002: Does increasing horizontal resolution produce more skillful forecasts? The results of two years of real-time numerical weather prediction over the Pacific Northwest. *Bull. Amer. Meteor. Soc.*, **83,** 407–430.

McCumber, M. C., and R. A. Pielke, 1981: Simulation of the effects of surface fluxes of heat and moisture in a mesoscale numerical model. *J. Geophys. Res.,* **86**, 9929–9938.

McInnes, K. J., 1981: Thermal conductivities of soils from dryland wheat regions of eastern Washington. M.S. thesis, Dept. of Agronomy and Soils, Washington State

University, Pullman, WA, 51 pp. [Available from Owen Science Library, Washington State University, Pullman, WA 99163-3200.].

Mlawer, E. J., S. J. Taubman, P. D. Brown, M. J. Iacono, and S. A. Clough, 1997: Radiative transfer for inhomogeneous atmospheres: RRTM, a validated correlated-*k* model for the longwave. *J. Geophys. Res.*, **102,** 16663–16682.

Mostovoy, G. V., and V. G. Anantharaj, 2008: Observed and simulated soil moisture variability over the lower Mississippi delta region. *J. Hydrometeor*, **9**, 1125–1150.

Ngan, F., H. Kim, P. Lee, B. Dornblaser, and K. Al-Wali, 2013: A study on nocturnal surface wind speed over-prediction by the WRF-ARW model in Southeastern Texas. *J. Appl. Meteor. Climatol.,* in press.

Noilhan, J., and S. Planton, 1989: A simple parameterization of land surface processes for meteorological models. *Mon. Wea. Rev.,* **117,** 536–549.

Ookouchi, Y., M. Segal, R. C. Kessler, and R. A. Pielke, 1984: Evaluation of soil moisture effects on the generation and modification of mesoscale circulations. *Mon. Wea. Rev.*, **112,** 2281–2292.

Overduin, P. P., D. L. Kane, and W. K. P. van Loon, 2006: Measuring thermal conductivity in freezing and thawing soil using the soil temperature response to heating. *Cold Reg. Sci. Technol.*, **45**, 8–22.

Peters-Lidard, C. D., E. Blackburn, X. Liang, and E. F. Wood, 1998: The effect of soil thermal conductivity parameterization on surface energy fluxes and temperatures. *J. Atmos. Sci.*, **55,** 1209–1224.

Reeves, H. D., K. L. Elmore, G. S. Manikin, and D. J. Stensrud. 2011: Assessment of forecasts during persistent valley cold pools in the Bonneville basin by the North American mesoscale model. *Weather and Forecasting,* **26**, 447-467.

Rife, D. L., T. T. Warner, F. Chen, and E. G. Astling, 2002: Mechanisms for diurnal boundary layer circulations in the Great Basin Desert. *Mon. Wea. Rev.*, **130**, 921–938.

Rife, D. L., C. A. Davis, Y. Liu, T. T. Warner, 2004: Predictability of low-level winds by mesoscale meteorological models. *Mon. Wea. Rev.*, **132**, 2553–2569.

Robock, A., and Coauthors. 2003: Validation of North American Land Data Assimilation Systems retrospective forcing over the southern Great Plains. *J. Geophys. Res.*,**108**, 8846.

Schaefer, G. L., M. H. Cosh, and T. J. Jackson, 2007: The USDA natural resources conservation service soil climate analysis network (SCAN). *J. Atmos. Oceanic Technol.*, **24**, 2073–2077.

Segal, M., J. R. Garratt, G. Kallos, and R. A. Pielke, 1989: The impact of wet soil and canopy temperatures on daytime boundary-layer growth. *J. Atmos. Sci.*, **46,** 3673–3684.

Seyfried, M. S., L. E. Grant, E. Du, and K. Humes, 2005: Dielectric loss and calibration of the Hydra Probe soil water sensor, *Vadose Zone J.*, **4**, 1070–1079.

Skamarock, W. C., and Coauthors, 2008: A description of the advanced research WRF version 3. NCAR Tech. Note TN-475_STR, 113 pp.

Steeneveld, G. J., T. Mauritsen, E. I. F. de Bruijn, J. Vilà-Guerau de Arellano, G. Svensson and A. A. M. Holtslag, 2008: Evaluation of limited area models for the representation of the diurnal cycle and contrasting nights in CASES99. *J. Appl. Meteor. Climatol.*, **47**, 869-887.

Tapper, N. J., 1988: Some evidence for a mesoscale thermal circulation at The Salt Lake, New South Wales. *Aust. Meteor. Mag.,* **36**, 101–102.

Tarnawski, V. R., and W. H. Leong, 2000: Thermal conductivity of soils at very low moisture content and moderate temperatures. *Transport Porous Med.*, **41**, 137–147.

Tarnawski, V. R., T. Momose, and W. H. Leong, 2009: Assessing the impact of quartz content on the prediction of soil thermal conductivity. *Géotechnique*, **59**, 331–338.

Viterbo, P., and A. C. M. Beljaars, 1995: An improved land surface parameterization scheme in the ECMWF model and its validation. *J. Climate,* **8,** 2716–2748.

Wen, X., S. Lu, and J. Jin, 2012: Integrating remote sensing data with WRF for improved simulations of oasis effects on local weather processes over an arid region in northwestern China. *J. Hydrometeor*, **13**, 573–587.

Zhang, H., Z. Pu, X. Zhang, 2013: Examination of errors in near-surface temperature and wind from WRF numerical simulations in regions of complex terrain. *Wea. Forecasting*, **28**, 893–914.

Zhou, X., and B. Geerts, 2013: The influence of soil moisture on the planetary boundary layer and on cumulus convection over an isolated mountain. Part I: observations. *Mon. Wea. Rev.*, **141**, 1061–1078.

CHAPTER 3

REGIONAL SOIL-MOISTURE BIASES AND THEIR INFLUENCE ON WRF MODEL TEMPERATURE FORECASTS OVER THE INTERMOUNTAIN WEST

3.1 Abstract

Operational Weather Research and Forecasting (WRF) model forecasts run over Dugway Proving Ground in northwest Utah (4DWX-DPG) underpredict the amplitude of the diurnal temperature cycle during September and October. Mean afternoon [2000 UTC (1300 LST)] and early morning [1100 UTC (0400 LST)] 2-m temperature bias errors evaluated against 195 surface stations using 6-h and 12-h forecasts are –1.37°C and 1.66°C, respectively. Bias errors relative to soundings and 4DWX-DPG analyses illustrate that the afternoon cold bias extends from the surface to above the top of the planetary boundary layer, whereas the early morning warm bias develops in the lowest model levels and is confined to valleys and basins. These biases are largest during mostly clear conditions and are caused primarily by a regional overestimation of near-surface soil-moisture in operational land-surface analyses, which do not currently assimilate in situ soil-moisture observations. Bias correction of these soil-moisture analyses using data from 42 North American Soil Moisture Database stations throughout

the Intermountain West reduces both the afternoon and early morning bias errors and improves forecasts of upper-level temperature and stability.

3.2 Introduction

Accurate temperature forecasts by numerical weather prediction (NWP) models are critical for the protection of life and property, economic and operational activities, and routine day-to-day planning. Temperature forecasts not only affect near-surface (2-m) conditions, but also atmospheric stability, planetary boundary layer (PBL) heights, near-surface winds, and precipitation type. Large systematic temperature errors from the Weather Research and Forecasting (WRF) model are observed throughout the world including over the European Alps (Garcia-Diez et al. 2013) and the continental US (Wyszogrodzki et al. 2013). Over the interior western US, several studies identify an underprediction of the 2-m diurnal temperature range (DTR) with a warm (i.e., positive) 2-m temperature bias at night and in the early morning and a cold (i.e., negative) 2-m temperature bias in the afternoon. These biases are found for a wide range of modeling systems, resolutions, and configurations (e.g., Cheng and Steenburgh 2005; Hart et al. 2005; Zhang et al. 2013; Massey et al. 2014).

Hypothesized contributors to the DTR underprediction include inadequate vertical or horizontal resolution, near-surface turbulence flux errors, or inaccurate land-surface characteristics and processes (e.g., Hanna and Yang 2001; Mass et al. 2002; Marshall et al. 2003; Cheng and Steenburgh 2005; Massey et al. 2014). Recently, Massey et al. (2014) reduced the early morning warm bias in WRF simulations of three fall days over northern Utah through the use of an alternate soil thermal conductivity parameterization

combined with soil moisture analyses based on in situ observations. The afternoon cold bias, however, remains associated with a myriad of plausible, yet untested, error sources including: 1) differences between model and observation site elevations (Liu et al. 2008b; Wyszogrodzki et al. 2013); 2) radiation parameterization errors due to the absence of 3-dimensional scattering in complex terrain or tuning for lower elevations (Zhong and Fast 2003; Liu et al. 2008b; Wyszogrodzki et al. 2013); 3) underprediction of thermally forced circulations due to smoother-than-real topography making the associated subsidence warming over valleys and basins less intense during the day (Liu et al. 2008b); 4) decreased solar radiation due to excessive mountain cloud development during the day (Wyszogrodzki et al. 2013); and 5) inaccurate initialization and parameterization of land surface characteristics and processes (Cheng and Steenburgh 2005; Wyszogrodzki et al. 2013). Additionally, Zhang et al. (2013) ran simulations with varying vertical resolution, forecast initialization times, and PBL schemes to test the influence of these parameters on the daytime cold bias over Utah, but noticed little improvement.

Soil moisture is a critical parameter for NWP because of its influence on surface sensible and latent fluxes, ground heat fluxes, surface and boundary layer winds, surface and boundary layer temperatures, and moist convection (e.g., Banta and Gannon 1995; Huang et al. 1996; Sun and Bosilovich 1996; Holt et al. 2006; Trier et al. 2008; Zhou and Geerts 2013). In general, lower soil moisture results in higher daytime and lower nighttime near-surface temperatures. Daniels et al. (2006) identified a daytime cold bias in their WRF simulations over Owens Valley, CA, which they reduced by decreasing their analyzed initial soil moisture by a factor of 3 based on in situ soil-moisture observations. Limited-area mesoscale models, like the WRF, typically obtain their soil

moisture initial conditions from operational modeling systems such as the National Centers for Environmental Prediction (NCEP) Global Forecast System (GFS) or the European Centre for Medium-Range Weather Forecasts (ECMWF) Integrated Forecast System (IFS). The land-surface models (LSMs) that predict the land-surface state in these operational modeling systems do not currently utilize in situ soil-moisture observations (Dirmeyer et al. 2002; Dee et al. 2014). Instead, the soil moisture in the GFS LSM is nudged towards a soil-moisture climatology (Dee et al. 2014), whereas the IFS uses an extended Kalman-filter data assimilation approach that utilizes surface temperature, relative humidity, and satellite data as proxy observations to analyze soil moisture (Albergel et al. 2012a). Although we know of no published study examining soil moisture biases in the GFS, the operational IFS and Era-Interim Reanalysis are known to overestimate soil moisture, especially in drier regions (Albergel et al. 2012b).

To improve global analyses of soil moisture, a number of studies have utilized near-surface soil moisture estimates from spaceborne microwave remote sensing platforms (e.g., Jackson et al. 2010; Kerr et al. 2010). Such platforms include the Soil Moisture and Ocean Salinity mission (SMOS; Kerr et al. 2010), Advanced Microwave Scanning Radiometer–Earth Observing System (AMSR–E), and the Advanced Scatterometer (ASCAT). Although satellite soil moisture retrieval algorithms have improved in recent years, their coarse spatial resolution (> 10–30 km) and large discrepancies with in situ soil moisture observations currently limit their utility (Crow et al. 2010; Jackson et al. 2010; Al Bitar et al 2012; Albergel et al. 2012a). However, the Soil Moisture Active/Passive (SMAP) mission launched in early 2015 will measure soil moisture at higher resolution (9 km) and will provide more detailed measurements.

In this chapter we examine how a regional overestimation of near-surface soil moisture in operational analyses over the Intermountain West during the fall (i.e., September and October) contributes to the underprediction of the DTR in a WRF-based forecasting system over Dugway Proving Ground (DPG) in the Great Salt Lake Desert of northwest Utah (Fig. 3.1). In particular, we extend the work of Massey et al. (2014) by examining the causes of the daytime cold bias and identifying differences in error structure and model sensitivity compared to the morning warm bias. We use idealized WRF single column model simulations to help quantify the significance of the soil moisture error contribution to the DTR errors, and retrospective WRF simulations run for the Mountain Terrain Atmospheric Modeling and Observations Program (MATERHORN) fall field campaign from 25 September 2012 – 25 October 2012 at DPG to show the temperature improvement in a fully cycled forecast system when near-surface soil moisture analyses are bias corrected and a modified soil thermal conductivity parameterization is implemented. These results suggest that efforts to incorporate soil moisture observations into land-surface analyses will likely yield improved temperature forecasts over the Intermountain West and possibly other dryland regions.

3.3 Data and Methods

3.3.1 WRF Modeling

3.3.1.1 Operational WRF (4DWX-DPG) Forecasts

We identify temperature errors in 8 months of operational WRF-based forecasts produced by the U.S. Army Test and Evaluation Command Four-Dimensional Weather System (4DWX) developed by the National Center for Atmospheric Research (NCAR)

and run at DPG (4DWX-DPG, Liu et al. 2008a). We concentrate on September and October of 2011, 2012, 2013, and 2014 because these months are most relevant to the MATERHORN fall 2012 field campaign (Fernando et al. 2015). They also follow the climatologically driest and warmest months of the year (June–August) at the DPG National Weather Service Cooperative Observer site (WRCC 2015) and thus it is anticipated that soil moistures across much of the region will be at or near the annual climatological minimum. For September and October 2011, 4DWX-DPG was based on WRF v3.2, with an upgrade to WRF v3.3.1 prior to September and October 2012. 4DWX-DPG features 30, 10, 3.3, and 1.1-km one-way nested domains centered over DPG. For this study, we use data from only the outer three domains (Fig. 3.1). 4DWX-DPG has 36 half-η levels, whose vertical spacing varies from ~30 m near the surface, with the lowest half-η level ~15 m AGL, to ~1250 m in the upper troposphere and lower stratosphere. The use of one-way nesting is based on its simplicity and superiority over two-way nesting in unpublished test cases. The physics packages include the Rapid Radiative Transfer Model (RRTM) longwave radiation parameterization (Mlawer et al. 1997), Dudhia shortwave radiation parameterization (Dudhia 1989), Noah LSM (Chen and Dudhia 2001), Yonsei University PBL parameterization (YSU; Hong et al. 2006), explicit sixth-order numerical diffusion (Knievel et al. 2007), and the new Kain-Fritsch cumulus parameterization (Kain 2004). The latter was used only in the 30- and 10-km domains through 2013, then on the 3.3-km domain thereafter. Thompson et al. (2004) microphysics replaced the Lin et al. (1983) microphysics prior to September and October 2012. Rayleigh damping and an updated land-cover and terrain elevation dataset based on the 33-category National Land Cover Database [NLCD (Fry et al. 2011)] were added

in September 2012. A special playa category is manually added to the NLCD and WRF soil texture class field to better account for the large playa in northwest Utah (Fig. 3.2).

4DWX-DPG produces 48-h forecasts every 3 hours, with nominal initialization times of 0200, 0500, 0800, 1100, 1400, 1700, 2000, and 2300 UTC. The atmospheric data assimilation stage of each forecast cycle uses Newtonian nudging for assimilating observations during the 3-h period prior to the nominal initialization time (an initialization time is conceptually equivalent to a forecast lead time of 0 h). Observations come from aviation routine weather report (METAR) stations, rawinsondes, profilers, buoys, aircraft, satellites, and other observing platforms. In practice, some nudging is still performed during the early parts of the forecast (i.e., after 0 h) as 4DWX-DPG — following the passing of some finite time during the assimilation stage and various preprocessing steps — catches up to what is commonly called "wall-clock time." The analysis that is produced at the conclusion of an assimilation stage is used to restart the assimilation of the next cycle, except for the 0500 UTC Sunday cycle when the system is "cold started" with an objective analysis using the 1.0-degree GFS analysis. At this time initial soil-moisture and temperature fields are set to GFS analysis values. The initialization of soil moisture in this step is fundamental to our results, as we explain below. We use the 4DWX-DPG analyses to calculate model forecast biases given the similarity between the analyses and observations (not shown). Liu et al. (2008a) provide additional information on the 4DWX-DPG physics packages and data assimilation.

3.3.1.2 Single-Column Model (SCM)

The WRF single-column model [SCM (Rostkier-Edelstein and Hacker 2010)] is based on WRF v3.5.1 and is run to test 2-m temperature sensitivity to soil moisture, the Zilitinkevich coefficient (C_{zil}, an empirical coefficient that helps control the strength of the land-atmosphere coupling), long- and shortwave radiation schemes, and PBL schemes. The SCM is run over a 3x3 grid-point stencil with periodic LBCs, no external forcing, and the same physics packages and vertical grid spacing as in 4DWX-DPG, except in sensitivity studies involving radiation or PBL schemes.

The SCM is initialized with mean morning [1400 UTC (0700 MST)] atmospheric profiles of temperature, wind, and specific humidity, and mean soil profiles of moisture and temperature obtained from 4DWX-DPG over the MATERHORN rawinsonde launch site (EFS-playa, Fig. 3.1) on 129 mostly clear days during the 8 study months that were identified using the approach described below. Solar radiation is based on 1 October conditions. We examine the 2-m DTR from hourly output during a 24-h period beginning at 1800 UTC, which allows for a 4-h spin up.

We identify mostly clear and mostly cloudy days using a domain-averaged atmospheric transmittance defined as:

$$Transmittance = \frac{\sum_{t=0000\ LST}^{2330\ LST} SW_{sfc}(t)}{\sum_{t=0000\ LST}^{2330\ LST} SW_{toa}(t)}$$

where $SW_{sfc}(t)$ is the domain-average downwelling shortwave radiation at the surface at time *t*, and $SW_{toa}(t)$ is the theoretical mean downwelling top-of-atmosphere shortwave radiation calculated from:

$$SW_{toa}(t) = S_0 \left(\frac{a}{r}\right)^2 \sin(\varphi)$$

where S_0 is the solar constant (approximated to be 1370 W m^{-2}), a is the annual mean distance between the sun and the earth, r is the daily mean distance, and φ is the solar elevation angle calculated following Reda and Andreas (2004). Mostly clear days are defined arbitrarily as those with a transmittance > 0.65 and all other days with lower transmittance due to more clouds and aerosols are classified as mostly cloudy.

3.3.1.3 Retrospective Simulations

To examine the influence of soil moisture bias and the soil thermal conductivity parameterization used by Massey et al. (2014) on the morning and afternoon temperature biases in a fully cycled modeling system, we produce a series of retrospective 4DWX simulations for the MATERHORN fall field campaign period of 25 September 2012 – 25 October 2012 (4DWX-MATERHORN). The MATERHORN fall field campaign period was relatively quiescent synoptically with limited precipitation (8.7 mm at the DPG National Weather Service Cooperative Observer site). The 4DWX-MATERHORN configuration is the same as the 2012 version of 4DWX-DPG except for use of (1) WRF v3.5.1, (2) updated data assimilation with the observation quality control done inside the model, (3) biweekly cold starts on Tuesdays and Fridays at 0500 UTC and (4) climatological Great Salt Lake temperatures obtained from Steenburgh et al. (2000).

3.3.2 Validation Data and Methods

Near-surface 2-m temperature forecasts, which are diagnosed from the WRF-model half-η and skin-level fields using similarity theory, are validated against 2-m temperature observations obtained from the Mesowest cooperative networks (Horel et al.

2002). Although no formal quality control was performed on any of the 2-m observations, missing and obviously erroneous observations were removed. In addition, we only consider stations with a site elevation within 100 m of the corresponding WRF elevation, and observations reported within 5 minutes of the top of each hour. We use bias error (BE) to validate 4DWX forecasts against observations or 4DWX analyses (i.e., forecast hour 0). BE is calculated following:

$$BE = \frac{1}{N}\sum_{i=1}^{N}(f_i - o_i),$$

wherein N is the number of forecast/observation pairs in the sample, f_i is the forecast, and o_i is the observation or analysis. Positive temperature BEs represent a warm bias and negative temperature BEs represent a cold bias.

3.3.3 Soil Moisture Observations

Soil moisture observations are from the North American Soil Moisture Database (NASMD) at Texas A&M University (http://soilmoisture.tamu.edu), which harmonizes and quality controls several in situ soil-moisture observing platforms. Within the region encompassed by 4DWX-DPG 10-km domain, observations come from 27 U.S. Department of Agriculture Soil Climate Analysis Network (SCAN; Schaefer et al. 2007) stations and 15 Global Positioning System (GPS) soil moisture stations (Larson et al. 2008). SCAN stations use Stevens Water Hydra Probes to measure soil moisture, and the probes are calibrated for each soil-texture class (Seyfried et al. 2005). Soil moisture is measured hourly at depths of 5.1, 10.2, 20.3, 50.8, and 101.6 cm, but the Noah LSM is configured with depths centered at 5, 25, 70, and 150 cm. Therefore we only consider the 5.1 and 20.3 cm SCAN levels relative to the 5 and 25 cm Noah LSM levels, respectively,

for initialization and validation. GPS stations receive L-band radiation (1.57742 and 1.22760 GHz) from GPS satellites, and the multipath signal that reflects off the land surface is used to calculate near-surface soil moisture (Ochsner et al. 2013). Unlike in situ measurements, such as those from SCAN, GPS soil-moisture measurements represent a ~300 m^2 area, with some variation depending on the height of the GPS antenna (Larson et al. 2008). The GPS soil-moisture measurements are influenced most strongly by 0–5 cm soil moisture in moist soils, but are more influenced by deeper soil moisture in drier soils. Rodriguez-Alvarez et al (2009) found root-mean squared errors < 0.03 m^3 m^{-3} relative to 5 cm in situ observations, so we conclude this dataset is useful for comparisons with 5 cm 4DWX-DPG soil moisture. Unfortunately the NASMDB data are not available from September and October 2014, limiting our 4DWX-DPG soil moisture validation to September and October 2011, 2012, and 2013.

3.4 Results

3.4.1 Bias Error Characteristics

The 2-m temperature BEs from 8 months of September and October operational 4DWX-DPG forecasts relative to observations are –1.37°C in the afternoon [2000 UTC (1300 MST)] using 6-h forecasts (Fig. 3.2a) and 1.66°C in the early morning [1100 UTC (0400 MST)] using 12-h forecasts for 195 stations in 3.3-km domain (Fig. 3.2b)[4]. An afternoon cold bias and early morning warm bias implies an underprediction of the amplitude of the 4DWX-DPG 2-m DTR. Although the early morning warm bias is

[4] We chose 6-h and 12-h forecasts for the afternoon and early morning, respectively, because they produce the largest BEs, as discussed later in this section. We chose 2000 UTC and 1100 UTC because they have the largest 2-m temperature biases.

slightly larger in magnitude than the afternoon cold bias, the early morning BEs are especially large (>2°C) over valleys and basins, including the eastern sites of DPG, the Rush Valley, and the Wasatch Front (see Fig. 3.1 for locations). During the afternoon, nearly all sites have neutral or negative BEs.

Daily domain-averaged afternoon 2-m temperature BEs calculated from 6-h forecasts and 4DWX-DPG analyses show a strong relationship between BE and the domain-averaged atmospheric transmittance in the afternoon (Fig. 3.3a). Although the overall BE for these forecasts is –0.77°C, on the 161 mostly clear days (i.e., transmittance > 0.65) the BE is –1.01°C, whereas on the 67 mostly cloudy days the BE is only –0.19°C. Only five mostly clear days have positive BEs, whereas 28 mostly cloudy days have positive BEs. An analysis of afternoon BE sensitivity to wind speed, wind direction, and atmospheric stability yielded little to no correlation (not shown). These results suggest that the underestimation of the afternoon 2-m temperature might be related to the magnitude of the sensible, ground, and latent heat fluxes during the day. Although the signal is weaker, the early morning BEs are also affected by sky cover. The overall BE is 0.77°C, the mostly clear day BE is 0.85°C, and the mostly cloudy day BE is 0.57°C (Fig. 3.3b). This weaker influence may partly reflect the presence of nocturnal clouds prior to some mostly clear days.

Relative to 4DWX-DPG analyses, the afternoon 2-m temperature BEs calculated from 6-h forecasts and 4DWX-DPG analyses are negative throughout the domain on mostly clear days and strongest over eastern DPG and valleys to the southeast (Fig. 3.4a). During mostly cloudy days, the afternoon BEs are weaker and even positive in some low-elevation basins and valleys (Fig. 3.4b). In contrast, the early morning 2-m temperature

BEs calculated from 12-h forecasts are primarily positive on mostly clear days except to the immediate west of the northern Great Salt Lake (Fig. 3.4c). These morning BEs also exhibit more spatial variability and are generally largest in valleys and basins. On mostly cloudy days, the early morning BEs are weaker and more uniform (Fig. 3.4d). The spatial distribution and magnitude of the mostly clear day BEs relative to 4DWX-DPG analyses are also similar to the BEs relative to observations (cf. Figs. 3.2 and 3.4), which justifies using 4DWX-DPG analyses for validation.

Comparison of mean observed and forecast (5–7 h) atmospheric soundings from EFS-Playa for the 15 soundings taken between 1800–0000 UTC during the MATERHORN fall 2012 field campaign show that the afternoon cold bias extends through 650 hPa (Fig. 3.5). The BE reaches –1.53°C at 805 hPa. There is very little dewpoint temperature bias in the low levels, but a slight dry bias exists above 780 hPa. Forecast wind speeds also close to observed, but below 800 hPa, the WRF winds are near northerly, whereas the observed are northeasterly or east-northeasterly.

EFS-Playa is located, however, over the playa of the western DPG (see Fig. 3.2 for location), which typically features higher soil moisture, higher thermal conductivity and lower afternoon temperatures than over the surrounding sparsely vegetated desert, including eastern DPG (Rife et al. 2002). We find weaker 2-m temperature BEs over the playa than the surrounding region because of these differences (Fig. 3.2). Cross sections of potential temperature (θ) BE calculated from 6-h forecasts and 4DWX-DPG analyses show that the afternoon cold bias extends through the planetary boundary layer (PBL) and is maximized over eastern DPG (Fig. 3.6a; see Fig. 3.1 for cross section location). In contrast, the early morning warm bias calculated from 12-h forecasts is confined

primarily to the lowest model levels over the valleys and basins and is strongest below ~1500m MSL (Fig. 3.6b). The domain-averaged potential temperature ($\bar{\theta}$) BE calculated between the lowest and 28th half-η levels (~surface–290 hPa) is –0.43 K in the afternoon and 0.21 K in the early morning. Thus, the afternoon cold bias has a greater impact on the regional tropospheric heat content than the early morning warm bias.

Mostly clear day $\bar{\theta}$ BEs calculated relative to 4DWX-DPG analyses show the diurnal modulation of BEs, but also an amplifying cold bias with increasing forecast lead time regardless of initialization time (Fig. 3.7). For example, forecasts initialized at 0200 UTC have a $\bar{\theta}$ BE maximum of 0.25 K at 1400 UTC on day 1 (12-h forecast) and second maximum of –0.06 K at 1400 UTC on day 2 (36-h forecast). Similarly, forecasts initialized at other times have $\bar{\theta}$ BE maxima at 1400 UTC on day 1 and day 2, as well as an intermediate minima at 2300 UTC. The use of 6- and 12-h forecasts to illustrate the afternoon and early morning BEs throughout this chapter reflects the fact that the 2000 UTC cold bias is most pronounced in the 1400 UTC initialized run, and the 1100 UTC warm bias is most pronounced in the 2300 UTC initialized run, respectively.

3.4.2 Near-Surface Soil Moisture Biases

Mean 0000 UTC 5-cm soil moisture values during September and October of 2011, 2012, and 2013 show that the 4DWX-DPG analyses have a pronounced regional-scale moist bias compared to the 42 NASMDB stations throughout the intermediate 10-km domain (Fig. 3.8), with similar biases in the 30-km and 3.3-km domains (not shown). The NASMDB station located within DPG has the highest mean soil moisture, yet is still drier than the 4DWX-DPG analyses. The NASMDB stations also exhibit more spatial

variability than the 4DWX-DPG analyzed soil moisture, with a range of 0.007–0.198 m^3 m^{-3} compared to 0.172–0.256 m^3 m^{-3}, respectively. The GPS stations have a smaller range (0.049–0.133 m^3 m^{-3}) than the SCAN stations (0.007–0.198 m^3 m^{-3}), but a similar mean (0.093 m^3 m^{-3} compared to 0.099 m^3 m^{-3}). Although the focus of this study is on the net contribution of soil moisture to temperature bias, we anticipate soil moisture analyses that capture this spatial variability will further improve temperature forecasts.

The mean 4DWX-DPG 5-cm soil moisture at all NADMSB station locations during September and October of 2011, 2012, and 2013 is 0.223 m^3 m^{-3}, compared to an observed mean of only 0.096 m^3 m^{-3}. Bias correcting for this 0.127 m^3 m^{-3} difference yields a close match for daily values (Fig. 3.9), although a slight moist bias remains during and immediately following heavy precipitation events (inferred from rapid soil-moisture increases). A similar analysis was conducted for the 4DWX-DPG 25-cm soil moisture using the 20.3-cm SCAN soil moisture, yielding a 0.079 m^3 m^{-3} moist bias (not shown). Since the 4DWX-DPG soil moisture analyses are set to GFS analysis values during weekly cold starts and change very little during the week, these soil moisture biases originate with the GFS analyses.

3.4.3 SCM Simulations

We use the SCM to test the sensitivity of the 2-m DTR to the 5-cm soil moisture, as well as other factors including the specification of C_{zil}, the choice of long- and short-wave radiation schemes, and the choice of PBL scheme. We test over the three most common land-use and soil-texture class combinations in the 3.3-km domain: shrubland with loam soil (S-L), shrubland with silt loam soil (S-SL), and playa with playa soil (P-

P). S-SL is also tested using the standard Noah LSM, and a modified version (S-SL-m) that incorporates the McCumber and Pielke (1981) soil thermal conductivity parameterization (MP81) for silt loam and sandy loam soils, which was shown by Massey et al. (2014) to improve the early morning warm bias over DPG.

3.4.3.1 Soil Moisture

In our SCM simulations over the range of allowable near-surface soil moistures in the Noah LSM (0.02–0.48 m^3 m^{-3}), the 2-m DTR increases rapidly with decreasing soil moisture, especially at lower soil moistures [e.g., < 0.15 m^3 m^{-3} (Fig. 3.10a)]. A soil moisture decrease from 0.22 m^3 m^{-3} (the approximate mean 4DWX-DPG soil moisture) to 0.10 m^3 m^{-3} (the approximate mean NASMDB soil moisture) yields 2-m DTR increases of 2.5°C for S-L, 3.1 °C for P-P, 2.5°C for S-SL, and 5.4°C for S-SL-m. The mean 2-m DTR for S-L, P-P, and S-SL-m is 16.4°C at 0.10 m^3 m^{-3}, which is 2.5°C higher than the maximum obtained in any other SCM experiment (Figs. 3.10b-d). These results strongly suggest that the soil moisture bias and the default parameterization of soil thermal conductivity are significant contributors to the 2-m DTR underprediction.

3.4.3.2 Zilitinkevich Coefficient

Another potential contributor to the 2-m DTR errors in 4DWX-DPG is the uncertainty associated with estimating C_{zil}. The relationship between the roughness lengths for heat (z_{0t}) and momentum (z_{0m}) in the Noah LSM currently follows Zilitinkevich (1995):

$$z_{0t} = z_{0m}\exp\left(-kC_{zil}\sqrt{R_e}\right),$$

where $k = 0.4$ is the von Karman constant and R_e is the roughness Reynolds number. C_{zil} serves as an empirical coefficient that helps control the surface heat exchange with the atmosphere. Higher C_{zil} values lead to higher surface skin temperatures, lower surface sensible heat fluxes, and lower atmospheric temperatures (Zheng et al. 2012; Zeng et al. 2012).

Previous WRF versions of the Noah LSM used a constant C_{zil} of 0.1, but Chen and Zhang (2009) implemented an option to use the following relationship, which was incorporated into 4DWX-DPG:

$$C_{zil} = 10^{[-0.4(z_0/0.07)]},$$

wherein z_o is the roughness length of the underlying land-use category. A realistic range of C_{zil} is between 0, which assumes an identical z_{0t} and z_{om}, and 1 (Chen et al. 1997). In our SCM simulations, the 2-m DTR increases with decreasing C_{zil} at a nearly constant rate for all four simulations (Fig. 3.10b). The mean maximizes at 13.9°C when C_{zil} is zero (Fig. 3.10b). This is 2.5°C lower than the mean 2-m DTR at a 0.10 m^3 m^{-3} soil moisture (cf. Figs. 3.10a and 3.10b). In addition, the low roughness lengths of S-L, S-SL, and P-P over DPG imply a higher C_{zil} value (Chen and Zhang 2009), so a C_{zil} of zero is unlikely. Therefore, errors stemming from the estimation of C_{zil} are not contributing significantly to the underestimation of the 2-m DTR in 4DWX-DPG.

3.4.3.3 Radiation Schemes

Long- and short-wave radiation schemes have a minor influence on the 2-m DTR, and only the Community Atmosphere Model schemes (CAM; Collins et al. 2003) increase the mean 2-m DTR (by 1.5°C or less) compared to the RRTM and Dudhia

schemes currently used in 4DWX-DPG (Fig. 3.10c, S-SL not presented). The 2-m DTR decreases marginally compared to RRTM and Dudhia using the global climate model version of the RRTM schemes (RRTMG; Iacono et al. 2008) or the Goddard schemes (Chou and Suarez 1999). Although the higher 2-m DTR from the CAM schemes suggests it could improve 2-m DTR errors, CAM schemes are tuned for global climate models and are not often used for mesoscale NWP simulations. We conclude that none of the radiation schemes tested significantly increases the DTR compared to the RRTM and Dudhia schemes currently used in 4DWX-DPG.

3.4.3.4 PBL Schemes

Here we test first-order, nonlocal, and 1.5-order TKE closure schemes that were also tested by Zhang et al. (2013) over the DPG region. The quasi-normal scale elimination PBL scheme (QNSE; Sukoriansky et al. 2005) and the Mellor–Yamada–Nakanishi–Niino level 2.5 PBL scheme (MYNN2; Nakanishi and Niino 2004) are 1.5-order TKE schemes and produce slightly higher mean 2-m DTRs than the YSU scheme currently used in 4DXW-DPG (Fig. 3.10d). The Asymmetric Convective Model version 2 scheme (ACM2; Pleim 2007) and the Mellor–Yamada–Janjić (MYJ) turbulent kinetic energy (TKE) scheme (Mellor and Yamada 1982) produce slightly lower DTRs than the YSU scheme. The small changes suggest that none of the PBL schemes presently available in WRF will significantly increase the DTR compared to the YSU scheme currently used in 4DWX-DPG. These results are consistent with the findings of Zhang et al. (2013).

3.4.4 Retrospective Simulations

Motivated by the results above, we test the influence of the overprediction of near-surface soil moisture on temperature forecasts in the fully cycled retrospective 4DWX-MATERHORN simulations. Table 3.1 summarizes the three different retrospective cycles, which use varying soil thermal conductivity parameterizations and varying regions of bias-corrected near-surface soil-moisture. The control 4DWX-MATERHORN cycle that is initialized from GFS soil moisture analyses and uses the default WRF soil thermal conductivity parameterization (hereafter referred to as Control) has afternoon and early morning BEs of –1.62°C (Fig. 3.11a) and 1.93°C (Fig. 3.11b), respectively, which are similar to, but slightly larger than, the BEs produced by 4DWX-DPG for all 8 validation months (cf. Figs. 3.2 and 3.11). Spatially, the BE distributions are also similar.

In SM-d03, we bias-correct the 5-cm soil moisture analyses of the 3.3-km domain by –0.131 m^3 m^{-3} and the 25-cm analyses by –0.072 m^{-3} m^{-3}, which are the mean soil moisture differences between NASMDB observations and the corresponding 4DWX-DPG values within the region encompassed by the 10-km domain during the MATERHORN period. Following Massey et al. (2014), we also replace the soil thermal conductivity parameterization in the Noah LSM with MP81 for silt loam and sandy loam soils. These changes reduce the afternoon and morning BEs to –0.90°C (Fig. 3.11c) and 0.64°C (Fig. 3.11d), improvements of 0.72°C and 1.29° relative to Control, respectively. In both cases, the greatest improvement occurs over DPG, with less improvement along the Wasatch Front. The Wasatch Front is urbanized and irrigated, and the bias-corrected

soil moisture might not be representative over this area. Overall, SM-d03 improves the early morning warm bias, but the improvement in the afternoon BE is smaller.

SM-Full is similar to SM-d03 except the soil moisture bias corrections are applied to the 3.3-km domain, the10-km domain, and the 10-km domain's footprint in the 30-km domain. This results in drier and more realistic soil moistures across the broader Intermountain West. These changes reduce the afternoon and morning BEs to –0.34°C (Fig. 3.11e) and 0.57°C (Fig. 3.11f), improvements of 0.56°C, and 0.07°C relative to SM-d03, respectively. Thus, the afternoon bias error improves from both local and regional soil moisture bias correction, but the early morning BEs are more sensitive to local soil moisture, with little improvement from soil moisture bias correction over the broader region. This result is consistent with the greater depth and regional coverage of the afternoon cold bias.

Hourly 2-m temperature BEs calculated from 11–14-h forecasts illustrate the underestimation of the 2-m DTR in Control, greatly improved nighttime forecasts in SM-d03, and greatly improved nighttime and daytime forecasts in SM-Full (Fig. 3.12). The mean 1700–0000 UTC daytime cold bias is –1.17°C in Control and improves to –0.68°C in SM-d03 and –0.20°C in SM-Full. The 0300–1400 UTC mean nighttime warm bias is 1.26°C in Control and improves to 0.23°C and 0.33°C in SM-d03 and SM-Full, respectively. However, SM-d03 and SM-Full introduce a brief morning-transition [1500 UTC (0800 LST)] warm bias and evening-transition [0100 UTC (1800 LST)] cold bias. These BEs may be related to the inaccurate partitioning of the surface energy budget during the transitions, which should be investigated in future work.

The 2-m temperature BEs relative to analyses have a local maximum near 1400 UTC and local minimum at 2000 UTC in Control for forecasts initialized at all nominal 4DWX-MATERHORN initialization times, but local maxima and minima are nearly eliminated in SM-Full (Fig. 3.13). Therefore, the diurnal modulation of 2-m BEs is almost nonexistent in SM-Full. However, an overall amplifying cold bias with increasing forecast lead time exists in both Control and SM-Full, similar to the amplifying cold bias observed in 4DWX-DPG (cf. 3.7 and 3.13), suggesting the presence of an unknown diurnally independent error source.

Comparison of mean MATERHORN atmospheric soundings taken between 1800 UTC and 0000 UTC at EFS-Playa with corresponding 5–7-h Control forecast soundings shows a deep cold bias (Fig. 3.14, red line) that was also present in the original 4DWX-DPG forecasts. The SM-Full forecasts (blue line) more closely match observations above 800 hPa, but exhibit a warm bias near the surface. This warm bias is consistent with positive 2000 UTC 2-m temperature bias at playa stations in SM-Full (Fig. 3.11e). The use of a spatially homogeneous soil-moisture bias correction based on data collected from the surrounding region may not be appropriate over this unique land-surface type.

Cross sections of θ BEs calculated from 6- and 12-h forecasts and 4DWX-MATERHORN analyses during the afternoon and early morning, respectively, also show temperature improvement in SM-d03 and SM-Full compared to Control (Fig. 3.15). Control has similar BEs to 4DWX-DPG with an afternoon cold bias extending through the depth of the mean PBL and into the middle troposphere, yielding a $\overline{\theta}$ of –0.54°C. In contrast, the early morning warm bias is confined to the lowest few model levels in valleys and basins (cf. Figs. 3.6 and 3.15a,b), yielding a $\overline{\theta}$ of –0.12°C. Compared to

4DWX-DPG forecasts for the entire 8-month validation period, $\bar{\theta}$ features a stronger afternoon cold bias and a weaker early morning warm bias, consistent with the stronger overall amplifying cold bias that exists in the 4DWX-MATERHORN simulations compared to the 4DWX-DPG forecasts for the entire 8-month validation period (cf. Figs. 3.15a,b and 3.6a,b). SM-d03 reduces the overall afternoon cold bias (Fig. 3.15c) and nearly eliminates the strong early morning warm BEs in the lowest few model levels (Fig. 3.15d). SM-Full further reduces the mean afternoon $\bar{\theta}$ cold bias (Fig. 3.15e) and largely eliminates the early morning near-surface warm bias (Fig. 3.15f). In SM-d03 and SM-Full, an upper level cold bias develops with increasing forecast lead time as the near-surface biases improve. We hypothesize that the upper level cold bias, which is also observed at 2-m (Fig. 3.13), is related to erroneous lateral boundary conditions given the vertical extent of the error.

Time-height θ cross-sections during the fifth intensive operating period of the MATERHORN fall 2012 field campaign (2100 UTC 9 October 2012 – 1200 UTC 10 October 2012) are created from 3-hourly observed EFS-playa soundings (Fig. 3.16a), the 1100 UTC 9 October 2012 Control simulation (Fig. 3.16b) and the 1100 UTC 9 October 2012 SM-Full simulation (Fig. 3.16c). This period has the most consecutive successful soundings during the MATERHORN fall 2012 field campaign. θ differences between observations and Control show a large underprediction of θ (Fig. 3.16b), whereas SM-Full shows θ within 1 K of observations (Fig. 3.16c). In addition to the improved θ forecasts, SM-Full also improves the 800–700 hPa atmospheric stability (cf. Figs. 3.16a and 3.16c), which is overpredicted in Control (cf. Figs. 3.16a and 3.16b). Therefore, SM-

Full may improve forecasts of other meteorological phenomena dependent on atmospheric stability such as winds and cloud development.

3.5 Conclusions

Eight months of operational WRF forecasts underpredict the strength of the diurnal temperature range (DTR) for Dugway Proving Ground in northwestern Utah (4DWX-DPG) during September and October of 2011, 2012, 2013, and 2014. In the afternoon [2000 UTC (1300 LST)], the 2-m temperature bias error (BE) in 12-h forecasts is –1.37°C relative to observations, with the cold bias extending through the top of the mean planetary boundary layer. In the early morning [1100 UTC (0400 LST)], the 2-m temperature BEs in 6-h forecasts is 1.66°C, but the warm bias is confined to the lowest few model levels in valleys and basins. The BEs are greatest during mostly clear skies.

The underprediction of the 2-m DTR is primarily the result of an overestimation of near-surface soil moisture in 4DWX-DPG analyses, which is initialized from the Global Forecast System (GFS) analyses once per week. 4DWX-DPG overestimates 5- and 25-cm soil moisture by a mean of 0.127 m^3 m^{-3} and 0.079 m^3 m^{-3}, respectively, compared to 42 North American Soil Moisture Database (NASMDB) soil-moisture observing stations. These biases are fairly consistent over a 6-month period enabling straightforward bias-correction of 4DWX-DPG soil moisture analyses. Results from WRF single column model (SCM) simulations illustrate that bias-corrected soil moisture combined with the McCumber and Pielke (1981) soil thermal conductivity parameterization for silt loam and sandy loam soils (Massey et al. 2014) greatly improves

the 2-m DTR forecast. The planetary boundary layer schemes, radiation schemes, and the estimation of the Zilitinkevich coefficient have a smaller influence on 2-m DTR.

Retrospective simulations for the MATERHORN fall 2012 field campaign period (4DWX-MATERHORN) show improved temperature forecasts using bias-corrected soil moisture analyses and a modified soil thermal conductivity parameterization. When the bias correction is only applied to the innermost 3.3-km domain (SM-d03), the early morning warm bias is nearly eliminated, but the afternoon cold bias is only slightly reduced. When the bias correction is applied regionally to the 3.3-km domain, the 10-km domain, and the 10-km domain's footprint in the 30-km domain (SM-Full), the afternoon cold bias is nearly eliminated. These results imply that the early morning warm bias is most sensitive to the local soil moisture, whereas afternoon cold bias is sensitive to both local and regional soil moisture. SM-Full also produces improvements in atmospheric temperature and stability above the surface.

Although the use of bias-corrected soil moisture yields significant 2-m temperature forecast improvements, an amplifying tropospheric cold bias develops in all simulations. The causes of this cold bias are unknown, but may be related to erroneous lateral boundary conditions or the 4DWX configuration. SM-d03 and SM-Full also introduce a brief 2-m temperature warm bias during the morning transition [1500 UTC (0800 LST)] and cold bias during the evening transition [0100 UTC (1800 LST)]. The source of these errors should be investigated in future work.

These results highlight a major consequence of the use of global soil moisture analyses for regional temperature prediction. These analyses, such as those produced by the National Centers for Environmental Prediction (NCEP) GFS or the European Centre

for Medium-Range Weather Forecasts (ECMWF) Integrated Forecast System (IFS), rely on land surface models that do not currently assimilate or utilize soil-moisture observations. Over the Intermountain West, this leads to a large positive soil-moisture bias that degrades temperature forecasts. Other regions may have similarly large soil-moisture biases and associated temperature forecasts errors. The global soil-moisture analyses can potentially be improved by incorporating existing soil moisture observations. Deployment of more soil moisture stations should also be considered over data-sparse regions, especially the cost-effective GPS-based stations. The recently launched NASA Soil Moisture Active/Passive (SMAP) mission that measures soil moisture with ~10-km pixels, also offers significant potential to improve soil-moisture analyses worldwide.

Table 3.1: Summary of 4DWX-MATERHORN simulations

	Control	**SM-d03**	**SM-Full**
Soil moisture initialization at cold start	1.0° GFS analysis	Bias-corrected on 3.3-km domain	Bias-corrected on 3.3-km, 10-km, and 10-km's footprint in 30-km domains
Noah LSM modifications	None	MP81 for silt loam and sandy loam soils	MP81 for silt loam and sandy loam soils

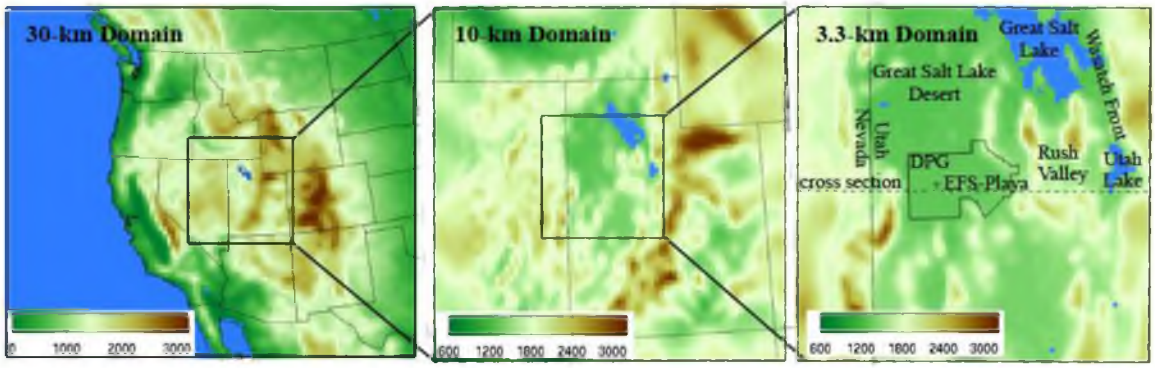

Fig. 3.1. 4DWX-DPG domains with model elevation (m, shaded following colorbar at lower left) and water bodies (blue). Within the 3.3-km domain, the perimeter of DPG is outlined, the dotted line represents the location of the cross sections, and the MATERHORN EFS-playa rawinsonde launch site is annotated.

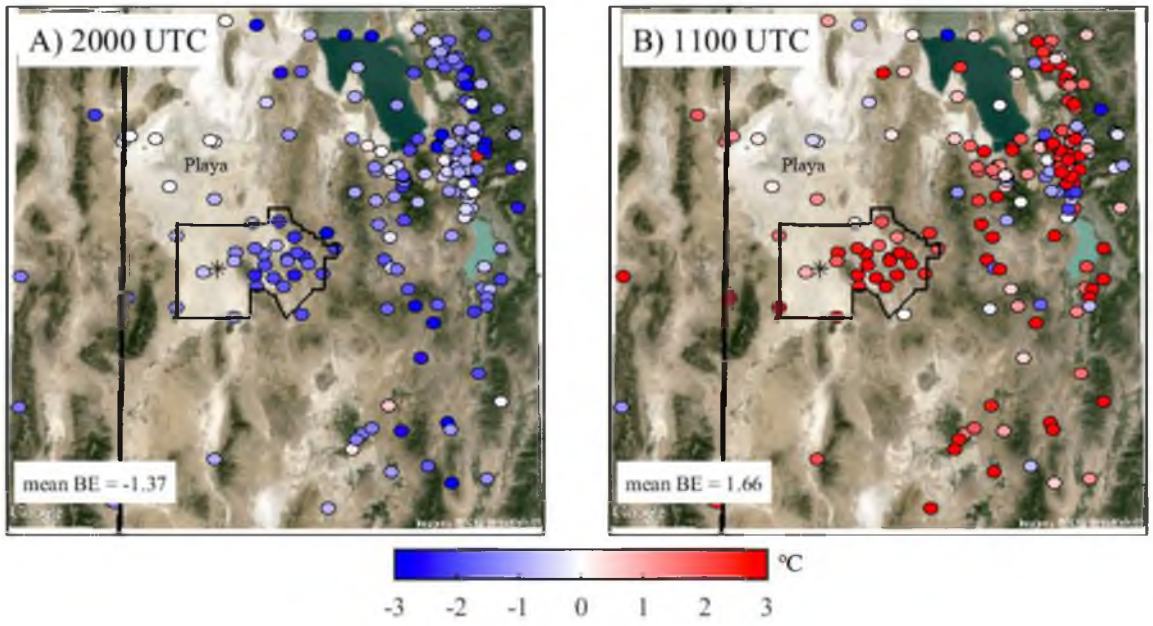

Fig. 3.2. Mean 4DWX-DPG 2-m temperature BEs (°C) at Mesowest stations during the (a) afternoon (2000 UTC) and (b) early morning (1100 UTC). Overall mean BE annotated. Background Google Earth image [©2015 Google; imagery ©2015 TerraMetrics]. The Utah/Nevada border, DPG boundary, EFS-playa (asterisk), and the playa annotated for reference.

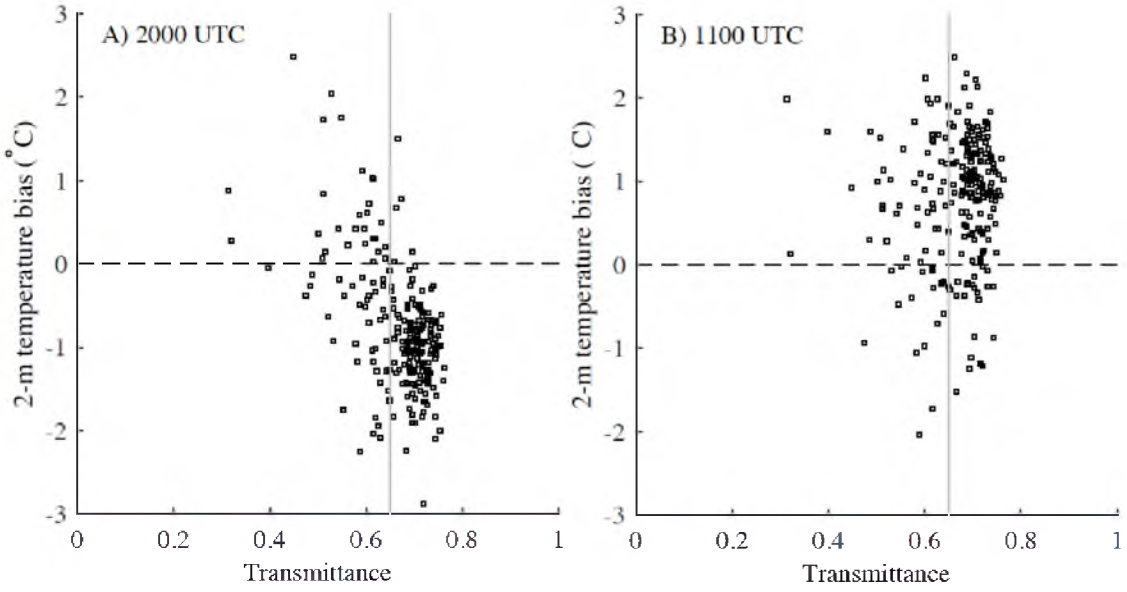

Fig. 3.3. Daily domain-averaged 4DWX-DPG 2-m temperature BEs (°C) at Mesowest stations versus daily domain-averaged atmospheric transmittance for (a) 6-h forecasts ending at 2000 UTC and (b) 12-h forecasts ending at 1100 UTC.

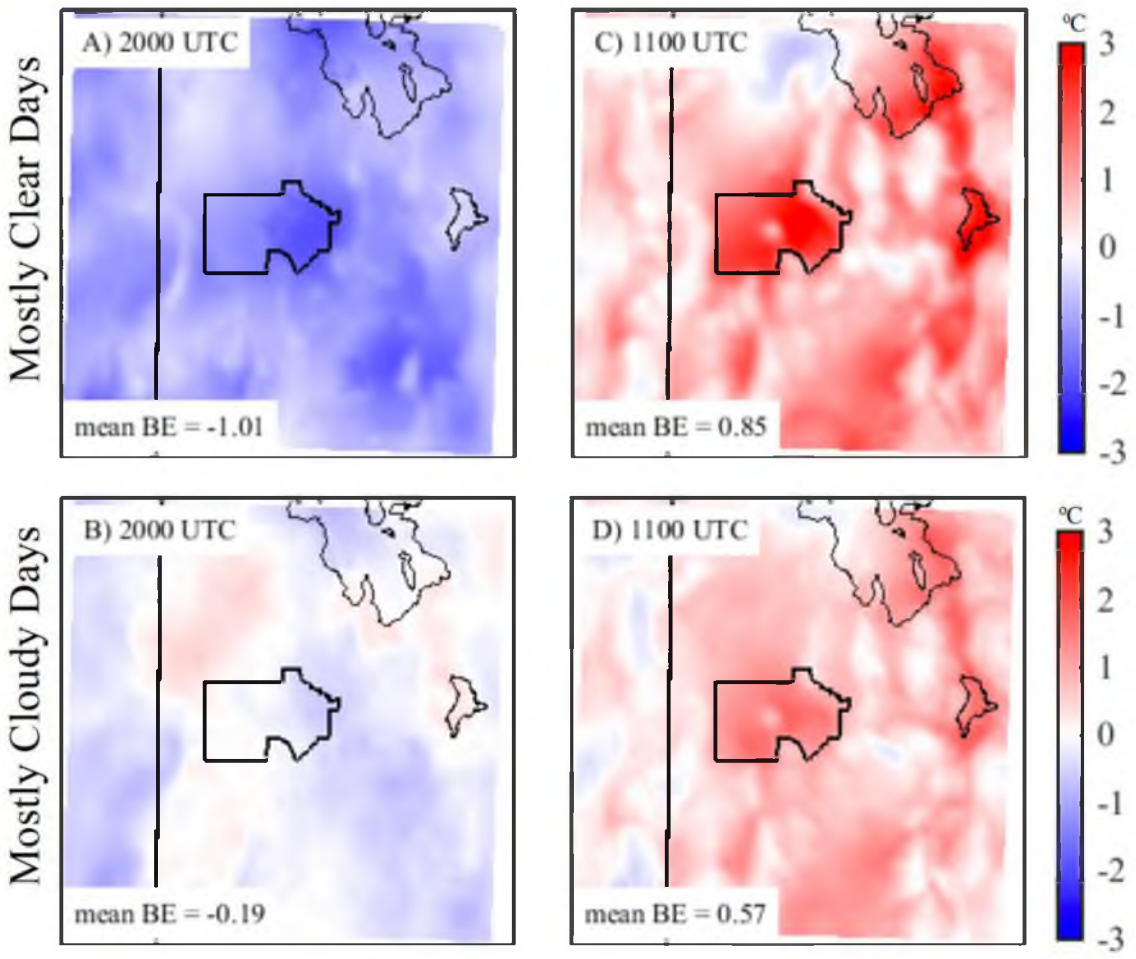

Fig. 3.4. Mean 4DWX-DPG 2-m temperature BEs (°C) relative to 4DWX-DPG analyses for (a) 2000 UTC on mostly clear days, (b) 2000 UTC on mostly cloudy days, (c) 1100 UTC on mostly clear days, and (d) 1100 UTC on mostly cloudy days. Overall mean BE annotated.

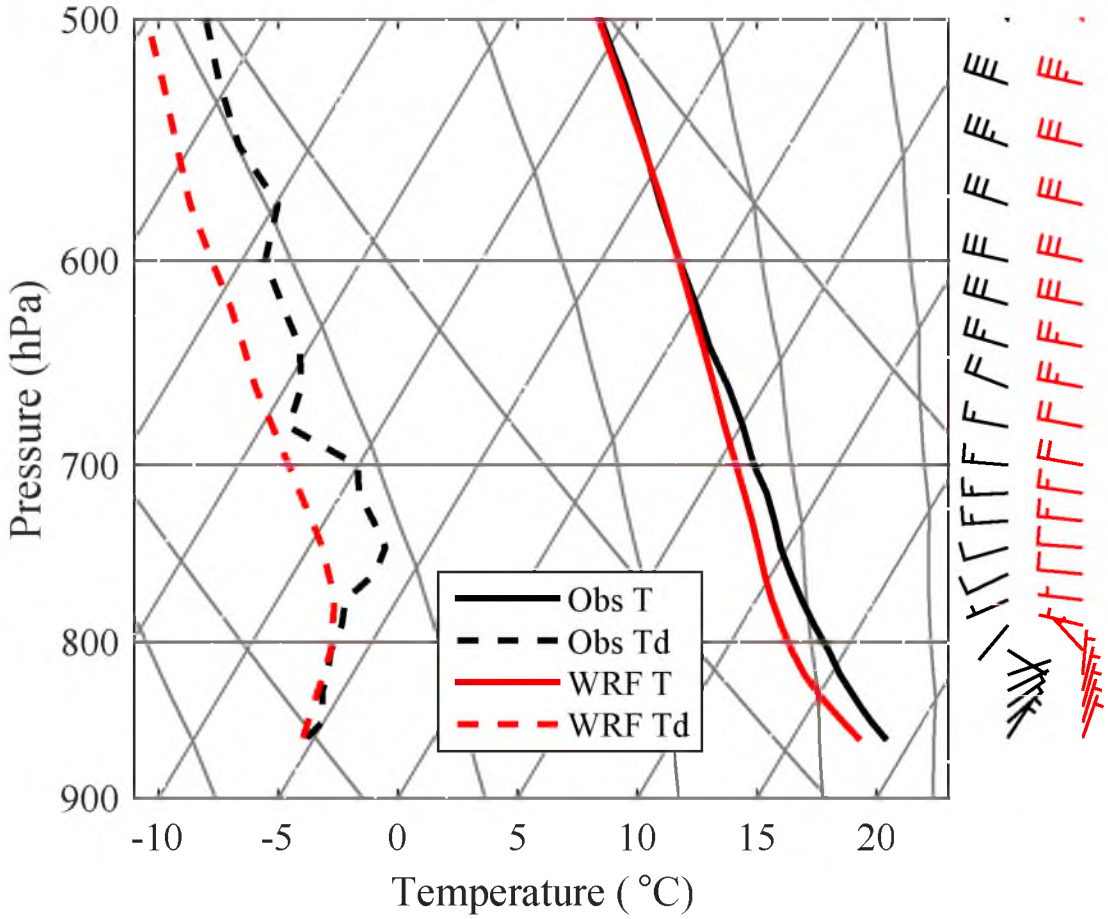

Fig. 3.5. Skew-t log-p diagrams of the mean of 15 soundings taken between 1800 – 0000 UTC during the MATERHORN fall field campaign from EFS-playa (black) compared to the corresponding mean 4DWX-DPG values (red) using 5–7 h forecasts. Wind barbs in m s^{-1} (half barb denotes 2.5 m s^{-1} and full barb denotes 5 m s^{-1}).

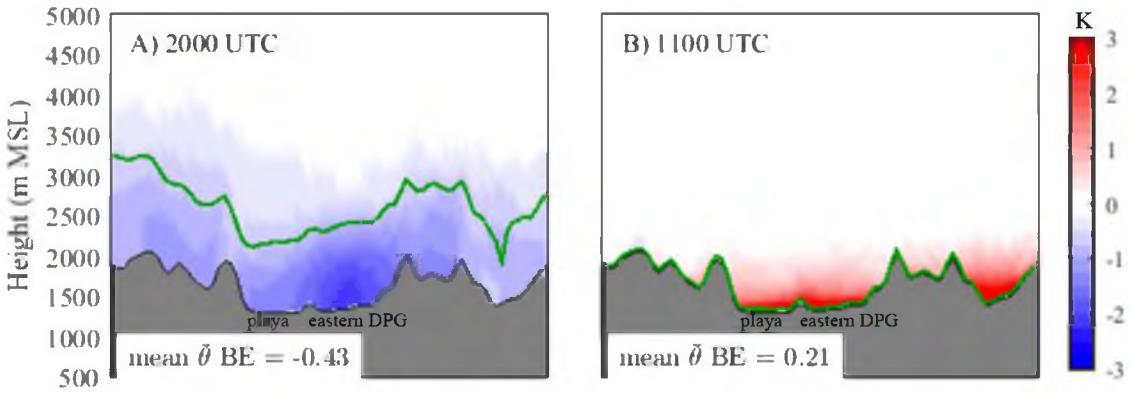

Fig. 3.6. Vertical cross sections of mean mostly clear day 4DWX-DPG θ BEs along dashed line of Fig. 3.1 at (a) 2000 UTC and (b) 1100 UTC. The mean diagnosed PBL height (green line) and overall domain-wide $\overline{\theta}$ BE annotated.

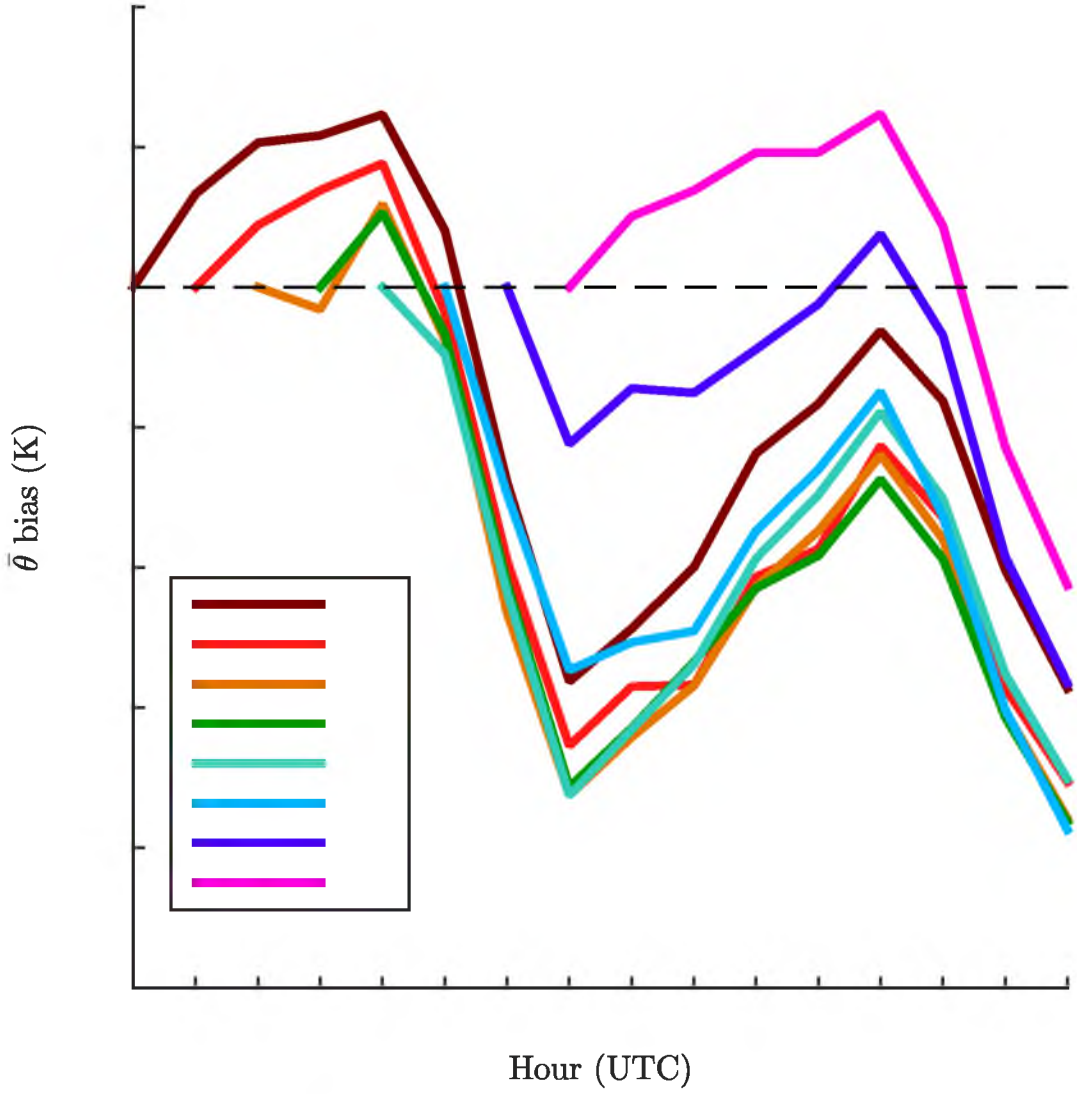

Fig. 3.7. Mostly clear day $\bar{\theta}$ BEs relative to 4DWX-DPG analyses for each nominal initialization time.

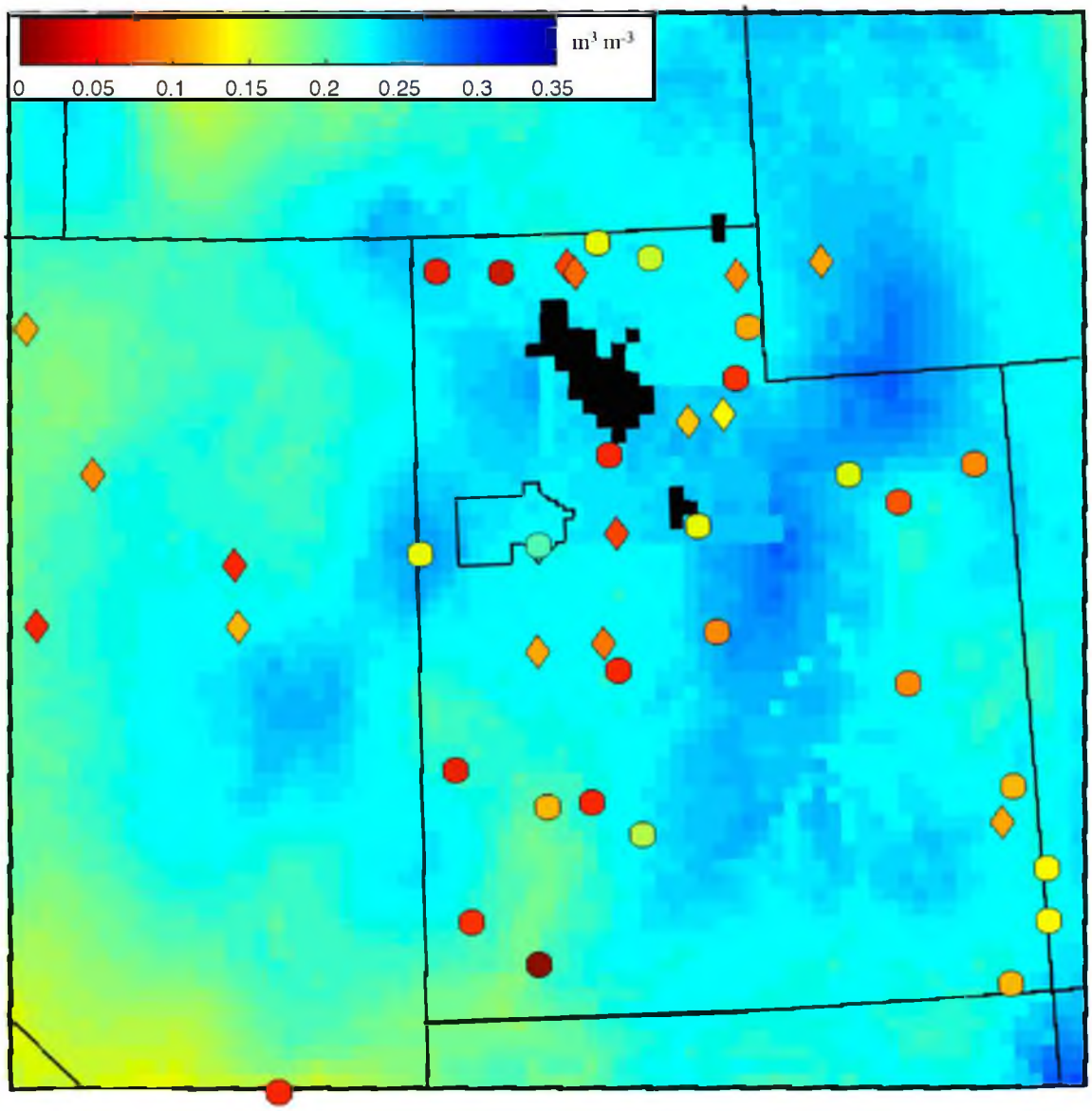

Fig. 3.8. Mean 0000 UTC 5-cm soil moisture (or equivalent) from the 4DWX-DPG 10-km domain and NASMDB stations (SCAN=circles, GPS=diamonds) during September and October 2011, 2012, and 2013.

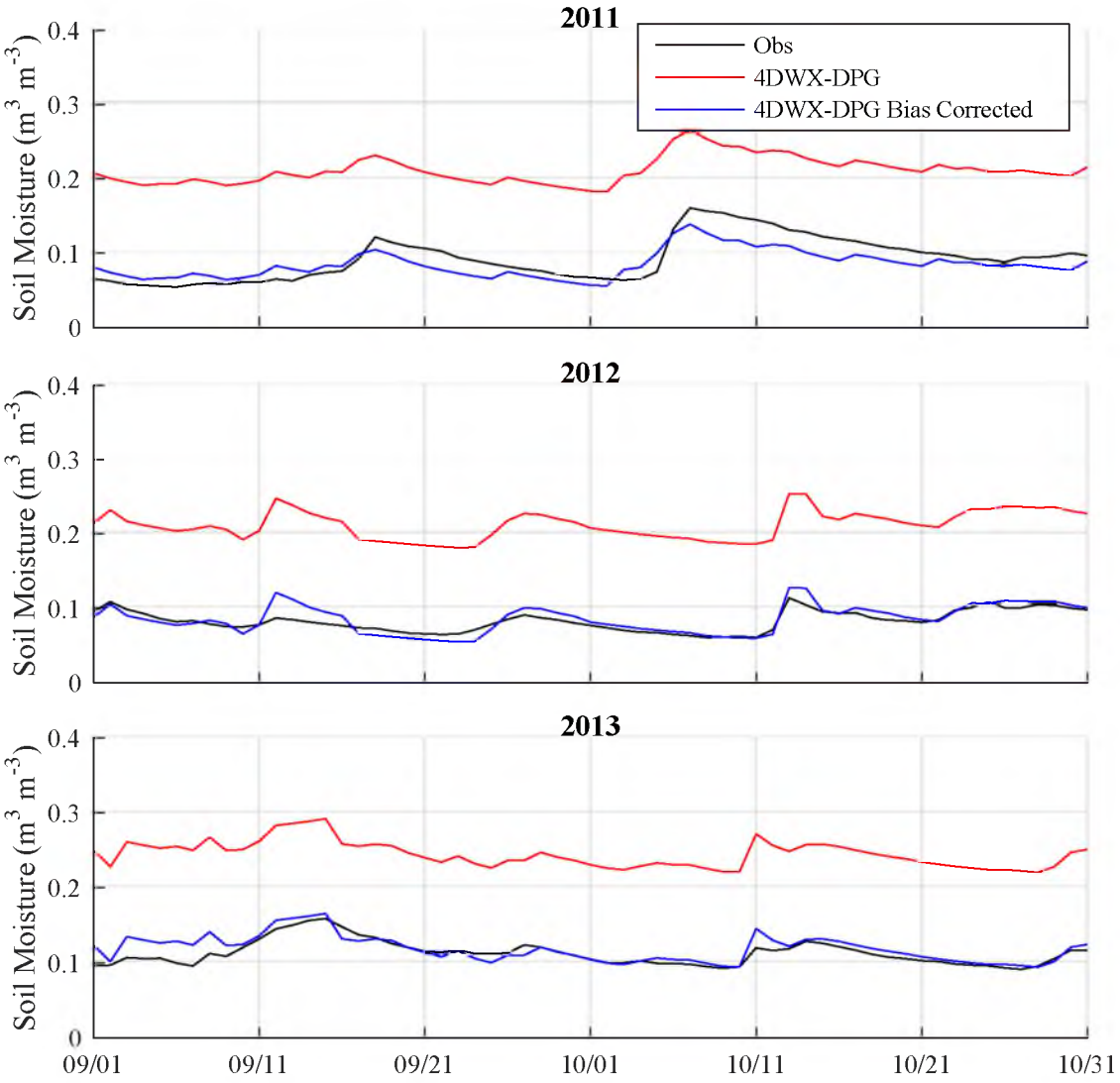

Fig. 3.9. Mean daily observed (black), 4DWX-DPG (red), and 4DWX-DPG bias corrected (blue) 5-cm soil moisture for all NASMDB stations in the 10-km domain.

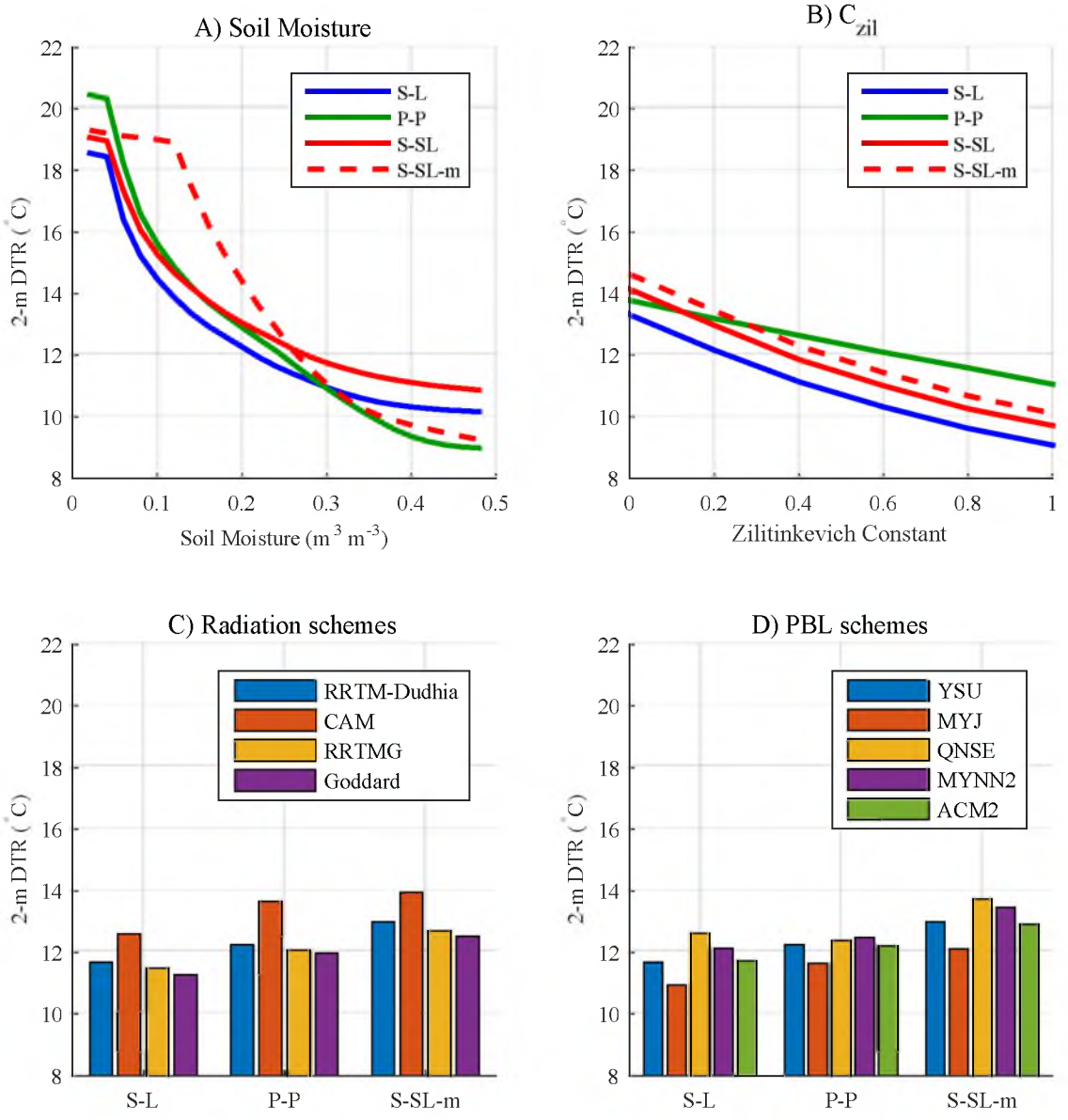

Fig. 3.10. The 2-m temperature DTR calculated from hourly SCM output for the 23-h period between 1800 UTC and 1700 UTC as a function of (a) soil moisture, (b) Zilitinkevich constant, (c) longwave and shortwave radiation schemes, and (d) PBL scheme. Simulations are initialized with shrubland and loam (S-L), shrubland and silt loam (S-SL) and Playa (P-P) land surfaces.

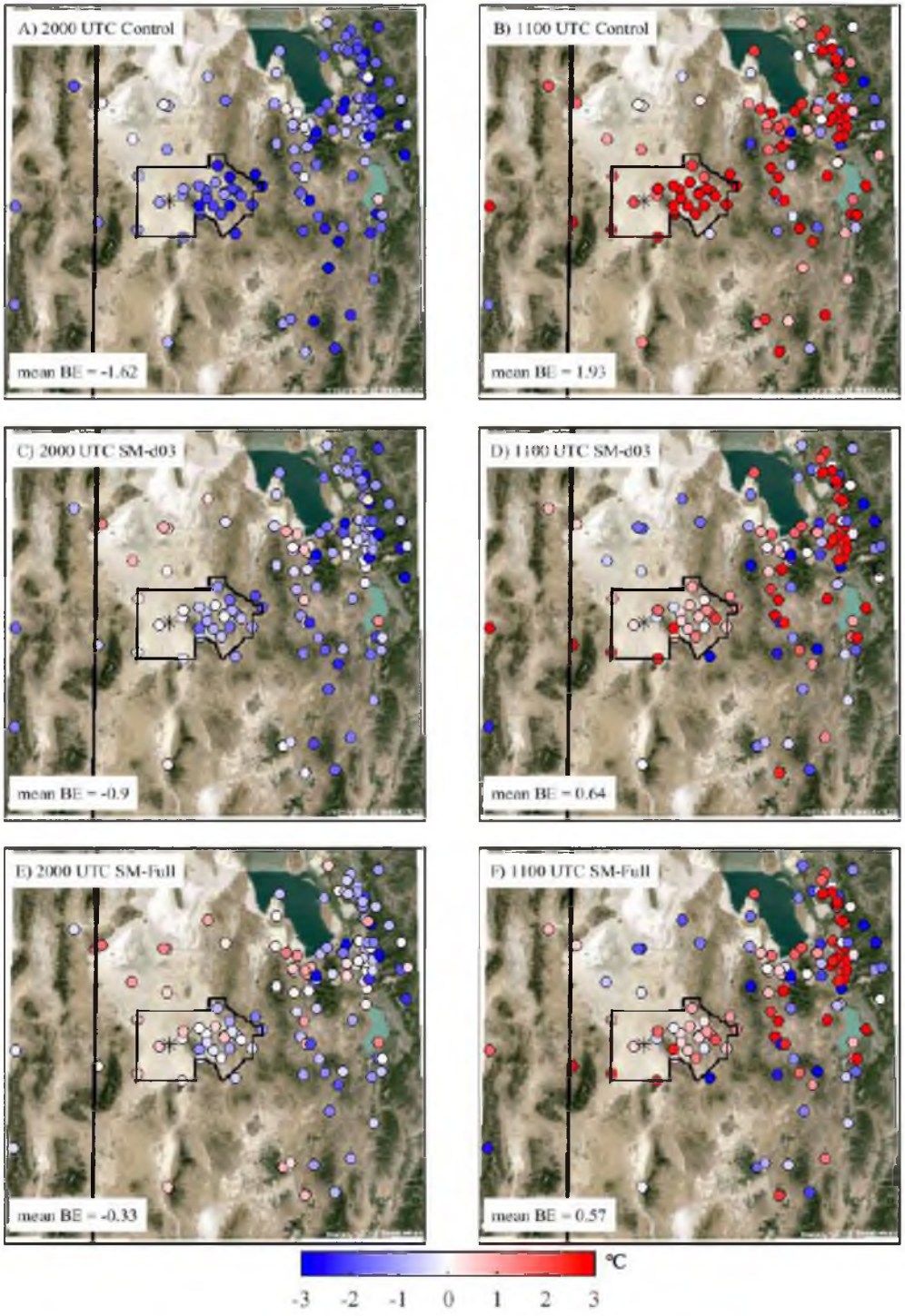

Fig. 3.11. Same as Fig. 3.3 except for the (a, b) Control, (c, d) SM-d03, and (e, f) SM-Full simulations of 4DWX-MATERHORN.

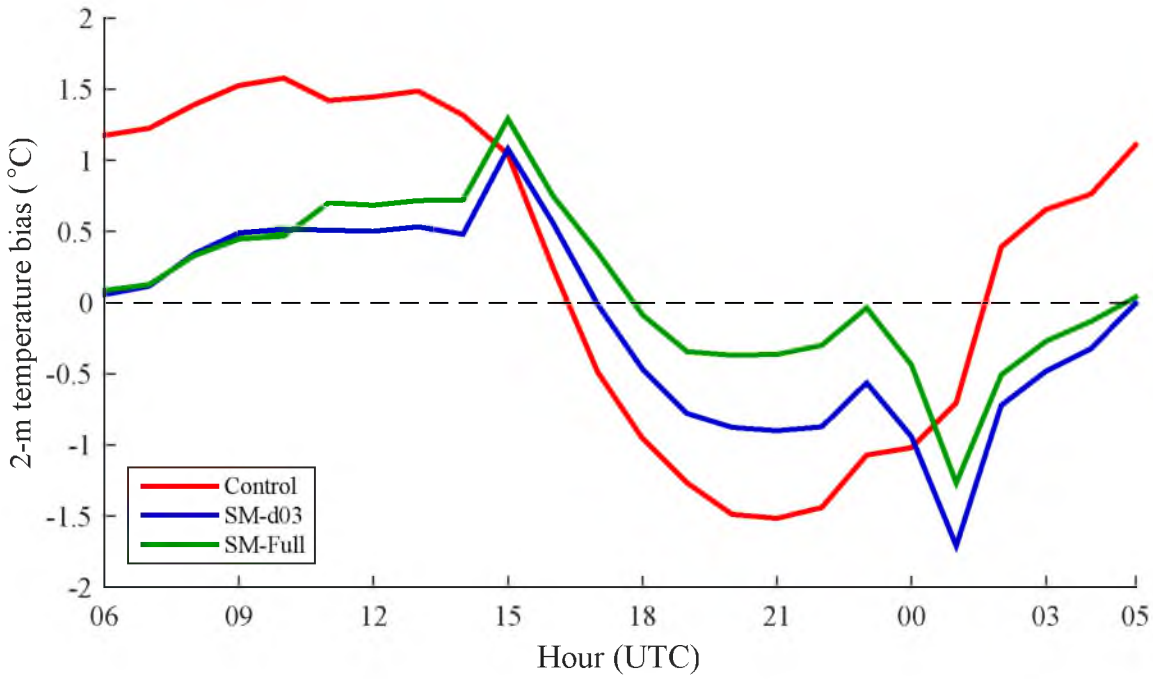

Fig. 3.12. Mean 11–14 h 2-m temperature BEs from Control (red), SM-d03 (blue), and SM-Full (green) at MesoWest stations during the 4DWX-MATERHORN period.

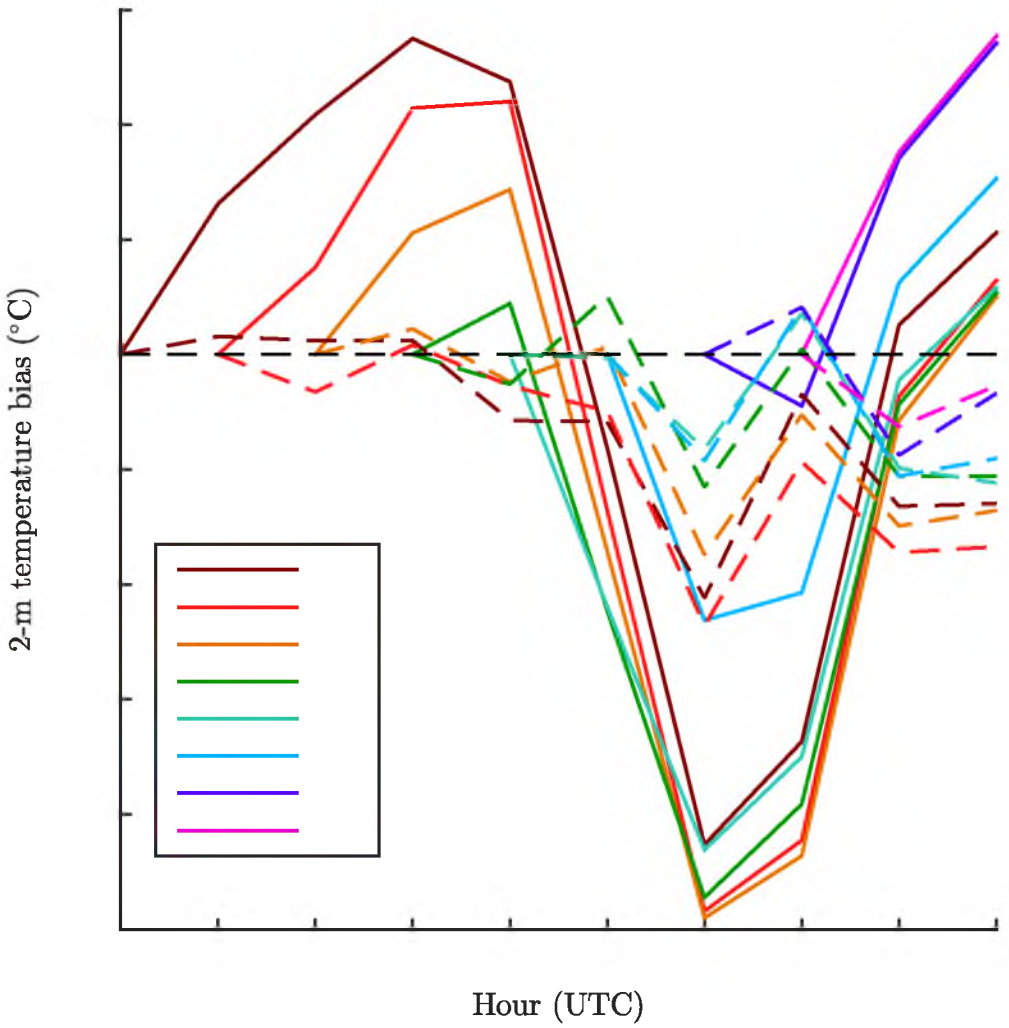

Fig. 3.13. Mean 2-m temperature BEs for each nominal initialization time from Control (solid lines) and SM-Full (dashed lines) during the 4DWX-MATERHORN period.

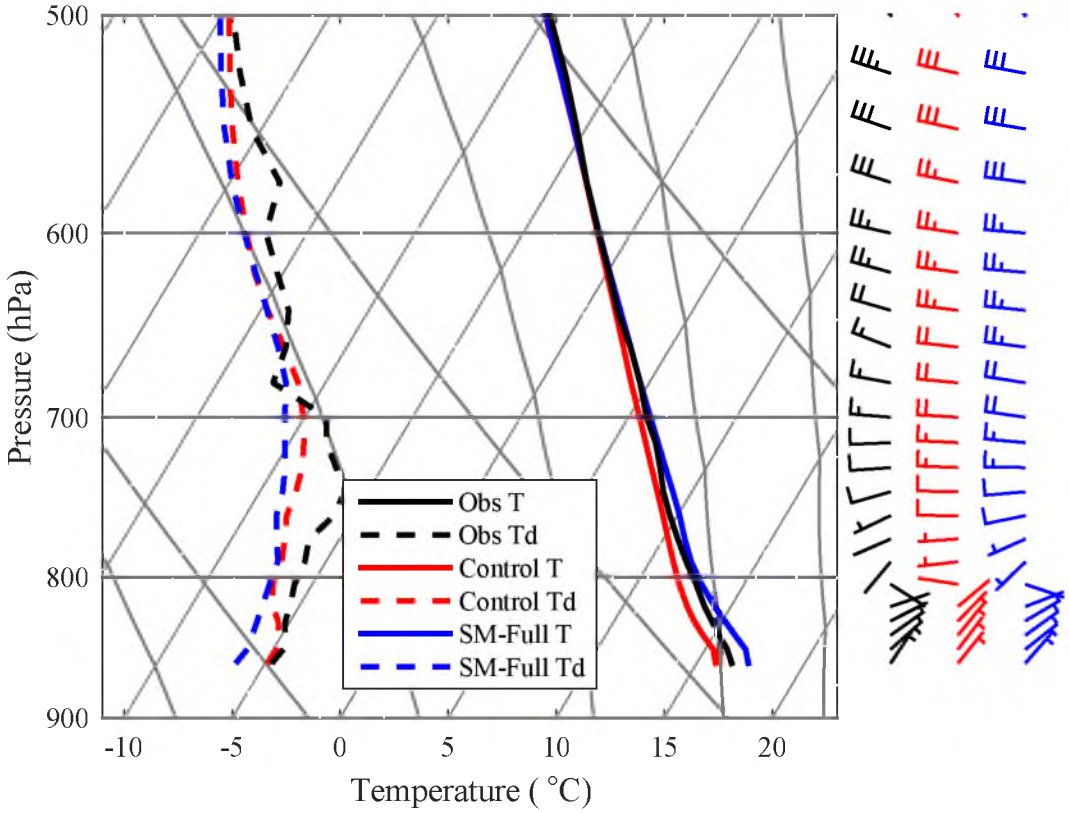

Fig. 3.14. Same as Fig. 3.5 except for Control (red) and SM-Full (blue).

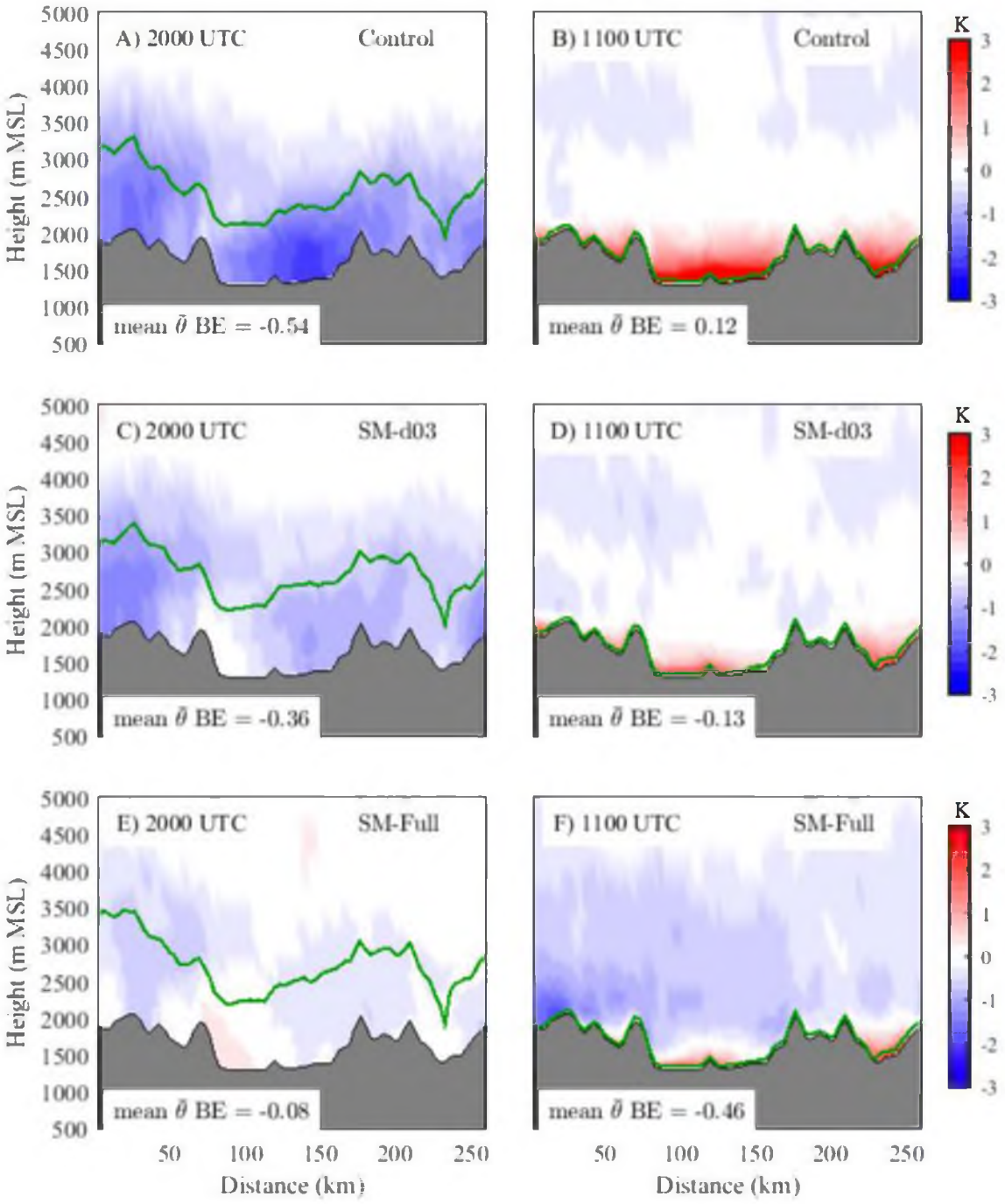

Fig. 3.15. Same as Fig. 3.6 except for (a-b) Control, (c-d) SM-d03, and (e-f) SM-Full.

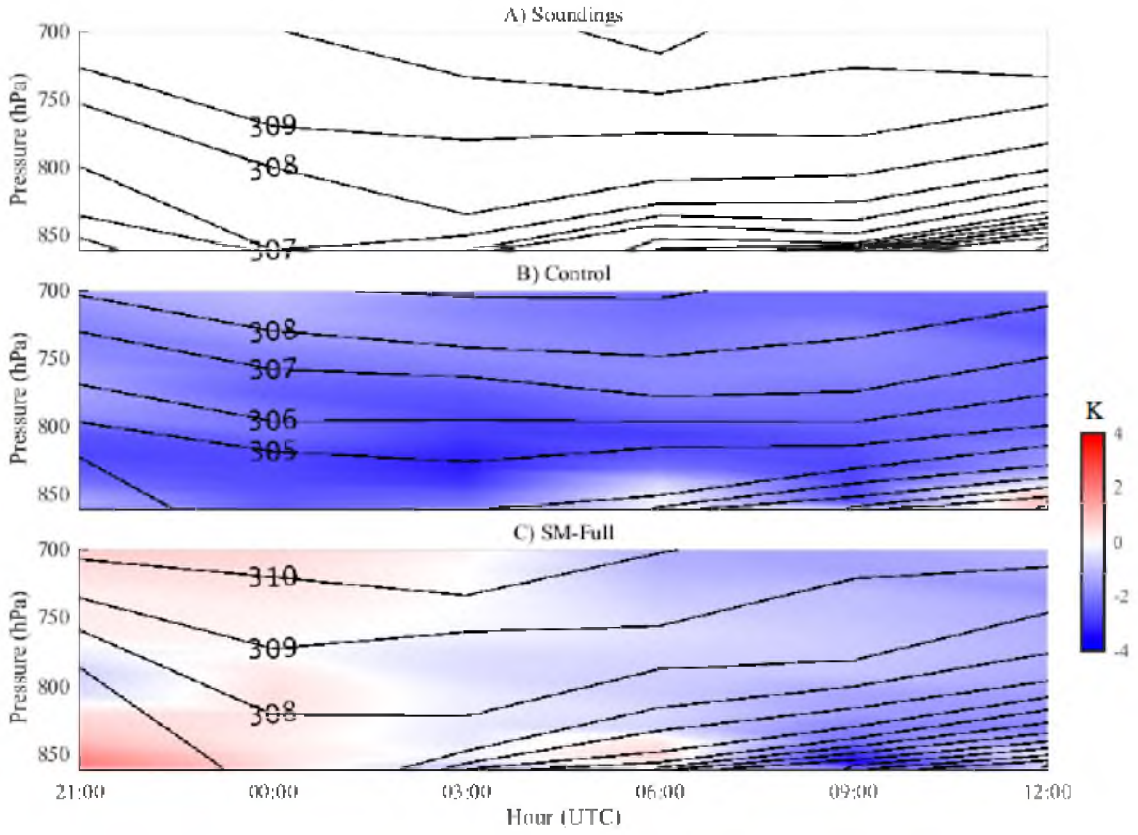

Fig. 3.16. Time-height sections of θ (contours every K) and bias (color fill based on scale at right) from 2100 UTC 9 October 2012 – 1200 UTC 10 October 2012. (a) Observed 3-h soundings from EFS-playa. (b) Control. (c) SM-Full. Control and SM-Full initialized at 1100 UTC 9 October 2012.

3.6 References

Al Bitar, A., D. Leroux, Y. H. Kerr, O. Merlin, P. Richaume, A. Sahoo, and E. F. Wood, 2012: Evaluation of SMOS soil moisture products over continental U.S. using the SCAN/SNOTEL network. *IEEE Trans. Geosci. Remote Sens.*, **50**, 1572–1586.

Albergel, C., P. de Rosnay, G. Balsamo, L. Isaksen, and J. Muñoz-Sabater, 2012a: Soil moisture analyses at ECMWF: Evaluation using global ground-based in situ observations. *J. Hydrometeor*, **13**, 1442–1460.

Albergel, C., P. de Rosnay, C. Gruhier, J. Muñoz-Sabater, S. Hasenauer, L. Isaksen, Y. Kerr, and W. Wagner, 2012b: Evaluation of remotely sensed and modelled soil moisture products using global ground-based in situ observations. *Remote Sens. Environ.*, **118**, 215–226.

Banta, R. M., and P. T. Gannon, 1995: Influence of soil moisture on simulations of katabatic flow. *Theor. Appl. Climatol.*, **52,** 85–94.

Chen, F., and J. Dudhia, 2001: Coupling an advanced land surface–hydrology model with the Penn State–NCAR MM5 modeling system. Part I: Model implementation and sensitivity. *Mon. Wea. Rev.*, **129**, 569–585.

Chen, F., Z. Janjic, and K. Mitchell, 1997: Impact of atmospheric surface-layer parameterization in the new land-surface scheme of the NCEP mesoscale Eta Model. *Bound.-Layer Meteor.*, **85**, 391–421.

Chen, F., and Y. Zhang, 2009: On the coupling strength between the land surface and the atmosphere: From viewpoint of surface exchange coefficients. *Geophys. Res. Lett.*, **36,** L10404.

Cheng, W. Y. Y., and W. J. Steenburgh, 2005: Evaluation of surface sensible weather forecasts by the WRF and the Eta Models over the western United States. *Wea. Forecasting*, **20**, 812–821.

Chou, M.-D., and M. J. Suarez, 1999: A solar radiation parameterization for atmospheric studies. NASA Tech. Rep. Series on Global Modeling and Data Assimilation, NASA/TM-1999-104606, Vol. 15, 40 pp.

Collins, W. D., and Coauthors, 2003: Description of the NCAR Community Atmosphere Model (CAM2). 171 pp. [Available online at http://www.ccsm.ucar.edu/models/atm-cam/docs/description.pdf.].

Crow W. T., D. G. Miralles, and M. H. Cosh, 2010: A quasi-global evaluation system for satellite-based surface soil moisture retrievals. *IEEE Trans. Geosci. Remote Sens.*, **48**, 2516–2527.

Daniels, M. H., F. K. Chow, and G. S. Poulos, 2006: Effects of soil moisture initialization on simulations of atmospheric boundary layer evolution in Owens Valley. *Extended Abstracts, 12th Conf. on Mountain Meteorology*, Santa Fe, NM, *Amer. Meteor. Soc.*, 7.2. [Available online at http://ams.confex.com/ams/pdfpapers/114757.pdf.].

Dee, D. P, M. Balmaseda, G. Balsamo, R. Engelen, A. J. Simmons, and J.-N. Thépaut, 2014: Toward a consistent reanalysis of the climate system. *Bull. Amer. Meteor. Soc.*, **95**, 1235–1248.

Dirmeyer, P. A., X. Gao, and T. Oki, 2002: The Second Global Soil Wetness Project (GSWP2). International GEWEX Project Office Publication, **37**, 75.

Dudhia, J., 1989: Numerical study of convection observed during the winter monsoon experiment using a mesoscale two-dimensional model. *J. Atmos. Sci.,* **46**, 3077–3107.

Fernando, H. J., and Coauthors, 2015: The MATERHORN – Unraveling the intricacies of mountain weather. *Bull. Amer. Meteor. Soc.*, in press.

Fry, J., G. Xian, S. Jin, J. Dewitz, C. Homer, L. Yang, C. Barnes, N. Herold, and J. Wickham, 2011: Completion of the 2006 national land cover database for the conterminous United States, *PE&RS*, 77, 858-864.

García-Díez, M., J. Fernández, L. Fita, and C. Yagüe, 2013, Seasonal dependence of WRF model biases and sensitivity to PBL schemes over Europe, *Q. J. R. Meteorol. Soc.*, **139**, 501–514.

Hanna, S. R., and R. Yang, 2001: Evaluations of mesoscale models' simulations of near-surface winds, temperature gradients, and mixing depths. *J. Appl. Meteor.*, **40**, 1095–1104.

Hart, K. A., W. J. Steenburgh, and D. J. Onton, 2005: Model forecast improvements with decreased horizontal grid spacing over finescale intermountain orography during the 2002 Olympic Winter Games. *Wea. Forecasting*, **20**, 558–576.

Holt, T. R., D. Niyogi, F. Chen, K. Manning, M. A. LeMone, and A. Qureshi, 2006: Effect of land–atmosphere interactions on the IHOP 24–25 May 2002 convection case. *Mon. Wea. Rev.*, **134**, 113–133.

Hong, S. Y., Y. Noh, and J. Dudhia, 2006: A new vertical diffusion package with an explicit treatment of entrainment processes. *Mon. Wea. Rev.*, **134**, 2318–2341.

Horel, J., and Coauthors, 2002: MesoWest: Cooperative mesonets in the western United States. *Bull. Amer. Meteor. Soc.*, **83,** 211–225.

Huang, J., H. M. van den Dool, and K. P. Georgarakos, 1996: Analysis of model-calculated soil moisture over the United States (1931–1993) and applications to long-range temperature forecasts. *J. Climate*, **9**, 1350–1362.

Iacono, M. J., J. S. Delamere, E. J. Mlawer, M. W. Shepard, S. A. Clough, and W. D. Collins, 2008: Radiative forcing by long-lived greenhouse gases: Calculations with the AER radiative transfer models. *J. Geophys. Res.*, **113.**D13103, doi:10.1029/2008JD009944.

Jackson, T. J., and Coauthors, 2010: Validation of advanced microwave scanning radiometer soil moisture products. *IEEE Trans. Geosci. Remote Sens.*, **48**, 4256–4272.

Kain, J. S., 2004: The Kain-Fritsch Convective Parameterization: An update. *Journal of Applied Meteorology*, **43**, 170-181.

Kerr, Y. H., and Coauthors, 2010: The SMOS mission: New tool for monitoring key elements of the global water cycle. *Proc. IEEE*, **98**, 666–687.

Knievel, J. C., G. H. Bryan, and J. P. Hacker, 2007: Explicit diffusion in the WRF model. *Mon. Wea. Rev.*, **135**, 3808–3824.

Larson, K. M., E. E. Small, E. Gutmann, A. Bilich, J. Braun, and V. Zavorotny, 2008: Use of GPS receivers as a soil moisture network for water cycle studies, *Geophys. Res. Lett.*, **35**, L24405.

Lin, Y.-L., R. D. Farley, and H. D. Orville, 1983: Bulk parameterization of the snow field in a cloud model. *J. Climate Appl. Meteor.*, **22**, 1065–1092.

Liu, Y., and Coauthors, 2008a: The operational mesogamma-scale analysis and forecast system of the U.S. army test and evaluation command. Part I: Overview of the modeling system, the forecast products, and how the products are used. *J. Appl. Meteor. Climatol.*, **47**, 1077–1092.

Liu, Y., and Coauthors, 2008b: The operational mesogamma-scale analysis and forecast system of the U.S. army test and evaluation command. Part II: Interrange comparison of the accuracy of model analyses and forecasts. *J. Appl. Meteor. Climatol.*, **47**, 1093–1104.

Marshall, C. H., K. C. Crawford, K. E. Mitchell, and D. J. Stensrud, 2003: The impact of the land surface physics in the operational NCEP eta model on simulating the diurnal cycle: evaluation and testing using Oklahoma mesonet data. *Wea. Forecasting*, **18**, 748–768.

Mass, C. F., D. Ovens, K. Westrick, and B. A. Colle, 2002: Does increasing horizontal resolution produce more skillful forecasts? The results of two years of real-time numerical weather prediction over the Pacific Northwest. *Bull. Amer. Meteor. Soc.*, **83,** 407–430.

Massey, J. D., W. J. Steenburgh, S. W. Hoch, and J. C. Knievel, 2014: Sensitivity of near-surface temperature forecasts to soil properties over a sparsely vegetated dryland region. *J. Appl. Meteor. Climatol.*, **53**, 1976–1995.

McCumber, M. C., and R. A. Pielke, 1981: Simulation of the effects of surface fluxes of heat and moisture in a mesoscale numerical model. *J. Geophys. Res.*, **86**, 9929–9938.

Mellor, G. L., and T. Yamada, 1982: Development of a turbulence closure model for geophysical fluid problems. *Rev. Geophys. Space Phys.*, **20**,851–875.

Mlawer, E. J., S. J. Taubman, P. D. Brown, M. J. Iacono, and S. A. Clough, 1997: Radiative transfer for inhomogeneous atmospheres: RRTM, a validated correlated-*k* model for the longwave. *J. Geophys. Res.*, **102,** 16663–16682.

Nakanishi, M., and H. Niino, 2004: An improved Mellor–Yamada level-3 model with condensation physics: Its design and verification. *Bound.-Layer Meteor.*, **112**, 1–31.

Ochsner, T. E. et al., 2013: State of the art in large-scale soil moisture monitoring. *Soil Sci. Soc. Amer. J.*, **77**, 1888–1919.

Pleim, J. E., 2007: A combined local and nonlocal closure model for the atmospheric boundary layer. Part I: Model description and testing. *J. Appl. Meteor. Climatol.*, **46**, 1383–1395.

Reda, I. and A. Andreas, 2004: Solar position algorithm for solar radiation applications. *Solar Energy*, **76**, 577–589.

Rife, D. L., T. T. Warner, F. Chen, and E. G. Astling, 2002: Mechanisms for diurnal boundary layer circulations in the great basin desert. *Mon. Wea. Rev.*, **130**, 921–938.

Rodriguez-Alvarez, N., X. Bosch-Lluis, A. Camps, M. Vall-Ilossera, E. Valencia, J. F. Marchan-Hernandez, and I Ramos-Perez, 2009: Soil moisture retrieval using GNSS-R techniques: Experimental results over a bare soil field. *IEEE Trans. Geosci. Remote Sens.*, **47**, 3616–3624.

Rostkier-Edelstein, D. and J. P. Hacker, 2010: The roles of surface-observation ensemble assimilation and model complexity for nowcasting of PBL profiles: A factor separation analysis. *Wea. Forecasting*, **25**, 1670–1690.

Schaefer, G. L., M. H. Cosh, and T. J. Jackson, 2007: The USDA natural resources conservation service soil climate analysis network (SCAN). *J. Atmos. Oceanic Technol.*, **24**, 2073–2077.

Seyfried, M. S., L. E. Grant, E. Du, and K. Humes, 2005: Dielectric loss and calibration of the Hydra Probe soil water sensor, *Vadose Zone J.*, **4**, 1070–1079.

Steenburgh, W. J., S. F. Halvorson, and D. J. Onton, 2000: Climatology of lake-effect snowstorms of the Great Salt Lake. *Mon. Wea. Rev.,* **128**, 709–727.

Sukoriansky, S., B. Galperin, and V. Perov, 2005: Application of a new spectral theory of stably stratified turbulence to atmospheric boundary layers over sea ice. *Bound.-Layer Meteor.*, **117**, 231–257.

Thompson, G., R. M. Rasmussen, and K. Manning, 2004: Explicit forecasts of winter precipitation using an improved bulk microphysics scheme. Part I: Description and sensitivity analysis. *Mon. Wea. Rev.*, **132,** 519–542.

WRCC, 2015: Western historical climate summaries, Dugway, Utah. Western Region Climate Center, http://www.wrcc.dri.edu/cgi-bin/cliMAIN.pl?ut2257.

Wyszogrodzki, A. A., Liu, Y., Jacobs, N., Childs, P., Zhang, Y., Roux, G., & Warner, T. T., 2013: Analysis of the surface temperature and wind forecast errors of the NCAR-AirDat operational CONUS 4-km WRF forecasting system. *Meteorology and Atmospheric Physics*, ***122***, 125-143.

Zeng, X., Z. Wang, and A. Wang, 2012: Surface skin temperature and the interplay between sensible and ground heat fluxes over arid regions. *J. Hydrometeor.*, **13**, 1359–1370.

Zhang, H., Z. Pu, X. Zhang, 2013: Examination of errors in near-surface temperature and wind from WRF numerical simulations in regions of complex terrain. *Wea. Forecasting*, **28**, 893–914.

Zheng, W., H. Wei, Z. Wang, X. Zeng, J. Meng, M. Ek, K. Mitchell, and J. Derber, 2012: Improvement of daytime land surface skin temperature over arid regions in the NCEP GFS model and its impact on satellite data assimilation. *J. Geophys. Res.*, **117**, D06117.

Zhong, S., and J. Fast, 2003: An evaluation of the MM5, RAMS, and Meso-Eta models at subkilometer resolution using VTMX field campaign data in the Salt Lake Valley. *Mon. Wea. Rev.*, **131,** 1301–1322.

Zhou, X., and B. Geerts, 2013: The Influence of soil moisture on the planetary boundary layer and on cumulus convection over an isolated mountain. Part I: observations. *Mon. Wea. Rev.*, **141**, 1061–1078.

CHAPTER 4

SIMULATED AND OBSERVED SURFACE ENERGY BALANCE CONTRASTS AND RESULTING PLAYA BREEZES DURING THE MATERHORN FIELD CAMPAIGNS

4.1 Abstract

Weather Research and Forecasting (WRF) model simulations of the fall 2012 and spring 2013 Mountain Terrain Atmospheric Modeling and Observations Program (MATERHORN) field campaigns are validated against surface energy balance observations collected over playa and desert shrub land surfaces in the Great Salt Lake Desert of northwest Utah. When in situ soil moisture observations are incorporated into the land surfaces analyses and a different soil thermal conductivity parameterization is used, the surface energy balance forecast generally improves over the desert shrub, but degrades over the playa. The desert shrub improvement is greatest during the fall and the playa errors are largest during the spring when the observed soil moisture is much wetter than the analyses. Simulations that also incorporate satellite-derived albedo into the land surface analyses, and a reduced saturation vapor pressure over the playa, only improve the playa surface energy balance marginally. The Noah land surface model does not capture unique playa land surface processes. Nevertheless, these changes produce an improved sensible heat flux and 2-m temperature difference between the playa and desert

shrub, which increases the strength of the daytime off-playa breeze, but the changes do not substantially improve 10-m wind speed and direction mean absolute errors. This work highlights some Noah land surface model deficiencies over two common arid land surfaces and demonstrates the importance of land surface analyses.

4.2 Introduction

The variability of regional land-surface characteristics in mesoscale numerical weather prediction (NWP) models has a potentially strong influence on near-surface forecasts. Some sources of land-surface variability, such as coastlines and topographic features, are easily represented in NWP, but other more subtle land-surface characteristics (e.g., albedo, emissivity, roughness length, soil porosity, soil texture, soil moisture, etc.) are more difficult to define and parameterize, and can exhibit significant variability on diurnal to interannual time scales (e.g., Malek 2003). Land-surface characteristics affect near-surface forecasts of temperature, moisture, and momentum through the surface energy balance (SEB), with radiation absorbed at the surface (i.e., net radiation, R_n) partitioned to surface sensible (H), latent (LE), and ground (G) heat fluxes

$$R_n = H + LE + G.$$

Near-surface forecasts are not only affected by the local SEB partitioning, but also the regional partitioning. For example, gradients in SEB components can drive mesoscale circulations (e.g., Segal and Arritt 1992) and influence cloud development, precipitation, and atmospheric stability (Stull 1988).

Soil moisture is the most important land-surface property for controlling the partitioning of the SEB components (Sun and Bosilovich 1996) because it affects the

ratio of H to LE (i.e., the Bowen ratio; Bowen 1926) through evapotranspiration, G since water has a higher thermal conductivity than the air it replaces (Cosenza et al. 2003), and R_n by altering the surface albedo (e.g., Malek 2003). Typically, higher soil moisture causes a greater percentage of R_n to be partitioned into LE and G, and a lesser percentage to be partitioned into H. As a result, the diurnal temperature cycle is smaller over a moist than dry soil under otherwise identical conditions.

Validating SEB forecasts using SEB observations offers significant potential to identify land-surface deficiencies in NWP models (e.g., Hu et al. 2010; Steeneveld et al. 2011; Svensson et al. 2011; Aas et al. 2015). For example, Aas et al. (2015) compared the simulated and observed SEB over the Svarlbard Archipelago in the Arctic Sea north of Europe, identifying overpredictions of R_n and the Bowen ratio, which they attributed to too few or too optically thin clouds and a low soil moisture bias, respectively. A major source of uncertainty with SEB validation studies, however, is that SEB observations do not close (e.g., $R_n > H + LE + G$) due to the presence of a residual storage term (Foken 2008).

This study focuses on the SEB and associated thermally driven flows in the Dugway Proving Ground (DPG) region of the Great Salt Lake Desert of northern Utah, an area of complex terrain characterized by two distinct land surfaces: playa and desert shrub (Fig. 4.1), which are found in dryland regions around the world (Warner 2004). The playa is a flat, salt-encrusted, vegetation-free, clay surface with a high water table. The adjacent desert shrub is sparsely vegetated with underlying silt loam and loam soils. The playa has a higher albedo, higher soil thermal conductivity, less vegetation, and higher soil moisture than the desert shrub, leading to SEB and temperature gradients

between the two surfaces (Rife et al. 2002). Generally, the playa is cooler during the day and warmer at night. Malek (2003) investigated the observed SEB over the playa and discovered unique characteristics compared to nonplaya land surfaces such as an early morning maxima in LE, rehydration of the topsoil at night, a shallow water table 0–60 cm below the surface, and nearly an order of magnitude difference between the mean daily evaporation and the potential evaporation.

The diurnally modulating temperature gradient between the playa and desert shrub can lead to an off-playa breeze during the day and on-playa breeze at night (Physick and Tapper 1990). Similar mesoscale circulations are observed elsewhere over soil moisture and vegetation gradients (e.g., Ookouchi et al. 1984; Avissar and Pielke 1989; Fast and McCorcle 1991; Segal and Arritt 1992). Observational and numerical modeling studies find that during quiescent large-scale conditions, the daytime off-playa breeze (sometimes called a salt breeze) extends to as high as ~1000 m AGL and has 10-m wind speeds of 3–4 m s^{-1} (e.g., Davis et al. 1999; Rife et al. 2002; Knievel et al. 2007). However, to produce a realistic off-playa breeze, Davis et al. (1999) specified a soil-dependent thermal inertia instead of using a land surface model (LSM) and Rife et al. (2002) increased soil temperature initial conditions by as much as 5°C over the playa.

This chapter validates SEB forecasts from the Weather Research and Forecasting (WRF) model over the playa and desert shrub against SEB observations collected during the Mountain Terrain Atmospheric Modeling and Observations Program (MATERHORN) field campaigns. Massey et al. (2014) and Massey et al. (2015) incorporated observed soil-moisture observations and a modified soil thermal conductivity parameterization in the Noah LSM over this region during the fall and noted

improved temperature forecasts. This chapter will validate these changes against SEB observations over two contrasting land surfaces. SEB differences will highlight the SEB sensitivity to land-surface analyses, and remaining disparities will highlight some WRF and Noah LSM deficiencies over these two common dryland land surfaces. We will also examine the influence of SEB changes on 10-m wind forecasts.

4.3 Data and Methods

4.3.1 Surface Energy Balance Stations

This study uses data collected during the MATERHORN field campaigns at DPG from 25 September 2012 – 25 October 2012 (MATERHORN-Fall) and 1 May 2013 – 31 May 2013 [MATERHORN-Spring (Fernando et al. 2015)]. MATERHORN-Fall was characterized by quiescent and fair weather conditions with only 8.7 mm of precipitation at the DPG National Weather Service Cooperative Observer site. MATERHORN-Spring was characterized by stronger synoptic forcing and 19.4 mm of precipitation at the DPG National Weather Service Cooperative Observer site. Our analysis concentrates on 20 days during MATERHORN-Fall (1 October 2012 – 20 October 2012) and 30 days during MATERHORN-Spring (2 May 2013 – 31 May 2013) with SEB data available from at least one extended flux site (EFS) located over the playa (EFS-Playa) or desert shrub (EFS-DS) (see Fig. 4.1 for locations and Fig. 4.2 for photos). During MATERHORN-Fall, each site only has data available for 14 nonconsecutive days, and only 8 nonconsecutive days have complete data for both sites (Table 4.1). Therefore, EFS-DS and EFS-Playa validate different MATERHORN-Fall days. During MATERHORN-Spring, data are available continuously at both sites (not shown).

We also delineate mostly clear and mostly cloudy days during the MATERHORN periods using atmospheric transmittance defined as:

$$Transmittance = \frac{\sum_{t=0000\ LST}^{2330\ LST} SW_{sfc}(t)}{\sum_{t=0000\ LST}^{2330\ LST} SW_{toa}(t)}$$

where $SW_{sfc}(t)$ is the observed downwelling shortwave radiation (SW) at the surface at time t, and $SW_{toa}(t)$ is the theoretical downwelling top-of-atmosphere SW calculated from:

$$SW_{toa}(t) = S_0 \left(\frac{a}{r}\right)^2 \sin(\varphi)$$

where S_0 is the solar constant (approximated to be 1370 W m^{-2}), a is the annual mean distance between the sun and the earth, r is the daily mean distance, and φ is the solar elevation angle calculated following Reda and Andreas (2004). Transmittance is calculated for each day at EFS-DS and EFS-Playa and mostly clear days are defined arbitrarily as those with a mean transmittance $\geq$ 0.65 and all other days with lower transmittance due to more clouds and aerosols are classified as mostly cloudy. Only 3 days are defined as mostly cloudy during MATERHORN-Fall (Table 4.1) and 11 days during MATERHORN-Spring.

4.3.1.1 SEB Measurements

H is calculated at 2 m AGL from sonic anemometer and sonic temperature measurements, and LE is calculated at 10 m from infrared gas analyzer measurements. The Utah Turbulence in Environmental Studies processing and analysis code (UTESpac; Jensen et al. 2015) quality controls the data and calculates 5 min averages. We treat the

2-m H and 10-m LE fluxes as a proxy for surface fluxes and define upward fluxes as positive.

G is calculated as the sum of the average 5-cm heat flux from two heat flux plates (Hukseflux HFP-SC) separated by approximately 1 m, and the change in the heat-storage in the 0–5 cm soil layer. The heat storage is calculated using the direct measurements of the 5-cm thermal heat capacity from thermal property sensors (model TP01; Hukseflux Thermal Sensors B.V) and 1, 2.5, and 5 cm soil temperature from thermocouples (Omega Engineering, Inc.). We define downwelling G as positive.

The individual SW and longwave radiation (LW) components of the surface radiation balance are measured with Kipp & Zonen B.V. up- and down-facing CMP21 pyranometers and CGR4 pyrgeometers, respectively, mounted at 2 m AGL on a sawhorse-type structure (Fig. 4.2). R_n is calculated by subtracting the outgoing from the incoming SW and LW components.

4.3.1.2 Residual Correction

We calculate a residual storage term (*Res*) following:

$$Res = R_n - H - LE - G.$$

Foken (2008) argues that the data quality and measurement accuracy of the instruments used in this study have improved sufficiently enough recently to rule out measurement quality as a major contributor to the magnitude of *Res*. He hypothesizes that the eddy covariance turbulent measurements cannot capture the larger eddies and, thus, underestimate H and LE. One approach to close the SEB, which we utilize, is to assume the Bowen ratio of the measured small eddies is the same as the Bowen ratio of the larger

eddies that are not measured. Therefore, we distribute *Res* according to the Bowen ratio to *H* and *LE*. This approach is used in previous studies (e.g., Twine et al. 2000) and is recommended by Foken (2008) as the best available method. However, more work is needed since the Bowen ratio similarity between large and small eddies varies by time of day and eddy size (Ruppert et al. 2006).

Given the high Bowen ratios at both sites during MATERHORN-Fall and MATERHORN-Spring, the majority of *Res* is transferred to *H* (Fig. 4.3). During MATERHORN-Fall at EFS-DS, *Res* is ~18% of R_n at night (i.e., when $R_n < 0$) and ~25% of R_n during the day (i.e., when $R_n > 0$), and nearly all of *Res* is transferred to *H* (Fig. 4.3a). *Res* is lower at EFS-Playa compared to EFS-DS during MATERHORN-Fall, but nearly all of *Res* is also transferred to *H* (Fig. 4.3b). During MATERHORN-Spring at EFS-DS, *Res* is near 0 at night, but as high as 31% during the afternoon and ~20% of *Res* gets transferred to *LE,* with the remainder going to *H* (Fig. 4.3c). At EFS-Playa, *Res* is also near 0 at night and ~15% of R_n gets transferred to *LE* during the day (Fig. 4.3d).

4.3.2 Surface Temperature and Wind Observations

Near-surface 2-m temperature and 10-m wind forecasts, which are diagnosed from the WRF-model half-η and skin-level fields using similarity theory, are validated against 2-m temperature and 10-m wind observations from 27 Surface Automated Meteorological Stations (SAMS) with a site elevation within 100 m of the corresponding WRF elevation. SAMS are located primarily in lowland areas in and around DPG (see Fig. 4.1 for locations), and observations represent 5-min or 15-min averages depending on location. Although no formal quality control was performed, missing and obviously

erroneous observations were removed. We also exclude observations < 1 m s^{-1} because propeller anemometers are not accurate at low wind speeds. Bias errors (BE) are calculated for temperature and wind speed using

$$BE = \frac{1}{N}\sum_{i=1}^{N}(f_i - o_i),$$

where f_i and o_i are the forecast and observed values for the ith stations, respectively, and N is the number of observation–forecast pairs. We also calculate a mean absolute error (MAE) for wind speed and direction using

$$MAE = \frac{1}{N}\sum_{i=1}^{N}|f_i - o_i|.$$

Wind-speed BEs and MAEs are calculated using scalar wind speed differences, whereas wind direction MAEs are calculated from mean u and v wind components.

4.3.3 WRF Modeling

We run 30-h WRF simulations during the MATERHORN periods that have SEB data available (i.e., 1 October 2012 – 20 October 2012 and 2 May 2013 – 31 May 2013). Simulations are initialized daily at 1800 UTC/1100 LST, with the 6–29.5 h forecasts valid 0000–2330 UTC (1700–1630 LST) used for validation to allow for a 6 h spin up period.

The domains, physics, land use categories, and soil categories follow that of the operational WRF-based Four-Dimensional Weather System (4DWX) run at DPG (4DWX-DPG, Liu et al. 2008). We use WRF v3.5.1 with 30-, 10-, and 3.3-km one-way nested domains centered over DPG, and 36 half-η levels with the lowest half-η level at ~15 m AGL. The vertical spacing varies from ~30 m near the surface to ~1250 m in the

upper troposphere and lower stratosphere. The physics packages include the Rapid Radiative Transfer Model (RRTM) longwave radiation parameterization (Mlawer et al. 1997), Dudhia shortwave radiation parameterization (Dudhia 1989), Noah LSM (Chen and Dudhia 2001), Yonsei University PBL parameterization (YSU; Hong et al. 2006), explicit sixth-order numerical diffusion (Knievel et al. 2007), and the new Kain-Fritsch cumulus parameterization (Kain 2004).

All simulations obtain their initial atmospheric and land surface analyses, and lateral boundary conditions, from the 0.5° Global Forecasting System (GFS) analyses, as is done in the operational 4DWX-DPG system. They also use an updated land-cover and terrain elevation dataset based on the 33-category National Land Cover Database [NLCD (Fry et al. 2011)]. A special playa category is manually added to the NLCD and WRF soil texture class field to better account for the large playa in northwest Utah. We also change the Great Salt Lake (GSL) surface temperature to a climatological value (Crosman and Horel 2009), and reduce the saturation vapor pressure over the GSL following Steenburgh et al. (2000).

Control simulations are based on the configuration above, but following Massey et al. (2014) the SM simulations adjust the 5- and 25-cm soil moisture analyses using soil moisture observations, and replace the default soil thermal conductivity parameterization with that proposed by McCumber and Pielke (1981) for silt loam and sandy loam soils. Specifically, in the SM 3.3-km domain, we apply the mean observed soil moisture from in situ stations locations over loam, sandy loam, silt loam, and silty clay loam to the geographical area defined by those soil texture classes. Observations come from the Texas A&M University North American Soil Moisture Database (NASMDB) product

(http://soilmoisture.tamu.edu) that harmonizes and quality controls several in situ soil-moisture observing platforms. We consider only stations from the U.S. Department of Agriculture's Soil Climate Analysis Network (SCAN; Schaefer et al. 2007) which measures 5- and 25-cm soil moisture and stations from the Global Positioning System (GPS) network that measure 5-cm soil moisture (Larson et al. 2008). Playa is the only soil texture class not represented by a NASMDB station, but manual observations are available near EFS-Playa during 9 MATERHORN-Spring intensive operating periods (IOPs), and 3 MATERHORN-Fall IOPs at 5- and 25-cm[5]. Therefore, we apply the playa soil moisture observed during the IOP nearest the initialization time to the playa soil texture class. Massey et al. (2014) applied soil moisture observations to soil texture classes in their innermost domain and noted nighttime temperature improvement.

For the SM 10-km domain, and 10-km domain footprint on the 30-km domain, we follow Massey et al. (2015) and bias-correct the 5- and 25-cm soil moisture analyses at initialization using the mean difference between observations from 27 SCAN and 15 GPS stations, and corresponding GFS values. This approach is used on the outer domains in lieu of the SM 3.3-km domain approach because the latter does not account for the large-scale soil moisture gradients present across the Intermountain West. Massey et al. (2015) bias-corrected soil-moisture analyses in all of their domains and noted nighttime and daytime temperature improvement.

The resulting 3.3-km domain 5-cm soil moisture differences are quite pronounced between Control and SM during MATERHORN-Fall (Fig. 4.4a). In Control, the EFS-DS and EFS-Playa soil moistures based on GFS soil moisture analyses are similar (on

[5] Soil moisture at 5- and 25-cm was calculated from soil samples taken between 4–6 cm and 24–26 cm, respectively.

average within .01 m^3 m^{-3}). However, SM soil moisture based on observations is on average 0.05 m^3 m^{-3} drier at EFS-DS and 0.07 m^3 m^{-3} wetter at EFS-Playa than Control. During MATERHORN-Spring, Control also features similar soil moistures at EFS-DS and EFS-Playa (Fig. 4.4b). The use of observed soil moisture in SM results in only a 0.01 m^3 m^{-3} decrease at EFS-DS, but a mean 0.13 m^3 m^{-3} increase at EFS-Playa.

In SM-Albedo we keep the SM soil moisture changes, but also change the albedo and the saturation vapor pressure over the playa. The WRF currently prescribes albedo based on landuse classification, snow depth, and green vegetation fraction, but SM-Albedo uses a derived multiday albedo product from the Moderate Resolution Imaging Spectroradiometer (MODIS) based on atmospherically corrected surface reflectance observations [MCD43B3 (Schaaf et al. 2002)]. MCD43B3 has three broadband albedos produced every 8 days using data from the previous 16 days at 500 m resolution, but we only use the shortwave albedo since it most closely matches pyranometer field measurements (Liu et al. 2009). We linearly interpolate the albedo measurements closest to the initialization time to the 3.3-km domain and fill missing data, which can occur due to persistent cloud cover, with the nearest available albedo. Meng et al. (2014) included a MODIS-derived albedo in their WRF simulations and found improved temperature forecasts.

The resulting mean albedo differences between Control and SM-Albedo for MATERHORN-Fall and MATERHORN-Spring are shown in Figure 4.5. During MATERHORN-Fall, the mean Control albedo features little contrast between the playa and the surrounding lower-elevation desert shrub region (Fig. 4.5a). In SM-Albedo, the mean albedo is higher over the playa and lower over the surrounding low-elevation desert

shrub region, with greater spatial variability (cf. Figs. 4.5a and 4.5b). These differences are also true for MATERHORN-Spring, although the playa albedo is even higher (Figs. 4.5c,d).

In SM-Albedo we also reduce the saturation vapor pressure over the playa because the very high salinity of the playa has a strong impact on the evaporation rate and *LE*, but this effect is not parameterized in the Noah LSM. Salinity reduces the osmotic potential at the soil surface and increases the resistance to water vapor diffusion due to the occasional formation of a salt crust (Fujimaki et al. 2006). Complex parameterizations capture these effects (e.g., Gowing et al. 2006), but cannot easily be incorporated into the Noah LSM. Onton and Steenburgh (2001) reduce the saturation vapor pressure over the GSL by 30% and 6% over the north and south arms, respectively, because the arms have varying degrees of salinity. We reduce the playa saturation vapor pressure by 44%, which is the mean reduction for saturated GSL brines samples between –10°C and 40°C (Dickson et al. 1965). This is a crude approach given that the playa soil water is fully saturated with brine identical to the GSL brine, and that playa soil water evaporation behaves identically to open water evaporation. The effects of a reduced osmotic potential and salt crust, which would further reduce evaporation and *LE,* are ignored.

4.4 Results

4.4.1 SEB Validation

4.4.1.1 MATERHORN-Fall

Comparing the mean mostly clear day SEB observations to the corresponding Control forecasts at EFS-DS during MATERHORN-Fall shows that Control captures the incoming SW, but slightly overpredicts the outgoing SW (Fig. 4.6a). The latter is because the mean WRF-derived albedo in Control is 0.03 higher than the albedo calculated from dividing the observed daily integrated outgoing SW from the incoming (Table 4.2). Control also underpredicts the incoming LW, especially during the day (i.e., when incoming SW is > 0), which could be related to a tropospheric cold bias, as identified in operational 4DWX forecasts over the region by Massey et al. (2015), or an underprediction of clouds[6] (Fig. 4.6b). The outgoing LW is underpredicted during the day and overpredicted at night (i.e., when incoming SW = 0) suggesting an underprediction of the diurnal skin temperature range. The SW and LW errors lead to a stronger negative R_n at night and a weaker positive R_n during the day (Fig. 4.6c).

The biggest SEB errors in Control are in the H and G forecasts. The daytime H maximum in Control is underpredicted by 74 W m^{-2} and occurs 30 min later than observations (Fig. 4.6d). The magnitude of G is overpredicted by as much as 65 W m^{-2} during the day and 60 W m^{-2} at night (Fig. 4.6e). LE only reaches a maximum of 18 W m^{-2} in the observations, which is slightly overpredicted (Fig. 4.6f).

Both SM and SM-Albedo produce nearly identical SEB forecasts at EFS-DS that are much improved compared to Control (Fig. 4.6). Although the incoming and outgoing

[6] Mostly clear days only require a transmittance ≥ .65 and, thus, may feature some clouds.

SW is virtually identical to Control, the latter because the mean MODIS-derived albedo is the same as the WRF-derived albedo, both SM and SM-Albedo improve the outgoing LW throughout the diurnal cycle (Fig. 4.6b). This improves R_n at night, but leads to a slight underprediction during the day (Fig. 4.6c).

The most substantial improvement compared to Control occurs in the H and G forecasts. The SM and SM-Albedo H maxima are 46 W m^{-2} greater than Control, though still underpredicted by 28 W m^{-2}, and are in phase with the observed maximum (Fig. 4.6d). The daytime G maxima improve by 58 W m^{-2}, leaving only a 7 W m^{-2} overprediction, and the nighttime upwelling G also improves, but remains overpredicted (Fig. 4.6e). LE is also closer to observations than Control, but exhibits a slight 6 W m^{-2} underprediction (Fig. 4.6f). Although the slight underprediction of H and overprediction of G suggests soil moisture is too high, the slight underprediction of LE suggests the soil moisture is too low. This discrepancy implies other soil parameters, or parameterized processes within the Noah LSM, may be contributing to these small errors. Overall, these results indicate that the Noah LSM, when driven with observed soil moisture, captures the SEB well at EFS-DS. Also, the nearly identical SM and SM-Albedo forecasts suggest that the MODIS-derived albedo had little effect.

In contrast to the results at EFS-DS, Control provides a closer match to the SEB observations at EFS-Playa during MATERHORN-Fall (Fig. 4.7). The mean WRF-derived albedo in Control is the same as the albedo derived from SW observations at EFS-Playa (0.30; Table 4.2) resulting in nearly perfect incoming and outgoing SW forecasts (Fig. 4.7a). The incoming LW remains underpredicted, indicating that the mean tropospheric cold bias or cloud cover underprediction is present at both sites (cf. Figs.

4.6b and 4.7b). Outgoing LW is predicted well at night, but underpredicted during the day (Fig. 4.7b). Nevertheless, these errors are relatively small and R_n is well captured (Fig. 4.7c).

The biggest SEB errors in Control at EFS-Playa are in the H and LE forecasts. The Control daytime H maximum is underpredicted by 25 W m^{-2} and occurs 1 h later than observations (Fig. 4.7d). The daytime LE maximum is overpredicted by 24 W m^{-2} and occurs 90 min later than observed (Fig. 4.7f). Rehydration of the near-surface soil at night likely leads to the early morning maximum, with LE decreasing during the day due to drying of the soil surface (Malek 2003). G is well captured during the day, but nighttime upwelling G is overpredicted by as much as 21 W m^{-2} (Fig. 4.7e).

SM-Full and SM-Albedo produce worse SEB forecasts at EFS-Playa compared to Control, but the forecast changes are small (Fig. 4.7). The outgoing LW daytime underprediction worsens slightly (Fig. 4.7b), although R_n remains close to observations (Fig 4.7c). The daytime H underprediction also worsens, especially in SM (Fig. 4.7d), consistent with an increase in LE, which is overpredicted by 60 W m^{-2} in SM and 37 W m^{-2} in SM-Albedo (Fig. 4.7f). In both SM and SM-Albedo, the LE maximum occurs 90 min later than observations. These results suggest that the use of observed soil moisture over the playa actually degrades the SEB forecast. The saturation vapor pressure adjustment in SM-Albedo reduces evaporation and improves the H and LE forecasts, but since the Noah LSM does not reduce the osmotic potential or parameterize the effects of a possible salt crust, LE remains overpredicted. Also, since the Noah LSM does not account for the uniquely high playa water table, LE remains out of phase with the

observations. In summary, SM and SM-Albedo improve the SEB at EFS-DS, but not at EFS-Playa during MATERHORN-Fall.

4.4.1.2 MATERHORN-Spring

MATERHORN-Spring features stronger synoptic forcing (Fernando et al. 2015), wetter soils (e.g., Fig. 4.4), and higher playa albedos (e.g., Fig. 4.5) compared to MATERHORN-Fall. During mostly clear days at EFS-DS, incoming and outgoing SW are slightly overpredicted by Control (Fig. 4.8a), and the incoming LW is underpredicted (Fig. 4.8b) suggesting that Control underpredicts intermittent daytime cloud cover. The overprediction of the outgoing SW occurs because the mean WRF-derived albedo in Control is higher than the albedo derived from SW observations by 0.03 (Table 4.2). Similar to EFS-DS and EFS-Playa during MATERHORN-Fall, the outgoing LW in Control is underpredicted during the day, consistent with an underprediction of daytime skin temperature, and the incoming LW is underpredicted (cf. Figs. 4.6b, 4.7b, and 4.8b). Collectively, these errors contribute to a slight overprediction of the magnitude of the positive R_n during the day and negative R_n at night (Fig. 4.8c).

Unlike MATERHORN-Fall, H is well captured by Control at EFS-DS during MATERHORN-Spring (Fig. 4.8d), and the maximum G is only slightly overpredicted by 25 W m^{-2} (Fig. 4.8e). LE is also well represented (Fig. 4.8f). Overall, the Control SEB at EFS-DS is closer to observations during MATERHORN-Spring than MATERHORN-Fall.

SM and SM-Albedo have only slightly drier near-surface soil moisture compared to Control at EFS-DS (i.e., Fig. 4.4), and thus the SEB forecasts are similar. However, the

slightly drier soil moisture does produce a marginally lower G than Control with a daytime maximum only 7 W m^{-2} greater than the observed maximum (Fig. 4.8e). SM-Albedo has a mean MODIS-derived albedo 0.02 higher than the WRF-derived SM albedo and 0.05 higher than the albedo derived from SW observations (Table 4.2), which results in higher outgoing SW (Fig. 4.6a), slightly lower daytime outgoing LW (Fig. 4.6b), and lower R_n (Fig. 4.6c) compared to Control. Therefore, the slight reduction of H (Fig. 4.6d) and G (Fig. 4.6e) by as much as 27 W m^{-2} and 7 W m^{-2}, respectively, compared to Control may only be due to an overestimate of the EFS-DS albedo.

On mostly cloudy days during MATERHORN-Spring at EFS-DS, SEB forecasts by Control, SM, and SM-Albedo are markedly worse than on mostly clear days (cf. Figs. 4.8 and 4.9). Incoming SW is overpredicted by as much as 322 W m^{-2} (Fig. 4.9a), which leads to overpredicted R_n (Fig. 4.9c), H (Fig. 4.9d), and G (Fig. 4.9e) during the day, but LE forecasts remain close to observations (Fig. 4.7f). These results suggest that all simulations underpredict cloud cover, or the influence of cloud cover on downwelling SW, over EFS-DS. Similar results are observed over EFS-Playa and during the small number of mostly cloudy days during MATERHORN-Fall at both sites (not shown).

On mostly clear days at EFS-Playa during MATERHORN-Spring, the biggest Control SEB errors are a LE and R_n overprediction (Fig. 4.10). The LE maximum is overpredicted by 47 W m^{-2} and occurs 3 h later than observations (Fig. 4.10f). Incoming SW is slightly overpredicted by Control (Fig. 4.10a), whereas both outgoing and incoming LW are underpredicted (Fig. 4.10b). These errors result in a daytime R_n overprediction by as much as 92 W m^{-2} (Fig. 4.10c). H (Fig. 4.10d) and G (Fig. 4.10e) are close to observations.

SM has much higher soil moisture than Control at EFS-Playa (i.e., Fig. 4.4b), which exacerbates the daytime *LE* and R_n overprediction, and also produces a daytime *H* and outgoing LW underprediction (Fig. 4.10). The SM *LE* maximum is 199 W m^{-2}, 156 W m^{-2} greater than the observed maximum (Fig. 4.10e), and *H* is underpredicted by 83 W m^{-2} (Fig. 4.10d). The mean MODIS-derived SM-Albedo albedo is 0.36 at EFS-Playa, which is 0.06 higher than the WRF-derived SM and Control albedos, and 0.03 higher than the albedo derived from SW observations (Table 4.2). This results in an outgoing SW overprediction in SM-Albedo (Fig. 4.10a), but also brings the daytime R_n closer to observations (Fig. 4.10c). The SM-Albedo albedo and saturation vapor pressure modification also reduces the *LE* maximum by 48 W m^{-2} compared to SM, but the *LE* maximum remains overpredicted by 108 W m^{-2}, and 61 W m^{-2} greater than Control (Fig. 4.10f).

Results from this section show how SM and SM-Albedo improve SEB forecasts substantially at EFS-DS during MATERHORN-Fall and slightly during MATERHORN-Spring. However, SM and SM-Albedo worsen SEB forecasts slightly at EFS-Playa during MATERHORN-Fall and substantially during MATERHORN-Spring, which is a likely consequence of unique playa land-surface processes not being represented in the Noah LSM.

4.4.2 *H* and 2-m Temperature Contrasts Between EFS-DS and EFS-Playa

H differences between EFS-DS and EFS-Playa produce local thermally forced daytime on-playa, and nighttime off-playa, flows during quiescent large-scale conditions

(e.g., Rife et al. 2002). Here we examine how well the WRF captures the *H* and temperature contrasts between these two sites.

On mostly clear days during MATERHORN-Fall, the observed *H* is larger at EFS-DS than at EFS-Playa, exceeding 83 W m^{-2} in the late afternoon (Fig. 4.11a). Control greatly underpredicts this *H* difference, due largely to the *H* underprediction at EFS-DS (Fig. 4.6d). This contributes to an underprediction of the mean daytime temperature difference between 7 SAMS over the desert shrub (SAMS-DS) and 7 SAMS over the playa (SAMS-Playa) that is as large as 1.5°C (Fig. 4.11b, see Fig. 4.1 for SAMS-DS and SAMS-Playa locations). At night, the observed EFS-DS and EFS-Playa 2-m temperature difference is as large as –3.9°C, but Control only predicts a maximum 2-m temperature difference of –0.6°C.

With greatly improved EFS-DS *H* forecasts, and only marginally worse EFS-Playa *H* forecasts, SM and SM-Albedo produce more realistic daytime *H* differences between the two sites (Fig. 4.11a). As a result, the daytime SAMS-DS and SAMS-Playa 2-m temperature difference is more accurately simulated, especially in SM-Albedo, though it remains underpredicted by as much as 0.9°C. At night, the 2-m temperature difference in SM, and especially SM-Albedo, improves substantially, but the magnitude remains underpredicted by as much a 1°C. This improvement is likely related to the improved *G* forecasts at EFS-DS.

On mostly clear days during MATERHORN-Spring, the observed *H* difference between EFS-DS and EFS-Playa is larger than during MATERHORN-Fall, exceeding 116 W m^{-2} in the late afternoon (Fig. 4.12a). Control only slightly underpredicts this *H* difference, but the 2-m temperature difference between SAMS-DS and SAMS-Playa is

underpredicted by as much as 1.3°C (Fig. 4.12b). At night, Control underpredicts the magnitude of the difference by as much as 3.1°C.

In SM and SM-Albedo during MATERHORN-Spring, the *H* difference between EFS-DS and EFS-Playa becomes overpredicted (Fig. 4.12a) because *H* in both simulations is greatly overpredicted at EFS-Playa (Fig. 4.10f). The SM and SM-Albedo *H* difference maximum is 50 W m^{-2} and 29 W m^{-2} greater than the observed maximum, respectively, and occurs 1 h earlier than in observations. Surprisingly, the overprediction of the daytime *H* difference does not result in an overpredicted 2-m temperature difference. This discrepancy may be the result of near-surface wind differences between observations and SM and SM-Albedo, which affects *H* and temperature advection. Mean daytime 2-m temperature differences increase in SM and SM-Albedo by as much as 1.1°C compared to Control, but remain less than observations, and little if any improvement occurs at night.

In summary, SM-Albedo, and especially SM, increase the *H* difference between EFS-DS and EFS-Playa compared to Control resulting in improved *H* difference forecasts during MATERHORN-Spring, but overpredicted *H* difference forecasts during MATERHORN-Fall. Daytime 2-m temperature differences between the desert shrub and playa improve during both periods, but remain underpredicted, and nighttime temperature differences only improve during MATERHORN-Fall when observed temperature differences are larger than those observed during MATERHORN-Spring (cf. Figs. 4.11b and 4.12b). Paradoxically, the daytime *H* difference is overpredicted in SM-Albedo, and especially SM, during MATERHORN-Spring, but the daytime 2-m temperature

difference is underpredicted in SM, and especially SM-Albedo. These discrepancies may be the result of changes to the near-surface wind that affect *H* and temperature advection.

4.4.3 Playa Breezes

The temperature differences between the desert shrub and playa contribute to diurnal boundary layer circulations, such as a playa breeze, that develop over the region under quiescent large-scale conditions (Rife et al. 2002). We only consider mostly clear days with a mean SAMS 1400 LST wind speed < 5 m s^{-1}, which eliminates 2 MATERHORN-Fall and 3 MATERHORN-Spring mostly clear days from validation. We also only compare SM-Albedo to Control given the slight 2-m temperature difference improvement in SM-Albedo relative to SM. During MATERHORN-Fall, there is a mean 10-m 1400 LST diffluent northerly off-playa breeze in Control (Fig. 4.13a). SAMS observations generally support this flow regime, especially over eastern DPG where most SAMS are located (Fig. 4.14a). Overall, the Control wind speed and direction MAEs at 1400 LST are 0.97 m s^{-1} and 42.9°, respectively, with a wind speed BE of –0.27 m s^{-1} (Figs. 4.15a-c). In general, MATERHORN-Fall wind direction and speed MAEs are lowest during this afternoon period.

At 0500 LST, Control produces a large-scale northwesterly flow over much of the Playa (Fig. 4.13d), with weak and variable flow over eastern DPG (Fig. 4.14d). These flows contrast some with SAMS observations, which show weaker flow over much of the playa and a stronger down-valley on-playa breeze over eastern DPG. Overall, the Control 0500 LST wind speed and direction MAEs are 1.39 m s^{-1} and 69.8°, respectively, and the wind speed BE is –0.29 m s^{-1} (Figs. 4.14a-c). These are higher than found at

1400 LST, consistent with poorer model performance overnight and in the early morning hours.

With a stronger 2-m temperature contrast between the desert shrub and playa, SM-Albedo produces a stronger off-playa breeze at 1400 LST compared to Control (cf. Figs. 4.13a and 4.13b). SM-Albedo winds appear close to SAMS observations along the playa boundary in eastern DPG, but overpredicted in southeastern DPG (Fig. 4.14b). Wind speed BEs increase from –0.27 m s^{-1} to 0.12 m s^{-1} in SM-Albedo, which is statistically significant at the 95% level[7] (Fig. 4.15c), but the wind speed and direction MAE improvement is not statistically significant relative to Control at 1400 LST (Figs. 4.15a,b). However, other daytime hours do have statistically significant wind direction MAE improvement (Fig. 4.15b). Daily mean wind speed MAE improvement is concentrated at stations located along and near the playa boundary in eastern DPG, and over the playa, with higher MAEs at other stations (Fig. 4.16a). Overall, the stronger afternoon off-playa breeze in SM-Albedo slightly improves both wind speed BE and wind direction MAE, but does not improve the wind speed MAE because wind speeds improve at some stations, but are overpredicted at others.

In the morning at 0500 LST, flow differences between Control and SM-Albedo are nearly indistinguishable (cf. Figs. 4.13c and 4.13d), with the exception of a slightly weaker off-playa breeze along the eastern DPG playa boundary (cf. Figs. 4.14c and 4.14d). The wind direction MAE improvement relative to Control is not statistically significant (Fig. 4.15b), although improvements are significant later in the morning. There is also a statistically significant wind speed MAE improvement, but the improvement is only 0.09 m s^{-1}, and the improvement at most other nighttime hours is not

[7] Statistical significance based off of paired-sample t-test.

statistically significant (Fig. 4.15a). Thus, the strength of the daytime off-playa breeze is the biggest difference between Control and SM-Albedo during MATERHORN-Fall.

During MATERHORN-Spring, there is a mean diffluent off-playa breeze at 1400 LST (Fig. 4.17a), but no overall northerly flow component as during MATERHORN-Fall (Fig. 4.13a). Over eastern DPG, Control has a weaker northerly wind component compared to observations (Fig. 4.18a), which contributes to the large wind speed and direction MAEs of 1.51 m s^{-1} and 52.7°, respectively (Figs. 4.15d,e), and large low wind bias of –0.38 m s^{-1} (Fig. 4.15f). Other daytime hours have similar errors. At 0500 LST during MATERHORN-Spring, Control produces a large-scale northwesterly flow that is supported by observations over much of the playa (Fig. 4.17c), but not supported over the lower elevations of eastern DPG because observations show a southeasterly on-playa breeze (Fig. 4.18c). The Control 0500 LST wind speed MAE is near its diurnal minimum at 1.42 m s^{-1}, the wind speed MAE is near its diurnal maximum at 64.3°, and the wind speed BE is –0.45 m s^{-1} and negative throughout its diurnal cycle (Figs. 4.15d-e).

SM-Albedo increases the 1400 LST MATERHORN-Spring off-playa breeze compared to Control, but the biggest changes occur away from eastern DPG (cf. Figs. 4.17a and 4.17b). Nevertheless, the weak westerly flow in Control becomes a slightly stronger northwesterly flow in SM-Albedo over eastern DPG that is supported by observations (Fig. 4.18b). This change, however, does not significantly improve wind speed or direction MAEs compared to Control at 1400 LST, or any other hour at the 95% level (Figs. 4.15d,e). Wind speed MAEs improve at stations along the playa boundary in eastern DPG, but worsen away from the boundary and over the playa. However, the wind speed BE at 1400 LST increases from –0.38 m s^{-1} in Control to 0.10 m s^{-1}, which is

statistically significant. Other daytime hours also have statistically significant BE differences. At 0500 LST, there are no discernable flow differences between Control and SM-Albedo (cf. Figs. 4.17c and Fig. 4.17d), and there are no statistically significant nighttime errors improvements (Figs. 4.15d-f).

In summary, the strength of the daytime off-playa breeze increases in SM-Albedo compared to Control causing the daytime negative wind speed bias to become slightly positive, but wind speed and direction MAEs only marginally improve during MATERHORN-Fall, and the improvement is only occasionally statistically significant. This discrepancy is the result of lower MAEs only occurring over certain regions, like the playa boundary in eastern DPG, with higher MAEs elsewhere.

4.5 Conclusions

Weather Research and Forecasting (WRF) model simulations of the fall 2012 (1 October – 20 October 2012; MATERHORN-Fall) and spring 2013 (2 May – 31 May 2013; MATERHORN-Spring) Mountain Terrain Atmospheric Modeling and Observations Program (MATERHORN) field campaigns are validated against surface energy balance (SEB) observations collected over playa (EFS-Playa) and desert shrub (EFS-DS) land surfaces in Dugway Proving Ground (DPG) of northwest Utah. MATERHORN-Spring features wetter soils and stronger synoptic forcing than MATERHORN-Fall, and EFS-Playa has considerably wetter soils and a higher albedo than EFS-DS, allowing for the SEB validation of two contrasting periods at two contrasting land surfaces.

The biggest SEB errors occur during MATERHORN-Fall at EFS-DS. The daytime sensible heat flux (H) is greatly underpredicted and the ground heat flux (G) is greatly overpredicted. The diurnal amplitude of the outgoing longwave radiation (LW) and the daytime latent heat flux (LE) are also overpredicted. Simulations that incorporate observed soil moisture into the land surface analyses and modify the soil thermal conductivity parameterization over silt loam and sandy loam soils (SM) significantly reduce these errors illustrating the importance of accurate land surface analyses and parameterizations for this region. Although EFS-DS SEB forecasts improve, a slight H and LE underprediction and G overprediction remain, which cannot be explained by a soil moisture estimation error. This discrepancy implies that other soil parameters or parameterized processes within the Noah land surface model (LSM) may be contributing to these small errors. The EFS-DS SEB also improves during MATERHORN-Spring, but improvement is less pronounced than during MATERHORN-Fall when observed soil moisture is lower and analyzed soil moisture is further from observations.

At EFS-Playa during MATERHORN-Fall and MATERHORN-Spring, the biggest error is an overprediction of LE, which is associated with an underprediction of H. The playa soil moisture is higher in the observations than the land surface analyses, which exacerbates the LE overprediction in SM. Simulations that also include observed albedo from a Moderate Resolution Imaging Spectroradiometer (MODIS) product, and a reduced saturation vapor pressure over the playa (SM-Albedo) only marginally improve these SEB errors at EFS-Playa. The playa is a very unique land surface, and the playa LE is overpredicted because the Noah LSM does not account for the effects of a salt crust, high water table, or reduced osmotic potential on evaporation. The net radiation (R_n)

during MATERHORN-Spring is also overpredicted due to either the underprediction of cloud cover, or the underprediction of the influence of cloud cover on downwelling SW. SM-Albedo improves R_n during MATERHORN-Spring, but only because the MODIS-derived albedo is higher than the local observed albedo.

The resulting H forecast improvement at EFS-DS, and H forecast deterioration at EFS-Playa in SM and SM-Albedo increases the H difference between EFS-DS and EFS-Playa. The larger H difference improves the 2-m temperature difference between the desert shrub and playa during MATERHORN-Fall and MATERHORN-Spring. This results in a stronger daytime off-playa 10-m flow in SM-Albedo, but the location of the greatest wind increases varies considerably between MATERHORN-Fall and MATERHORN-Spring. Nighttime wind speed and direction improvement is minimal. The increase in daytime wind speed improves the wind speed bias error (BE), but does not necessarily improve wind speed and direction mean absolute errors (MAE). Wind speed MAE improvement is concentrated over the playa during MATERHORN-Fall and along the playa boundary in eastern DPG during both periods, but MAEs increase at other stations resulting in little to no overall improvement. The stronger daytime off-playa breeze may be penetrating too far from the playa.

This work highlights WRF and Noah LSM deficiencies over two common dryland land surfaces. Massey et al. (2014) and Massey et al. (2015) showed impressive temperature forecast improvement when land surface analyses incorporate observed soil moisture and a modified soil thermal conductivity parameterization, and these results illustrate how these changes also improve SEB forecasts over the desert shrub, but degrade forecasts over the playa. More work is needed refining land surface analyses,

especially soil moisture analyses, to mitigate SEB errors, but land surface parameterizations also need to be improved, especially for playa, so improvements to land surface analyses can lead to better near-surface forecasts. We anticipate similar results over other playa and desert shrub land surfaces.

Table 4.1 MATERHORN-Fall EFS site availability

Date	EFS-DS availability	EFS-Playa availability
1 October 2012	X	X
2 October 2012	X	
3 October 2012	X	
4 October 2012	X	
5 October 2012	X	
6 October 2012	X	X
7 October 2012	X	X
8 October 2012	X	X
9 October 2012	X	
10 October 2012	X	
11 October 2012	X	X
12 October 2012 (mostly cloudy)	X	X
13 October 2012 (mostly cloudy)		X
14 October 2012		X
15 October 2012 (mostly cloudy)		X
16 October 2012		X
17 October 2012		X
18 October 2012	X	X
19 October 2012	X	X
20 October 2012		X

Table 4.2. Mean albedos at EFS-DS and EFS-Playa during MATERHORN-Fall and MATERHORN-Spring.

Period	Location	WRF-derived albedo	MODIS-derived albedo	Observed albedo
MATERHORN-Fall	EFS-DS	0.30	0.30	0.27
	EFS-Playa	0.30	0.30	0.30
MATERHORN-Spring	EFS-DS	0.26	0.29	0.24
	EFS-Playa	0.30	0.36	0.33

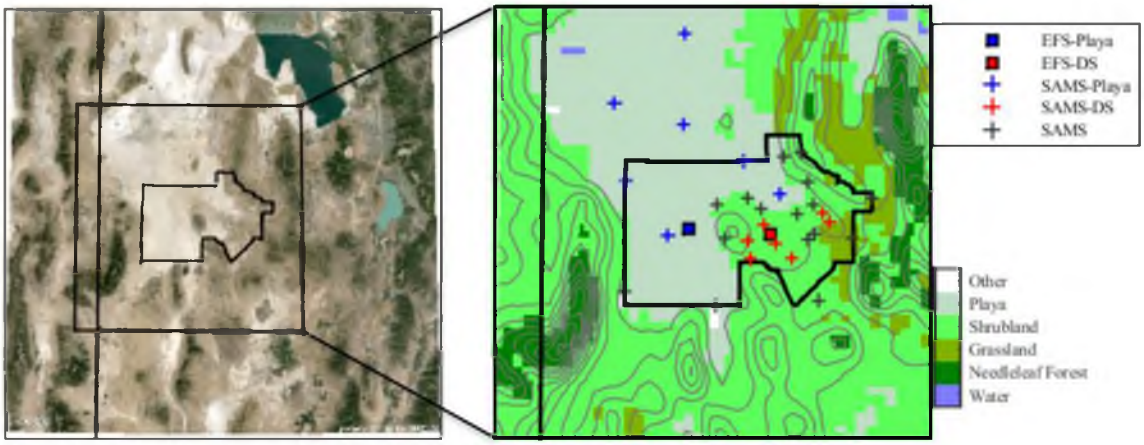

Fig. 4.1. Google Earth image of the 3.3-km domain [©2015 Google; imagery ©2015 TerraMetrics] and inset of WRF landuse (color-filled) and terrain (contoured every 150 m) for the DPG region. Relevant surface stations, the perimeter of DPG, and Utah/Nevada border are annotated.

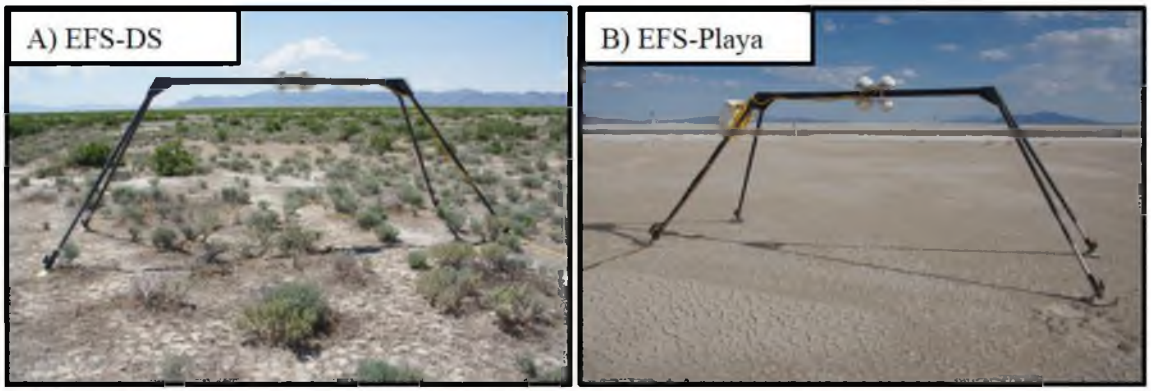

Fig. 4.2. Photos of (a) EFS-DS and (b) EFS-Playa.

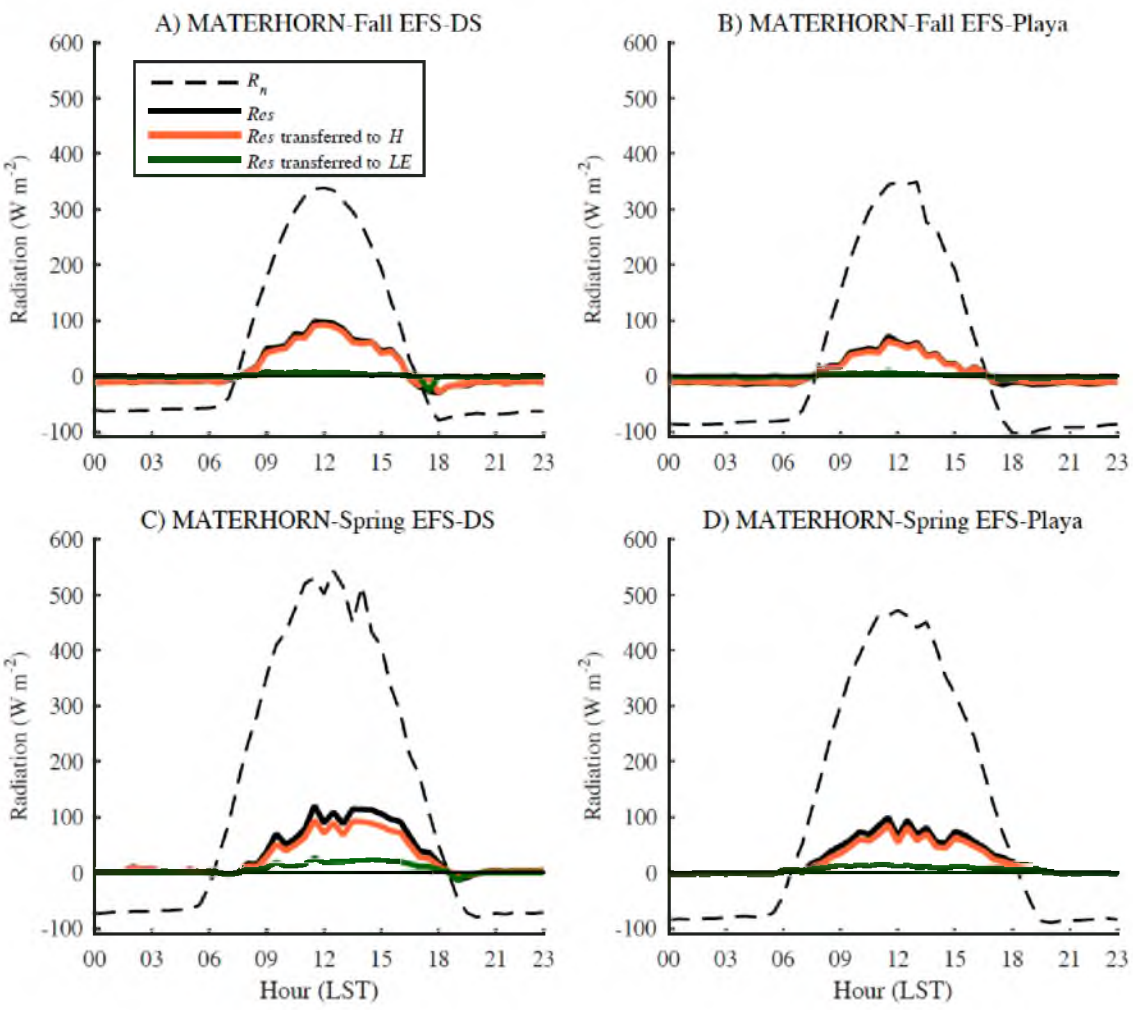

Fig. 4.3. Mostly clear day observed R_n, *Res*, *Res* transferred to *H*, and *Res* transferred to *LE* during MATERHORN-Fall at (a) EFS-DS and (b) EFS-Playa and during MATERHORN-Spring at (c) EFS-DS and (d) EFS-Playa.

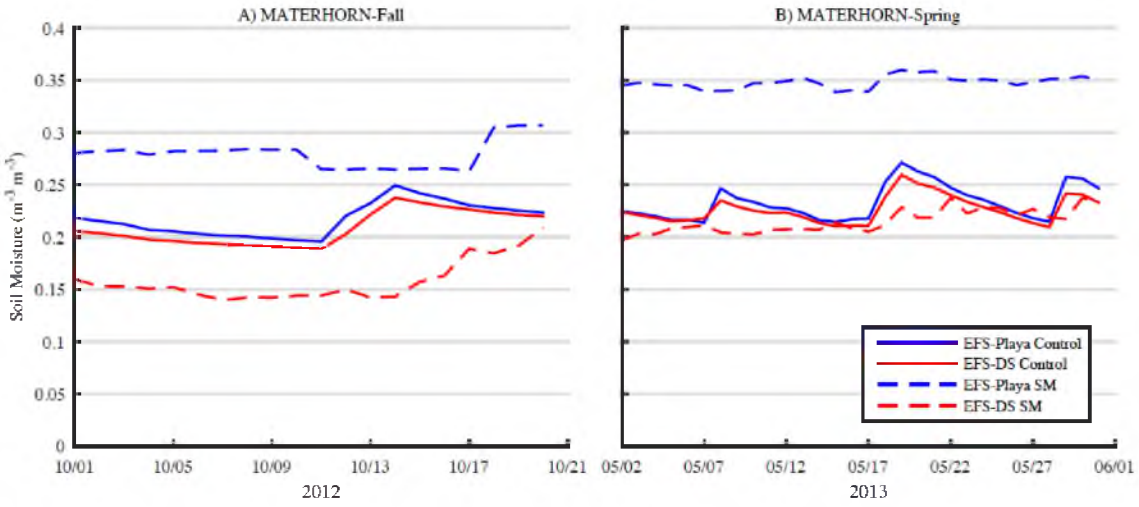

Fig. 4.4. Daily 0000 UTC 5-cm soil moisture at EFS-DS and EFS-Playa during (a) MATERHORN-Fall and (b) MATERHORN-Spring using unmodified (solid) and modified (dashed) soil moisture analyses.

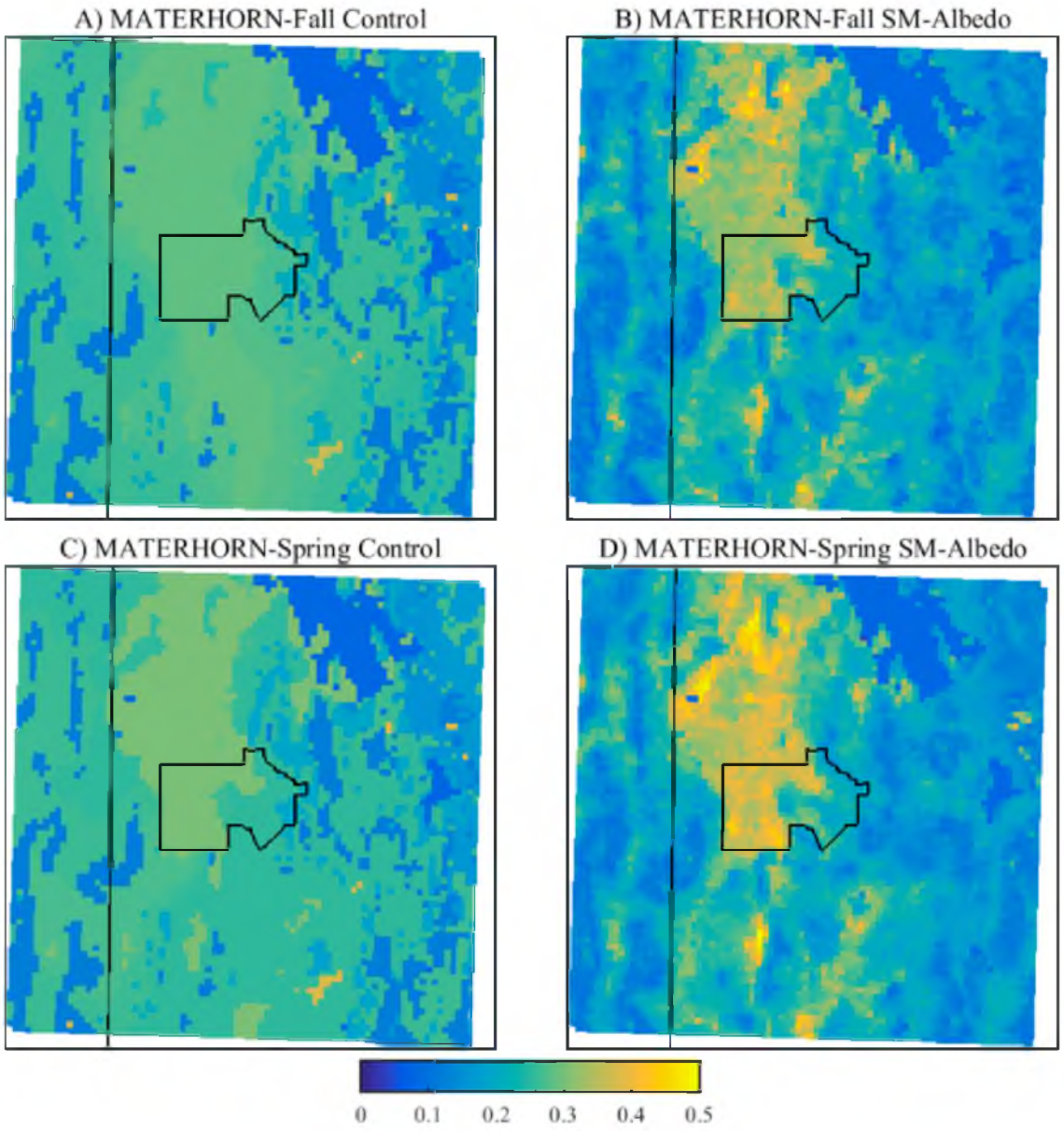

Fig. 4.5. Mean daily 3.3-km domain WRF-derived albedo in Control during (a) MATERHORN-Fall and (c) MATERHORN-Spring and MODIS-derived albedo in SM-Albedo during (b) MATERHORN-Fall and (d) MATERHORN-Spring. DPG, and the Utah/Nevada border are annotated for reference.

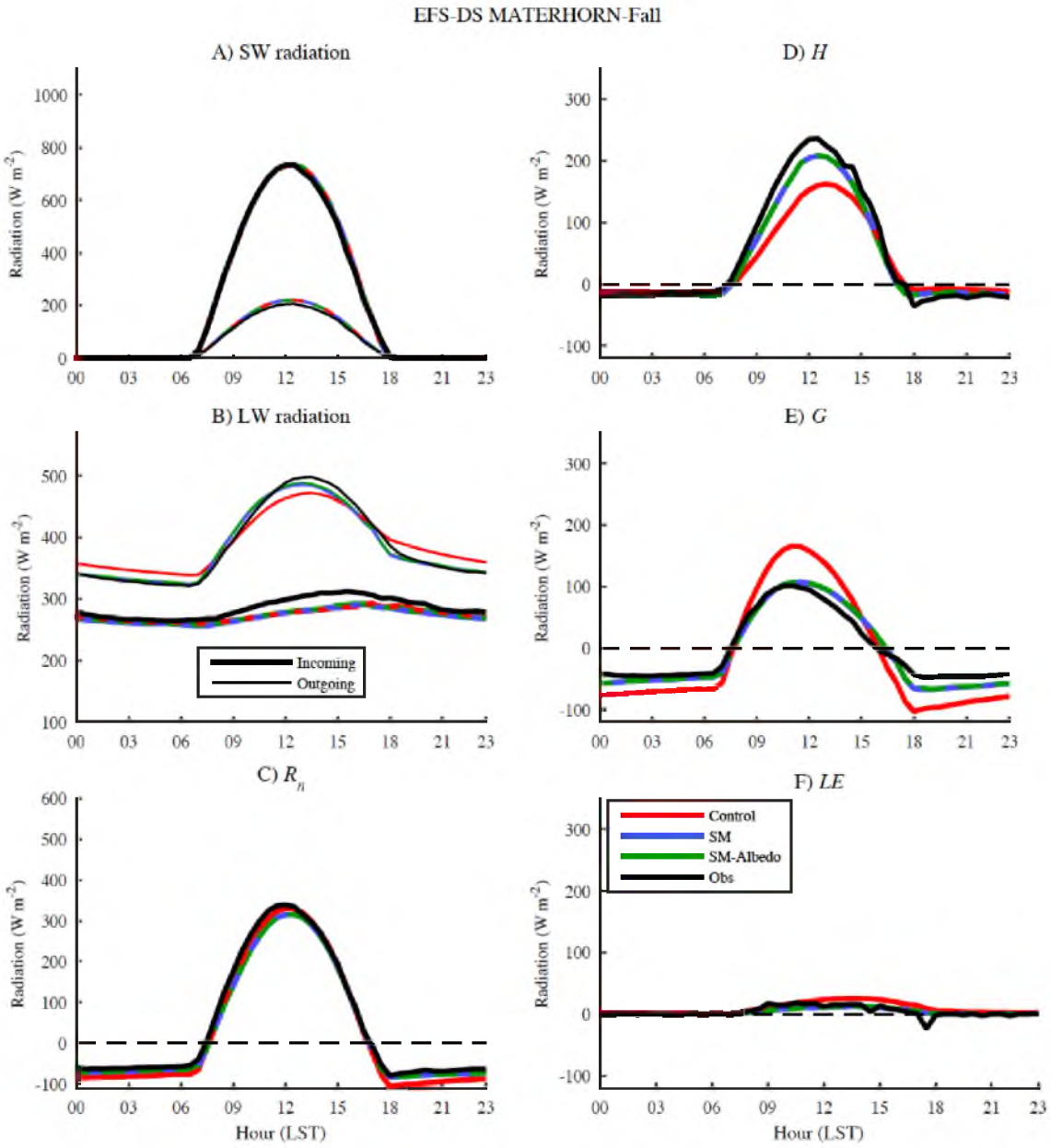

Fig. 4.6. Mostly clear day observed (black), and Control (red), SM (blue), and SM-Albedo (green) forecasts of (a) SW, (b) LW, (c) R_n, (d) H, (e) G, and (f) LE at EFS-DS during MATERHORN-Fall. Circles help distinguish overlapping simulations.

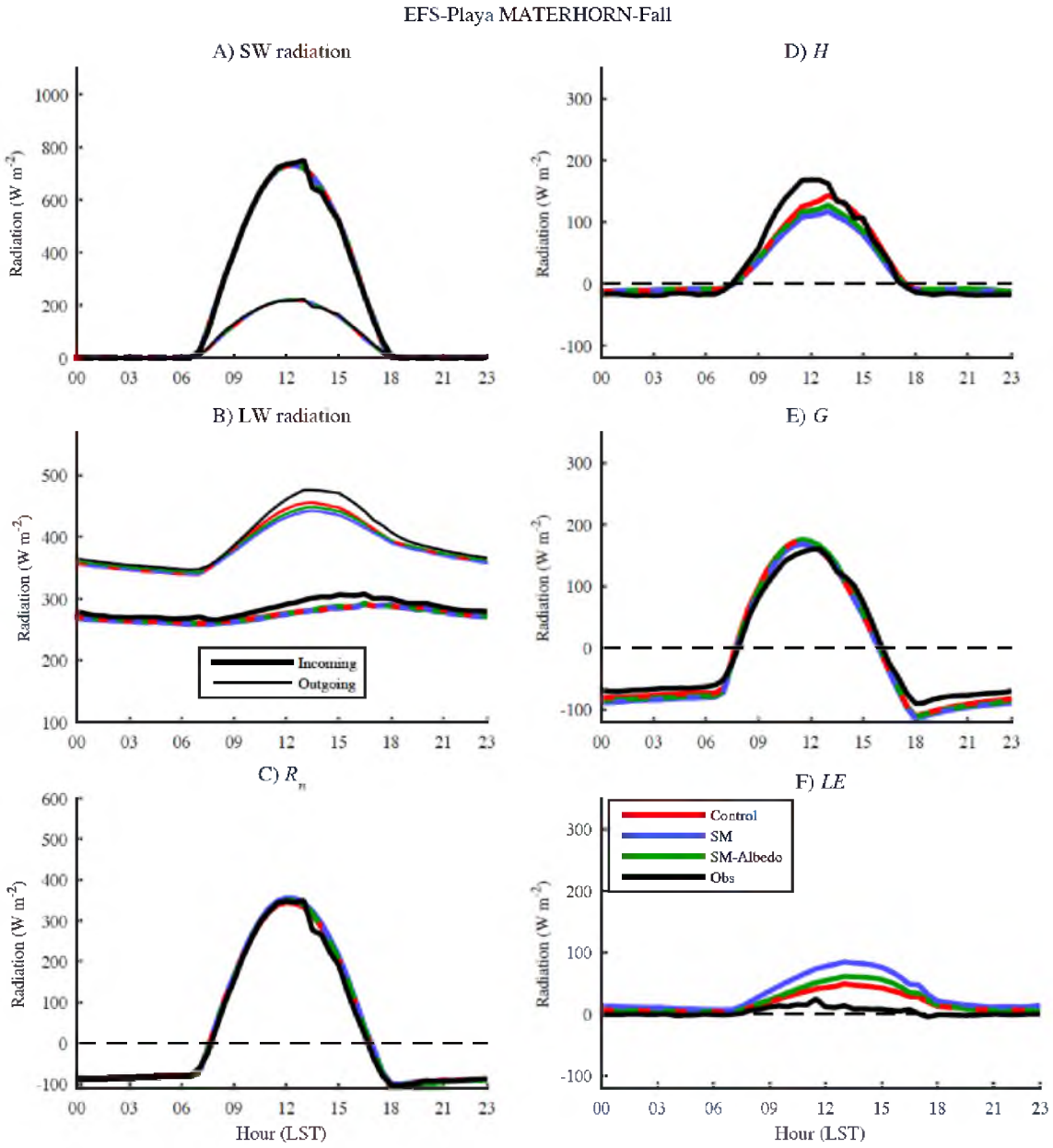

Fig. 4.7. Same as Fig. 4.6 except for EFS-Playa during MATERHORN-Fall.

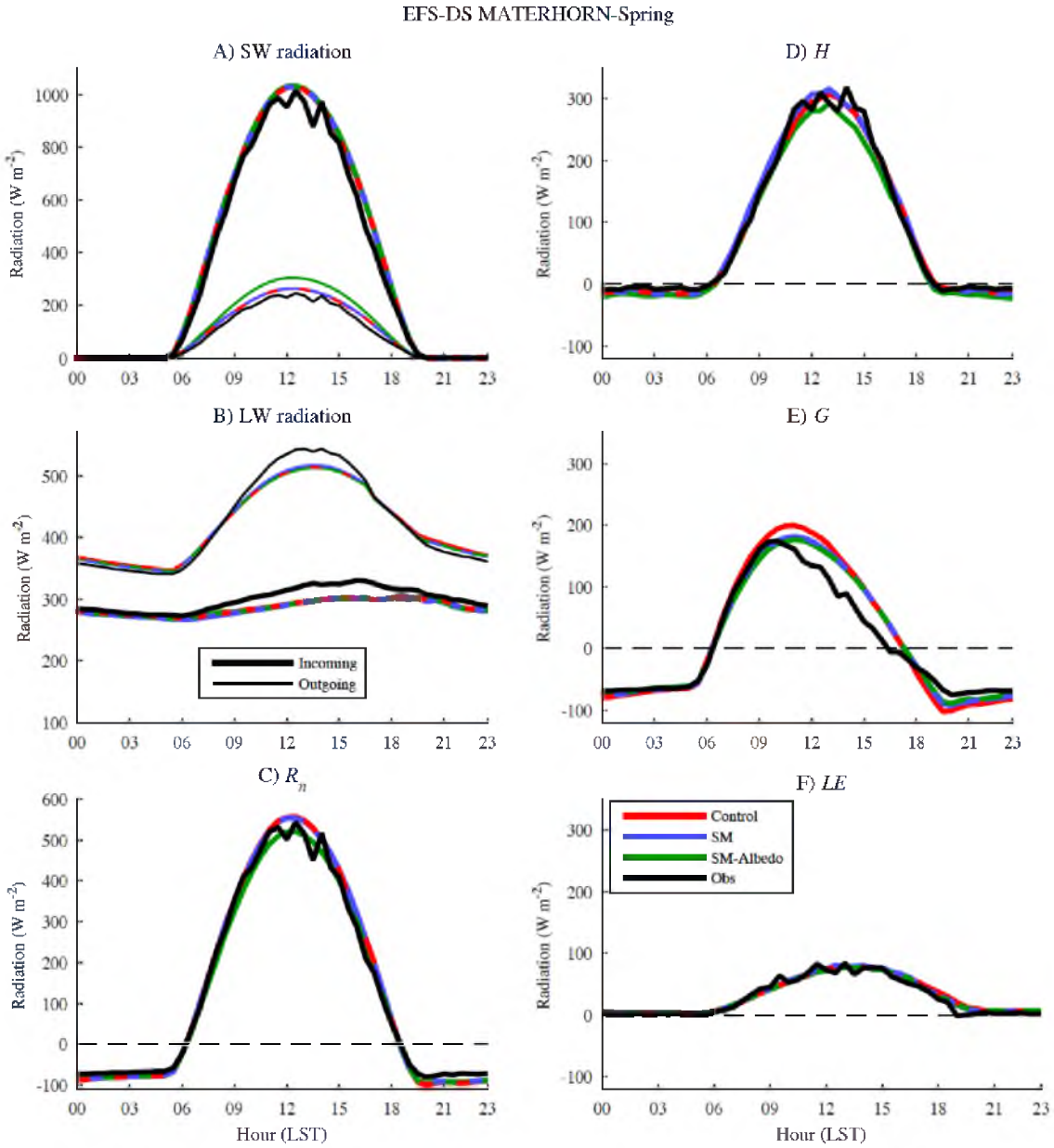

Fig. 4.8. Same as Fig. 4.6 except for EFS-DS during MATERHORN-Spring.

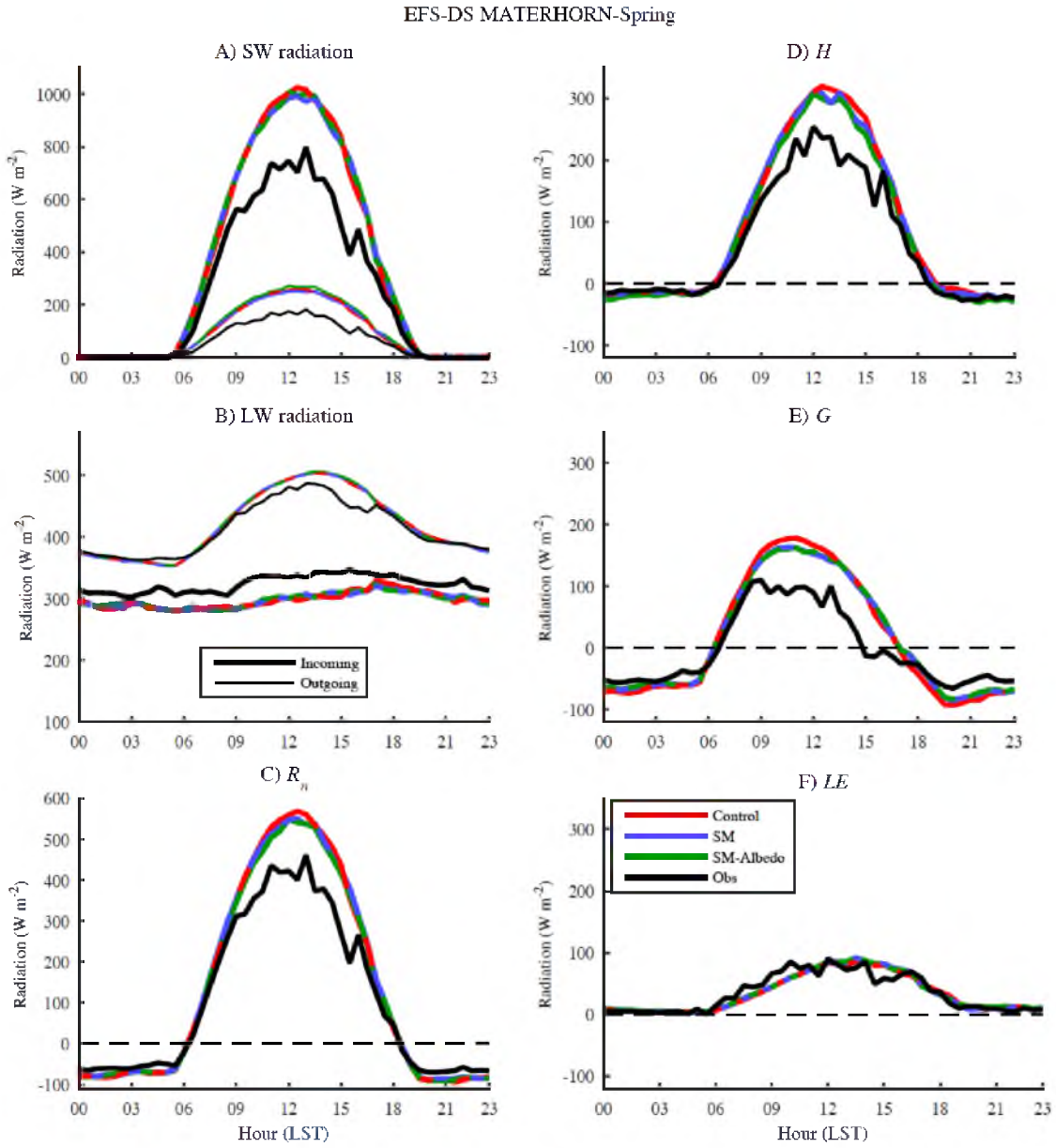

Fig. 4.9. Same as Fig. 4.6 except for mostly cloudy days at EFS-DS during MATERHORN-Spring.

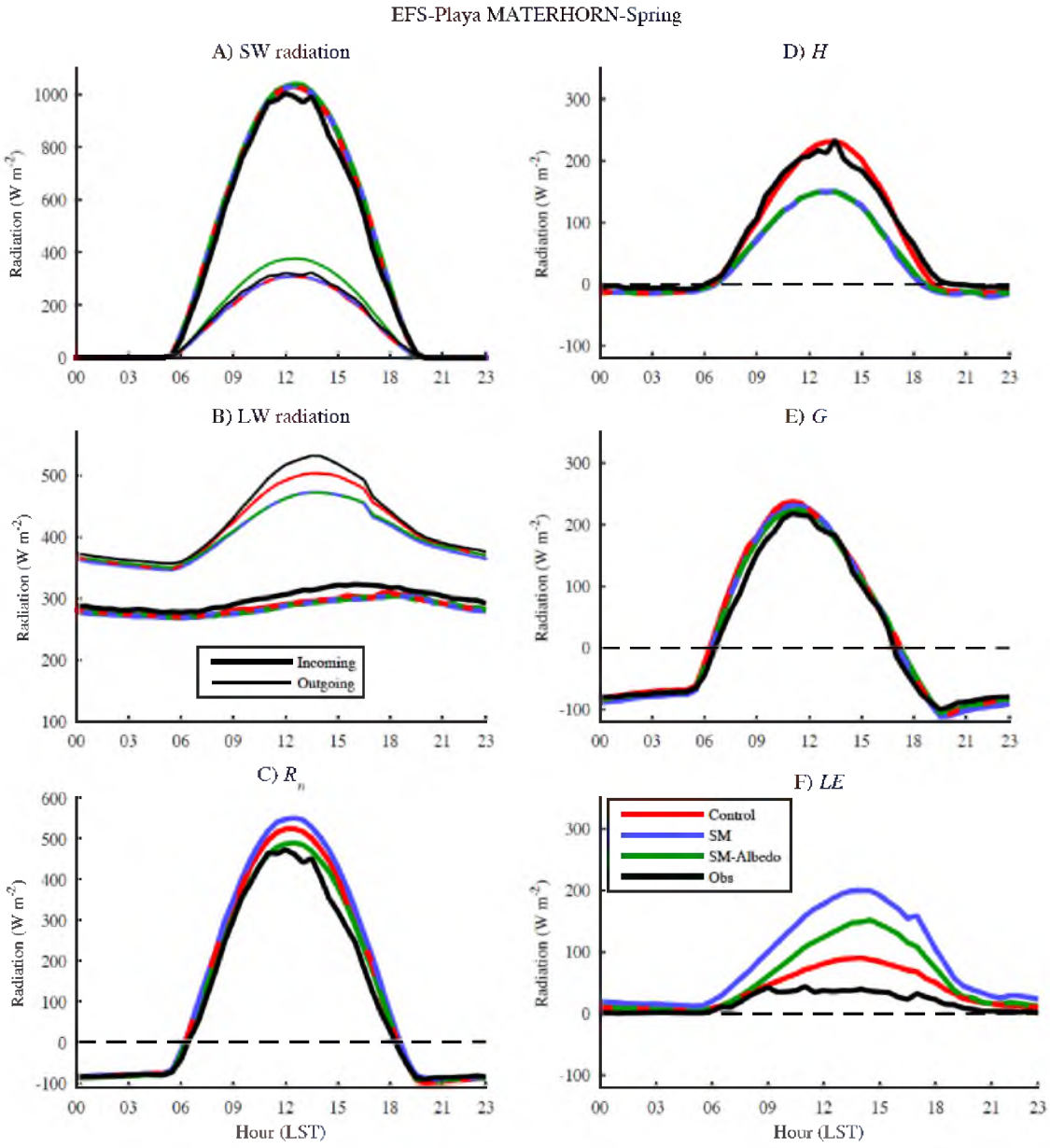

Fig. 4.10. Same as Fig. 4.6 except for EFS-Playa during MATERHORN-Spring.

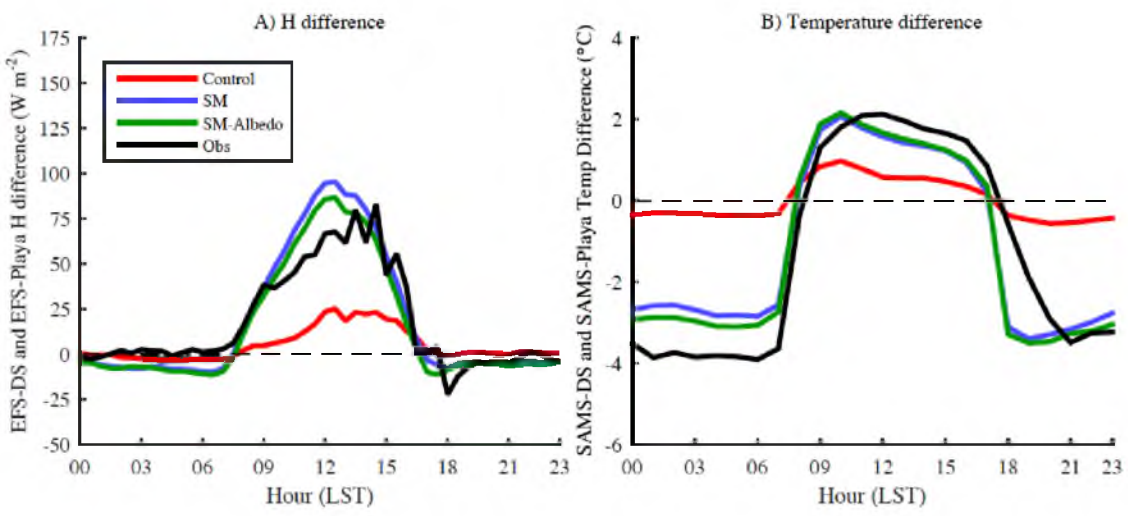

Fig. 4.11. MATERHORN-Fall mostly clear day (a) *H* differences between EFS-DS and EFS-Playa and (b) 2-m temperature differences between SAMS-DS and SAMS-Playa (see Fig. 4.1 for SAMS-DS and SAMS-Playa locations). Differences calculated for observations (black), and Control (red), SM (blue), and SM-Albedo (green) forecasts.

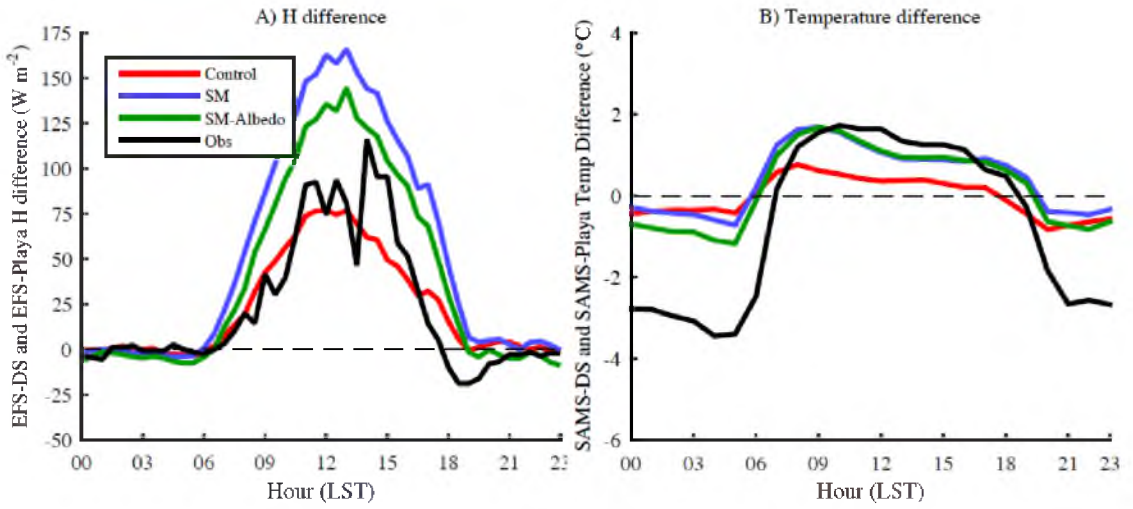

Fig. 4.12. Same as Fig. 4.11 except for MATERHORN-Spring.

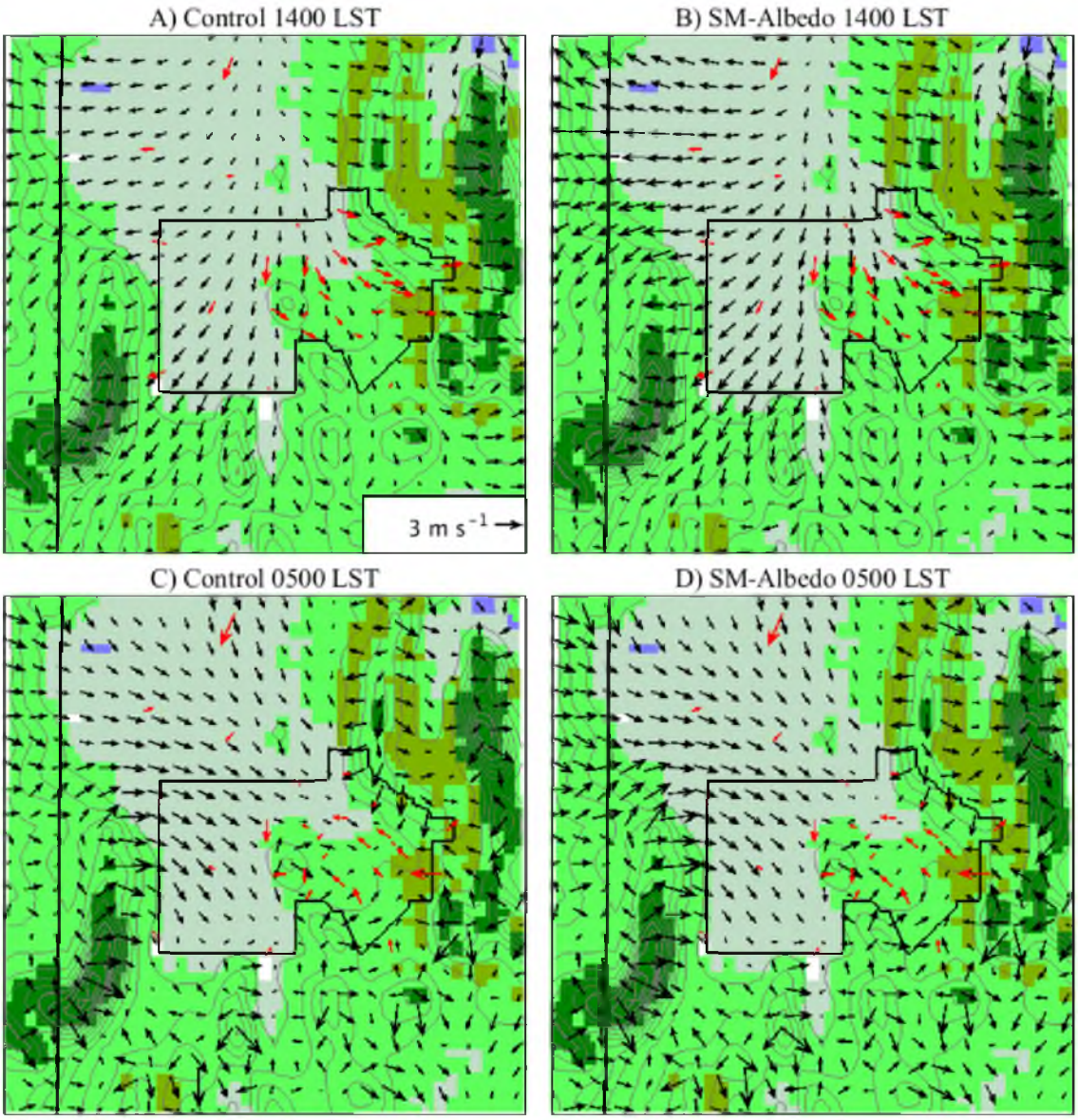

Fig. 4.13. MATERHORN-Fall mean vector winds from (a) Control and (b) SM-Albedo at 1400 LST and (c) Control and (d) SM-Albedo at 0500 LST (black vectors) and SAMS observations (red vectors) during mostly clear days with light winds. Background WRF landuse (color-filled; see Fig. 4.1 for categories) and terrain (gray contours every 150 m).

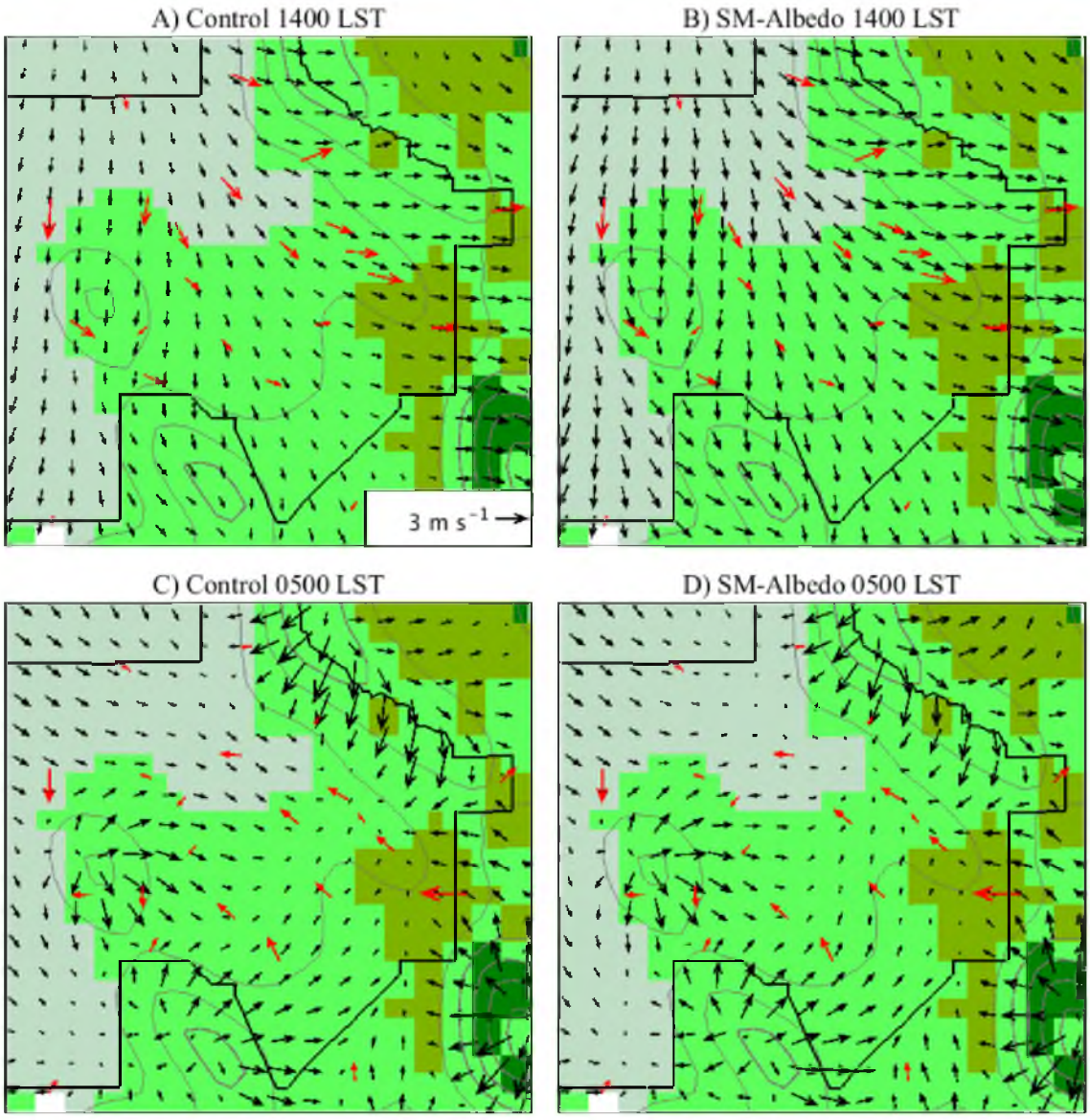

Fig. 4.14. Same as Fig. 4.13 except for eastern DPG.

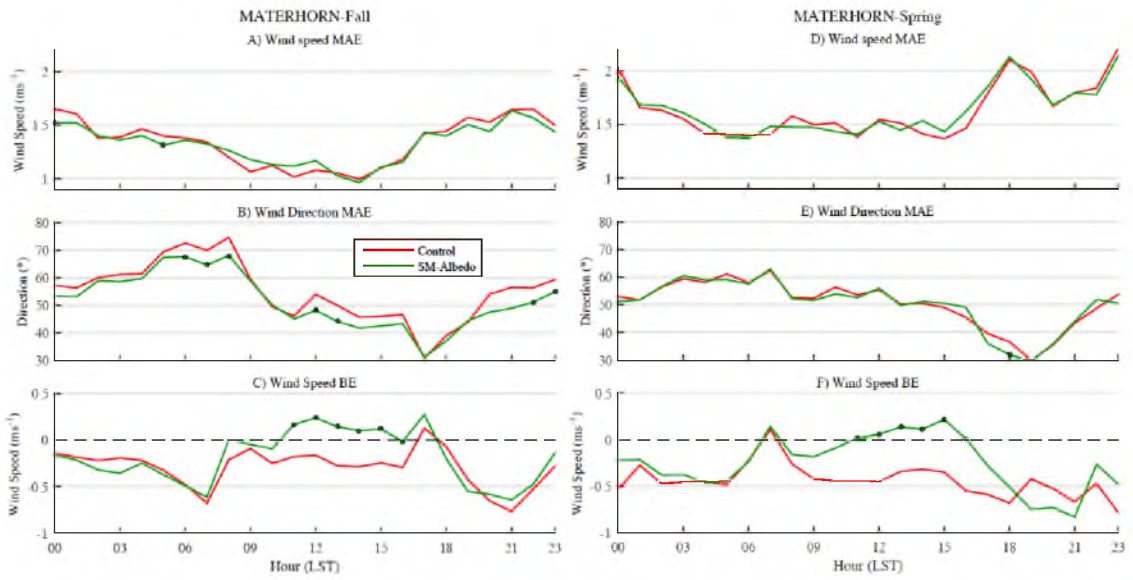

Fig. 4.15. The 10-m wind (a) speed MAE, (b) direction MAE, and (c) speed BE during MATERHORN-Fall and wind (d) speed MAE, (e) direction MAE, and (f) speed BE during MATERHORN-Spring for Control (red) and SM-Albedo green) using SAMS (see Fig. 4.1 for locations) during mostly clear days with light winds. Circles represent statistically significant differences compared to Control at the 95% level. All errors in m s^{-1}.

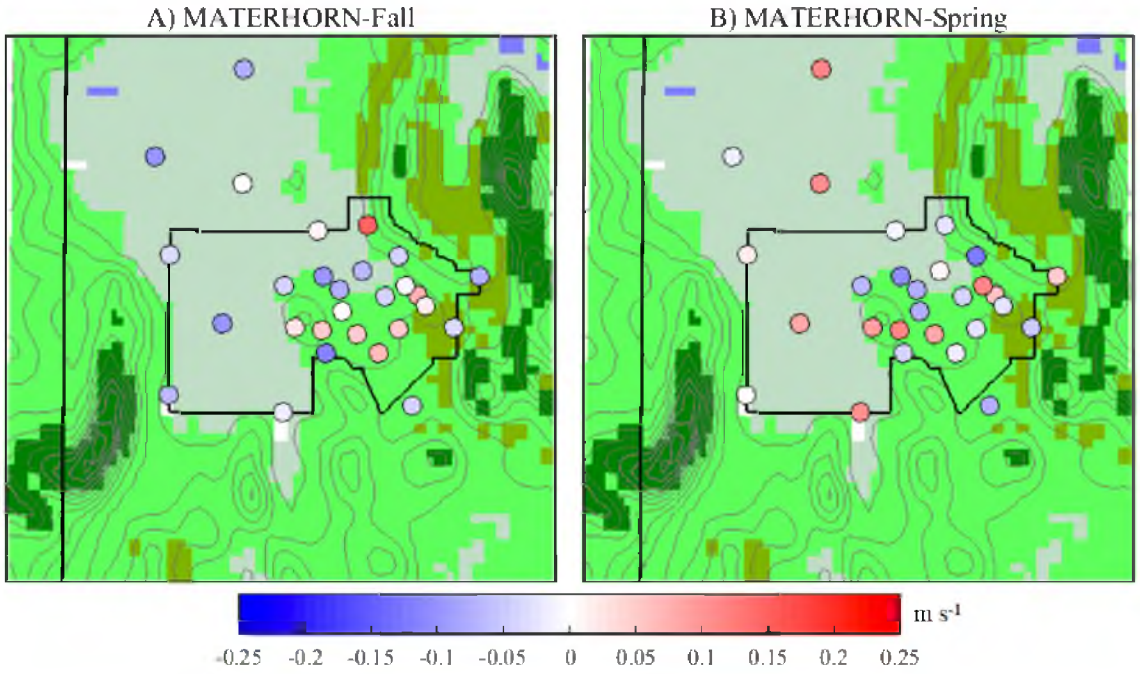

Fig. 4.16. Change in mean daily wind speed MAE (m s^{-1}) at each SAMS from Control to SM-Albedo during (a) MATERHORN-Fall and (b) MATERHORN-Spring. Background WRF landuse (color-filled; see Fig. 4.1 for categories) and terrain (gray contours every 150 m).

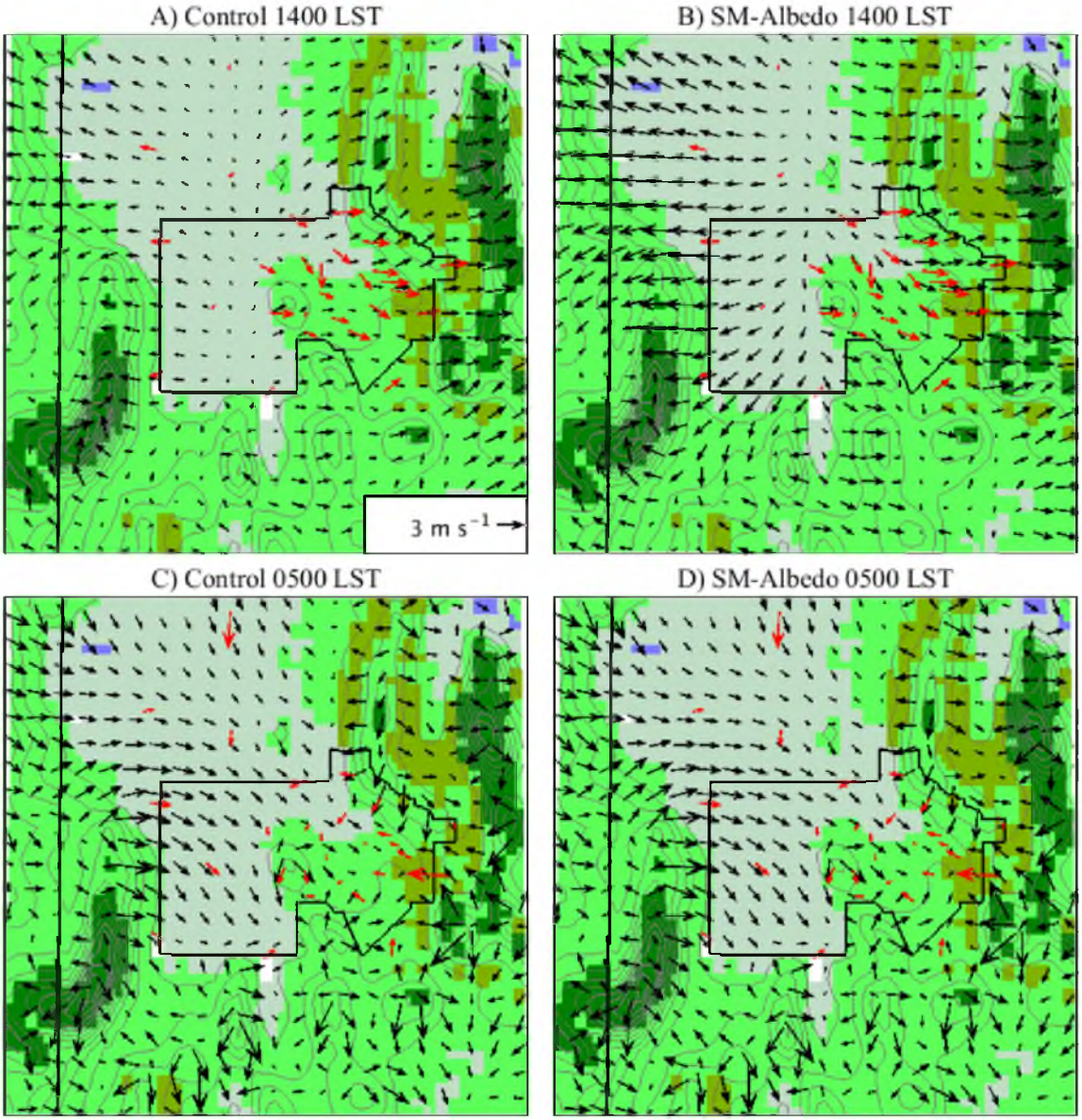

Fig. 4.17. Same as Fig. 4.13 except for MATERHORN-Spring.

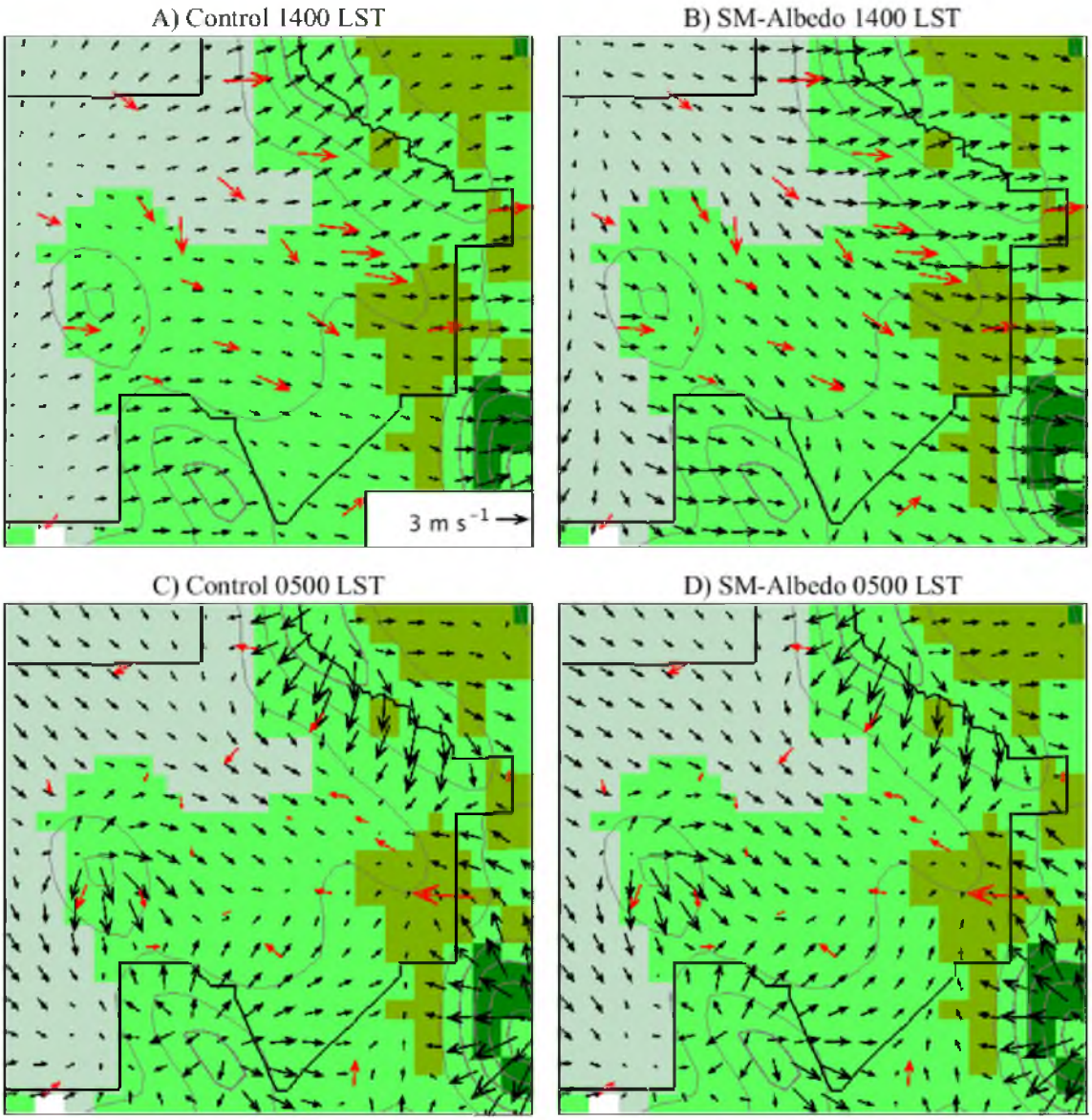

Fig. 4.18. Same as Fig. 4.14 except for MATERHORN-Spring.

4.6 References

Aas, K. S., T. K. Berntsen, J. Boike, B. Etzelmüller, J. E. Kristjánsson, M. Maturilli, T. V. Schuler, F. Stordal, and S. Westermann, 2015: A comparison between simulated and observed surface energy balance at the Svalbard archipelago. *J. Appl. Meteor. Climatol.*, in press.

Avissar, R., and R. A. Pielke, 1989: A parameterization of heterogeneous land surfaces for atmospheric numerical models and its impact on regional meteorology. *Mon. Wea. Rev.*, **117,** 2113–2136.

Bowen, I. S., 1926: The ratio of heat losses by conduction and by evaporation from any water surface. *Phys. Rev.*, **27**, 779–787.

Chen, F., and J. Dudhia, 2001: Coupling an advanced land surface–hydrology model with the Penn State–NCAR MM5 modeling system. Part I: Model implementation and sensitivity. *Mon. Wea. Rev.*, **129**, 569–585.

Cosenza, P., R. Guerin, and A. Tabbagh, 2003: Relationship between thermal conductivity and water content of soils using numerical modeling. *Eur. J. Soil Sci.*, **54**, 581–587.

Crosman, E., and J. Horel, 2009: Remote sensing of the surface temperature of the Great Salt Lake. *Remote Sens, of Environ.*, **113**, 73-81.

Davis, C., T. Warner, E. Astling, and J. Bowers, 1999: Development and application of an operational, relocatable, meso-gammascale weather analysis and forecasting system. *Tellus*, **51A**, 710–727.

Dickson, D. R., J. H. Yepsen, and J. V. Hales, 1965: Saturated vapor pressures over Great Salt Lake brine. *J. Geophys. Res.,* **70,** 500–503.

Dudhia, J., 1989: Numerical study of convection observed during the winter monsoon experiment using a mesoscale two-dimensional model. *J. Atmos. Sci.,* **46**, 3077–3107.

Fast, J. D., M. D. McCorcle, 1991: The effect of heterogeneous soil moisture on a summer baroclinic circulation in the central United States. *Mon. Wea. Rev.*, **119**, 2140–2167.

Fernando, H. J., and Coauthors, 2015: The MATERHORN – Unraveling the intricacies of mountain weather. *Bull. Amer. Meteor. Soc.*, in press.

Foken, T., 2008: The energy balance closure problem: An overview. *Ecol. Appl.*, **18**, 1351–1367.

Fry, J., G. Xian, S. Jin, J. Dewitz, C. Homer, L. Yang, C. Barnes, N. Herold, and J. Wickham, 2011: Completion of the 2006 national land cover database for the conterminous United States, *PE&RS*, **77**, 858-864.

Fujimaki, H., T. Shimano, M. Inoue, and K. Nakane, 2006: Effect of a salt crust on evaporation from a bare saline soil, *Vadose Zone J.*, **5**, 1246–1256.

Gowing, J. W., R. Konukcu, D. A. Rose, 2006: Evaporative flux from a shallow watertable: The influence of a vapour-liquid phase transition. *Journal of Hydrology*, **321**, 77–89.

Hong, S. Y., Y. Noh, and J. Dudhia, 2006: A new vertical diffusion package with an explicit treatment of entrainment processes. *Mon. Wea. Rev.*, **134**, 2318–2341.

Hu, X-M., J. W. Nielsen-Gammon, and F. Zhang, 2010a: Evaluation of three planetary boundary layer schemes in the WRF model. *J. Appl. Meteor. Climatol.*, **49**, 1831–1844.

Jensen, D. D., D. F. Nadeau, S. W. Hoch, E. R. Pardyjak, 2015: Observations of near-surface heat flux and temperature profiles through the early evening transition over contrasting surfaces. *Boundary-Layer Meteorology*, in press.

Kain, J. S., 2004: The Kain-Fritsch Convective Parameterization: An update. *Journal of Applied Meteorology*, **43**, 170-181.

Knievel, J. C., G. H. Bryan, and J. P. Hacker, 2007: Explicit diffusion in the WRF model. *Mon. Wea. Rev.*, **135**, 3808–3824.

Larson, K. M., E. E. Small, E. Gutmann, A. Bilich, J. Braun, and V. Zavorotny, 2008: Use of GPS receivers as a soil moisture network for water cycle studies, *Geophys. Res. Lett.*, **35**, L24405.

Liu, J., C. Schaaf, A. Strahler, Z. Jiao, Y. Shuai, Q. Zhang, M. Roman, J. A. Augustine, and E. G. Dutton, 2009: Validation of Moderate Resolution Imaging Spectroradiometer (MODIS) albedo retrieval algorithm: Dependence of albedo on solar zenith angle. *Journal of Geophysical Research*, **114**, D01106.

Liu, Y., and Coauthors, 2008: The operational mesogamma-scale analysis and forecast system of the U.S. army test and evaluation command. Part I: Overview of the modeling system, the forecast products, and how the products are used. *J. Appl. Meteor. Climatol.*, **47**, 1077–1092.

Malek, E., C. Biltoft, J. Klewicki, B. Giles, 2002: Evaluation of annual radiation and windiness over a playa: Possibility of harvesting the solar and wind energies. *J. Arid Environ.*, **52**, 555–564.

Malek, E., G. E. Bingham, G. D. McCurdy, 2003: Evapotranspiration from the margin and moist playa of a closed desert. *Journal of Hydrology*, **120**, 15–23.

Massey, J. D., W. J. Steenburgh, S. W. Hoch, and J. C. Knievel, 2014: Sensitivity of near-surface temperature forecasts to soil properties over a sparsely vegetated dryland region. *J. Appl. Meteor. Climatol.*, **53**, 1976–1995.

Massey, J. D., W. J. Steenburgh, J. C. Knievel, and W. Y. Y. Cheng, 2015: Regional soil-moisture biases and their influence on WRF model temperature forecasts over the Intermountain West. *To be submitted to Weather and Forecasting.*

McCumber, M. C., and R. A. Pielke, 1981: Simulation of the effects of surface fluxes of heat and moisture in a mesoscale numerical model. *J. Geophys. Res.*, **86**, 9929–9938.

Meng, X., J. P. Evans, and M. F. McCabe, 2014: The influence of inter-annually varying albedo on regional climate and drought. *Climate Dyn.*, **42**,787–803.

Mlawer, E. J., S. J. Taubman, P. D. Brown, M. J. Iacono, and S. A. Clough, 1997: Radiative transfer for inhomogeneous atmospheres: RRTM, a validated correlated-*k* model for the longwave. *J. Geophys. Res.*, **102,** 16663–16682.

Onton, D. J., and W. J. Steenburgh, 2001: Diagnostic and sensitivity studies of the 7 December 1998 Great Salt Lake–Effect Snowstorm. *Mon. Wea. Rev.*, **129**, 1318–1338.

Ookouchi, Y., M. Segal, R. C. Kessler, and R. A. Pielke, 1984: Evaluation of soil moisture effects on the generation and modification of mesoscale circulations. *Mon. Wea. Rev.*, **112,** 2281–2292.

Physick, W. L., and N. J. Tapper, 1990: A numerical study of circulations induced by a dry salt lake. *Mon. Wea. Rev.*, **118,** 1029–1042.

Reda, I. and A. Andreas, 2004: Solar position algorithm for solar radiation applications. *Solar Energy*, **76**, 577–589.

Rife, D. L., T. T. Warner, F. Chen, and E. G. Astling, 2002: Mechanisms for diurnal boundary layer circulations in the great basin desert. *Mon. Wea. Rev.*, **130**, 921–938.

Ruppert, J., C. Thomas, and T. Foken, 2006: Scalar similarity for relaxed eddy accumulation methods. *Boundary-Layer Meteorology,* **120**, 39–63.

Schaaf, C. B., and Coauthors, 2002: First operational BRDF, albedo nadir reflectance products from MODIS. *Remote Sensing of Environment*, **83**, 135–148.

Schaefer, G. L., M. H. Cosh, and T. J. Jackson, 2007: The USDA natural resources conservation service soil climate analysis network (SCAN). *J. Atmos. Oceanic Technol.*, **24**, 2073–2077.

Segal, M. and R. W. Arritt, 1992: Nonclassical mesoscale circulations caused by surface sensible heat-flux gradients. *Bull. Amer. Meteor. Soc.,* **73**, 1593–1604.

Steenburgh, W. J., S. F. Halvorson, and D. J. Onton, 2000: Climatology of lake-effect snowstorms of the Great Salt Lake. *Mon. Wea. Rev.,* **128**, 709–727.

Steeneveld, G. J., T. Mauritsen, E. I. F. de Bruijn, J. Vilà-Guerau de Arellano, G. Svensson, and A. A. M. Holtslag, 2008: Evaluation of limited area models for the representation of the diurnal cycle and contrasting nights in CASES99. *J. Appl. Meteor. Climatol.*, **47**, 869–887.

Stull, R. B., 1988: *An Introduction to Boundary Layer Meteorology*. Kluwer Academic, 670 pp.

Sun, W. Y., and M. G. Bosilovich, 1996: Planetary boundary layer and surface layer sensitivity to land surface parameters. *Boundary-Layer Meteorology*, **77**, 353−378.

Svensson G, and Coauthors, 2011: Evaluation of the diurnal cycle in the atmospheric boundary layer over land as represented by a variety of single-column models: The second GABLS experiment. *Boundary-Layer Meteorology*, **140,** 177–206.

Twine, T. E., W. P. Kustas, J. M. Norman, D. R. Cook, P. R. Houser, T. P. Meyers, J. H. Prueger, P. J. Starks, and M. L. Wesely, 2000: Correcting eddy-covariance flux underestimates over a grassland. *Agricultural and Forest Meteorology,* **103**, 279–300.

Warner, T. T., 2004: *Desert Meteorology*. Cambridge University Press, Cambridge, UK. 595 pp.

CHAPTER 5[8]

EPISODIC DUST EVENTS OF UTAH'S WASATCH FRONT AND ADJOINING REGION

5.1 Abstract

Episodic dust events cause hazardous air quality along Utah's Wasatch Front and dust loading of the snowpack in the adjacent Wasatch Mountains. This paper presents a climatology of episodic dust events of the Wasatch Front and adjoining region that is based on surface weather observations from the Salt Lake City International Airport (KSLC), Geostationary Operational Environmental Satellite (GOES) imagery, and additional meteorological datasets. Dust events at KSLC—defined as any day [mountain standard time (MST)] with at least one report of a dust storm, blowing dust, and/or dust in suspension with a visibility of 10 km or less—average 4.3 per water year (WY: October–September), with considerable interannual variability and a general decline in frequency during the 1930–2010 observational record. The distributions of monthly dust-event frequency and total dust flux are bimodal, with primary and secondary maxima in April and September, respectively. Dust reports are most common in the late afternoon

[8] Chapter 5 is reprinted from the following journal article W. James Steenburgh, Jeffrey D. Massey, and Thomas H. Painter, 2012: Episodic dust events of Utah's Wasatch Front and adjoining region. *J. Appl. Meteor. Climatol.*, **51**, 1654–1669.

and evening. An analysis of the 33 most recent (2001–10 WY) events at KSLC indicates that 11 were associated with airmass convection, 16 were associated with a cold front or baroclinic trough entering Utah from the west or northwest, 4 were associated with a stationary or slowly moving front or baroclinic trough west of Utah, and 2 were associated with other synoptic patterns. GOES imagery from these 33 events, as well as 61 additional events from the surrounding region, illustrates that emission sources are located primarily in low-elevation Late Pleistocene–Holocene alluvial environments in southern and western Utah and southern and western Nevada.

5.2 Introduction

Dust storms have an impact on air quality (Pope et al. 1995; Gebhart et al. 2001), precipitation (Goudie and Middleton 2001), soil erosion (Gillette 1988; Zobeck et al. 1989), the global radiation budget (Ramanathan et al. 2001), and regional climate (Nicholson 2000; Goudie and Middleton 2001). Recent research examining dust-related radiative forcing of the mountain snowpack of western North America and other regions of the world has initiated a newfound interest in dust research (Painter et al. 2007; Flanner et al. 2009; Painter et al. 2010). For example, observations from Colorado's San Juan Mountains indicate that dust loading increases the snowpack's absorption of solar radiation, decreasing seasonal snow-cover duration by several weeks (Painter et al. 2007). Modeling studies further suggest that radiative forcing from increased dust deposition during the past 150 years results in an earlier runoff with reduced annual volume in the upper Colorado River Basin (Painter et al. 2010).

Synoptic and mesoscale weather systems are the primary drivers of global dust emissions and transport. Mesoscale convective systems that propagate eastward from Africa over the Atlantic Ocean produce one-half of the dust emissions from the Sahara Desert, the world's largest aeolian dust source (Swap et al. 1996; Goudie and Middleton 2001). Dust plumes generated by these systems travel for several days in the large-scale easterly flow (Carlson 1979), with human health and ecological impacts across the tropical Atlantic and Caribbean Sea (Goudie and Middleton 2001; Prospero and Lamb 2003). In northeastern Asia, strong winds in the post-cold-frontal environment of Mongolian cyclones drive much of the dust emissions (Yasunori and Masao 2002; Shao and Wang 2003; Qian et al. 2002). The highest frequency of Asian dust storms occurs over the Taklimakan and Gobi Deserts of northern China, where dust is observed 200 days yr−1 (Qian et al. 2002). Fine dust from these regions can be transported to the United States, producing aerosol concentrations that are above National Ambient Air Quality Standards (Jaffe et al. 1999; Husar et al. 2001; VanCuren and Cahill 2002; Fairlie et al. 2007).

In North America, the Great Basin, Colorado Plateau, and Mojave and Sonoran Deserts produce most of the dust emissions (Reynolds et al. 2001; Tanaka and Chiba 2006; see Fig. 5.1 for geographic and topographic locations). Desert land surfaces are naturally resistant to wind erosion because of the presence of physical, biological, and other crusts (Gillette et al. 1980) but are easily disturbed, in some cases leading to increased dust emissions long after the initial disturbance (e.g., Belnap et al. 2009). From alpine lake sediments collected over the interior western United States, Neff et al. (2008) and Reynolds et al. (2010) find dramatically larger dust deposition rates since the mid–

nineteenth century, a likely consequence of land surface disturbance by livestock grazing, plowing of agricultural soils, and other human activities.

Several studies suggest that the synoptic and mesoscale weather systems that generate dust emissions and transport over western North America vary geographically and seasonally. Orgill and Sehmel (1976) identified a spring maximum in suspended dust frequency over the contiguous United States as a whole, which they attributed to cyclonic and convective storm activity, but found that some locations in the Pacific Coast and Rocky Mountain regions have an autumn maximum. Brazel and Nickling (1986, 1987) found that fronts, thunderstorms, cutoff lows, and tropical disturbances (i.e., decaying tropical depressions and cyclones originating over the eastern Pacific Ocean) are the primary drivers of dust emissions in Arizona. The frequency of dust emissions from fronts is highest from late autumn to spring, that from thunderstorms is highest during the summer, and that from cutoff lows is highest from May to June and from September to November. Dust emissions produced by tropical disturbances are infrequent but are likely confined to June–October during which tropical cyclone remnants move across the southwestern United States (Ritchie et al. 2011). For dust events in nearby California and southern Nevada, Changery (1983) and Brazel and Nickling (1987) established linkages with frontal passages and cyclone activity, respectively, with land surface conditions (e.g., soil moisture and vegetation) affecting dust-event seasonality and spatial distribution. In northwestern Nevada, dust storms originating over the Black Rock Desert have been linked to strong winds associated with cold-frontal passages and geostrophic adjustment, with emissions being strongly dependent on antecedent rainfall and soil conditions (Lewis et al. 2011; Kaplan et al. 2011).

Episodic dust events of Utah's Wasatch Front and adjoining region produce hazardous air quality in the Salt Lake City, Utah, metropolitan area and dust loading of the snowpack in the Wasatch Mountains (Fig. 5.2). From 2002 to 2010 in Utah, wind-blown dust events contributed to 13 exceedances of the National Ambient Air Quality Standard for particulate matter of less than 2.5 (PM2.5) or 10 (PM10) μm in diameter (T. Cruickshank, Utah Division of Air Quality, 2011, personal communication). Dust loading in the Wasatch Mountains affects a snowpack that serves as the primary water resource for approximately 400 000 people and enables a $1.2 billion winter sports industry, known internationally for the "Greatest Snow on Earth" (Bear West Consulting Team 1999; Steenburgh and Alcott 2008; Gorrell 2011).

This paper examines the climatological characteristics (or "climatology") of episodic dust events of the Wasatch Front and adjoining region. The available meteorological data illustrate that dust events occur throughout the historical record and that they are associated primarily with synoptic cold fronts, baroclinic troughs (i.e., a pressure trough with a modest temperature gradient that is insufficiently strong to be called a front; Sanders 1999), and airmass convection. Emission sources are located primarily in low-elevation Late Pleistocene–Holocene alluvial environments in southern and western Utah and southern and western Nevada.

5.3 Data and Methods

5.3.1 Long-Term Climatology

Our long-term dust-event climatology derives from hourly surface weather observations from the Salt Lake City International Airport (KSLC), which we obtained

from the Global Integrated Surface Hourly Database (DS-3505) at the National Climatic Data Center (NCDC). KSLC is located in the Salt Lake Valley just west of downtown Salt Lake City and the Wasatch Mountains (Fig. 5.1) and provides the longest quasi-continuous record of hourly weather observations in northern Utah. The analysis covers the 1930–2010 water years (October–September) when 97.9% of all possible hourly observations are available.[9]

The hourly weather observations included in DS-3505 derive from multiple sources, with decoding and processing occurring at either operational weather centers or the Federal Climate Complex in Asheville, North Carolina (Lott et al. 2001; NCDC 2008). Studies of dust events frequently use similar datasets (e.g., Orgill and Sehmel 1976; Hall 1981; Changery 1983; Nickling and Brazel 1984; Brazel and Nickling 1986, 1987; Brazel 1989; Qian et al. 2002; Yasunori and Masao 2002; Shao and Wang 2003; Shao et al. 2003; Song et al. 2007). Nevertheless, although hourly weather observations are useful for examining the general climatological and meteorological characteristics of dust events, they do not quantify dust concentrations, making the identification and classification of dust somewhat subjective. Inconsistencies arise from observer biases, changes in instrumentation, reporting guidelines, and processing algorithms. These inconsistencies result in the misreporting of some events (e.g., dust erroneously reported as haze) and limit confident assessment and interpretation of long-term trends and variability.

Consistent with World Meteorological Organization (WMO) guidelines (WMO 2009), the present-weather record in DS-3505 includes 11 dust categories (Table 5.1).

---

[9] Hereinafter, all years in this paper are water years.

During the study period, there were 916 reports of blowing dust (category 7), 178 of dust in suspension (category 6), 7 of dust storm (categories 9, 30–32, and 98), and 1 of dust or sand whirl (category 8) at KSLC. There were no reports of severe dust storm (categories 33–35). Among the reports of blowing dust, dust in suspension, and dust storm, there were 69 with a visibility of greater than 6 statute mi (10 km), the threshold currently used by the WMO and national weather agencies for reporting blowing dust or dust in suspension (Shao et al. 2003; OFCM 2005). Because these events are weak or may be erroneous, they were removed from the analysis. They include all but one of the seven dust-storm reports. The report of dust or sand whirl was also removed because we are interested in widespread events rather than localized dust whirl(s) (also called "dust devils"). The resulting long-term dust-event climatology is based on the remaining 1033 reports. A dust event is any day [mountain standard time (MST)] with at least one such dust report.

5.3.2 Synoptic Classification of Recent Dust Events

Our analysis of the synoptic conditions contributing to Wasatch Front dust events concentrates on events at KSLC during the most recent 10-yr period (2001–10). This enables the use of modern satellite and reanalysis data and limits the number of events, making the synoptic classification of each event feasible.

Resources used in our manual analysis to subjectively classify dust events and prepare case studies include the North American Regional Reanalysis (NARR), Geostationary Operational Environmental Satellite (GOES) imagery, Salt Lake City (KMTX) radar imagery, and hourly KSLC surface weather observations and remarks

from DS-3505. The NARR is a 32-km, 45-layer reanalysis for North America that is based on the National Centers for Environmental Predication (NCEP) Eta Model and data assimilation system (Mesinger et al. 2006). Relative to the European Centre for Medium-Range Weather Forecasts Interim Re-Analysis (ERA-Interim) and NCEP–National Center for Atmospheric Research (NCAR) reanalysis, the NARR better resolves the complex terrain of the Intermountain West but still has a poor representation of the basin-and-range topography over Nevada (Jeglum et al. 2010). We obtained the NARR data from the National Oceanic and Atmospheric Administration (NOAA) Operational Model Archive Distribution System (NOMADS) at NCDC (online at http://nomads.ncdc.noaa.gov/#narr_datasets), the level-II KMTX radar data from NCDC (online at http://www.ncdc.noaa.gov/nexradinv/), and the GOES data from the NOAA Comprehensive Large Array–Data Stewardship System (CLASS; online at http://www.class.ncdc.noaa.gov).

5.3.3 Dust Emission Sources

We identify dust emission sources during 2001–10 using a dust-retrieval algorithm applied to GOES data. Because the algorithm only works in cloud-free areas and many dust events occur in conjunction with cloud cover, we expand the number of events to include those identified in 1) DS-3505 reports from stations in the surrounding region with at least 5 years of hourly data [Delta, Utah (KU24); Elko, Nevada (KEKO); and Pocatello, Idaho (KPIH); see Fig. 5.1]; 2) the authors' personal notes, which derive from weather analysis over the past several years and include events identified visually in the Salt Lake Valley or using satellite imagery from the surrounding region; and 3) Utah

Avalanche Center annual reports. This analysis is thus not specific to KSLC but does identify emissions sources that contribute to dust events in the region.

The dust-retrieval algorithm is a modified version of that used by Zhao et al. (2010, p. 2349) to detect dust over land with Moderate Resolution Imaging Spectroradiometer (MODIS) data, which uses brightness temperature T_b from three infrared channels (3.9, 11, and 12 μm) and reflectance from four visible channels (0.47, 0.64, 0.86, and 1.38 μm). GOES has three corresponding infrared channels (3.9, 10.7, and 12 μm) but only one visible channel (0.65 μm). Therefore, we use an albedo of 0.25 or greater in the 0.65-μm visible channel to screen for clouds. Then, we substitute the GOES 10.7-μm channel for the MODIS 11-μm channel and identify the existence of dust if $T_b(3.9\ \mu m) \leq T_b(10.7\ \mu m)$ and $T_b(10.7\ \mu m) - 10\ K \geq T_b(12\ \mu m)$. These thresholds are slightly modified from those used by Zhao et al. (2010) and were selected through experimentation and comparison with dust detected visually and using the Zhao et al. (2010) technique applied to MODIS imagery from several events. Because uncertainties arise when the sun angle is low and when dust is near cloud edges, the algorithm is applied approximately every 15 min during the daylight hours (0700–1900 MST), with plume origin and orientation identified subjectively. Because the footprint of the GOES infrared channels is 4 km and the algorithm fails to identify shallow dust (Zhao et al. 2010), the plume origin is approximate.

5.4 Results

5.4.1 Long-Term Climatology

Dust events at KSLC occur throughout the historical record, with an average of 4.3 per water year (Fig. 5.3). Considerable interannual variability exists, with no events reported in seven years (1941, 1957, 1981, 1999, 2000, 2001, and 2007) and a maximum of 15 in 1934. No effort was made to quantify or assess long-term trends or interdecadal/interannual variability given the subjective nature of the reports and changes in observers, observing methods, and instrumentation during the study period. The general decline in dust-event frequency, however, is broadly consistent with a decrease in mass accumulation rates related to dust deposition in alpine lakes of western Colorado following the passage of the Taylor Grazing Act of 1934 (Neff et al. 2008).

On the basis of current weather-observing practices (Glickman 2000; Shao and Wang 2003), the minimum visibility when dust is reported meets the criteria for blowing dust [1 km (⅝ statute mi) < visibility ≤ 10 km (6 statute mi)], a dust storm [0.5 km (statute mi) < visibility ≤ 1 km (⅝ statute mi)], or a severe dust storm [visibility ≤ 0.5 km (statute mi)] in 95.4%, 2.6%, and 2.0% of the dust events, respectively (Fig. 5.4).[10] Therefore, only a small fraction of the dust events and observations meet the criteria for dust storm or severe dust storm.

To integrate the effects of KSLC event severity, frequency, and duration, we first estimate the dust concentration C (μg m^{-3}), for each dust report following Eqs. (6) and (7) of Shao et al. (2003):

$$C = 3802.29 D_v^{-0.84} \qquad D_v < 3.5km$$

[10] The visibility observations are taken and stored in statute miles, but approximate metric thresholds are used hereinafter.

$$C = exp(-0.11D_v + 7.62) \quad D_v \leq 3.5km$$

where D_v is the visibility. Multiplying C by the sustained wind speed (currently a 2-min average, although the averaging period may have varied during the observational record) yields the scalar dust flux, which after time integration yields an estimate for the total dust flux during the period of interest. On an annual basis, the total dust flux averages 399.4 g m^{-2}, with a maximum of 2810.2 g m^{-2} in 1935 (Fig. 5.5). Because it integrates event severity, frequency, and duration, the annual total dust flux provides a somewhat different perspective from the annual number of dust events (cf. Figs. 5.3 and 5.5). For example, 1934 featured the most dust events, but the greatest total dust flux occurred in 1935. In 2010, there were only two dust events, but they were major events that produced a decadal-scale maximum in total dust flux. Nevertheless, the annual total dust flux exhibits an overall decline, similar to event frequency.

The monthly distribution of dust events is bimodal, with primary and secondary peaks in April and September, respectively (Fig. 5.6). Similar peaks are observed in the mean monthly total dust flux, but with an additional peak in January (Fig. 5.7). This January peak is surprising, but it results primarily from an unusually strong multiday event in January of 1943 that contributed to 83% of the January monthly mean. In the summer, the mean monthly near-surface minimum is distinctly lower relative to the dust-event frequency (cf. Figs. 5.6 and 5.7), suggesting that summer dust events are shorter and weaker. For March–May, which usually encompasses the climatological peak in snowpack snow water equivalent and the onset of the spring runoff, the mean monthly total dust flux is 237 g m^{-2}, or 59% of the mean annual total dust flux.

Similar bimodal or modal distributions with a primary or single spring dust peak have been identified in the Taklimakan desert of China (Yasunori and Masao 2002), southern Great Plains of the United States (Stout 2001), Mexico City, Mexico (Jauregui 1989), and the Canadian prairies (Wheaton and Chakravarti 1990). The spring peak appears to be the result of a high frequency of wind events driven by cyclones and fronts passing over a recently dried, erodible land surface. Indeed, the bimodal distributions of dust events and mean monthly total dust flux at KSLC are very similar to that of cold fronts and cyclones in the Intermountain West, which are strongest and most frequent in the spring and have a secondary peak in the autumn (Shafer and Steenburgh 2008; Jeglum et al. 2010). These cold fronts and cyclones produce persistently strong winds that have been implicated in sand transport and dune morphology (Jewell and Nicoll 2011) and are capable of generating dust emissions and transport during favorable land surface conditions. In fact, dust was reported at KSLC within 3 h of the passage of 12 of the 25 strongest cold fronts identified by Shafer and Steenburgh (2008).

The mean sustained wind speed during dust reports at KSLC is 11.6 m s^{-1} (with a standard deviation of 4.0 m s^{-1}), slightly higher than the 8.5 and 9.29 m s^{-1} found by Holcombe et al. (1997) for Yuma, Arizona, and Blythe, California, respectively. Therefore, we use 10 m s^{-1} as an approximate threshold velocity for dust emissions and transport assuming favorable boundary layer and land surface conditions. At KSLC, reports of sustained winds $\geq$ 10 m s^{-1} are most common in March and April, with additional, but weaker maxima in August and January (Fig. 5.8). The March and April peak resembles the springtime peak in dust events and mean monthly total dust flux, but the lack of an autumn secondary maximum and winter minimum suggests that other

factors related to the spatial scale of the strong winds (e.g., convective vs. synoptically driven), and seasonal changes to vegetation, soil conditions, and soil moisture (Gillette 1999; Neff et al. 2008; Belnap et al. 2009) contribute to the seasonality of dust events and total dust flux.

Dust reports exhibit a strong diurnal cycle and are most common in the late afternoon and evening hours (Fig. 5.9), as observed in other regions (Jauregui 1989; N'Tchayi Mbourou et al. 1997). The frequency of sustained winds ≥ 10 m s^{-1} at KSLC is about 3 times as high in the afternoon as in the morning (Fig. 5.10), which is consistent with the development of the daytime convective boundary layer. The peak for sustained winds ≥ 10 m s^{-1} occurs at 1400 MST, 4 h earlier than the peak in dust reports, a likely consequence of the time needed for dust to travel from its sources to KSLC.

The frequency distribution of wind directions during dust events is bimodal, with peaks at southerly and north-northwesterly (Fig. 5.11). About 49% of the time, the wind is from the south-southwest through the south-southeast, and about 29% of the time the wind is northwesterly through northerly. Total dust flux is also greatest for winds from the south-southwest through south-southeast (Fig. 5.12).

5.4.2 Recent (2001–10) Events

To classify dust events synoptically, we concentrate on 2001–10, which enables the use of modern reanalysis, satellite, and radar data. The monthly frequency distribution of the 33 dust events during this period resembles that of the long-term climatology except for a disproportionately high number of summer events (cf. Figs. 5.6 and 5.13).

The 33 recent dust events were classified subjectively into one of four groups depending on the primary synoptic conditions responsible for the dust emissions and transport: 1) airmass convection, 2) a cold front or baroclinic trough entering Utah from the west or northwest, 3) a stationary or slowly moving front or baroclinic trough to the west or northwest of Utah, and 4) other synoptic conditions (Table 5.2). The 11 (33%) events generated by airmass convection featured a thunderstorm, thunderstorm in the vicinity, or squall comment in the DS-3505 reports within an hour of the dust observation, and/or nearby convection in satellite or radar imagery, but no significant large-scale temperature gradient at 700 hPa. These events tended to be short lived (usually less than 2 h) and all occurred between mid-May and mid-September. For example, at 1600 MST 19 May 2006, KSLC observed a 5 m s^{-1} southerly wind but KMTX radar imagery showed strong convection just to the south (Fig. 5.14a; KSLC observation not shown). The passage of a convective outflow boundary (i.e., gust front; Wakimoto 1982) at KSLC at 1607 MST was accompanied by south-southwest winds of 24 m s^{-1} with gusts to 28 m s^{-1}, blowing dust, and a visibility of 6.4 km. By 1624 MST, blowing dust was no longer reported. A lack of strong flow and baroclinity at 700 hPa over northern Utah during this period further supports the classification of this event as airmass convection (Fig. 5.14b).

The 16 (48%) recent events produced by a cold front or baroclinic trough from the west or northwest featured at least one dust report at KSLC within 3 h of the cold-frontal or baroclinic-trough passage and a distinct frontal cloud band in visible satellite images. Thirteen of these events accompanied a cyclone over the Great Basin or adjoining northwestern United States as based on the existence of a closed 850-hPa isohypse at 30-

m intervals, although dust reports at KSLC are concentrated around the timing of the accompanying frontal or baroclinic-trough passage [Fig. 5.15; see West and Steenburgh (2010) for a detailed case study of one of these 13 events (15 Apr 2002)]. Of the 16 events, 4 reported dust more than 3 h before the frontal passage, 8 reported dust within the 3 h before frontal passage, 14 reported dust within the 3 h after the frontal passage, and 2 reported dust more than 3 h after the frontal passage. A representative example occurred on 10 May 2004, when strong southerly–southwesterly flow ahead of a cold front and concomitant pressure trough produced several dust plumes that extended from southwest Utah to the Wasatch Front (Figs. 5.16a–c). Hourly and special aviation routine weather reports (METAR) archived by the MesoWest cooperative networks (Horel et al. 2002) show that dust was first reported at KSLC at 1655 MST, just before the frontal passage, which occurred between the 1655 and 1710 MST observations. The visibility was 8 km, with sustained winds of 18 m s^{-1} and wind gusts to 22 m s^{-1}. The dust-limited visibility dropped to 2.8 km following the frontal passage at 1710 MST, but by 1955 MST the visibility was greater than 10 km and dust was no longer reported. The entrainment of dust into the postfrontal air mass, combined with cold-frontal convergence, appeared to contribute to increased dust concentrations and decreased visibility during and immediately following frontal passage, as occurs in many events.

Strong prefrontal southerly flow within a deep convective boundary layer contributes to dust emissions and transport during these 16 cold-frontal or baroclinic-trough events. In comparison with a 21-day weighted climatology centered on the event dates, the NARR 700-hPa wind speed at KSLC at the time of the initial dust report during these events is skewed to much higher values, with the distribution of flow directions

from 160° to 260° (Figs. 5.17a,b). Maximum boundary layer depths on these dust-event days are skewed toward much higher values than climatological values, with a mode at 5000 m AGL (Fig. 5.17c). As shown by Shafer and Steenburgh (2008), strong winds within a deep convective boundary layer are common during strong Intermountain West cold-frontal events. As noted previously, of the 25 strong Intermountain West cold fronts identified at KSLC by Shafer and Steenburgh (2008, see their Table 1), 12 were accompanied by at least one dust report within 3 h of frontal passage. These results indicate that Intermountain West cold fronts and baroclinic troughs play an important role in regional dust emissions and transport. Further, the frequency of these cold-frontal and baroclinic-trough passages is greatest in the spring when dust-related radiative forcing can have its greatest impact on snowmelt (Painter et al. 2007).

Closely related to the cold-frontal and baroclinic-trough events noted above are four (18%) additional events that were produced by stationary or slowly moving fronts or baroclinic troughs to the west or northwest that remained upstream of KSLC for at least 24 h after the initial dust observation. During these events, dust emissions and transport occur in the strong southerly or southwesterly flow ahead of the frontal or baroclinic trough, as discussed above. One event (30 Aug 2009) may be erroneous since observer comments and satellite imagery indicate that smoke, not dust, likely reduced visibilities.

Two (6%) events were associated with other synoptic conditions. On 16 September 2003, KSLC reported dust in intensifying northwesterly flow as a surface trough and cyclone developed to the south. On 13 March 2005, dust was produced by strong winds following the passage of a cold front from the north. The large-scale evolution of this event resembled that found to contribute to two dust storms originating

over the Black Rock Desert of northwestern Nevada by Lewis et al. (2011) and Kaplan et al. (2011).

The fraction of the total dust flux by event type clearly shows the dominant contribution of cold and quasi-stationary fronts and baroclinic troughs (81%; Fig. 5.18). Although airmass convection produces 11 of the 33 recent events, it only generates 8% of the total dust flux.

5.4.3 Dust Emission Sources

As described in section 2, we use a dust-retrieval algorithm applied to GOES imagery to identify the origin and orientation of dust plumes during the recent dust events. Given that plumes are not identifiable in some events because of cloud cover and/or an insufficient solar zenith angle, we include in this analysis the 33 recent (2001–10) events described above, as well as 61 additional events observed in DS-3505 reports from three weather stations in the surrounding region (Delta, Elko, and Pocatello; see Fig. 5.1) or identified in the authors' notes and annual Utah Avalanche Center reports. After applying the GOES dust-retrieval algorithm, 120 independent dust plumes were subjectively identified during 47 (50%) of the 94 dust events. Airmass convection and cold- or stationary-frontal or baroclinic-trough events with two or fewer dust observations most commonly were without visible plumes.

The origins of the 120 identifiable dust plumes are clustered primarily in low-elevation Late Pleistocene–Holocene alluvial environments in southern and western Utah and southern and western Nevada (Fig. 5.19). These include the Sevier Desert, Sevier Dry Lake Bed, Escalante Desert, Milford Valley, and West Desert of Utah and the Black

Rock Desert, Carson Sink, and Great Basin and Mojave Deserts of Nevada. Since July of 2007, dust emissions from the Milford Valley likely include contributions from the Milford Flat fire scar (Miller et al. 2012). Plumes oriented toward KSLC, the Wasatch Front, and northern Utah originate primarily from southern and western Utah, consistent with what might be inferred from Figs. 5.11, 5.12, and 5.17 given the dominance of southerly flow. On average 2.6 plumes are identified on days with visible plumes, indicating that synoptic conditions that contribute to episodic dust events frequently activate multiple emissions sources. Because of obscuration, these results do not include dust plumes that form beneath existing plumes.

Not all of the dust identified in satellite imagery could be traced to a clear origin as there were 11 examples of broad areal dust emissions. The dust in a majority of these examples originated over western Nevada and moved to the southeast, but there was one event with areal dust emissions over central Utah and another with areal dust emissions over the Snake River Plain.

5.5 Conclusions

Episodic dust events contribute to hazardous air quality and dust loading of the snowpack along Utah's Wasatch Front and adjoining region. Surface weather observations from the Salt Lake City International Airport show that these dust events occur throughout the 1930–2010 study period, with considerable interannual variability. The annual dust-event frequency and total dust flux exhibit a general decline during the study period that is broadly consistent with decreased mass sedimentation rates related to

dust deposition in alpine lakes of western Colorado that followed passage of the 1934 Taylor Grazing Act (e.g., Neff et al. 2008).

The distributions of monthly dust-event frequency and mean total dust flux are bimodal, with a primary peak in spring (April) and a secondary peak in autumn (September) that closely resemble the monthly frequency of strong Intermountain West cold fronts and Intermountain West cyclones (Shafer and Steenburgh 2008; Jeglum et al. 2010). The total dust flux is greatest during periods of strong southerly winds, with a weaker secondary maximum associated with flow from the northwest.

An analysis of 33 recent (2001–10) events shows that 11 were associated with airmass convection, 16 were associated with a cold front or baroclinic trough entering Utah from the west or northwest, 4 were associated with a stationary or slowly moving front or baroclinic trough west of Utah, and 2 were associated with other synoptic patterns. The fraction of total dust flux observed at KSLC is strongly dominated by cold- and quasi-stationary-frontal or baroclinic-trough events, many of which feature strong southerly winds in a deep convective boundary layer.

Subjective analysis of dust plumes identified using GOES imagery indicates that regional dust emission sources during these episodic dust events are clustered primarily in low-elevation Late Pleistocene–Holocene alluvial environments in southern and western Utah and southern and western Nevada. Areas with the greatest concentration of emission sources include the Sevier Desert, Sevier Dry Lake Bed, Escalante Desert, Milford Valley, and West Desert of Utah and the Black Rock Desert, Carson Sink, and Great Basin and Mojave Deserts of Nevada.

These findings are based on the analysis of episodic dust events identified in conventional meteorological observations. Dust emissions, transport, and deposition during other periods may also influence snowpack, soil, and lake-sediment composition over the region. In addition, an important aspect of episodic dust events not investigated here is land surface variability and its contribution to enhanced dust fluxes under climate change (Munson et al. 2011; Okin et al. 2011). Improved understanding of soil moisture, vegetation, and anthropogenic disturbance (e.g., Neff et al. 2005; Reynolds et al. 2007; Belnap et al. 2009; Miller et al. 2012) may help to improve the prediction of these events. Moreover, mitigation efforts in the areas of frequent emissions identified above, especially those in southern and western Utah, may reduce the frequency and severity of episodic dust events over the Wasatch Front and adjoining region. Such mitigation efforts are currently being investigated by regional and federal land and water management agencies.

Table 5.1. The DS-3505 dust-related present-weather categories, along with full and abbreviated descriptions (the latter are used in the text), total number of reports, and number of reports used in the analysis (in parentheses).

Category	Full description	Abbreviated description used in text	Total Reports (Reports used in analysis)
06	Widespread dust in suspension in the air, not raised by wind at or near the station at the time of observation	Dust in suspension	178 (155)
07	Dust or sand raised by wind at or near the station at the time of observation, but no well-developed dust whirl(s) or sand whirl(s), and no duststorm or sandstorm seen	Blowing dust	916 (877)
08	Well developed dust whirl(s) or sand whirl(s) seen at or near the station during the preceding hour or at the time of observation, but no duststorm or sandstorm	Dust whirl(s)	1 (0)
09	Duststorm or sandstorm within sight at the time of observation, or at the station during the preceding hour	Duststorm	2(1)
30	Slight or moderate duststorm or sandstorm has decreased during the preceding hour	Duststorm	1 (0)
31	Slight or moderate duststorm or sandstorm no appreciable change during the preceding hour	Duststorm	1 (0)
32	Slight or moderate duststorm or sandstorm has begun or has increased during the preceding hour	Duststorm	1 (0)
33	Severe duststorm or sandstorm has decreased during the preceding hour	Duststorm	0 (0)
34	Severe duststorm or sandstorm no appreciable change during the preceding hour	Duststorm	0 (0)
35	Severe duststorm or sandstorm has begun or has increased during the preceding hour	Duststorm	0 (0)
98	Thunderstorm combined with duststorm or sandstorm at time of observation, thunderstorm at time of observation	Duststorm	2 (0)

Table 5.2. Date and primary synoptic conditions of recent (2001–10) dust events at KSLC. Abbreviations are AC (airmass convection), CF/BT (cold front or baroclinic trough entering Utah from the west or northwest), SF/BT (stationary or slowly moving front or baroclinic trough to the west or northwest of Utah), and O (other synoptic conditions).

Date	Synoptic Conditions	Date	Synoptic Conditions	Date	Synoptic Conditions
23 Mar 2002	CF/BT	17 Oct 2004	SF/BT	27 Jul 2008	AC
15 Apr 2002	CF/BT	13 Mar 2005	O	31 Aug 2008	CF/BT
1 Jun 2002	AC	13 Apr 2005	CF/BT	4 Mar 2009	CF/BT
16 Sep 2002	AC	16 May 2005	CF/BT	21 Mar 2009	SF/BT
1 Feb 2003	CF/BT	22 Jul 2005	AC	30 Jun 2009	AC
1 Apr 2003	SF/BT	30 Jul 2005	AC	5 Aug 2009	AC
2 Apr 2003	CF/BT	19 May 2006	AC	6 Aug 2009	CF/BT
16 Sep 2003	O	19 Jul 2006	AC	30 Aug 2009	SF/BT
28 Apr 2004	CF/BT	26 Jul 2006	AC	30 Sep 2009	CF/BT
10 May 2004	CF/BT	29 Apr 2008	CF/BT	30 Mar 2010	CF/BT
9 Jul 2004	AC	20 May 2008	CF/BT	28 Apr 2010	CF/BT

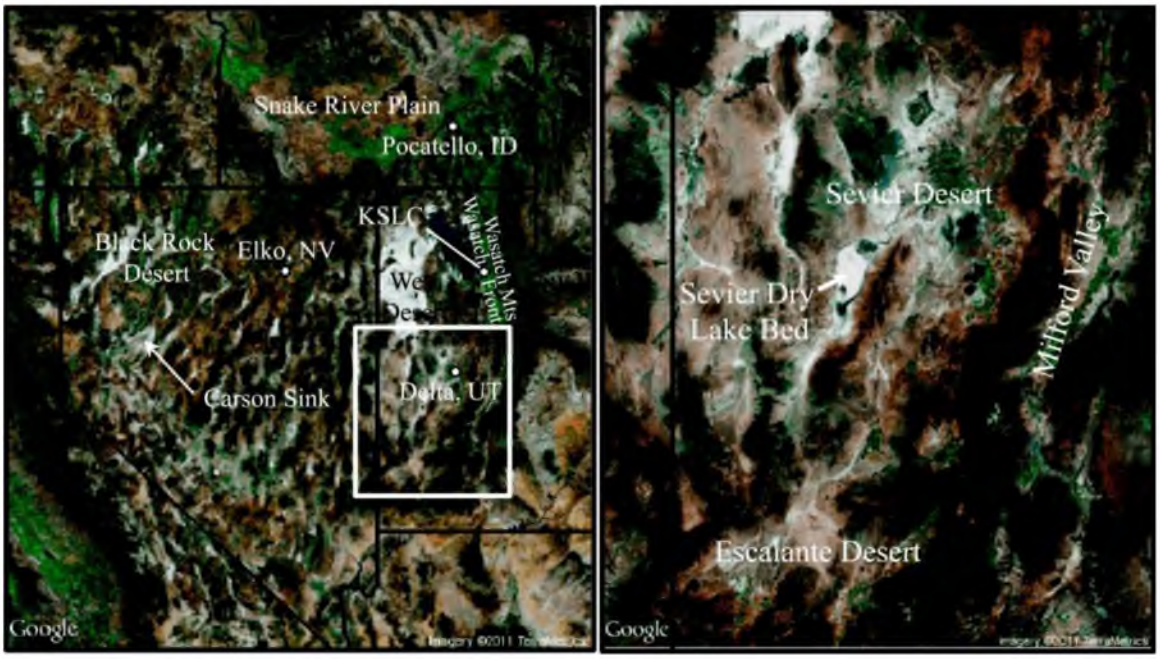

Fig. 5.1. Google Earth image of the Intermountain West with geographic features that are discussed in the text annotated. The inset box in the left panel shows the location of the right panel, which encompasses the Sevier Desert, Sevier Dry Lake Bed, Escalante Desert, and Milford Valley region. [©2011 Google; imagery ©2011 TerraMetrics.]

Fig. 5.2. A snowpit from Alta, Utah, on 30 Apr 2009 that exhibits dust layers from episodic dust events.

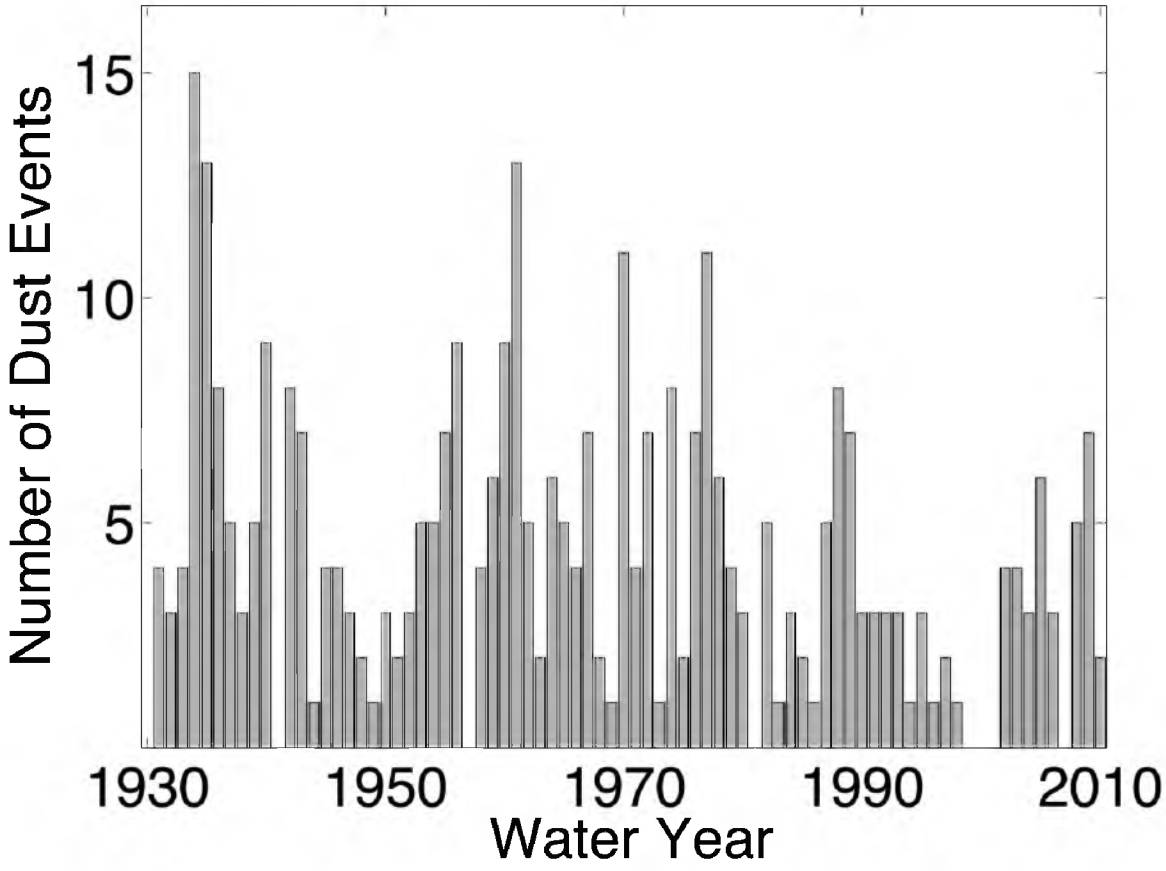

Fig. 5.3. Number of dust events at KSLC by water year.

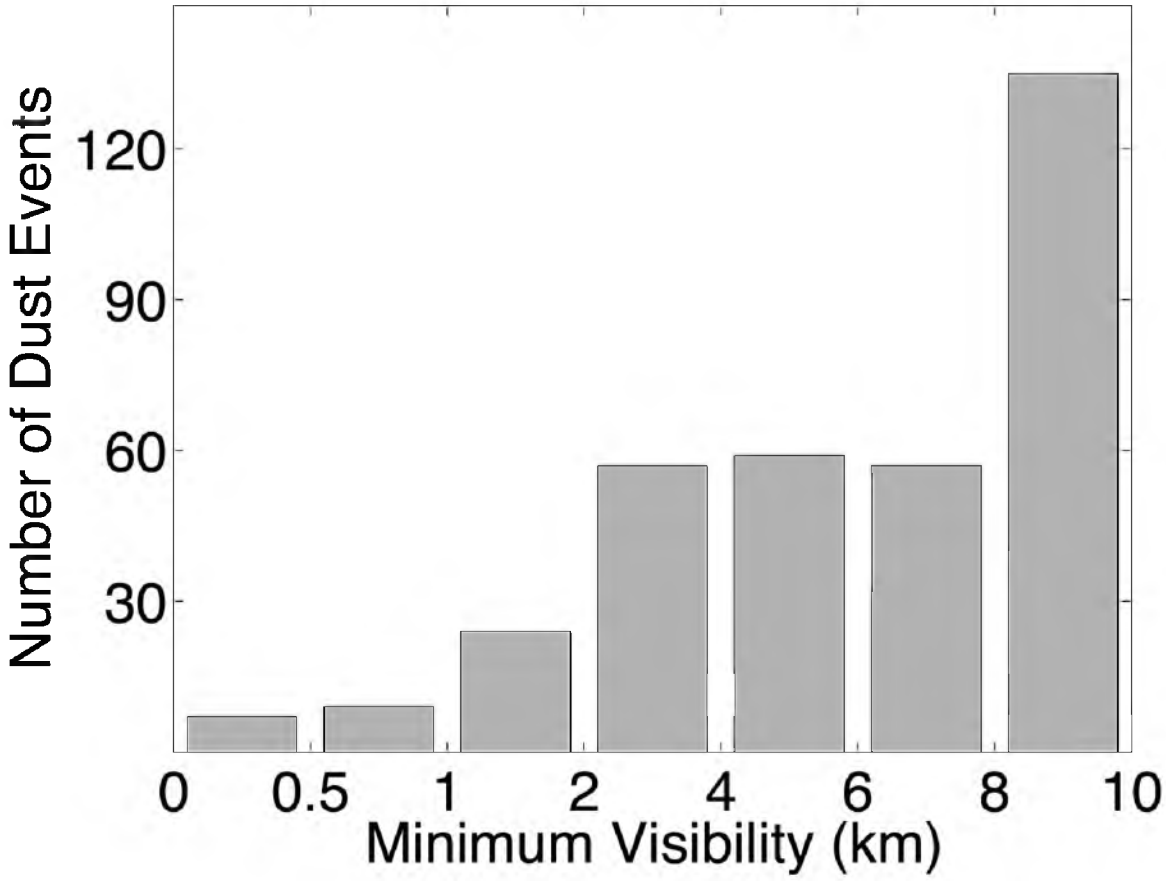

Fig. 5.4. Minimum visibility (km) during KSLC dust events

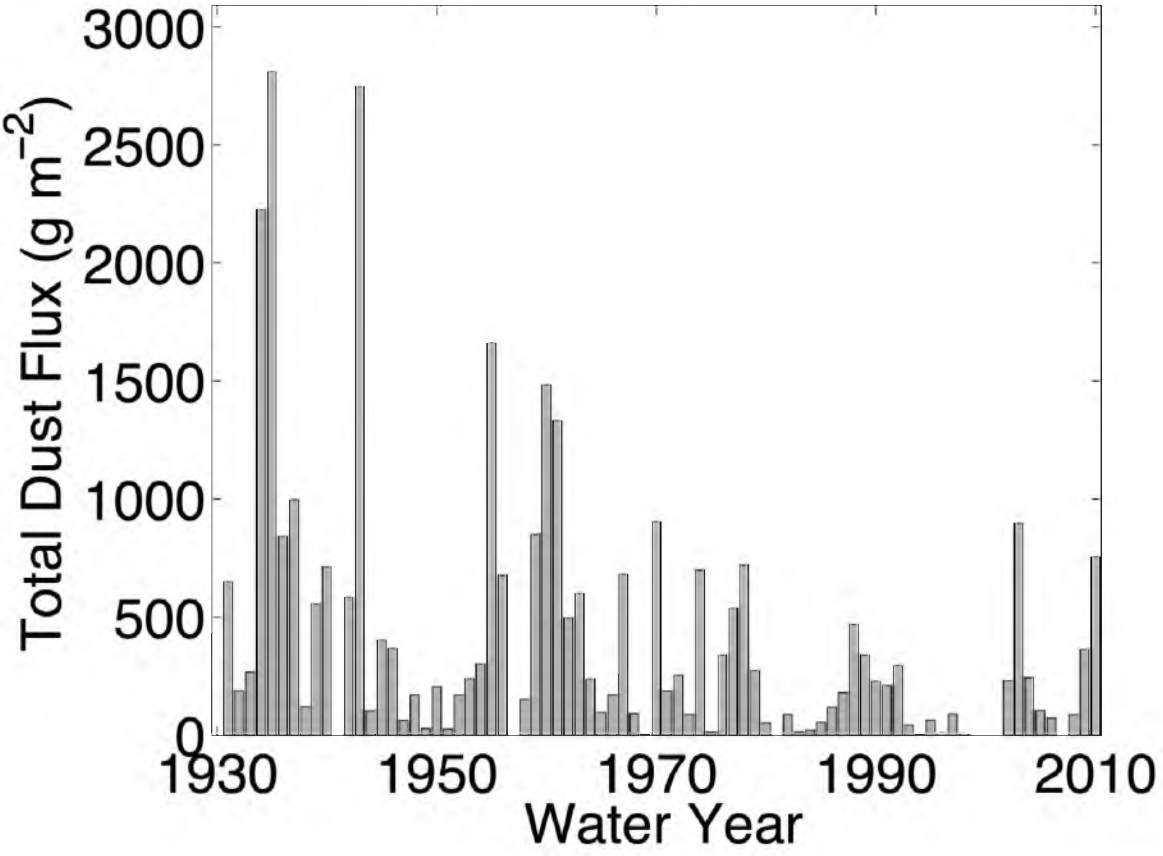

Fig. 5.5. Total dust flux during KSLC dust events by water year.

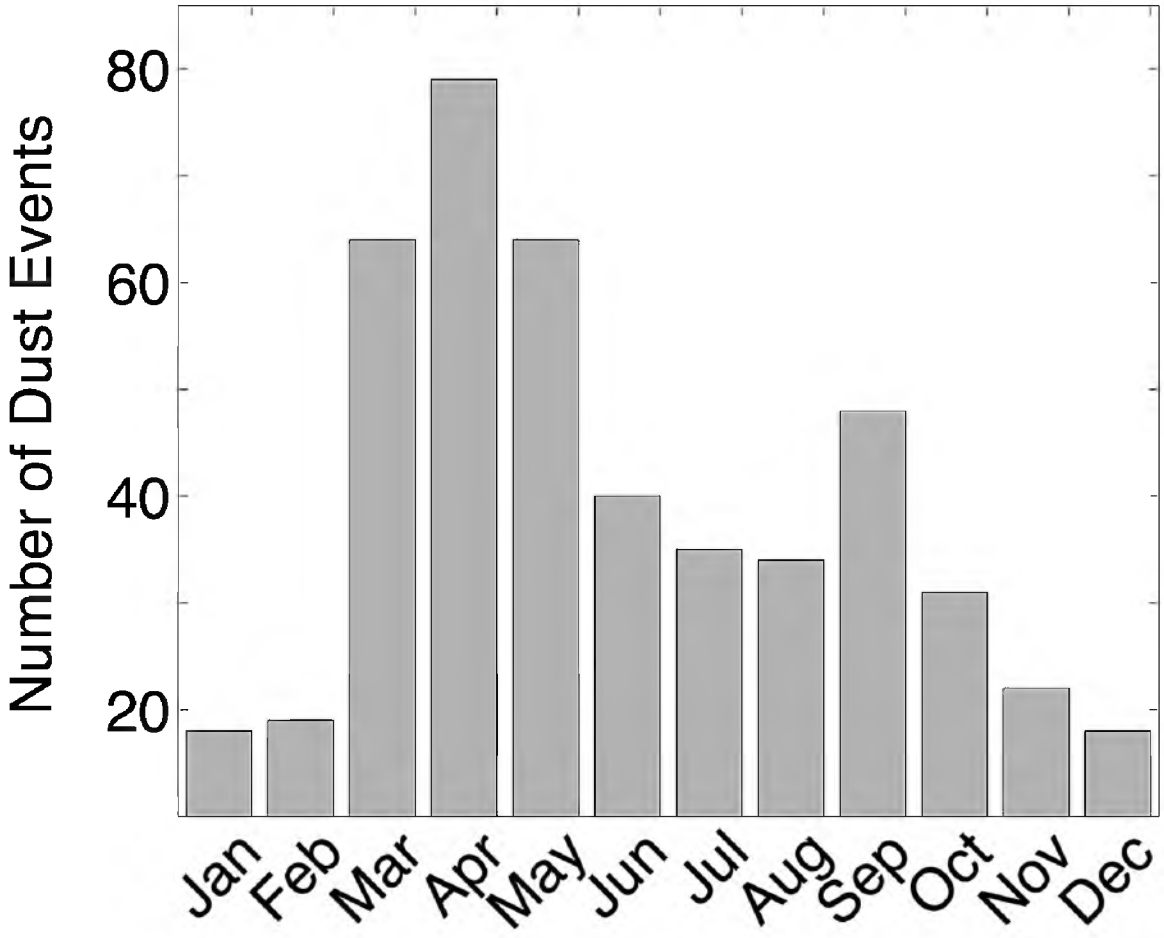

Fig. 5.6. Number of dust events at KSLC by month.

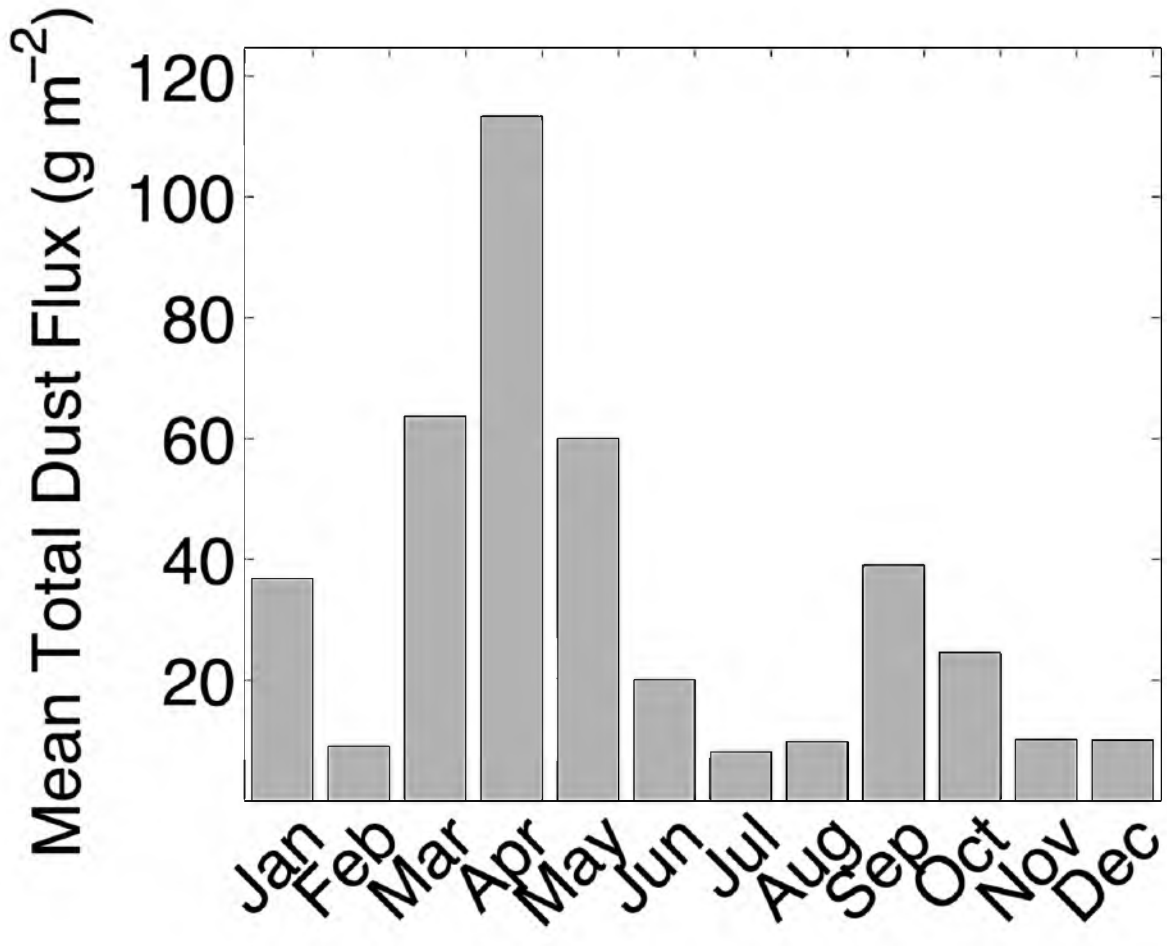

Fig. 5.7. Mean monthly total dust flux during KSLC dust events.

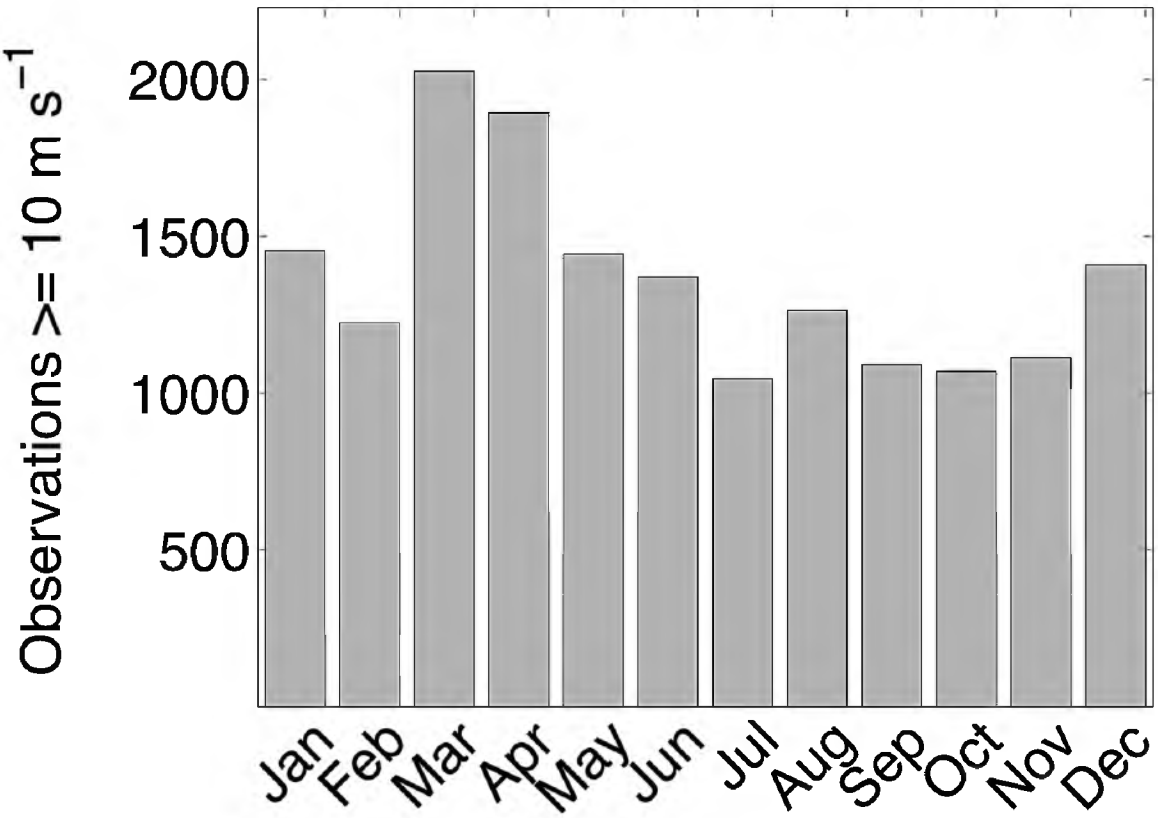

Fig. 5.8. Number of observations at KSLC with a sustained wind $\geq$ 10 m s^{-1} by month.

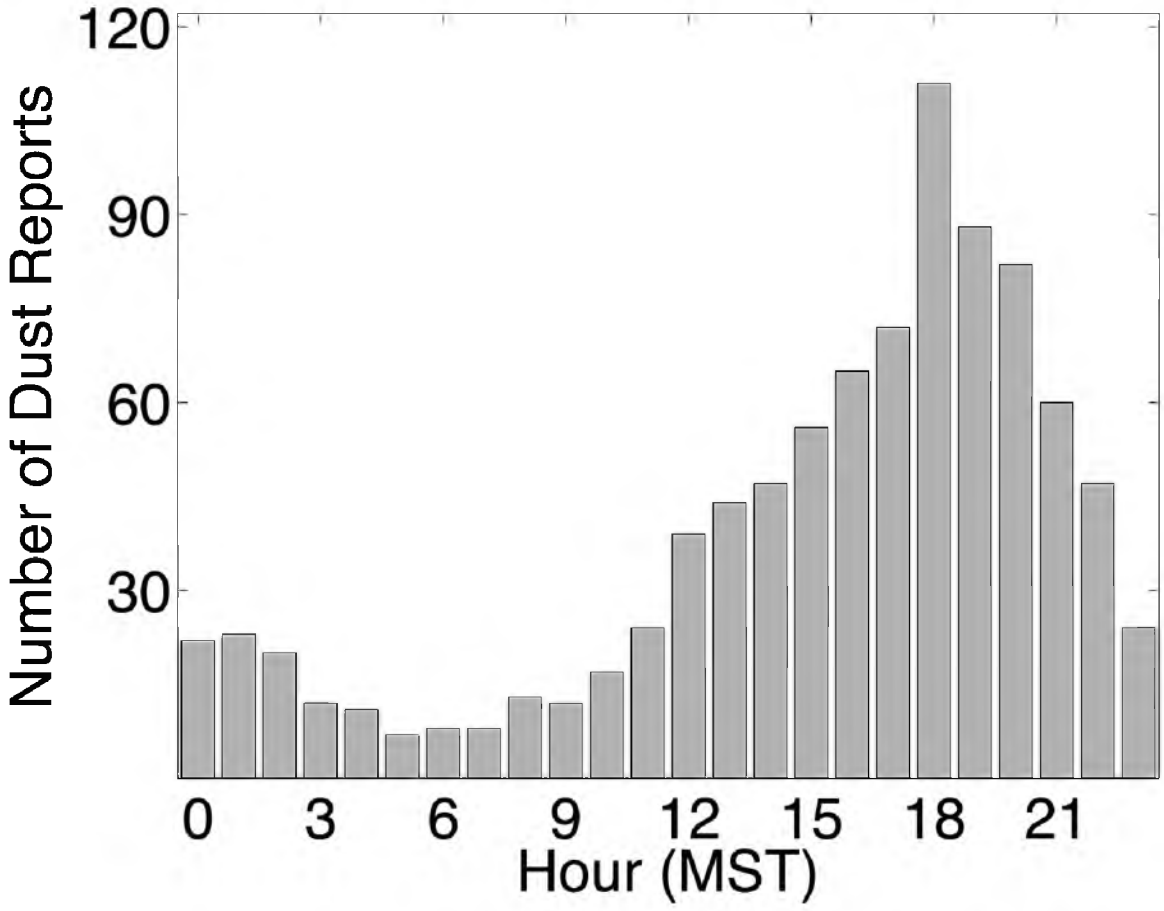

Fig. 5.9. Number of dust reports at KSLC by hour (MST).

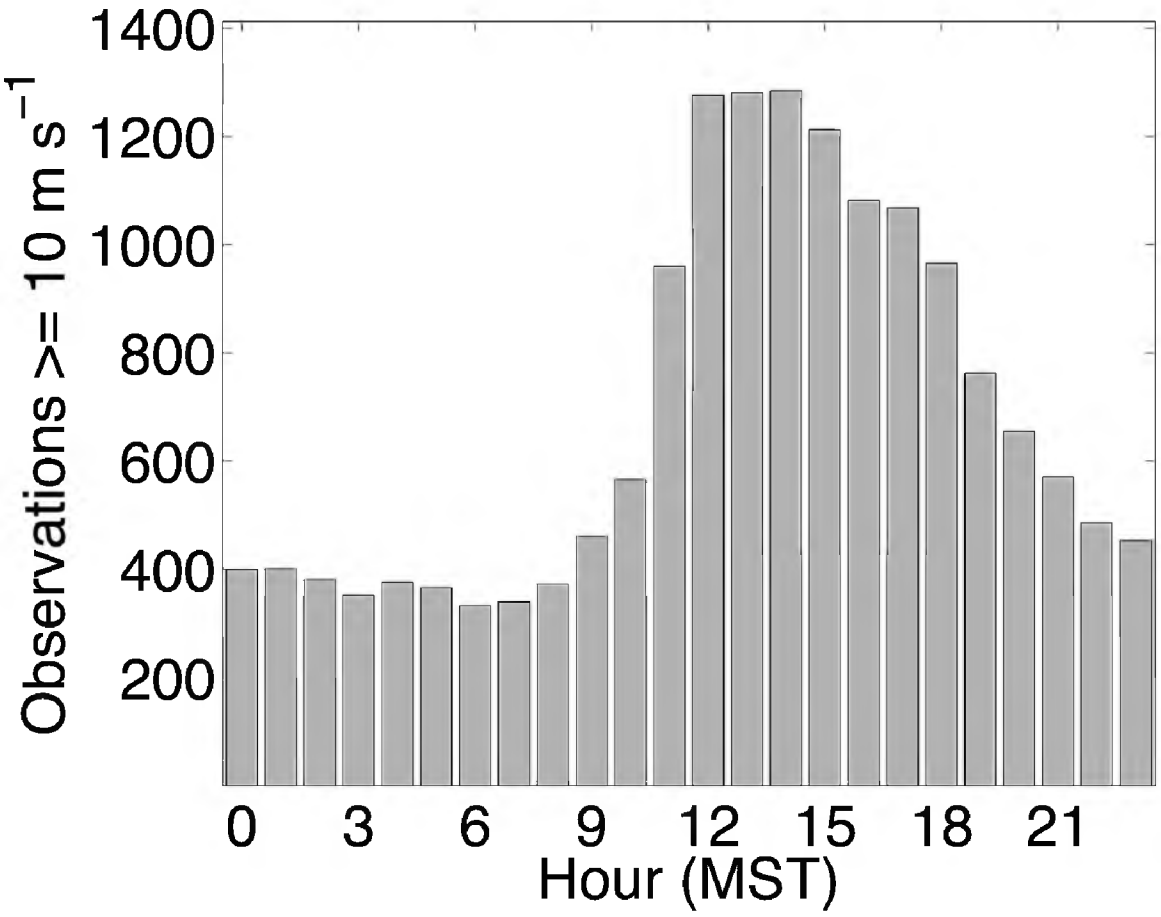

Fig. 5.10. Number of observations at KSLC with a sustained wind $\geq$ 10 m s^{-1} by hour (MST).

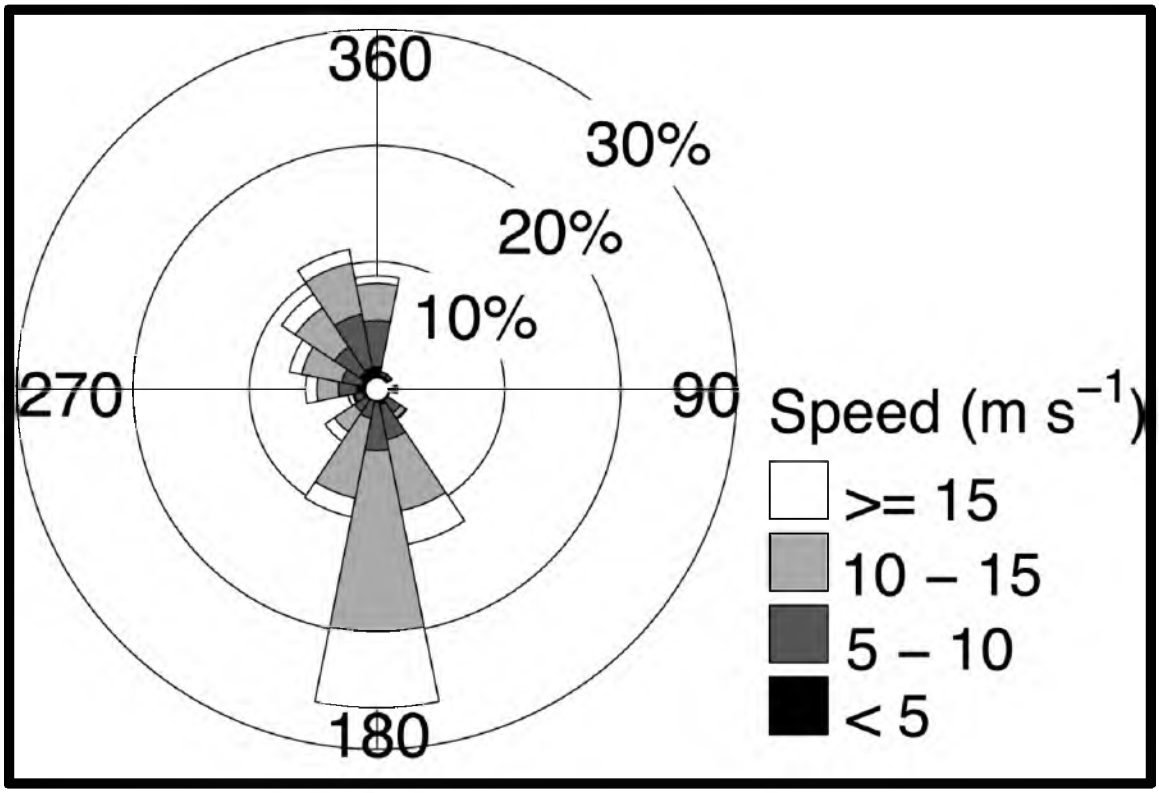

Fig. 5.11. Wind rose for KSLC dust reports.

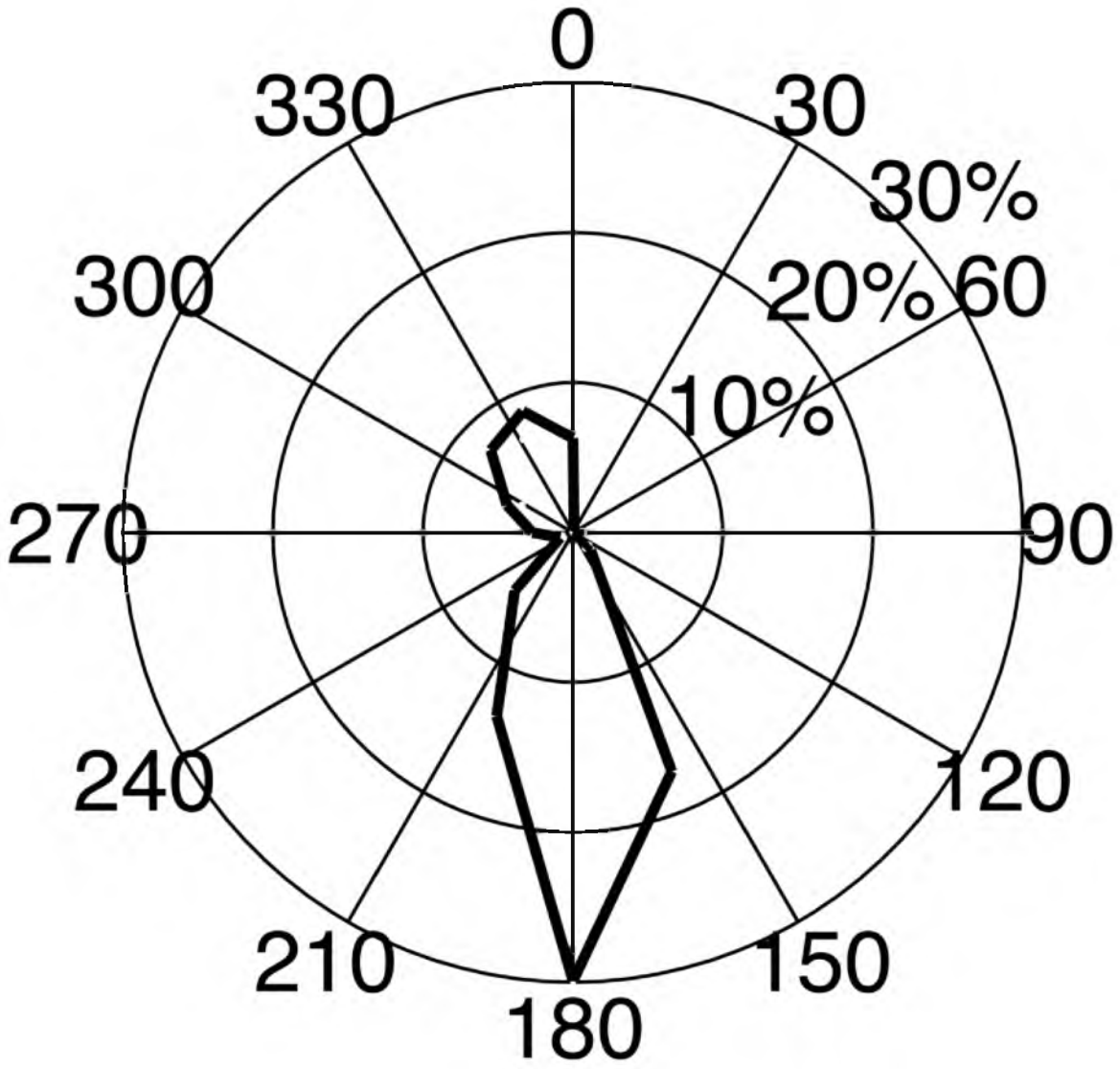

Fig. 5.12. Fraction (%) of total dust flux as a function of wind direction at KSLC.

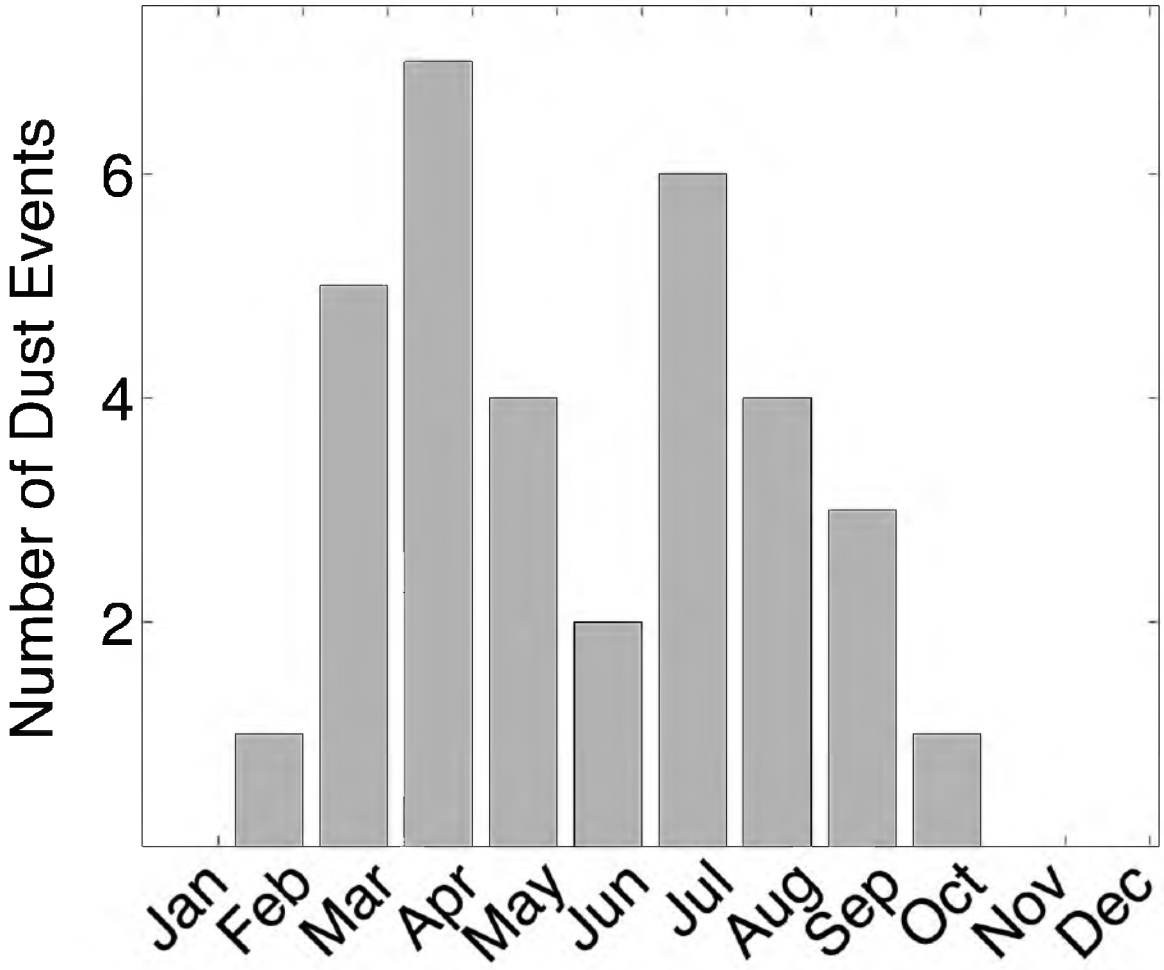

Fig. 5.13. Number of recent (2001–10) dust events at KSLC by month.

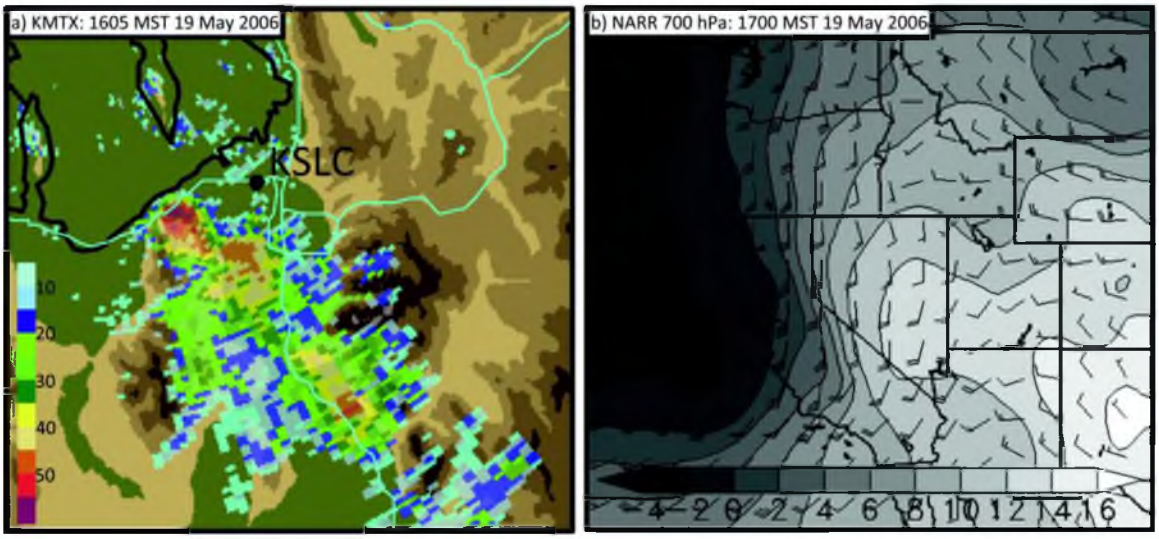

Fig. 5.14. Meteorological conditions during the 19 May 2006 dust event: (a) 1605 MST KMTX 0.5° radar reflectivity (dBZ; color scale at lower left) and topography (color filled with transitions at 1350, 1700, 2050, and 2400 m) and (b) 1700 MST NARR 700-hPa temperature (shaded; scale at bottom) and wind (full and half barb denote 2.5 and 5 m s^{-1}, respectively).

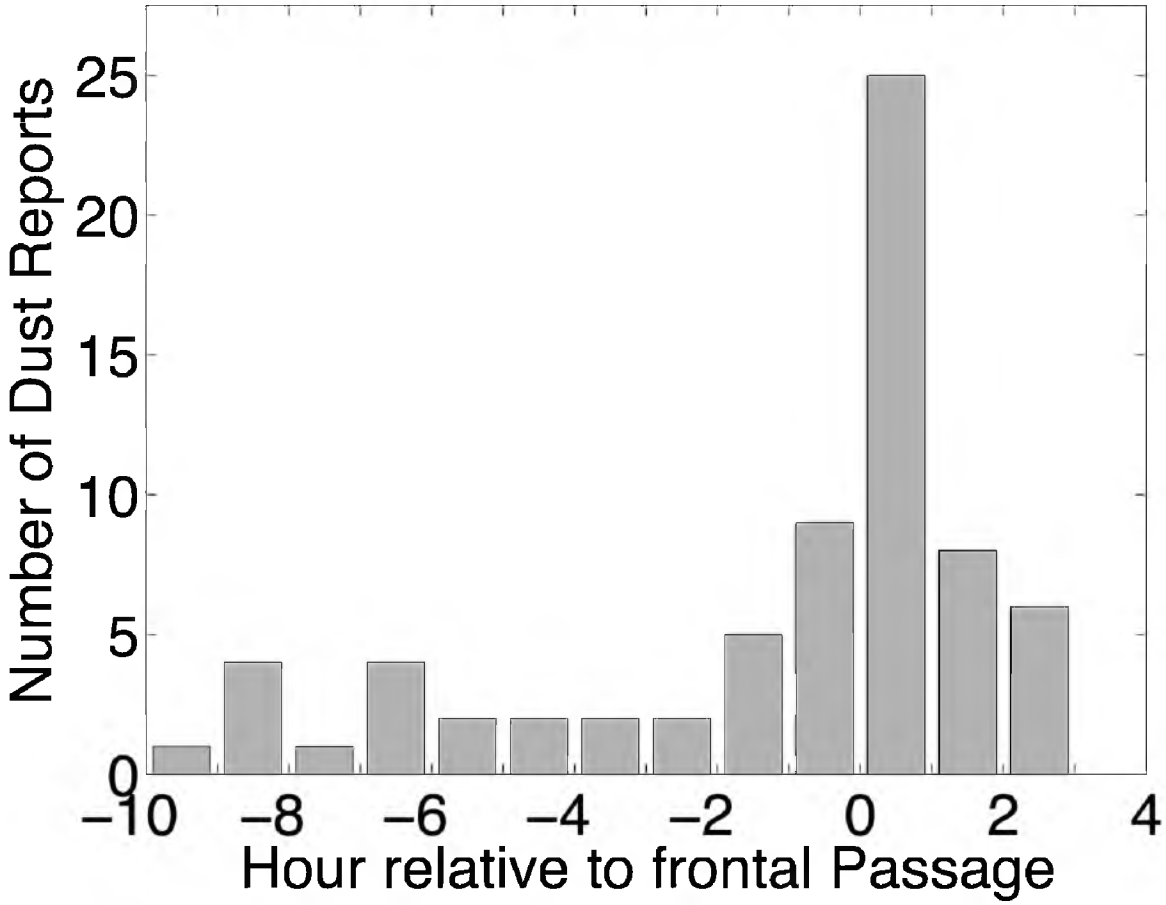

Fig. 5.15. Number of dust reports relative to frontal passage during recent (2001–10) dust events at KSLC with a cold-frontal or baroclinic-trough passage from the west or northwest.

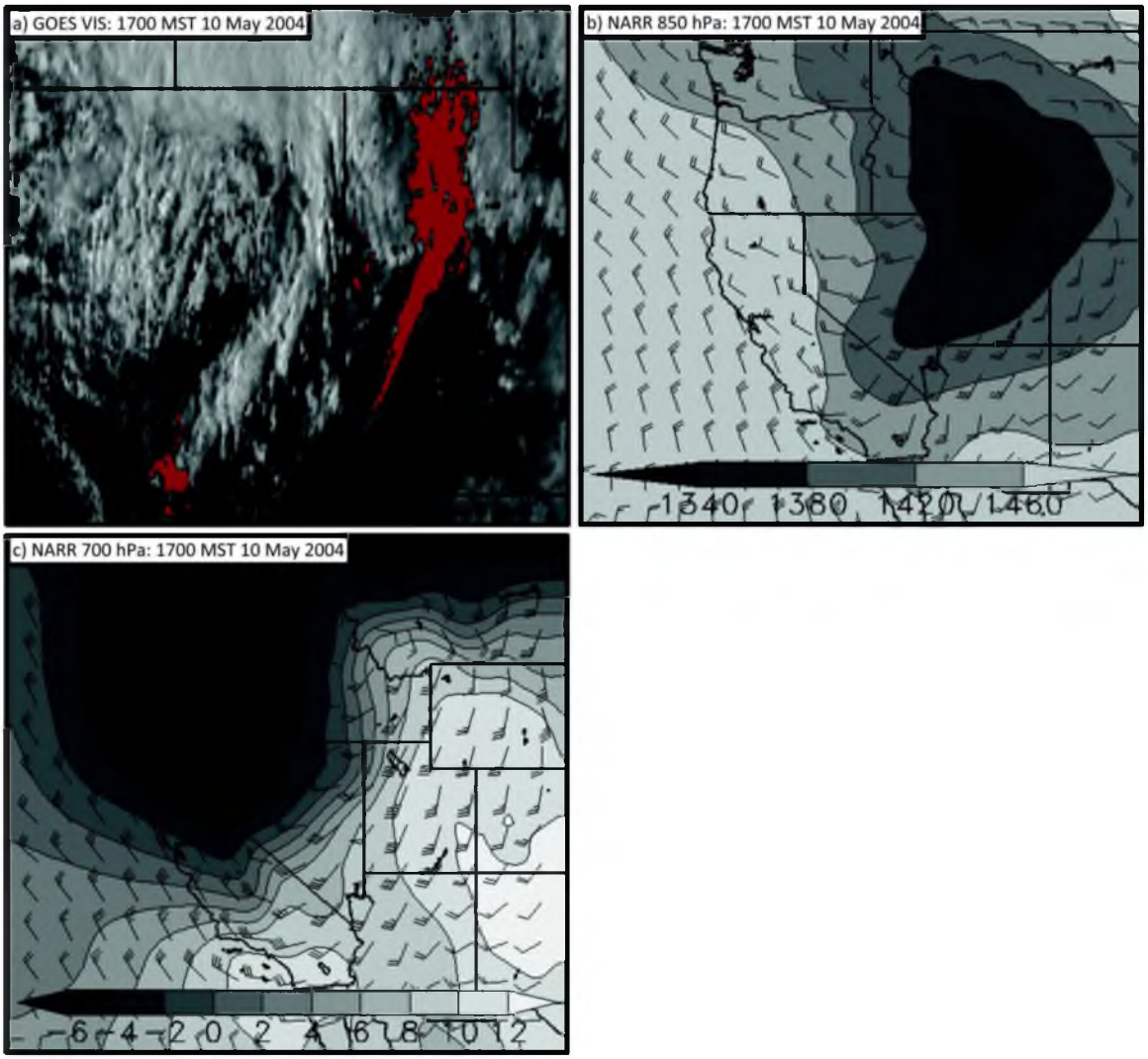

Fig. 5.16. Meteorological conditions at 1700 MST during the 10 May 2004 dust event: (a) GOES visible satellite imagery with dust identified in red, (b) NARR 850-hPa geopotential height (m; shaded, with scale at bottom) and wind (full and half barb denote 2.5 and 5 m s^{-1}, respectively), and (c) NARR 700-hPa temperature (°C; shaded, with scale at bottom) and wind [as in (b)].

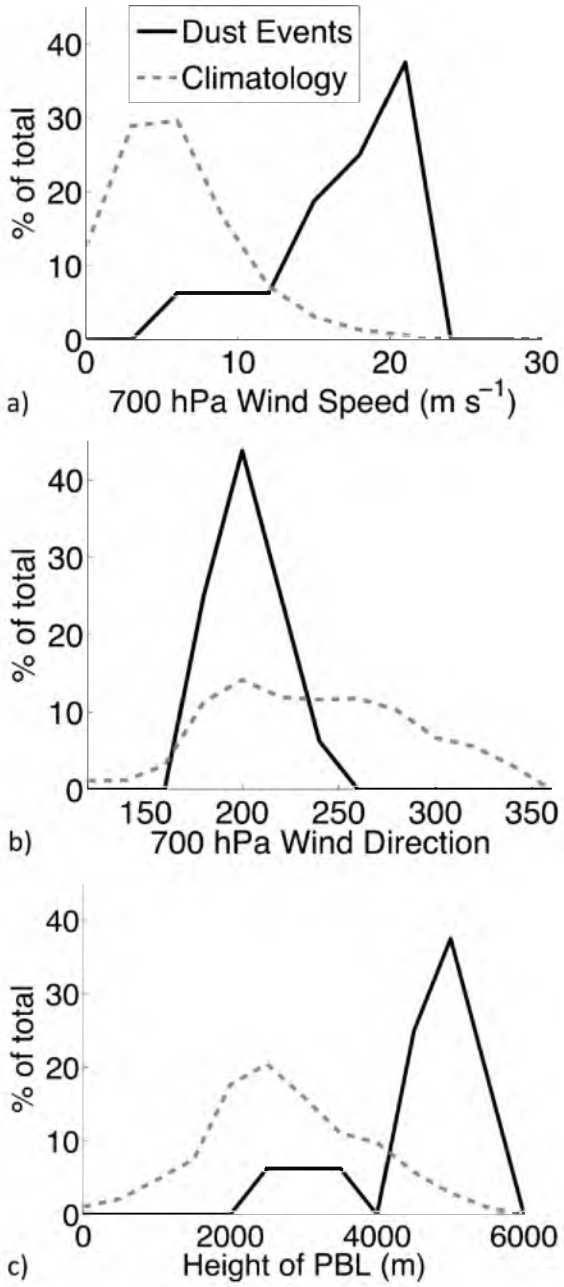

Fig. 5.17. Frequency of NARR (a) 700-hPa wind speed (m s^{-1}) at initial dust report, (b) 700-hPa wind direction (°) at initial dust report, and (c) maximum boundary layer depth (m AGL) at KSLC during recent (2001–10) dust events associated with a cold front or baroclinic trough entering Utah from the west or northwest (solid) relative to a weighted climatology that is based on 21 days centered on each event date (dashed).

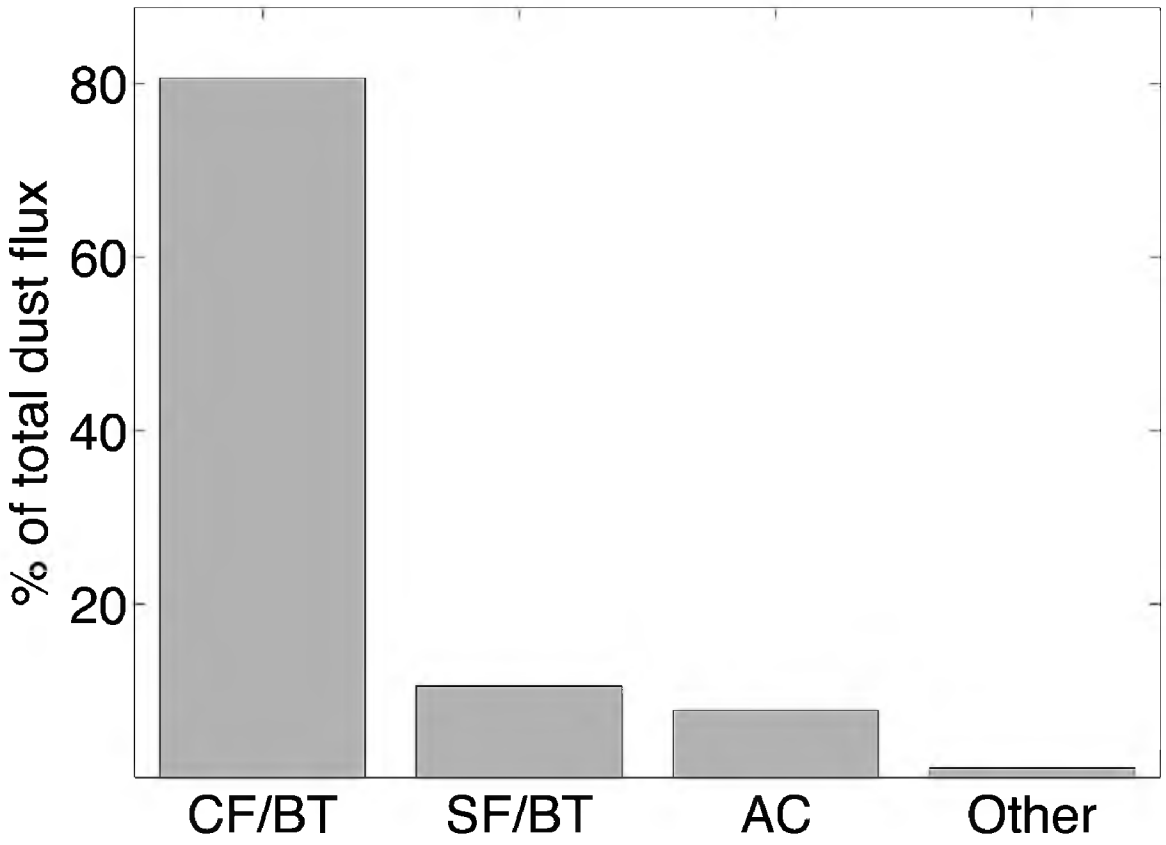

Fig. 5.18. Fraction (%) of total dust flux at KSLC by synoptic condition. Abbreviations are CF/BT (cold fronts and baroclinic troughs entering Utah from the west or northwest), SF/BT (stationary or slowly moving fronts and baroclinic troughs to the west or northwest of Utah), AC (airmass convection), and Other (other synoptic conditions).

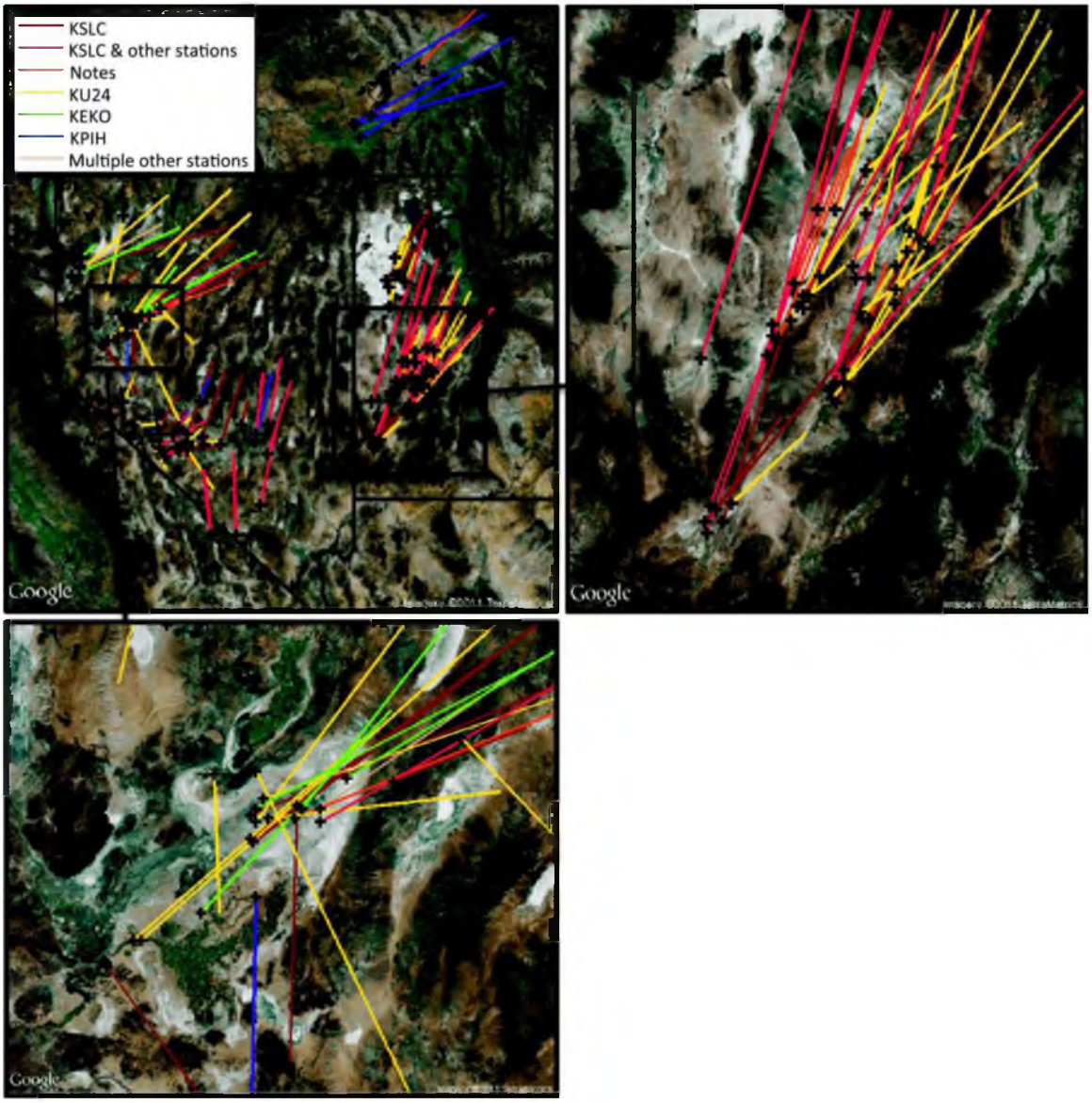

Fig. 5.19. Google Earth image with GOES-derived dust-plume origins and orientations on days during which dust is reported at KSLC, at KSLC and other stations, in the authors' notes or Utah avalanche center reports, at KU24, at KEKO, at KPIH, or at multiple stations other than KSLC. The rectangles in the upper-left panel show the locations of the areas shown in the other two panels. [©2011 Google; imagery ©2011 TerraMetrics].

5.6 References

Bear West Consulting Team, 1999: *Salt Lake City Watershed Management Plan*. Salt Lake City Department of Public Utilities, 129 pp. [Available online at http://www.slcgov.com/utilities/PDF%20Files/slcwatershedmgtplan.pdf].

Belnap, J., R. L. Reynolds, M. C. Reheis, S. L. Phillips, F. E. Urban, and H. L. Goldstein, 2009: Sediment losses and gains across a gradient of livestock grazing and plant invasion in a cool, semi-arid grassland, Colorado Plateau, USA. *Aeolian Res.*, **1**, 27–43.

Brazel, A. J., 1989: Dust and climate in the American southwest. *Paleoclimatology and Paleometeorology: Modern and Past Patterns of Global Atmospheric Transport,* M. Leinen and M. Sarnthein, Eds., Kluwer Academic Publishers, 65–96.

Brazel, A. J., and W. G. Nickling, 1986: The relationship of weather types to dust storm generation in Arizona (1965–1980). *J. Climate.*, **6**, 255–275.

Brazel, A. J., and W. G. Nickling, 1987: Dust storms and their relation to moisture in the Sonoran–Mojave desert region of the south-western United States. *J. Environ. Manage.*, **24**, 279–291.

Carlson, T. N., 1979: Atmospheric turbidity in Saharan dust outbreaks as determined by analyses of satellite brightness data. *Mon. Wea. Rev.,* **107**, 322–335.

Changery, M. J., 1983: A dust climatology of the western United States. National Climatic Data Center Tech. Rep. NUREG/CR-3211, 44 pp.

Fairlie, T. D., D. J. Jacob, and R. J. Park, 2007: The impact of transpacific transport of mineral dust in the United States. *Atmos. Environ.,* **41**, 1251–1266.

Flanner, M. G., C. S. Zender, P. G. Hess, N. M. Mahowald, T. H. Painter, V. Ramanathan, and P. J. Rasch, 2009: Springtime warming and reduced snow cover from carbonaceous particles. *Atmos. Chem. Phys.*, **9**, 2481–2497.

Gebhart, K. A., S. M. Kreidenweis, and W. C. Malm, 2001: Back-trajectory analyses of fine particulate matter measured at Big Bend National Park in the historical database and the 1996 scoping study. *Sci. Total Environ.*, **276**, 185–204.

Gillette, D. A., 1999: A qualitative geophysical explanation for hot spot dust emitting source regions. *Contr. Atmos. Phys.,* **72**, 67–77.

Gillette, D. A., 1988: Threshold friction velocities for dust production for agricultural soils. *J. Geophys. Res.*, **93** (D10), 12645–12662.

Gillette, D. A., J. Adams, A. Endo, and D. Smith, 1980: Threshold velocities for input of soil particulates into the air by desert soils. *J. Geophys. Res.*, **85** (C10), 5621–5630.

Glickman, T., 2000: *Glossary of Meteorology*. 2nd ed., Amer, Meteor. Soc., 855 pp.

Glickman, T., Ed., 2000: *Glossary of Meteorology*. 2nd ed. Amer. Meteor. Soc., 855 pp.

Gorrell, M., 2011: Ski season was Utah's 2nd-busiest. *The Salt Lake Tribune*. 21 Nov 2011 [Available online at http://www.sltrib.com/sltrib/money/52134347-79/ski-utah-season-2010-11.html.csp].

Goudie, A. S., and N. J. Middleton, 2001: Saharan dust storms: Nature and consequences. *Earth-Sci Rev.*, **56**, 197–204.

Hall Jr., F. F., 1981: Visibility reductions from soil dust in the western U.S. *Atmos. Environ.*, **15**, 1929–1933.

Holcombe, T. L., T. Ley, and D. A. Gillette, 1997: Effects of prior precipitation and source area characteristics on threshold wind velocities for blowing dust episodes, Sonoran Desert 1948–78. *J. Appl. Meteor.*, **36**, 1160–1175.

Husar, R. B., and Coauthors, 2001: Asian dust events of April 1998. *J. Geophys. Res.*, **106** (D16), 18317–18330.

Jaffe, D., and Coauthors, 1999: Transport of Asian air pollution to North America. *Geophys. Res. Lett.*, **26**, 711–714.

Jauregui, E., 1989: The dust storms of Mexico City. *Int. J. Climatol.*, **9**, 169–180.

Jeglum, M. E., W. J. Steenburgh, T. P. Lee, L. F. Bosart, 2010: Multi-reanalysis climatology of Intermountain cyclones. *Mon. Wea. Rev.*, **138**, 4035–4053.

Jewell, P. W., and K. Nicoll, 2011: Wind regimes and Aeolian transport in the Great Basin, U.S.A. *Geomorphology*, **129**, 1–13.

Kaplan, M. L., R. K. Vellore, J. M. Lewis, and M. Young, 2011: The role of unbalanced mesoscale circulations in dust storms. *J. Geophys. Res.*, **116**.

Lewis, J. M., M. L. Kaplan, R. Vellore, R. M. Rabin, J. Hallett, and S. A. Cohn, 2011: Dust storm over the Black Rock Desert: Larger-scale dynamic signatures. *J. Geophys. Res.*, **116**, D06113.

Lott, N., R. Baldwin, and P. Jones, 2001: *The FCC Integrated Surface Hourly Database, A New Resource of Global Climate Data*. National Climatic Data Center Tech. Rep. 2001-01, 42 pp. [Available online at http://www1.ncdc.noaa.gov/pub/data/inventories/ish-tech-report.pdf].

Mesinger, F., and Coauthors, 2006: North American Regional Reanalysis. *Bull. Amer. Meteor. Soc.*, **87**, 343–360.

Munson, S. M., J. Belnap, and G. S. Okin, 2011: Responses of wind erosion to climate-induced vegetation changes on the Colorado Plateau. *Proc. Natl. Acad. Sci.*, **108**, 3854–3859.

NCDC, 2008: *Data Documentation for Data Set 3505 (DSI-3505) Integrated Surface Data*. National Climatic Data Center, 121 pp. [Available online at http://www1.ncdc.noaa.gov/pub/data/documentlibrary/tddoc/td3505.doc].

Neff, J. C., R. L. Reynolds, J. Belnap, and P. Lamothe, 2005: Multi-decadal impacts of grazing on soil physical and biogeochemical properties in Southeast Utah. *Ecol. Appl.*, **15**, 87–95.

Neff, J. C., and Coauthors, 2008: Increasing eolian dust deposition in the western United States linked to human activity. *Nature Geosci.*, **1**, 189–195.

Nicholson, S., 2000: Land surface processes and Sahel climate. *Rev. Geophys.*, **38**, 117–139.

Nickling, W. G., and A. J. Brazel, 1984: Temporal and spatial characteristics of Arizona dust storms (1965–1980). *Int. J. Climatol.*, **4**, 645–660.

N'Tchayi Mbourou, G., J. J. Bertrand, and S. E. Nicholson, 1997: The diurnal and seasonal cycles of wind-borne dust over Africa north of the equator. *J. Appl. Meteor.*, **36**, 868–882.

OFCM, 2005: *Federal Meteorological Handbook No. 1: Surface Weather Observations and Reports*. Office of the Federal Coordinator for Meteorological Services and Supporting Research, Surface Weather Observations and Reports. [Available online at http://www.ofcm.gov/fmh-1/fmh1.htm].

Okin, G. S, and Coauthors, 2011. Dust: Small-scale processes with global consequences. *EOS Trans. Am. Geophys. Union*, 92, 241–242.

Orgill, M. M., and G. A. Sehmel, 1976: Frequency and diurnal variation of dust storms in the contiguous U.S.A. *Atmos. Environ.*, **10**, 813–825.

Painter, T. H., and Coauthors, 2007: Impact of disturbed desert soils on duration of mountain snow cover. *Geophys. Res. Lett.*, **34**, L12502, doi:10.1029/2007GL030284.

Painter, T. H., J. S. Deems, J. Belnap, A. F. Hamlet, C. C. Landry, and B. Udall, 2010: Response of Colorado River runoff to dust radiative forcing in snow. *Proc. Natl. Acad. Sci.*, **107**, 17125–17130.

Pope, C. A., D. V. Bates, and M. E. Raizenne, 1995: Health effects of particulate air pollution: Time for reassessment? *Env. Health Perspect.*, **103**, 472–480.

Prospero, J. M., and P. J. Lamb, 2003: African droughts and dust transport to the Caribbean: Climate change implications. *Science*, **302**, 1024–1027.

Qian, W., L. Quan, and S. Shi, 2002: Variations of the dust storm in China and its climatic control. *J. Climate*, **15**, 1216–1229.

Ramanathan, V., P. J. Crutzen, J. T. Kiehl, and D. Rosenfeld, 2001: Aerosols, climate, and the hydrological cycle. *Science*, **294**, 2119–2124.

Reynolds, R., J. Belnap, M. Reheis, P. Lamothe, and F. Luiszer, 2001: Aeolian dust in Colorado Plateau soils: Nutrient inputs and recent change in source. *Proc. Natl. Acad. Sci.*, **98**, 7123–7127.

Reynolds, R., and Coauthors, 2007: Dust emissions from wet and dry playas in the Mojave Desert, USA. *Earth Surf Processes Landforms*, **32**, 1811–1827.

Reynolds, R. L., J. S. Mordecai, J. G. Rosenbaum, M. E. Ketterer, M. K. Walsh, and K. A. Moser, 2010: Compositional changes in sediments of subalpine lakes, Uinta Mountains (Utah): Evidence for the effects of human activity on atmospheric dust inputs. *J. Paleolimnol.*, **44**, 161–175.

Ritchie, E. A., K. M. Wood, D. S. Gutzler, and S. R. White, 2011: The influence of Eastern Pacific tropical cyclone remnants on the Southwestern United States. *Mon. Wea. Rev.*, **139**, 192–210.

Sanders, F., 1999: A proposed method of surface map analysis. *Mon. Wea. Rev.*, **127**, 945–955.

Shafer, J. C., and W. J. Steenburgh, 2008: Climatology of strong intermountain cold fronts. *Mon. Wea. Rev.*, **136**, 784–807.

Shao, Y., and J. Wang, 2003: A climatology of Northeast Asian dust events. *Meteor. Zeitschrift*, **12**, 187–196.

Shao, Y., and Coauthors, 2003: Northeast Asian dust storms: Real-time numerical prediction and validation. *J. Geophys. Res.*, **108**, 4691, doi:10.1029/2003JD003667.

Song, Z., J. Wang, and S. Wang, 2007: Quantitative classification of northeast Asian dust events. *J. Geophys. Res.*, **112**, D04211, doi:10.1029/2006JD007048.

Steenburgh, W. J., and T. I. Alcott, 2008: Secrets of the "Greatest Snow on Earth". *Bull. Amer. Meteor. Soc.*, **89**, 1285–1293.

Stout, J. E., 2001: Dust and environment in the Southern High Plains of North America. *J. Arid Environ.*, **47**, 425–441.

Swap, R., S. Ulanski, M. Cobbett, and M. Garstang, 1996: Temporal and spatial characteristics of Saharan dust outbreaks. *J. Geophys. Res.,* **101** (D2), 4205–4220.

Tanaka, T. Y., and M. Chiba, 2006: A numerical study of the contributions of dust source regions to the global dust budget. *Glob. Planet. Change*, **52**, 88–104.

VanCuren, R. A., and T. A. Cahill, 2002: Asian aerosols in North America: Frequency and concentration of fine dust. *J. Geophys. Res.*, **107**, 4804, doi:10.1029/2002JD002204.

Wakimoto, R. M., 1982: The life cycle of thunderstorm gust fronts as viewed with Doppler radar and rawinsonde data. *Mon. Wea. Rev.*, **110**, 1060–1082.

West, G. L., and W. J. Steenburgh, 2010: Life cycle and mesoscale frontal structure of an Intermountain cyclone. *Mon. Wea. Rev.,* **138**, 2528–2545.

Wheaton, E. E. and A. K. Chakravarti, 1990: Dust storms in the Canadian prairies. *Int. J. Climatol.*, **10**, 829–837.

WMO, 2009: *Manual on Codes: International Codes*, Vol. I.1 (Part A – Alphanumeric Codes). World Meteorological Organization Report WMO-No. 306. [Available online at http://www.wmo.int/pages/prog/www/WMOCodes/VolumeI1.html#VolumeI1].

Yasunori, K., and M. Masao, 2002: Seasonal and regional characteristics of dust event in the Taklimakan Desert. *J. Arid Land Studies*, **11**, 245–252.

Zhoa, T., S. Ackerman, and W. Guo, 2010: Dust and smoke detection for multi-channel imagers. *Remote Sens.*, **2**, 2347–2368.

Zobeck, T. M., D. W. Fryrear, and R. D. Pettit, 1989: Management effects on wind-eroded sediment and plant nutrients. *J. Soil Water Cons.*, **44**, 160–163

CHAPTER 6

CONCLUSION

6.1 Summary of Findings

Eight months of September and October operational WRF forecasts (4DWX-DPG) underpredict the strength of the diurnal temperature range (DTR) over Dugway Proving Ground in northwest Utah during September and October of 2011, 2012, 2013, and 2014. The nighttime warm bias is confined to the lowest few model levels in valleys and basins and the daytime cold bias exists through the top of the planetary boundary layer. The diurnally dependent biases are strongest during mostly clear days and vary geographically depending on the underlying land surface. This suggests that the underprediction of the DTR is related to the partitioning of net radiation into sensible, ground, and latent heat fluxes.

The nighttime warm bias is primarily related to an overestimation of local near-surface soil moisture and an inaccurate soil thermal conductivity parameterization. The Noah land surface model (LSM) currently coupled to the WRF uses a modified version of the Johansen (1975; J75) soil thermal conductivity parameterization, but this method replaced the McCumber and Pielke (1981; MP81) parameterization in 2001. The use of MP81 over silt loam and sandy loam soils and J75 elsewhere, along with soil moisture analyses derived from observations, greatly reduces the nighttime warm bias errors over

northern Utah. These changes are also supported by soil thermal conductivity and ground heat flux observations collected during the Mountain Terrain Atmospheric Modeling and Observations (MATERHORN) fall field campaign. We expect other dryland regions with silt loam and sandy loam soil textures to have improved nighttime temperature forecasts when MP81 is used in conjunction with improved soil moisture initialization.

The daytime cold bias is the result of a regional soil moisture overestimation in land surface analyses across the Intermountain West. Using 42 North American Soil Moisture Database (NASMDB) stations, we bias corrected the 5- and 25-cm soil moisture analyses over the Intermountain West in a fully-cycled forecasting system and nearly eliminate the daytime cold bias. Upper-level temperature forecasts and atmospheric stability also improved. The soil moisture overestimation is the result of inadequate global soil moisture analyses that do not currently assimilate soil moisture observations. Utilization of surface station observations or spaceborne microwave remote sensing platforms, such as the recently launched Soil Moisture Active/Passive (SMAP) mission, could improve global soil moisture analyses and near-surface meteorological weather forecasts worldwide.

WRF simulations are also are validated against surface energy balance observations collected over playa and desert shrub land surfaces. When NASMDB soil moisture observations are incorporated into the land surfaces analyses and MP81 is used over silt loam and sandy loam soils, the surface energy balance forecast generally improves over the desert shrub, but degrades over the playa. The desert shrub improvement is greatest during the MATERHORN fall field campaign and the playa errors are largest during the MATERHORN spring field campaign when observed soil

moisture is higher. Simulations that also incorporate satellite-derived albedo into the land surface analyses, and a reduced saturation vapor pressure over the playa, only improve the playa surface energy balance marginally. Over the playa, the latent heat flux is overpredicted likely because the Noah land surface model does not currently account for the effects of a salt crust, high water table, or reduced osmotic potential at the playa soil surface on evaporation. Nevertheless, these changes produce improved sensible heat flux and 2-m temperature difference between the playa and desert shrub, which increases the strength of the daytime off-playa breeze. The increase of daytime wind speed improves the overall wind speed bias error, but does not necessarily improve wind speed and direction mean absolute errors because errors improve over some regions, like the playa boundary in eastern DPG, but worsen over other areas. This work highlights some Noah land surface model deficiencies over two common arid land surfaces and demonstrates the importance of land surface analyses.

Episodic dust events are a land-surface phenomena that occur over the Great Basin with significant interannual variability, and a bimodal monthly distribution, with a primary maximum in April and secondary maximum in September. Events are driven primarily by cold fronts, baroclinic troughs, and airmass convection. A dust retrieval algorithm adapted for data from geostationary operational environmental satellites identified dust source regions, which are primarily located in low-elevation Late Pleistocene–Holocene alluvial environments in southern and western Utah and southern and western Nevada.

6.2 Future Work

One straightforward extension of this dissertation is to test the soil moisture, soil thermal conductivity, and albedo changes proposed in these studies over other regions. We hypothesize other dryland regions, especially those with silt loam and sandy loam soils, would benefit from these changes. Forecasts may also improve over regions that have a large near-surface soil moisture discrepancy between observations and global soil moisture analyses.

The global soil moisture analyses should not only be validated against all available in situ soil moisture observations and spaceborne measurements, such as the soon-to-be-available SMAP analyses, but these observations should also be assimilated into the analyses. Better global land surface analyses could improve near-surface atmospheric predictability, and also have implications for hydrological and biological modeling.

In Chapter 3, we describe the development of an evening transition 2-m temperature cold bias and morning transition warm bias in the simulations that bias-correct the soil moisture analyses. Single-column model experiments not presented in this dissertation suggest these biases are very sensitive to small soil thermal conductivity and soil heat capacity estimation errors. MP81 may be the best available soil thermal conductivity parameterization over silt loam and sandy loam soils, and J75 may be the best available parameterization elsewhere, but these parameterizations have limitations. There is a strong need for a more accurate and universal soil thermal conductivity parameterization. The parameterization of heat capacity is a function of the soil mass, water content, and air content. These variables all depend on the soil moisture and soil

porosity, which is defined for each soil texture class. Improving the estimation of soil and landuse properties, like porosity, will likely improve near-surface forecasts.

In Chapter 5, we show significant latent heat flux (LE) errors over the playa that worsen with observed soil moisture. The playa is a very unique land surface due to its high water table and salinity, and a different evaporation parameterization needs to be developed to capture some of its unique processes. For example, during dry periods the high water table rehydrates the surface at night and the high salinity causes a salt crust to form preventing evaporation. Also, during wet periods the playa can flood, which greatly reduces the albedo. Some parameterizations have already been developed to capture some of these effects (e.g., Gowing et al. 2006), but cannot easily be incorporated into the Noah land surface model. More work is needed developing a feasible playa parameterization for the Noah land surface model.